PLANE WAVE SYNTHESIS : A NEW APPROACH TO THE PROBLEM OF ANTENNA NEAR-FIELD/FAR-FIELD TRANSFORMATION

by

E. P. Schoessow, B.Eng.

A thesis presented in candidature for the degree of Doctor of Philosophy, University of Sheffield, Department of Electronic and Electrical Engineering.

September 1980.

To my Parents

SUMMARY

In the recently evolved fields of satellite and space communications as well as in a number of related areas, a vital requirement is an accurate knowledge of the radiating and receiving characteristics of the transmitting and receiving antennas as they appear at a large distance (in the so called far-field region). It is often impossible to obtain a direct measurement of the performance of an antenna and in such cases where it is possible, the accuracy obtainable is frequently limited by the many difficulties associated with the process.

Over recent years, a number of techniques have begun to appear which allow measurement of data close to the test antenna (in the near-field region) and then by mathematical processing (the transformation) predict what the far-field performance will be. The earlier techniques while being basically simple from a mathematical viewpoint, were not completely general and tended to involve special, sophisticated, hardware. The later techniques use the most general spherical scanning system but involve much more complicated processing.

A new approach to the problem is presented in which much of the computational burden is pre-processed so that the size and complexity of the ultimate prediction task is reduced. The various measurement systems are considered briefly and the spherical system is formulated in detail. Simulated and experimental predictions are carried out

and studies are included of the various errors likely to be present and their effects. The important parameters, including the sampling criterion, are discussed in some detail.

It is shown that this technique has the potential for producing rapid and accurate predictions of antenna far-field patterns including the facility of compensation for the characteristics of the measurement probe.

PUBLICATIONS

Parts of the work described in this thesis have formed the basis of a number of publications. These are:

Bennett, J.C. and Schoessow, E.P., 'Near-field/far-field transformation using a plane wave synthesis technique', 3rd Antenna Symposium, Queen Mary College, London, 1977.

Bennett, J.C. and Schoessow, E.P., 'Near-field/far-field transformation using a plane wave synthesis technique', Proc., Workshop on antenna testing techniques, ESTEC, Noordwijk, Netherlands, 1977, pp.135-136.

Bennett, J.C. and Schoessow, E.P., 'Near-field/far-field transformation using a plane wave synthesis technique', Proc.IEE, 125, 1978, pp.179-184.

Schoessow, E.P. and Bennett, J.C., 'Recent progress in the plane wave synthesis technique for antenna near-field/far-field transformation', Proc.International Conference on Antennas and Propagation, IEE, London, 1978, pp.123-127.

Bennett, J.C. and Schoessow, E.P., 'Near-field to far-field transformation using a plane wave synthesis technique', Proc.seminar on Compact Antenna Ranges, Royal Signals and Radar Establishment, Malvern, 1980.

ACKNOWLEDGEMENTS

The author wishes to express his appreciation to a number of individuals and organisations whose help has been of great value to the work described in this thesis:

- Professor F.A. Benson and the University of Sheffield, Department of Electronic and Electrical Engineering for the facilities made available during the work.
- Dr. J.C. Bennett and Dr. A.J.T. Whitaker both of whom have made invaluable practical contributions to the work and always made themselves available for discussions when requested.
- The many other members of the Department of Electronic and Electrical Engineering who have made contributions to the progress including David Cox (the test site technician) and Haydn Flower and his workshop staff.
- Mr. K. Kilford and the Department of Civil and Structural Engineering for the temporary loan of a sensitive optical level.
- The U.K. Science Research Council and latterly the Ministry of Defence for financial support.
- Margaret Eddell for kindly offering her services as typist for this thesis.

LIST OF PRINCIPAL SYMBOLS

θ, ϕ	-	spherical coordinates, particularly in near-field data.
θ_w, ϕ_w	-	spherical coordinates in weighting function.
θ_F, ϕ_F	-	far-field spherical coordinates.
θ_p, ϕ_p	-	spherical coordinates in probe measurement system.
x, y, z	-	general Cartesian coordinate.
x_p, y_p, z_p	-	Cartesian coordinates of probe.
λ	-	wavelength.
$k = 2\pi/\lambda$	-	propagation (phase) constant.
r	-	general distance.
R	-	radius of near-field measurement sphere.
D	-	diameter of synthesised plane wave.
$g(\theta,\phi)$	-	weighting function.
θ_m, ϕ_m	-	limits of $g(\theta, \phi)$.
$P(\theta_F,\phi_F)$	-	predicted far-field at (θ_F, ϕ_F)
r_{pw}, θ_{pw}	-	polar coordinates of point in plane wave.
E_x	-	electric field component in x-direction (other directions denoted with different subscripts).

CONTENTS

1. INTRODUCTION

1.1 Background to the Subject

In the very early days of radio communication, with so much available space in the frequency spectrum, multiple use of the same wavelength was largely unnecessary and therefore the problems caused for the receiver operator by interference from unwanted transmissions were slight. As time progressed and the number of transmitting stations increased, the phenomenon of multiple-source interference became more apparent. Clearly partial solutions to the problem were readily available:

(a) A limit could be imposed on the power to be radiated from any particular transmitter. Space attenuation could then be relied upon to reduce the unwanted signal to acceptable levels.

(b) The receiver could be made more frequency-selective so that transmissions on even very similar wavelengths could be adequately separated.

These are indeed two of the basic methods used for avoiding interference as far as public broadcasting is concerned. A few moments, however, spent listening to the medium-wave A.M. broadcast band, for instance, are ample demonstration that these techniques alone are, in many circumstances, far from sufficient.

The other obvious remedial action was the use of a receiving antenna with particular, non-isotropic reception characteristics (and in the case where a particular transmitter-receiver link was involved, this was equally

applicable to the transmitting antenna). Engineers applied their talents, therefore, to the design of suitable antennas.

Originally certain types of directive antennas were constructed on an essentially empirical basis but their performance still had to be evaluated. At the frequencies then most used, this seldom presented serious difficulty, since the far-field patterns of the antennas were established at quite short ranges. This meant that the radiation patterns could be measured directly. In any case, the antennas were required usually for ground-to-ground fixed station communication and therefore the ground coverage could be (and indeed had to be) investigated in situ.

The situation is vastly different nowadays. With the increasing use of higher frequencies and, in particular, the associated progression in the electrical size of antennas from a fraction of a wavelength to, in some cases, many hundreds or even thousands of wavelengths, the distances required to perform direct far-field measurements have become impossibly large. In such applications as radio astronomy and satellite and space communications, it is almost invariably the far-field pattern which is of importance and, in the latter instances, bearing in mind the vast sums of money involved, it is essential that the measurements should be carried out on Earth so that any faults can be corrected before launch. At best, an incorrect radiation pattern means that a satellite antenna, for instance, may be wasteful of the precious power available. At worst,

for example where security is important, a high sidelobe in the wrong place may mean that the device is useless. In a deep space probe, where achieving the maximum possible gain is vital, an antenna fault may mean total failure of the mission.

Even when a direct measurement of a far-field radiation pattern is possible, there are many problems accompanying the use of long outdoor measurement ranges:

(a) Range reflections.

(b) Atmospheric effects, dependence upon weather conditions and lack of climatic control.

(c) The relatively high power requirement to achieve a usable signal-to-noise ratio.

(d) Interference from unwanted signals.

(e) Interference created for other people.

(f) Lack of security.

(g) Cost of real estate.

These mean that the order of accuracy now being sought is often unattainable (or unaffordable). As a result, other techniques for evaluating the performance of antennas have been developed. These may be divided broadly into two groups: those that attempt to simulate the far-field measurement conditions in the near-field and those that use numerical manipulation of measured near-field data to predict the far-field pattern (the so called near-field/ far-field transformation).

1.2 Far-Field Simulation Techniques

1.2.1 Antenna Refocussing

This technique[1][2] relies on the principle that, "if the probe cannot be taken to the far-field, the far-field must be brought to the probe". This is relevant, in particular, to reflector antennas and uses the property that if the feed position is suitably adjusted in the axial direction, a pattern often quite similar to the far-field pattern can be made to exist in the near-field. This suffers from several serious drawbacks:

(a) Limited applicability. The method can only be applied to certain reflector antennas.

(b) It requires the ability precisely to adjust (and subsequently reset) the axial position of the feed.

(c) It is not totally accurate and gives particularly poor results at large angles from boresight.

1.2.2 The Compact Range

The compact range near-field technique is particularly relevant to the main body of this thesis. It relies on the fact that in the region a short distance in front of a precisely made (and suitably fed) parabolic reflector antenna, the field distribution is essentially that of a plane wave (Fig. 1.1). Thus the plane wave response (which is identically the far-field response) can be measured for a test antenna placed within that region. Various publications have described compact ranges in more detail[3][4][5]. The main disadvantages seem to be:

(a) The specialised hardware - the reflector.

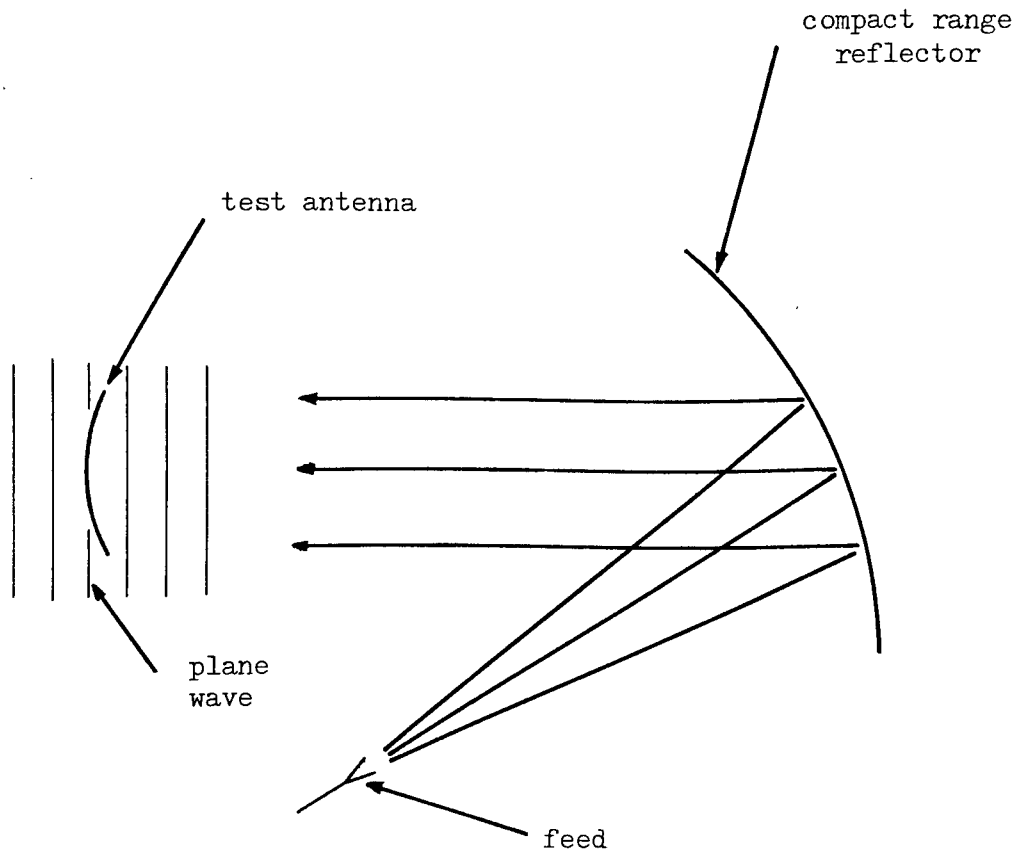

Fig. 1.1. The compact range principle.

(b) The test antenna size is limited to being rather smaller than the compact range reflector.

It has been proposed that a dielectric lens might be used instead of the reflector [6]. Similar drawbacks to those above apply in this case.

Compact ranges have become established tools in antenna measurement and quite a number are now in use throughout the world.

1.3 Near-Field/Far-Field Transformation

In the near-field/far-field transformation, mathematical processing of data acquired close to the antenna is employed in an effort to predict what would be measured by an ideal far-field test range. An ideal test range may be taken to be one in which an infinitesimal probe, correctly polarised, is placed a very large distance from the test antenna. Both the antenna and the probe should be suspended in free-space with no extraneous support or feed structures and remote from any other bodies. The receiving system should be totally noise-free and no other signal sources (whether man-made or natural) should exist. This is not, of course, practically realisable.

The theory relating the fields existing near to an antenna to those remote from it is far from simple and it has, in general, been considered necessary to solve a substantial number of field equations. Analytical solution of the equations is usually either impossible or so tedious as to be impracticable but with the rapidly increasing power of modern computing equipment, numerical treatment has become

feasible. Even so, the complexity of hardware and software requirements has meant that although the theoretical basis for performing the near-field/far-field transformation has been in existence for a few years, it is only comparatively recently that operational ranges have appeared (e.g. U.S. National Bureau of Standards, Georgia Institute of Technology, Technical University of Denmark). It may be useful, at this point, to review briefly some of the existing techniques.

1.3.1 Fourier Transformation based upon the Scalar Diffraction Formula

The Fourier transform relationship approximation between the field distribution over a radiating aperture and its far-field pattern is well known. It relies essentially upon the Kirchoff scalar diffraction formula[7] and has been investigated and exploited in various schemes[8][9][10]. The process in a simplified form is as follows. A two dimensional Fourier transform (normally effected by means of a "fast Fourier transform" - FFT - algorithm) is performed upon the measured near-field data to yield (after some phase corrections and within the limits of the paraxial approximations made) the field distribution over the antenna aperture (or over an arbitrary plane passing through or near the origin of the coordinate system). Subsequent inverse transformation gives a prediction of the far-field pattern. Unfortunately, because of the paraxial approximations made, the technique is strictly only useful for a very directive antenna and for the prediction of the pattern near to boresight. Nevertheless, it is a tool which

can prove very useful if these limitations are acceptable.

1.3.2 Planar Scanning

Another concept which has been utilised successfully in antenna work is that of the infinite plane wave spectrum of a radiated field. It can be shown[11] that the fields radiated by an antenna can be rewritten as the sum of a series of plane waves propagating in different directions. The object of the technique, termed plane wave expansion, is to determine the unknown amplitudes and phases of these different plane waves obtaining what is known as a modal expansion of the field. This is achieved using the measured near-field over a planar surface (Fig. 1.2). The expansion may then be extrapolated to the far-field to provide the pattern prediction. The process is described in more detail by Paris et al[12], Joy et al[13] and Joy and Paris[14] (and also in a slightly modified approach by Kerns[15]) and it is demonstrated that it becomes computationally efficient since an FFT algorithm can be employed to perform the numerical integrations involved.

Antenna pattern prediction utilising planar scanning is possibly the most deeply investigated method and has been shown to give good prediction accuracy. It has the advantage (particularly as compared with spherical scanning methods) of numerical simplicity and, because the scan is performed by the probe, no positioning system is required for the test antenna. Under certain circumstances, this latter can prove to be an advantage but at other times becomes a drawback:

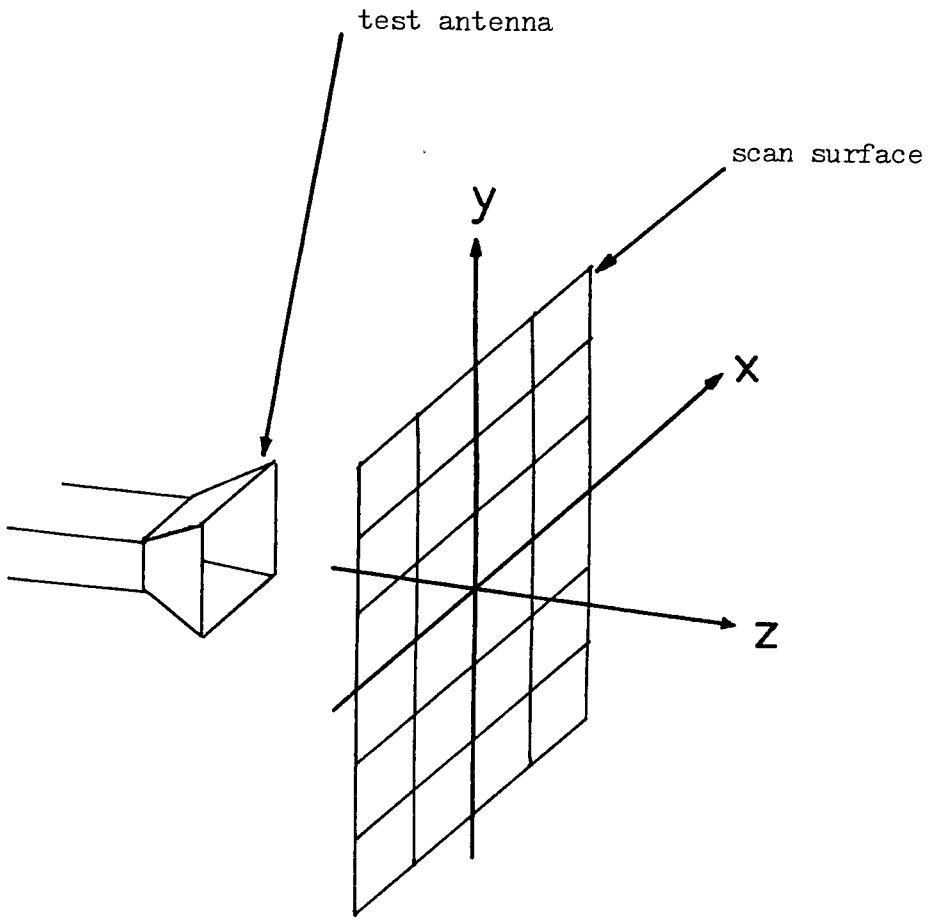

Fig. 1.2. Planar scanning.

(a) The planar scanning system itself is a fairly complicated device presenting probably more mechanical problems than the more conventional positioner systems. Therefore the capital cost involved in actually setting up a measurement facility could be greater.

(b) The size of antenna which can be accommodated is limited by the size of the scanning device whereas a spherical scanning method might be applicable even to a very large antenna if it can be measured in situ using its own positioner system.

The other chief disadvantage is that a set of measurements can provide predictions over only a limited angular range (as determined by the size of the scanning device and in any event limited to less than the half-space behind the scan plane). Another point particularly significant in this scheme is the need to incorporate compensation for the radiating characteristics of the near-field probe being used. Because, in a spherical scanning technique, the probe always points towards the origin of the coordinate system, the need for compensation is not so vital if the probe is suitably chosen since the variations in the illumination of the test antenna will be small (although for maximum accuracy, the possibility of including probe compensation is desirable). This argument does not apply in the case of planar scanning since, even with a small (and therefore wide-beam) probe, the test antenna can pass through an appreciably greater angular range of the probe pattern to introduce large variations in the illumination. This becomes even more

important when one realises that the requirement of achieving the best signal-to-noise ratio in the measurements tends to favour narrower beam probes.

1.3.3 Cylindrical Scanning

Here, the radiated fields are generally evaluated in the form of a cylindrical wave expansion[16][17] (although the method devised by Borgiotti[18] utilises a superposition of plane waves) and again the problem reduces to that of determining the various coefficients. Once more, computational efficiency is enhanced by the possibility of using the FFT to perform the numerical integrations.

An advantage of the cylindrical scheme over the planar one is that in one of the scan coordinates, prediction is possible right around the antenna. Additionally, the mechanical requirements are less severe since the probe positioner is a simple linear device and the other scanning coordinate is achieved by virtue of a conventional azimuth positioner (Figures 1.3 and 1.4). A disadvantage is that the numerical processing is a little more complicated. Probe compensation is again important.

The cylindrical scanning approach has not been so widely utilised as planar scanning but it has been demonstrated to be experimentally and computationally viable[19].

1.3.4 Spherical Scanning

The major advantage of using a spherical surface is that a single set of measurements can provide radiation pattern predictions over the full spherical far-field surface. Additionally, as already mentioned, because of the nature of

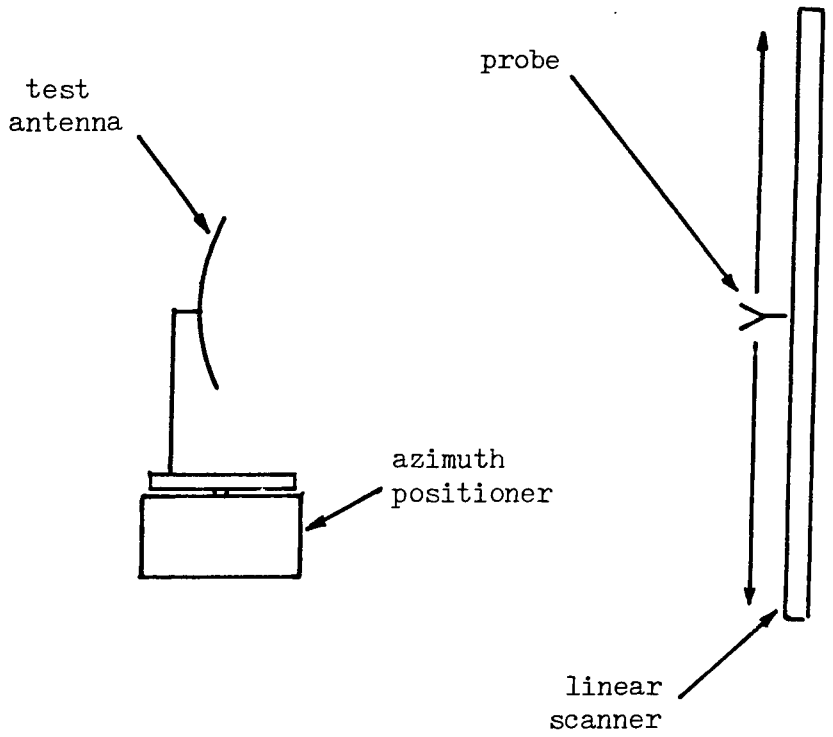

Fig. 1.3. The cylindrical scan system.

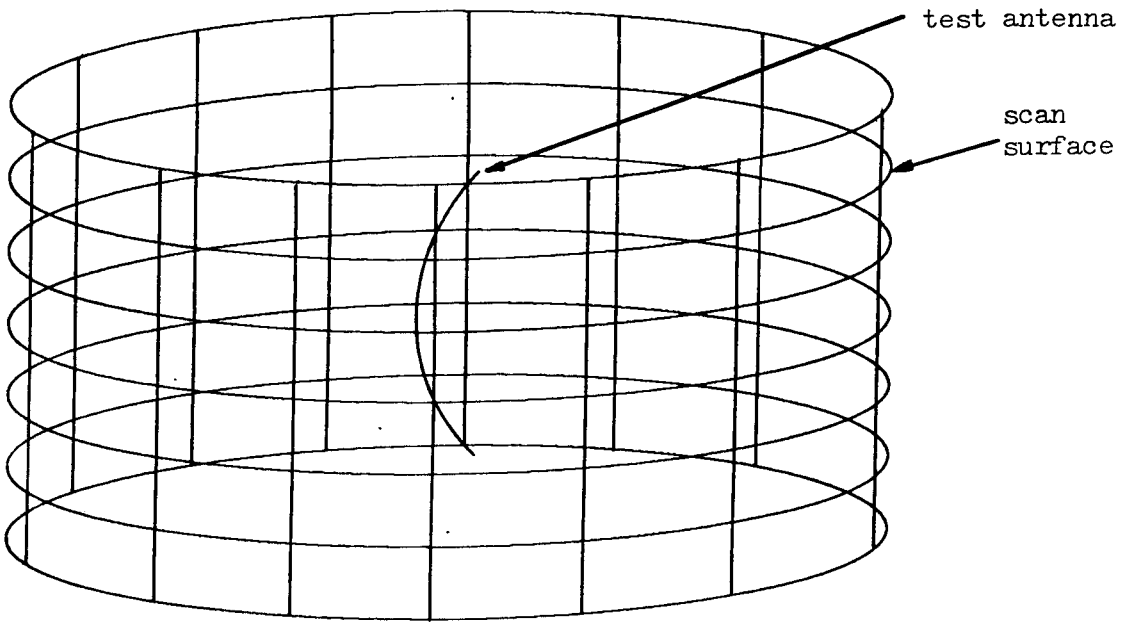

Fig. 1.4. The sample geometry produced by a cylindrical scan.

this scan geometry, probe compensation is not so necessary as in the other systems (although for maximum accuracy, it should certainly be incorporated - Chapter 5 provides information about the errors likely to be introduced by incorrect probe compensation).

Conventionally, the spherical measurement geometry has been regarded as presenting the greatest problems as regards the necessary computing power. The near-fields are analysed in the form of a spherical wave expansion [20] [21] [22] which can then be extrapolated to another measurement range, usually the far-field. It has been found difficult to express the formulae in such a way as to enable efficient computation (such as the FFT) to be utilised for the numerical integrations although recent work [23] has considerably improved the efficiency. Nevertheless, the memory requirements are very heavy, a figure of 1200 k words being quoted as the requirement for processing a 1^{o} x 1^{o} data scan (equivalent to about 50 λ antenna) with 90 k being needed even for a 30^{o} x 30^{o} set.

From the hardware point of view, spherical scanning is possibly the most straightforward since a conventional dual-positioner configuration (elevation-over-azimuth, azimuth-over-elevation or polarisation-over-azimuth) is all that is required. Furthermore there is effectively no limit on the size of antenna which can be measured (at least as regards hardware) in contrast to the previous two schemes in which the probe positioning systems provided a limit.

The limit on the size of antenna which can be measured is provided by two factors; the time taken to acquire the data (which can run into many hours) and the processing

requirements (in terms of time and of the amount of storage needed). The constraint is thus on the electrical size rather than the physical size of the test antenna and figures quoted for maximum possible antenna size are typically in the region of 100 λ or less.

1.4 The Objectives of the Present Work

As has been seen, the least demanding computational requirements for a near-field/far-field transformation correspond to what is probably the least flexible and least general scan geometry; planar. At the opposite end of the scale, the most general and probably the easiest scanning system to implement (spherical) requires the greatest computing power. At the end of the present study, it would be desirable to have a scheme which can utilise certainly the spherical scan geometry (and ideally be applicable to the others) but requires simpler processing. In particular, the processing which takes place after the measurements have been obtained should be kept to a minimum, i.e. as much of the work as possible should be accomplished by preprocessing. Accuracy should, of course, be preserved.

The idea which emerged from this line of thought is based on a concept similar to that described by Martsafey[24] (although this publication came to light some considerable time after the present approach evolved and some of the main features of the present method are given little or no consideration). It is termed plane wave synthesis and relies on the precomputation of a weighting function to be applied to the measured data. The details of the technique

are given in later chapters. It is noted here that this volume is devoted almost entirely to the implementation of the technique in the spherical scan case, and we now proceed to introduce the spherical scan geometry and the conventions used.

1.5 The Spherical Scan Geometry

Only two forms of spherical scan geometry are used in this thesis, elevation-over-azimuth and polarisation-over-azimuth. The azimuth-over-elevation geometry can be regarded as an elevation-over-azimuth system rotated through 90^{o}.

1.5.1 Elevation-Over-Azimuth System

In the elevation-over-azimuth scanning system, the lower of the two positioners is an azimuth device with its axis vertical. Mounted on this turntable is an elevation positioner with its axis horizontal. The resulting arrangement is such that a stationary probe covers an effective measurement surface (when a test antenna is scanned on the system) which is spherical (if the two positioner axes intersect) and of the form shown in Fig.1.5 with the two poles of the scan geometry occurring at either end of the elevation axis. The conventions used throughout this thesis as regards the Cartesian coordinates, x, y and z, and the angular coordinates, θ and ϕ, are shown in Fig. 1.5 and also in more detail in Fig. 1.6. It may be worth noting that these coordinates as used here do not necessarily correspond exactly with their usage elsewhere.

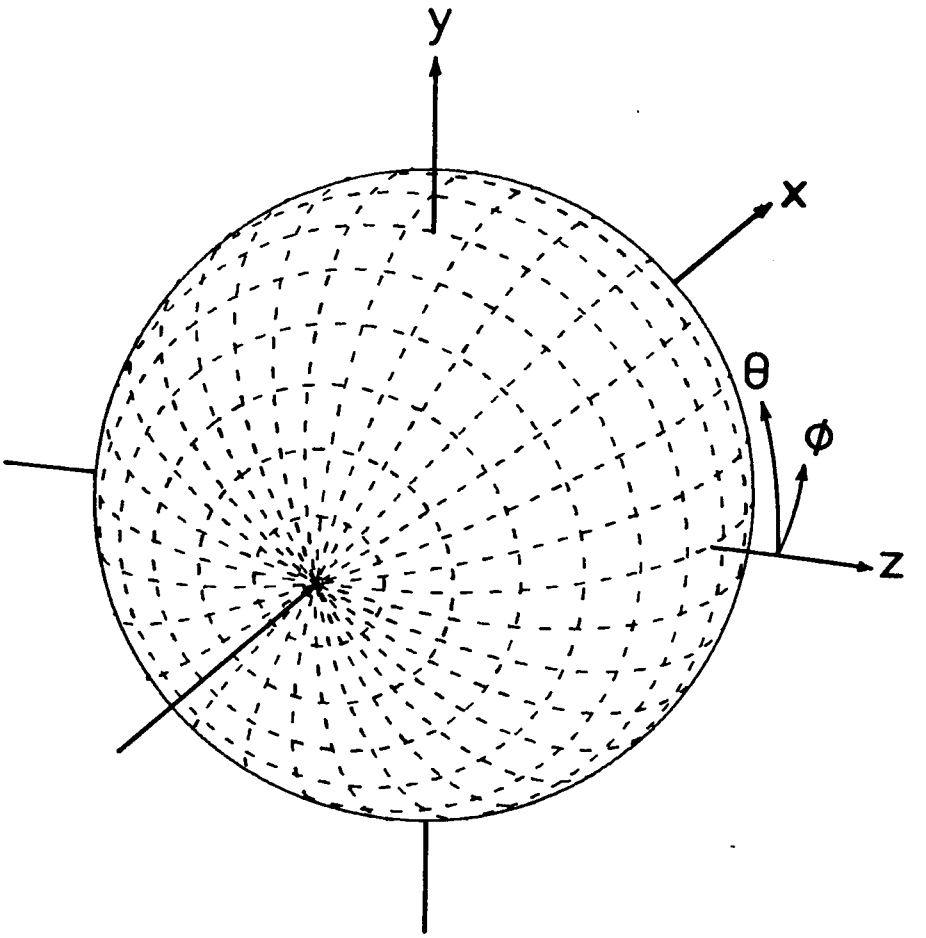

Fig. 1.5. The sample geometry produced by an elevation-over-azimuth spherical scan system.

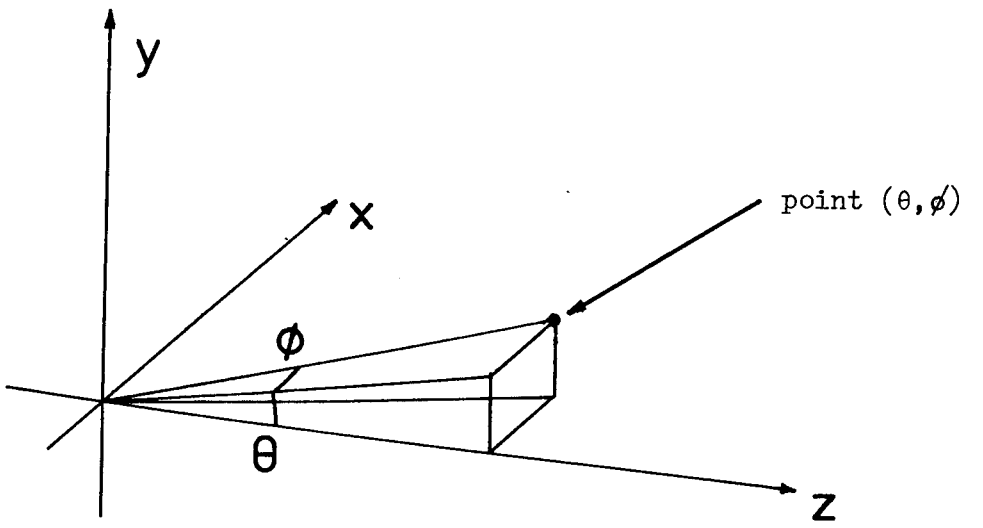

Fig. 1.6. Detail of the elevation-over-azimuth spherical coordinates as used throughout this thesis.

Two possibilities for the form of the elevation positioner exist: the side-pivoted and the rear-pivoted (illustrated in Fig. 1.7). The rear-pivoted system is the more popular since the mounting structure is more compact and further from the front of the test antenna but it suffers from the drawback that it cannot execute a full spherical scan (since it cannot point directly downwards). The side pivoted system has, in principle, the capability for performing an all-space scan but has the disadvantage of a more prominent (and therefore reflection-prone) structure and furthermore, when the antenna is at -90^{o} elevation (looking downwards) it is pointing directly at the nearby support structure (and azimuth turntable) which will cause quite serious reflection problems in many cases. The spherical positioning system which overcomes, to a large extent, these difficulties is the polarisation-over-azimuth system which will now be described.

1.5.2 Polarisation-Over-Azimuth System

Because the polarisation-over-azimuth scan geometry (illustrated in Fig. 1.8) is such that at no time does the test antenna point towards the support structure, it suffers rather less from problems of reflection. It still provides, however, the capability for an all-space scan. A minor drawback is that with a single-polarisation probe only one principal plane cut can be made with co-polarisation, all the other possible cuts being at various other polarisations. An elevation-over-azimuth system can produce co-polar

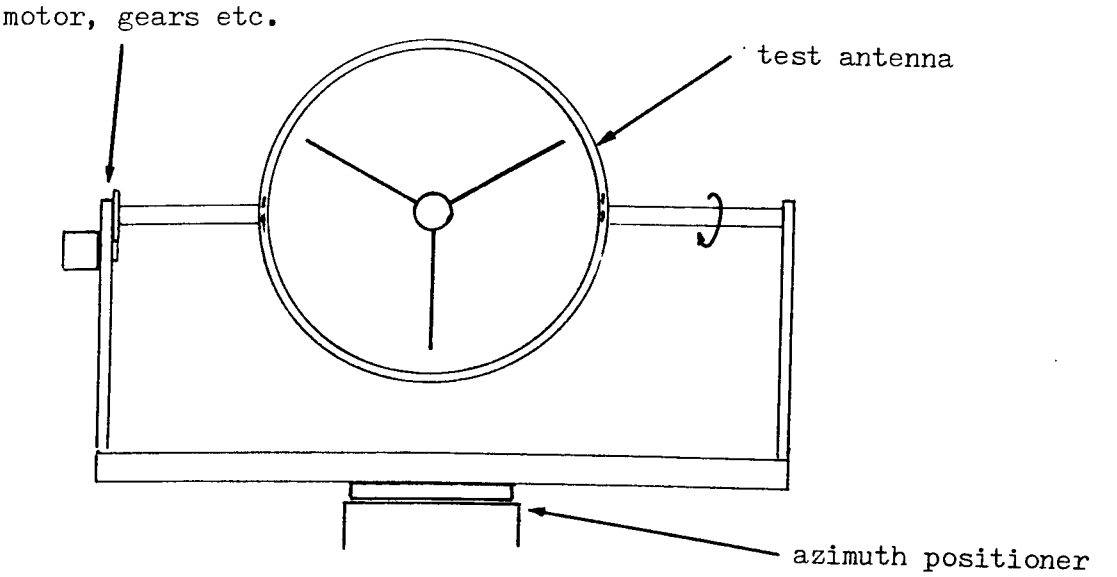

(a) Side-pivoted

(b) Rear-pivoted

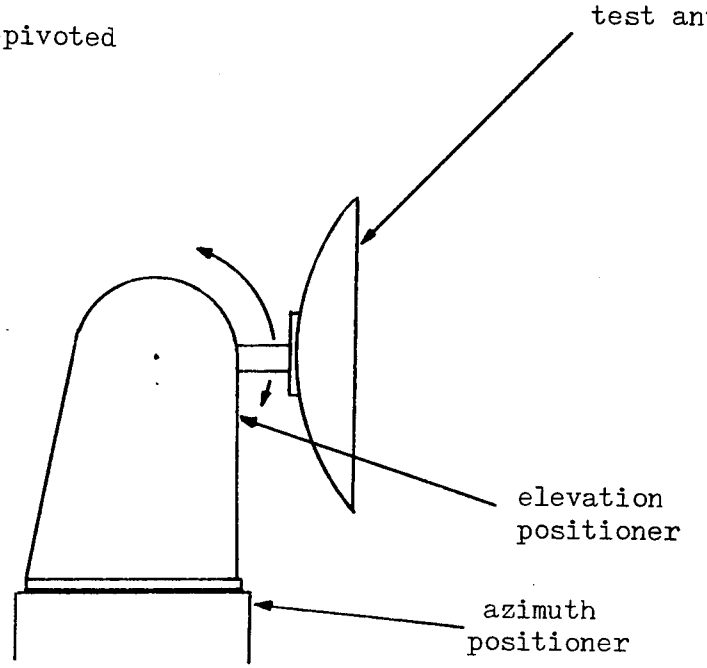

Fig. 1.7. Types of elevation positioner

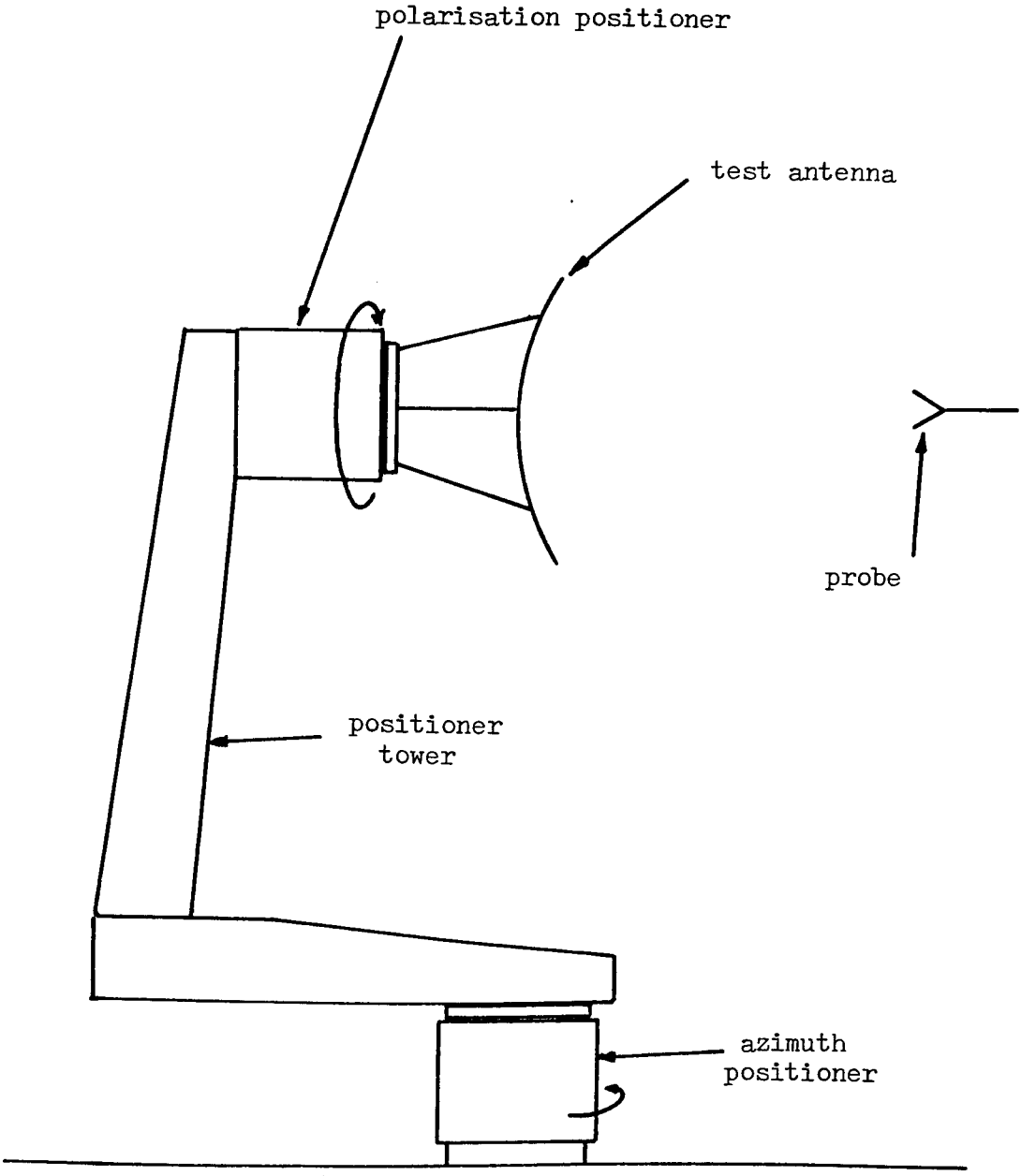

Fig. 1.8. The polarisation-over-azimuth spherical scan system.

pattern cuts along both principal planes and indeed, if Ludwig's second definition[25] of polarisation (rotated through 90^{o}) is used, along any other cut also. The equivalent can only be done on a polarisation-over-azimuth system if a dual polarised probe is used and then only by combining the two polarisations of data correctly. Since, however, any practical spherical near-field measurement system is likely to incorporate a dual-polarised probe, the disadvantage is very slight. It may be worth noting here, that if the probe is also mounted on a polarisation turntable, then cuts of polarisation in accordance with Ludwig's third definition[25] can be measured simply.

The spherical measurement surface produced by a polarisation-over-azimuth scan system together with the coordinates x, y, z, θ and ϕ used as the convention throughout the thesis, for this geometry, are illustrated in Fig. 1.9 and the coordinate system in greater detail in Fig. 1.10.

1.6 Phase Convention

Firstly it should be mentioned that, in the usual way, where field quantities are referred to in the text, the factor exp $j\omega t$, embodying the sinusoidal time variation, is assumed. The second point is that throughout the thesis the convention is employed that leading phase is to be regarded as positive so that for radiation from a particular point, for instance, the phase variation at any particular moment in time will become increasingly negative with increasing distance (i.e. of the form exp - jkr where

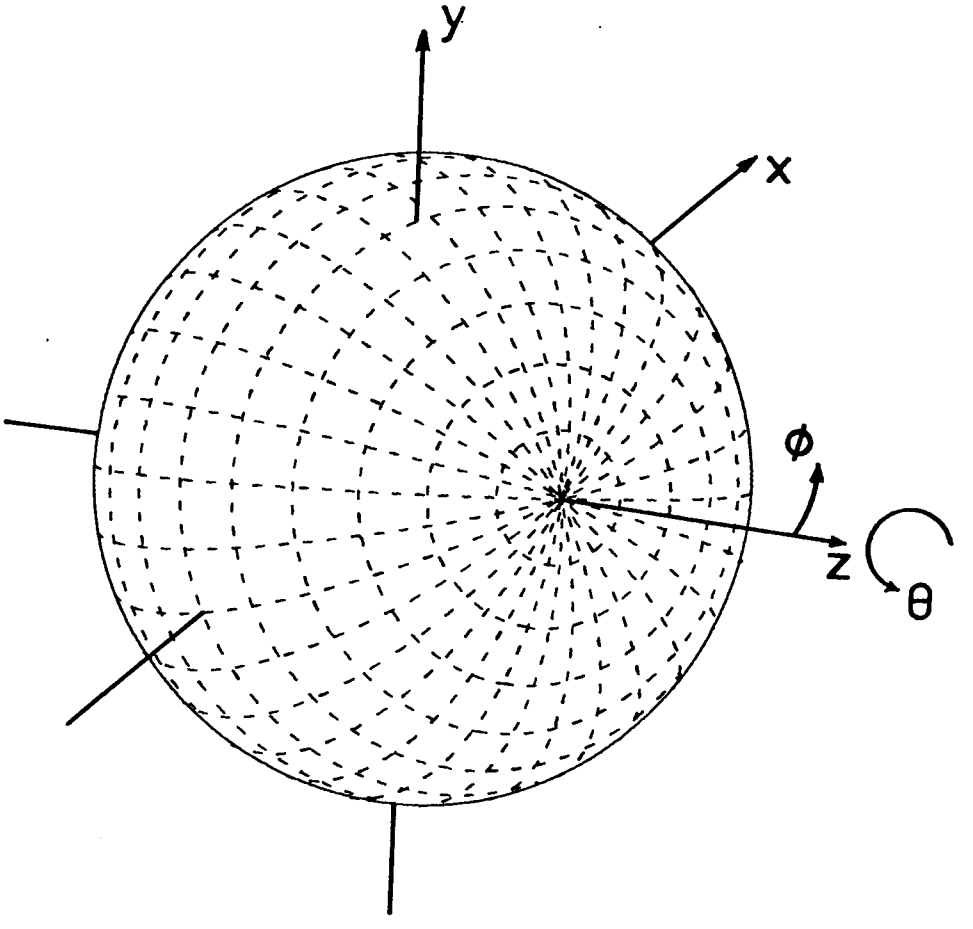

Fig. 1.9. The sample geometry produced by a polarisation-over-azimuth spherical scan system.

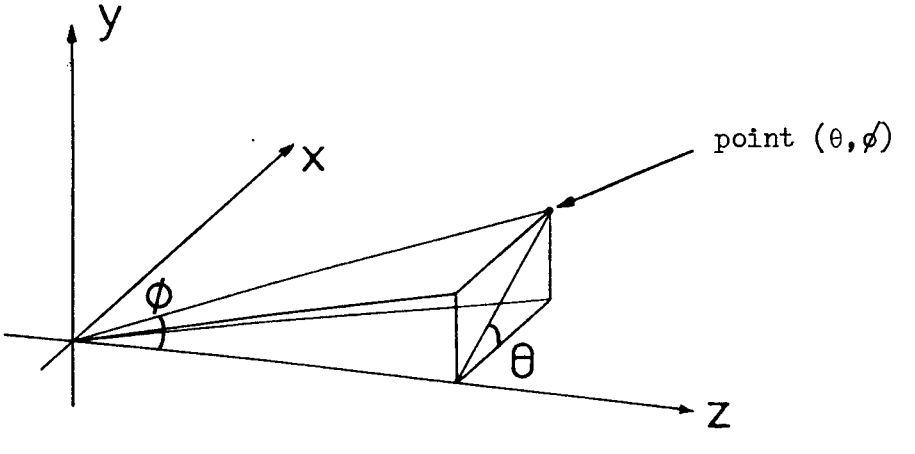

Fig. 1.10. Detail of the polarisation-over-azimuth spherical coordinates as used throughout this thesis.

$k = 2\pi/\lambda$). Where phase is presented graphically, it will be arranged to assume its principal value which will be within the range $\pm 180^{o}$.

1.7 Simulation Program PCMP1D

Throughout this thesis, examples are presented of weighting functions, synthesised plane waves, etc. (see later chapters for the significance of these) for very many different conditions. Because of the amount of computing time involved with producing full-scale three-dimensional weighting functions and constructing the synthesised plane waves, it would have been totally impractical to produce the large number of illustrations in that way. To facilitate a much more convenient investigation, a two-dimensional simulation, termed PCMP1D, was written.

The program synthesises a one-dimensional plane wave (two field components, E_y and E_z) from a weighting function extending over a single circular cut. The probe polarisation is arranged to be tangential to the circle. The program allows selection of any frequency and measurement range and any plane of iteration. The number of points and spacing in plane wave and weighting function are also selectable together with the probe beamwidth. Output of the weighting function and synthesised plane wave over any selected area may be by printer, incremental plotter or oscilloscope display.

The calculation of the synthesised plane wave can be on any desired transverse plane and various errors may be

introduced, either random noise at a specified level or systematic errors such as incorrect frequency, incorrect measurement range or incorrect probe beamwidth. Any longitudinal cut may also be constructed. The difference vector between the synthesised plane wave and the ideal may be displayed and in addition the synthesised plane wave or its non-ideal residual can be Fourier transformed using a fast Fourier transform (FFT) algorithm, for the purpose of quantifying the level of errors liable to be introduced, by the means described in section 5.1.2

The facility is provided for saving the weighting function on a file for the use of another program such as that used in Chapter 2 for producing a T.V. display of a synthesised field distribution.

Having introduced the background to near-field/far-field transformation and some of the important concepts, we now move on, in the next chapter, to discuss the basic aspects of the new approach developed in the present project.

2. THE PLANE WAVE SYNTHESIS TECHNIQUE

2.1 The Basic Concept

As has already been mentioned, a limitation of some of the existing near-field/far-field transformation schemes (particularly those involving spherical scanning geometry) has been the mathematical complexity of the data manipulation necessary in the prediction process. The plane wave synthesis technique was envisaged as an attempt to achieve the transformation with as little post-measurement processing as possible and preferably with hardware no more sophisticated than that likely already to exist on a standard test range.

Plane wave synthesis relies on the fact that an element of an antenna far-field pattern represents the antenna's response to a point-source radiator located at a fixed far-field distance in the direction concerned. For the purpose of the argument, we make the assumption that reciprocity applies to the test antenna in that the radiation pattern when it is operated in the receiving mode is identical to that when operated in the transmitting mode. If this is not in reality the case (for instance, if the antenna contains active elements) and the antenna is to be operated purely in the transmitting mode, then clearly the statement defining the far-field pattern as the response to a point-source is not strictly valid. In such a situation, the point-source becomes a point-receiver with a response essentially uniform (in amplitude and phase) to sources over a suitably large planar area in the region of the test antenna. Notwithstanding possible

non-reciprocal properties of the practical measurement environment, from the point of view of processing of near-field data, the mode of operation is not important, although, if the antenna is non-reciprocal in nature, the near-field data should be acquired in the appropriate mode.

It may then be said that in the region of the test antenna, the far-field point-source produces a uniform plane wave propagating in a direction away from the source. If such a plane wave field distribution can be created in the region of the test antenna by some means other than the far-field source, the far-field response may equally well be measured. This fact is exploited in the compact range (described in Chapter 1) in which a comparatively large reflector antenna is employed to collimate the fields radiated from its feed into a plane wave of limited size in the region just in front of its aperture.

It is possible that a compact range could be constructed using, instead of a reflector, a radiating array, but the problems entailed in exciting each element of the array with precisely the correct amplitude and phase values could be significant and furthermore, the behaviour of the array under the influence of mutual coupling between elements might be difficult to control. In any event, such an array would be a relatively sophisticated and probably expensive piece of hardware to create.

The idea can, however, be extended by applying the principles of aperture synthesis to suggest that, rather than physically realising the radiating array, it is

possible to scan a single probe over the measurement surface,* feeding it with the correct amplitude and phase functions and sampling the response of the test antenna at the appropriate points in the scan. Invoking the theory of superposition, one can state that the overall response to the "array" of probes is the sum of the samples. The element of the far-field pattern is therefore obtained merely by summing a matrix of sampled data. The prediction at the required angle is obtained by centring the scan at the appropriate angle relative to the test antenna. This reasoning may be carried one step further by noting that, because we are dealing with what may be assumed to be a linear system (if this were not true then a unique far-field pattern would not exist), the following applies:

$$R_S\{a \exp(j\psi)\} = a \exp(j\psi)\ R_S\{1\} \qquad (2.1)$$

where $R_S\{\omega\}$ denotes the antenna response, at a particular sample position, to the probe fed with complex (amplitude and phase) function ω. This implies that it is not necessary to equip the probe with a precisely controlled variable-feed network since it is possible to use a "unit-probe" (a probe with fixed amplitude - regarded under normalisation as unity - and constant phase, taken to define phase zero) and subsequently to multiply the sampled antenna response by the appropriate complex weighting coefficient as part of the computational prediction process.

* A spherical surface is put forward initially as being the most suitable because it corresponds to the most usual positioning systems and also for its complete spherical prediction-capability. Nevertheless, other scanning geometries are by no means precluded.

2.2 Initial Scalar Approach

2.2.1 Generation of Weighting-Function

It has been seen that to obtain a prediction in a particular direction, an array of samples are multiplied by complex weighting coefficients and the results added. It is necessary, therefore, to have available the matrix of weighting coefficients, termed the weighting function. In the basic scalar approach, the function is obtained by firstly specifying that, over a particular area of a plane in the region of the test antenna, a plane wave exists, the extent of which is greater than the largest dimension of the test antenna. The weighting function, denoted $g(\theta,\phi)$, may now be approximated using a simple diffraction integral of the form,

$$g(\theta,\phi) = \int_x \int_y \frac{\exp(jkr)}{r}\, dy\, dx \qquad (2.2)$$

where the plane wave is specified to exist over an area centred at the origin of the plane x - y and $k = 2\pi/\lambda$. The parameter r is the general distance from a point (x, y) in the plane to the point (θ,ϕ) on the spherical measurement surface (the coordinate system in use was explained in Chapter 1). The ranges of x and y for the integration may be limited to those necessary completely to enclose the test antenna at all angles (with a small peripheral margin). The function of equation (2.2) will not, in most cases, be sufficient to yield, without modification, a satisfactory plane wave, for reasons which will become clear. In order to improve upon the initial approximation, an iterative approach has been developed to modify $g(\theta,\phi)$ and thereby

to improve the quality of the plane wave. Details of the full three-dimensional iterative procedure will be given in Chapter 3.

2.2.2 Depth of Field and Limits of $g(\theta,\phi)$

To enable predictions to be made at all desired angles, the plane wave properties of the synthesised field distribution need not only to exist over a particular area of the x-y plane but also to be maintained over a sufficient depth (in z) to encompass the (usually spheroidal) volume needed to contain the test antenna at all angles. Intuitively, it would appear that the depth of field requirement can be fulfilled by limiting the angular range over which $g(\theta,\phi)$ is allowed to extend (in addition, of course, angular limiting of the weighting function reduces the data processing burden). It is therefore specified that over some angular region defined by $-\theta_m<\theta<\theta_m$ and $-\phi_m<\phi<\phi_m$, a source distribution corresponding to $g(\theta,\phi)$ is sufficient to yield a satisfactory plane wave.

Having decided that angular limiting of $g(\theta,\phi)$ is necessary, the next step would seem to be to examine qualitatively (making such approximations as necessary) the formation of the plane wave and the effects of imposing the angular limits on the weighting function. For the purposes of the investigation we make the assumption that each coordinate can be dealt with essentially independently and so a two-dimensional scheme is used considering only y, z and θ variations.

It has already been seen that $g(\theta,\phi)$ is produced by an integral of the form,

$$g(\theta,\phi) = \int_x \int_y \frac{\exp(jkr)}{r}\, dy\, dx \qquad (2.3)$$

In the two-dimensional case, this can be rewritten (referring to Fig. 2.1) as,

$$g(\theta) = \int_{-\infty}^{\infty} A(y)\, \frac{\exp(jkr)}{r}\, dy \qquad (2.4)$$

where A(y) is included to account for the truncation of the plane wave, being unity for the range of the desired plane wave and zero elsewhere. It is now necessary to determine r. Using the cosine rule and rearranging,

$$r = (R^2 + y^2 - 2Ry \sin\theta)^{\frac{1}{2}} \qquad (2.5)$$

and, using binomial expansion, neglecting terms of order y^3/R^2 and above and, assuming, initially, small θ so that terms in $\sin^2\theta$ are also negligible,

$$r \simeq R + y^2/2R - y \sin\theta \qquad (2.6)$$

This is used as the approximation for r in the exponent of equation (2.4). For r in the denominator, it is convenient to use the more crude approximation

$$r \simeq R \qquad (2.7)$$

This is permissible because the straightforward dividing factor r is relatively insensitive to inaccuracy whereas, in the exponent, much smaller errors can cause large phase variations (e.g. at 10GHz, with 2m measurement radius, R, an inaccuracy of 1.5cm in the value of r in the denominator causes ~ 0.75% error in the integrand, but a complete 180^o phase inversion occurs if the same error is present in the exponent.). Using these approximations:

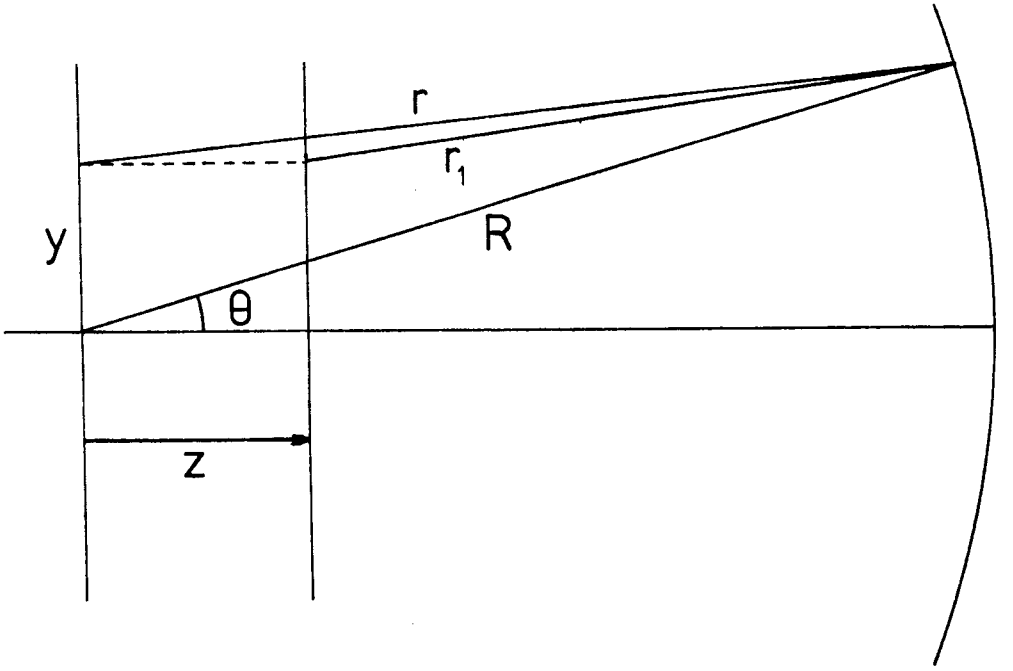

Fig. 2.1. The geometry considered in the two-dimensional analysis of the weighting function/plane wave relationship.

$$g(\theta) \simeq \frac{1}{R} \int_{-\infty}^{\infty} A(y) \exp jk \left(R + \frac{y^2}{2R} - y \sin\theta\right) dy \qquad (2.8)$$

the factor exp(jkR) being constant, may also be taken outside the integral leaving,

$$g(\theta) \simeq \frac{\exp jkR}{R} \int_{-\infty}^{\infty} A(y) \exp(jky^2/2R) \exp(-jky \sin\theta) dy \qquad (2.9)$$

which is the form of the Fourier transform of the function $A(y) \exp(jky^2/2R)$.

The synthesised plane wave can be regarded as resulting from an integral of a similar form to that of equation (2.4),

$$f(y) = \int_{-\infty}^{\infty} T(\theta)\, g(\theta)\, \frac{\exp(-jkr)}{r}\, d\theta \qquad (2.10)$$

where $T(\theta)$ is introduced to account for the angular truncation of $g(\theta)$, being unity for $-\theta_m < \theta < \theta_m$ and zero elsewhere. To determine $f(y)$ on different planes (i.e. $z \neq o$), the expressions for r should be modified. One such displaced plane, distant z from the original, is shown in Fig. 2.1. In this case,

$$r_1 = (R^2 + y^2 + z^2 - 2Ry \sin\theta - 2Rz \cos\theta)^{\frac{1}{2}} \qquad (2.11)$$

Using approximations similar to those used in obtaining equation (2.6),

$$r_1 \simeq R + \frac{y^2}{2R} + \frac{z^2}{2R} - y \sin\theta - z \cos\theta - \frac{z^2 \cos^2\theta}{2R} - \frac{yz \sin\theta \cos\theta}{2R} \qquad (2.12)$$

so that,

$$f(y) \simeq \int_{-\infty}^{\infty} T(\theta)\, g(\theta)\, \frac{1}{r_1} \exp - jk \left(R + \frac{y^2}{2R} + \frac{z^2}{2R} - y \sin\theta - z \cos\theta - \frac{z^2 \cos^2\theta}{2R} - \frac{yz \sin\theta \cos\theta}{2R}\right) d\theta \qquad (2.13)$$

If the approximation,

$$\frac{1}{r_1} \simeq \frac{1}{R - z} \qquad (2.14)$$

can be made, then substituting the expression of equation (2.9) for $g(\theta)$ into equation (2.13) and rearranging gives:

$$f(y) \simeq \frac{\exp -jk\left(\frac{y^2+z^2}{2R}\right)}{R(R - z)} \int_{-\infty}^{\infty} T(\theta) \exp jk\left(y \sin\theta + z \cos\theta + \frac{z^2 \cos^2\theta}{2R} + \frac{yz \sin\theta \cos\theta}{2R}\right) \int_{-\infty}^{\infty} \left(A(y) \exp(jky^2/2R)\right) \exp(-jky \sin\theta)\, dy\, d\theta \qquad (2.15)$$

It is noted that the angular range (in θ) of the function under the outer integral is truncated by $T(\theta)$ and the limits will certainly be within the range $\pm\pi/2$. It is therefore possible to replace the limits of integration by $\pm\pi/2$. Replacing the factor $d\theta$ by $d(\sin\theta)/\cos\theta$ and modifying the limits of integration accordingly gives:

$$f(y) \simeq \frac{\exp -jk\left(\frac{y^2+z^2}{2R}\right)}{R(R - z)} \int_{-1}^{1} \frac{T(\theta)}{\cos\theta} \exp jk\left(y \sin\theta + z \cos\theta + \frac{z^2 \cos^2\theta}{2R} + \frac{yz \sin\theta \cos\theta}{2R}\right) \int_{-\infty}^{\infty} A(y) \exp(jky^2/2R)) \exp(-jky \sin\theta)\, dy\, d(\sin\theta) \qquad (2.16$$

Letting

$$s = \sin\theta \qquad (2.17$$

replacing $\cos\theta$ by $(1 - s^2)^{\frac{1}{2}}$ and rewriting $T(\theta)$ as $T_1(s)$:

$$f(y) \simeq \frac{\exp -jk\left(\frac{y^2+z^2}{2R}\right)}{R(R-z)} \int_{-1}^{1} T_1(s)(1-s^2)^{-\frac{1}{2}} \exp jk\left(ys + z(1-s^2)^{\frac{1}{2}} + \frac{z(1-s^2)}{2R} + \frac{yzs(1-s^2)^{\frac{1}{2}}}{2R}\right)$$

$$\int_{-\infty}^{\infty} (A(y)\exp(jky^2/2R))\exp(-jkys)\,dy\,ds \qquad (2.18)$$

It has already been seen that the inner integral (over y) of equation (2.18) is of the form of a Fourier transform from the y-domain to the s-domain and, for z = 0, it is noticed that the outer integral takes on the form of an inverse Fourier transform back to the y-domain so that equation (2.18) may be approximated, for z = 0, by,

$$f(y) = \frac{\exp(-jky^2/2R)}{R^2} F^{-1}\{T_1(s)(1-s^2)^{-\frac{1}{2}} F\{A(y)\exp(jky^2/2R)\}\} \qquad (2.19)$$

where F{} denotes the Fourier transform of the function within the parentheses and $F^{-1}\{\}$ denotes the inverse Fourier transform. This can now be expressed in the form of a convolution :

$$f(y) = \frac{\exp(-jky^2/2R)}{R^2} F^{-1}\{T_1(s)(1-s)^{-\frac{1}{2}}\} \circledast (A(y)\exp(jky^2/2R)) \qquad (2.20)$$

For small θ, such that $s^2 \ll 1$, the quantity $T_1(s)(1-s^2)^{-\frac{1}{2}}$

becomes an approximate rect* function so that its transform will be of the form sinc(ay)+ where the constant a is proportional to the width of $T_1(s)$. In this case, a will be small so that the sinc function will be relatively wide. This in turn means that (since many of the ill effects of the convolution are caused where the convolving sinc function encounters the edge of the plane wave) the ringing effects will tend to be serious and spread over a wide area of the plane wave.

If, however, the range of $T_1(s)$ is increased somewhat, the transform (the sinc function) will become narrower tending more towards a delta function (the increasing effect of $(1-s^2)^{-\frac{1}{2}}$ will tend to narrow the sinc even further but bring up the sidelobes). The theory of convolution[26] tells us that convolution with a delta function is equivalent to multiplication by unity, i.e.

$$F^{-1}\{T_1(s)(1-s^2)^{-\frac{1}{2}}\}\circledast(A(y)\exp(jky^2/2R))\simeq A(y)\exp(jky^2/2R) \tag{2.21}$$

* The function rect(s) may be defined as,

$$\text{rect}(s) = \begin{cases} 1, & |s| < s_{max} \\ 0, & |s| > s_{max} \end{cases}$$

+The function sinc(x) is defined as

$$\text{sinc}(x) = \sin(x)/x$$

In this particular case the sinc function may be regarded as almost analogous to the impulse response of a lens in optics, the image quality being better if the response function is narrower.

in which case the exponentials of equation (2.19) cancel leaving :

$$f(y) \simeq A(y)/R^2 \qquad (2.22)$$

Under normalisation, the factor $1/R^2$ may, of course, be ignored. A perfect delta function can never, in reality, be achieved for a number of reasons, notably :

a) For large θ, the approximations used in deriving equation (2.20) begin to break down.

b) For large θ, the effect of $(1-s^2)^{-\frac{1}{2}}$ becomes pronounced raising the sidelobes of the impulse response and hence causing more serious ripple in the convolution.

In equation (2.18) terms in z are present in the exponential and for $z \neq 0$, the influence of these must be taken into account. We use binomial expansion and neglect terms in s^3 to obtain the following approximations,

$$z(1-s^2)^{\frac{1}{2}} \simeq z - \frac{zs^2}{2} \qquad (2.23)$$

and

$$\frac{yzs(1-s^2)^{\frac{1}{2}}}{2R} \simeq \frac{yzs}{2R} \qquad (2.24)$$

so a little rearrangement of the exponent terms of equation (2.18) gives :

$$ys+z(1-s^2)^{\frac{1}{2}} + \frac{z\ (1-s^2)}{2R} + \frac{yzs(1-s^2)^{\frac{1}{2}}}{2R} =$$

$$z(1+\frac{z}{2R})+ ys(1+\frac{z}{2R}) - \frac{zs^2}{2R}\ (1+\frac{z}{R}) \qquad (2.25)$$

The first term of the right-hand side of equation (2.25) is a constant so that a factor $\exp jkz\ (1+\frac{z}{2R})$ may be taken

outside the integral of equation (2.18) and accounts (within the limits of negligibility of the term z/2R) for a linear phase variation with z which is, of course, what is desired for the plane wave. It is observed that, to first order, the remaining two terms in equation (2.25) are equal to :

$$ys_1 + \frac{zs_1^2}{2} \tag{2.26}$$

where

$$s_1 = s(1+\frac{z}{R})^{\frac{1}{2}} \tag{2.27}$$

Thus, noting that,

$$ds = ds_1(1+\frac{z}{R})^{-\frac{1}{2}} \tag{2.28}$$

equation (2.18) can be rewritten :

$$f(y) = \frac{\exp jk(z-\frac{y^2}{2R})}{r(R-z)(1+\frac{z}{R})^{\frac{1}{2}}} \int_{-(1+\frac{z}{R})^{\frac{1}{2}}}^{(1+\frac{z}{R})^{\frac{1}{2}}} T_1(s)(1-s^2)^{-\frac{1}{2}} \exp jk(ys_1 - \frac{zs_1^2}{2})$$

$$\int_{-\infty}^{\infty} (A(y)\exp(jky^2/2R))\ \exp(-jkys)dy\, ds_1 \tag{2.29}$$

The factor outside the integral of equation (2.29) can be simplified by noting that, to first order,

$$(1+\frac{z}{R})^{\frac{1}{2}} \simeq (1-\frac{z}{R})^{-\frac{1}{2}} \tag{2.30}$$

so that

$$R(R-z)(1+\frac{z}{R})^{\frac{1}{2}} \simeq R^2(1-\frac{z}{R})^{\frac{1}{2}} \tag{2.31}$$

giving

$$f(y) = \frac{\exp jk(z - \frac{y^2}{2R})}{R^2(1-\frac{z}{R})^{\frac{1}{2}}} \int_{-(1+\frac{z}{R})^{\frac{1}{2}}}^{(1+\frac{z}{R})^{\frac{1}{2}}} T_1(s)(1-s^2)^{-\frac{1}{2}} \exp jk(ys_1 - \frac{zs_1^2}{2})$$

$$\int_{-\infty}^{\infty} (A(y)\exp(jky^2/2R))\exp(-jkys)\,dy\,ds_1 \qquad (2.32)$$

The inner integral (over y) yields the function $g(\theta)$ which may be expressed as a function of s_1, say $g'(s_1)$, and $T_1(s)(1-s^2)^{-\frac{1}{2}}$ can also be rewritten as a function of s_1, say $T'(s_1)$, so that,

$$f(y) = \frac{\exp jk(z - \frac{y^2}{2R})}{R\ (1-\frac{z}{R})^{\frac{1}{2}}} \int_{-(1+\frac{z}{R})^{\frac{1}{2}}}^{(1+\frac{z}{R})^{\frac{1}{2}}} T'(s_1)\exp jk(ys - \frac{zs_1^2}{2})g'(s_1)\,ds_1 \qquad (2.33)$$

We note :

a) The desired linear phase variation of the plane wave with z combined with a quadratic variation in y. This tends to be cancelled out by the quadratic phase variation included in $g'(s_1)$, the exactness of the cancellation depending on the approximations made during the derivation of equation (2.33).

b) An amplitude variation of the form $(1-\frac{z}{R})^{-\frac{1}{2}}$. This can be interpreted as the amplitude fall-off due to a cylindrical wave propagating outwards in the -z direction and at this point we qualify the term "plane wave" as used in the preceeding two-dimensional analysis.

The "plane wave" is defined in one dimension only and from the nature of the geometry, one might expect that there would be something other than plane wave properties in the other dimension. What has happened is that the process has compensated in one dimension for sphericity of the outwardly propagating wave and turned it into a cylindrical wave over a finite region in space. It should be noted that, in the plots of computed synthesised field distributions, compensation has been incorporated for this variation.

c) Change of the value of z will cause an angular scale change in $g'(s_1)$ and $T'(s_1)$ since the conversion factor between s_1 and s is a function of z. This means that the transform of $g'(s_1)$ into the y-domain (i.e. the basic plane wave) will suffer compression or expansion (depending on the sign of z) in y. The modified sinc function of the impulse response will undergo a similar scale change. In the former case, the change may be difficult to observe since it is only of order $(1+\frac{z}{R})^{\frac{1}{2}}$ and the other effects which are particularly significant at the edges of the plane wave may tend to mask it. In the latter case, the transform of $T'(s_1)$ will widen for negative z and conversely narrow for positive z indicating that the influence of the scale change is likely to be more serious for negative z. In fact, the computer results presented later show that this effect is more than compensated for by other effects which are more serious for positive z. Such an effect is :

d) The term $-\frac{zs_1^2}{2}$ in the exponent of the transform is a straightforward defocussing term appearing for $z \neq 0$. This causes the form of the impulse response function to deteriorate from that of a sinc and thus the convolution with the plane wave produces more severe ringing effects. It will also be noticed that the term is proportional to s_1^2 which means that its influence will be much more marked for larger-angle weighting functions. One other point to note is that, from equation (2.27), the defocussing term is greater for positive z than for negative (vanishing in fact for $z = -R$, but this corresponds to the meaningless situation $s_1 = 0$).

By the nature of the convolution, while the modified sinc function of the impulse response is positioned near to the centre of the plane wave, the integrated product will be comparatively constant but when the sinc encounters the edges of the plane wave, the variations become much greater so that the ringing effects naturally appear most serious near the edges. One more effect, not immediately apparent from the above analysis, is caused by grating lobe effects due to the sampled nature of the data. This will be illustrated later in this chapter.

An approximate qualitative relationship has been established between the angular range of the weighting function and the maintenance of plane wave properties over a suitable range of z. This cannot, however, be regarded as defining the magnitude of the influence of various factors because;

a) many higher order terms have been neglected in making the approximations necessary in the derivation of equation (2.33) and

b) the weighting function is ultimately determined with the help of an iterative process and it is difficult to assess exactly how this is likely to affect the results.

It seems, however, from the results of the computational simulations, that the iterative process tends to alter $g(\theta)$ so as to compensate, to some extent, for the presence of the higher order terms so that, as will be observed, the conclusions drawn from equation (2.33) are largely borne out. In Appendix 1, the behaviour of the impulse response of a weighting function is investigated and many of the effects described above are apparent. In addition, the various illustrations of synthesised plane waves provide ample demonstration of the behaviour.

2.2.3 Basic Prediction Process

In section 2.1 the essential idea behind the plane wave synthesis technique was outlined. It was shown that the prediction was achieved by weighting the measured data according to a predetermined weighting function, positioned correctly in the data, and then summing the resulting matrix to achieve a prediction of a single far-field element. It may be worth noting at this stage that the prediction is not, in fact, limited to the far-field. By specifying initially a required field distribution (in the region of the test antenna) equivalent to some other measurement distance, the pattern may be predicted for this distance. The prediction range should not normally be less than the

measurement range because spatial frequency components may appear here which are not propagated out to the measurement sphere, thus the information is not available in the measured data to predict the pattern with confidence[27].

From a simplified viewpoint, the prediction process may be formulated as follows :

$$P(\theta_F,\phi_F) = \sum_{m=-m_o}^{m_o} \sum_{n=-n_o}^{n_o} g(m\Delta\theta,n\Delta\phi) f(\theta_F+m\Delta\theta,\phi_F+n\Delta\phi) \qquad (2.34)$$

where $P(\theta_F,\phi_F)$ is the predicted element of the far-field radiation pattern for angular coordinates (θ_F,ϕ_F), $f(\theta,\phi)$ is the measured near-field response at coordinates (θ,ϕ) and where $m_o\Delta\theta = \theta_m$ and $n_o\Delta\phi = \phi_m$, the limits on weighting function $g(\theta,\phi)$. The process has, therefore, become merely one of complex number multiplication and addition, simple operations well within the capabilities of a relatively unsophisticated hardware unit. It may also be noted, at this point, that for principal axis predictions, only a limited band of data along the axis is required and, for a system with particularly severe storage limitations, a routine might be written allowing data to be taken when required and discarded at a later stage when no longer needed. This implies that a very limited system might still be capable of making all-space predictions.

Various complicating factors will be discussed in later chapters, particularly those caused by the three-dimensional sampling geometry. The first experiment performed was designed to be a relatively simple case avoiding the problems and, as will be described, used an antenna assumed to be

one-dimensional and the prediction was performed around a single cut of data. The modified version of equation (2.34) to do this was :

$$P(\theta_F) = \sum_{m=-m_o}^{m_o} g(m\Delta\theta) f(\theta_F + m\Delta\theta) \qquad (2.35)$$

The process in this case was to acquire a single circular scan of data. A weighting function was created for the same parameters and a simple routine of shifting, multiplication and summing (as indicated in Figs. 2.2 and 2.3) performed the prediction. The details of the experiment together with the results are presented later in this chapter.

2.3 Sampling Criterion

The technique requires that the weighting function distribution should be sufficient to yield an acceptable quality plane wave field distribution over the desired volume. The standard sampling criterion indicates (treating θ and ϕ independently) that the greatest spatial frequency which can occur due to an antenna of maximum dimension D is $\pi D/\lambda$ cycles per revolution requiring for complete characterisation samples to be angularly separated by no more than λ/D radians. This calculation is based on the requirement to sample sufficiently frequently the radiated field. The conceptual basis of the present approach is somewhat different so that the idea behind the derivation of the sampling criterion needs likewise to be modified. It is, nevertheless, to be expected that the procedure adopted will indicate a similar minimum sampling rate.

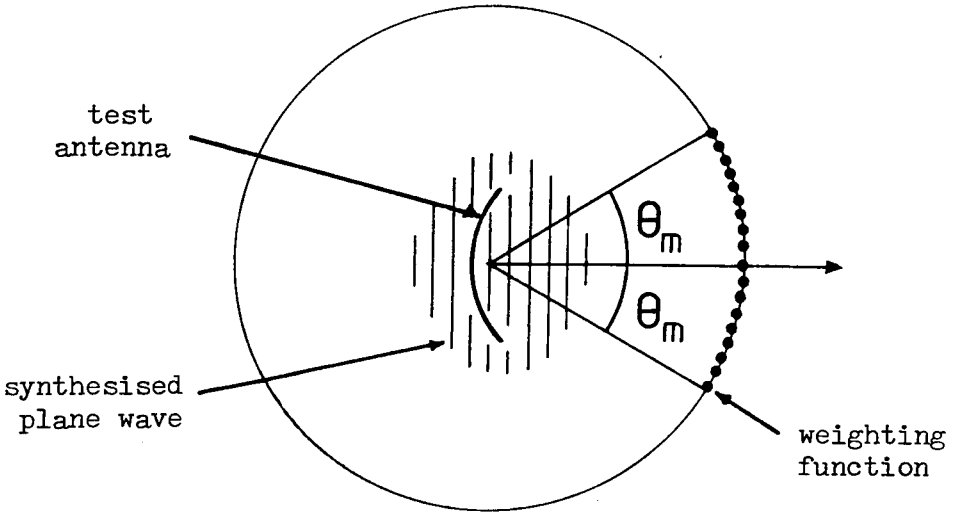

Fig. 2.2. The weighting function would, if practically realised, produce a plane wave in the region of the test antenna. Here, the configuration for a boresight prediction is shown.

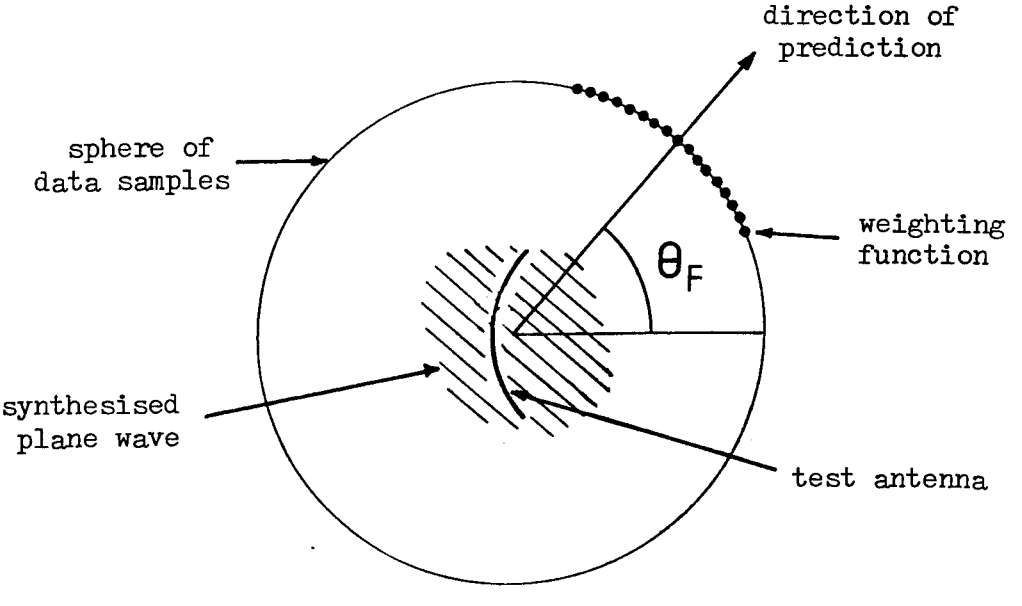

Fig. 2.3. A prediction at any angle, θ_F, off boresight is produced simply by positioning the weighting function correctly in the measured data.

We began by noting the Fourier transform relationship between a far-field ($R \to \infty$) weighting function and its synthesised plane wave (analogous to the relationship between an antenna aperture illumination and its far-field radiation pattern). Since the weighting function is a sampled rather than continuous function, the relationship is, in fact, that of the discrete Fourier transform (DFT). One important property of the DFT is its periodic nature. Thus the width of one period of the plane wave function is such that radiation from the edge of the period would contribute a spatial frequency, in the far-field, of half the sample frequency. Beyond this point, the synthesised plane wave is repeated. If the width of the desired plane wave is small enough to lie completely within a single period of the periodic function, no problem arises. If, however, the sampling rate, in the far-field, is less than twice the maximum spatial frequency due to the required plane wave, it begins to be overlapped by its counterpart from the neighbouring period with consequent deterioration in quality. It is, in fact, demonstrated in Appendix 2 that for the far-field case, with an undersampled weighting function, the iterative process succeeds in suppressing the outer points to a very low amplitude reducing the weighting function effectively to what is the usual far-field "weighting function", a single point. Thus the problem of undersampling is insignificant in the far-field measurement situation. Clearly, since the weighting function is, in reality, to be positioned in the near-field region, the Fourier transform relationship begins to break down. As illustrated in

Appendix 2, the off-axis periods of the "periodic" plane wave function cease to be good replicas of the central period, displaying instead a marked amplitude taper (due to space attenuation) and, additionally the disappearance of the linear phase portions apparent in the far-field case. It is still evident, however, that the onset of overlap occurs at the expected sample spacing so we see that in this initial consideration, for the plane z = 0, the sampling criterion is established as :

$$\Delta\theta < \lambda/D \qquad (2.36)$$

To take account of the depth of field requirement, it is necessary to carry out some adjustment of this criterion. The maintenance of the plane wave over a spheroidal volume requires not only that adjacent periods of the plane wave function should not overlap on the plane z = 0 but also that the same condition should apply for all values of z falling within the compass of the sphere. Dealing again with one scan coordinate alone, we say that adjacent periods of the synthesised plane wave should not overlap so far as to impinge upon the circular region of radius D/2 shown in Fig.2.4. This implies, not, as one might superficially assume, that the sampling criterion outlined above should be fulfilled for all points within the circle but rather, making allowance for the width of the region of overlap (see Fig.2.5), it should apply for all points within the special area also shown in Fig.2.4.

Consider (referring to Fig.2.6) a point S situated at angle θ in a circular data scan of radius R centred at

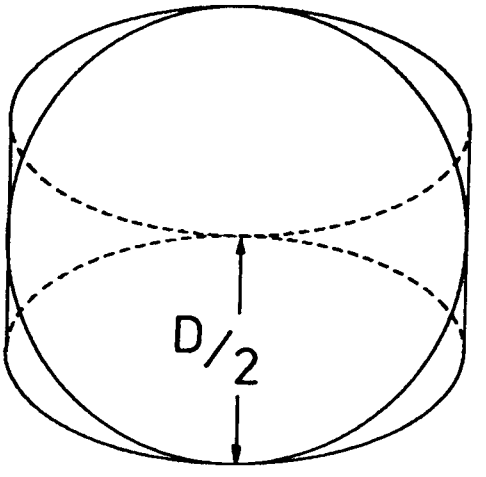

Fig. 2.4. The circular region enclosing the test antenna and the special area for fulfilment of the sampling criterion. The special area is, in fact, that within and between two ellipses placed side-by-side, as shown.

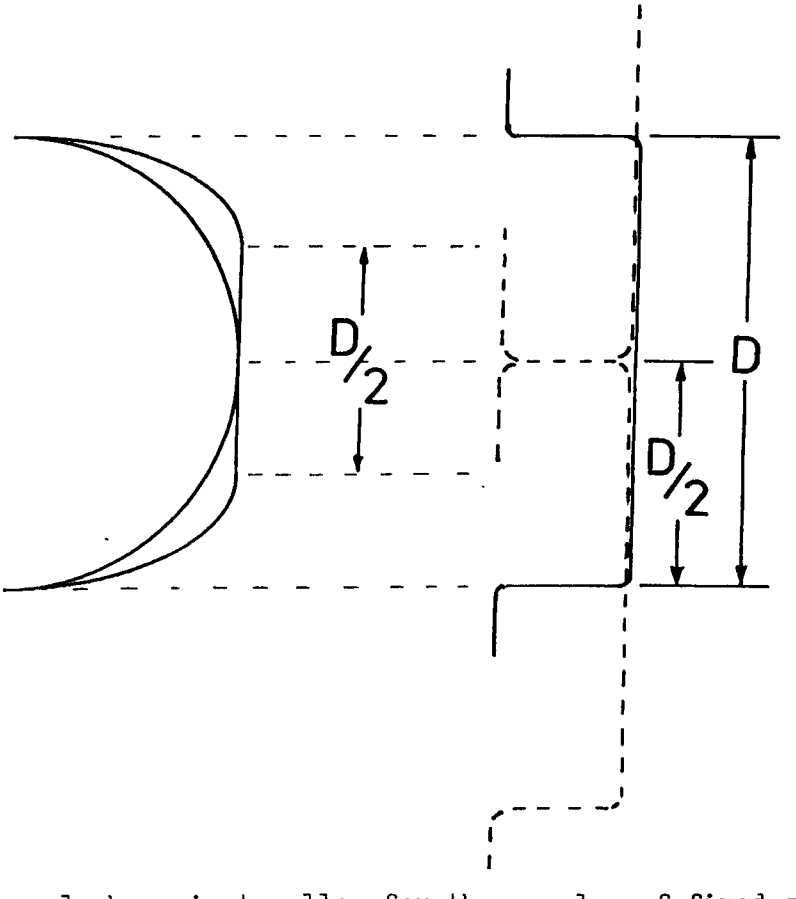

Fig. 2.5. The unusual shape is to allow for the overlap of fixed-size synthesised plane waves; the maximum allowable overlap on the end plane z = D/2 is illustrated on the right showing that this implies a sampling criterion for a region of width D/2.

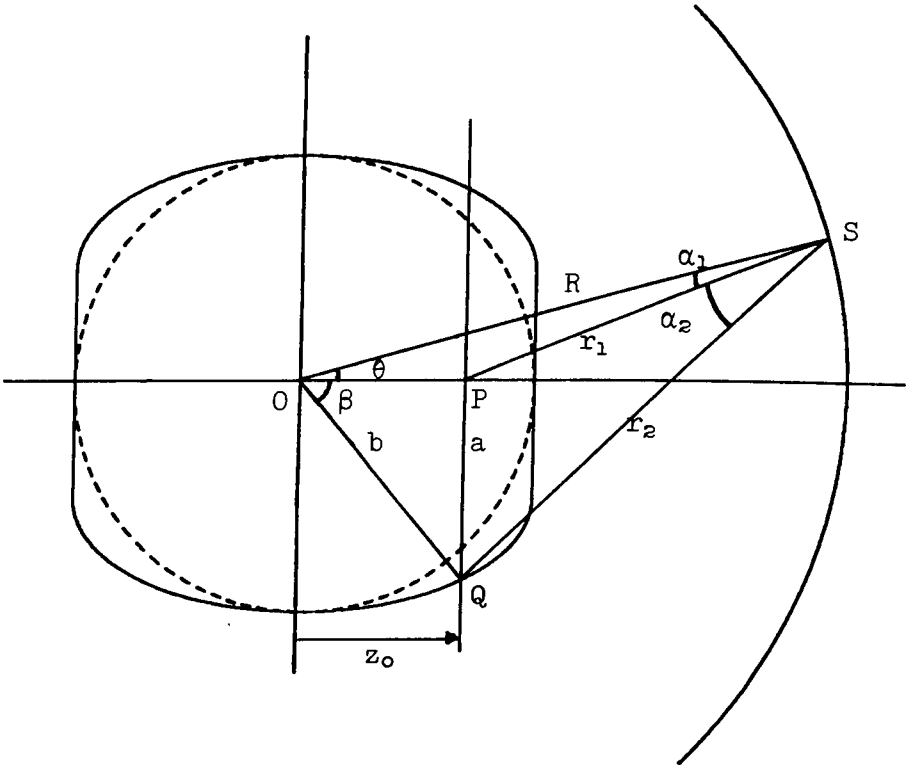

Fig. 2.6. The geometry for analysis of the near-field sampling criterion for plane wave synthesis.

point O. Adjacent periods of the plane wave distribution on the plane $z = z_o$ overlap to within the circle enclosing the test antenna if the near-field sampling rate is less than twice the maximum spatial frequency, around the measurement circle, of radiation from point Q relative to radiation from point P (i.e. less than twice the maximum value of the difference between the spatial frequencies of radiation from the two points), Q being an extreme point on $z = z_o$ within the special area.

Let us denote the "spatial wavelength" around the measurement circle due to radiation from point P by the symbol λ_1 and, similarly, the "spatial wavelength" due to radiation from point Q by the symbol λ_2. Then :

$$\lambda_1 = \lambda/\sin\alpha_1 \tag{2.37}$$

and

$$\lambda_2 = \lambda/\sin\alpha_2 \tag{2.38}$$

With the object of expressing $\sin\alpha_1$ in terms of θ, R, D and z_o, the sine rule is invoked to give :

$$\sin\alpha_1 = \frac{z_o \sin\theta}{r_1} \tag{2.39}$$

and by the cosine rule,

$$r_1 = (R^2+z_0{}^2-2Rz_0\cos\theta)^{\frac{1}{2}} \tag{2.40}$$

Substituting from equation (2.40) for r_1 in equation (2.39) yields,

$$\sin\alpha_1 = \frac{z_o \sin\theta}{(R^2+z_0{}^2-2Rz_0\cos\theta)^{\frac{1}{2}}} \tag{2.41}$$

We also require $\sin\alpha_2$. By the cosine rule again,

$$r_2 = (R^2+b^2-2Rb\cos(\theta+\beta))^{\frac{1}{2}} \qquad (2.42)$$

where

$$b = a/\sin\beta \qquad (2.43)$$

and

$$\beta = \tan^{-1}(a/z_o) \qquad (2.44)$$

a being given by,

$$a = \frac{D}{4} + (\frac{D^2}{16} - \frac{z_o^2}{4})^{\frac{1}{2}} \qquad (2.45)$$

Invoking the sine rule,

$$\sin\alpha_2 = \frac{b\sin(\theta+\beta)}{r_2} \qquad (2.46)$$

Substituting for r_2 from equation (2.42)

$$\sin\alpha_2 = \frac{b\sin(\theta+\beta)}{(R^2+b^2-2Rb\cos(\theta+\beta))^{\frac{1}{2}}} \qquad (2.47)$$

where b and β are as defined by equations (2.43), (2.44) and (2.45).

Having now defined $\sin\alpha_1$ and $\sin\alpha_2$, we can determine the difference in spatial frequency between radiation from P and Q as :

$$\frac{1}{\lambda_{12}} = \frac{1}{\lambda_2} - \frac{1}{\lambda_1} \qquad (2.48)$$

where λ_{12} is the "spatial wavelength", along the measurement circle, of the radiated field from Q relative to that from P. Thus,

$$\lambda_{12} = \frac{\lambda}{\sin\alpha_2-\sin\alpha_1} \qquad (2.49)$$

Given the values of R, θ, D and z_o, we can therefore determine the relative spatial frequency of radiation from points P and Q. To establish a sampling criterion, it is necessary to find the minimum value of λ_{12} with varying z_o

and θ over the appropriate ranges. The expressions are, unfortunately, not of a form which yields readily an analytical expression for the minimum "spatial wavelength" but it is, on the other hand, quite a simple matter to obtain, computationally, the value of $\lambda_{12\,min}$ for given values of λ, R and D (if only by calculating values for a range of z_o and θ and examining them by hand - it is, of course, faster and more accurate to employ a suitable search technique as was used to obtain the results shown here). The maximum allowable angular sampling interval is then given by :

$$\Delta\theta_{max} = \lambda_{12min}/2R \qquad (2.50)$$

Fig.2.7 is an example of such a calculation illustrating the variation of critical sampling interval with R for a range of values of D. It is found that for distant measurements ($R \to \infty$) the maximum sampling interval is, as expected :

$$\Delta\theta_{max} = \lambda/D \qquad (2.51)$$

but, as R is reduced, the values of λ_{12} corresponding to negative values of z_o begin to increase while a minimum value of λ_{12} forms for small positive z_o. As R is further decreased, this minimum deepens and the corresponding value of z_o increases until the limit of $z_o = D/2$ for minimum λ_{12} is reached in the case of very short range measurement. It is seen, therefore, that a near-field measurement system requires a sampling rate in excess of that indicated by equation (2.36). It turns out, in fact, that the critical sampling interval, expressed in terms of a proportion of the standard λ/D criterion is dependent purely upon the ratio R/D and so the

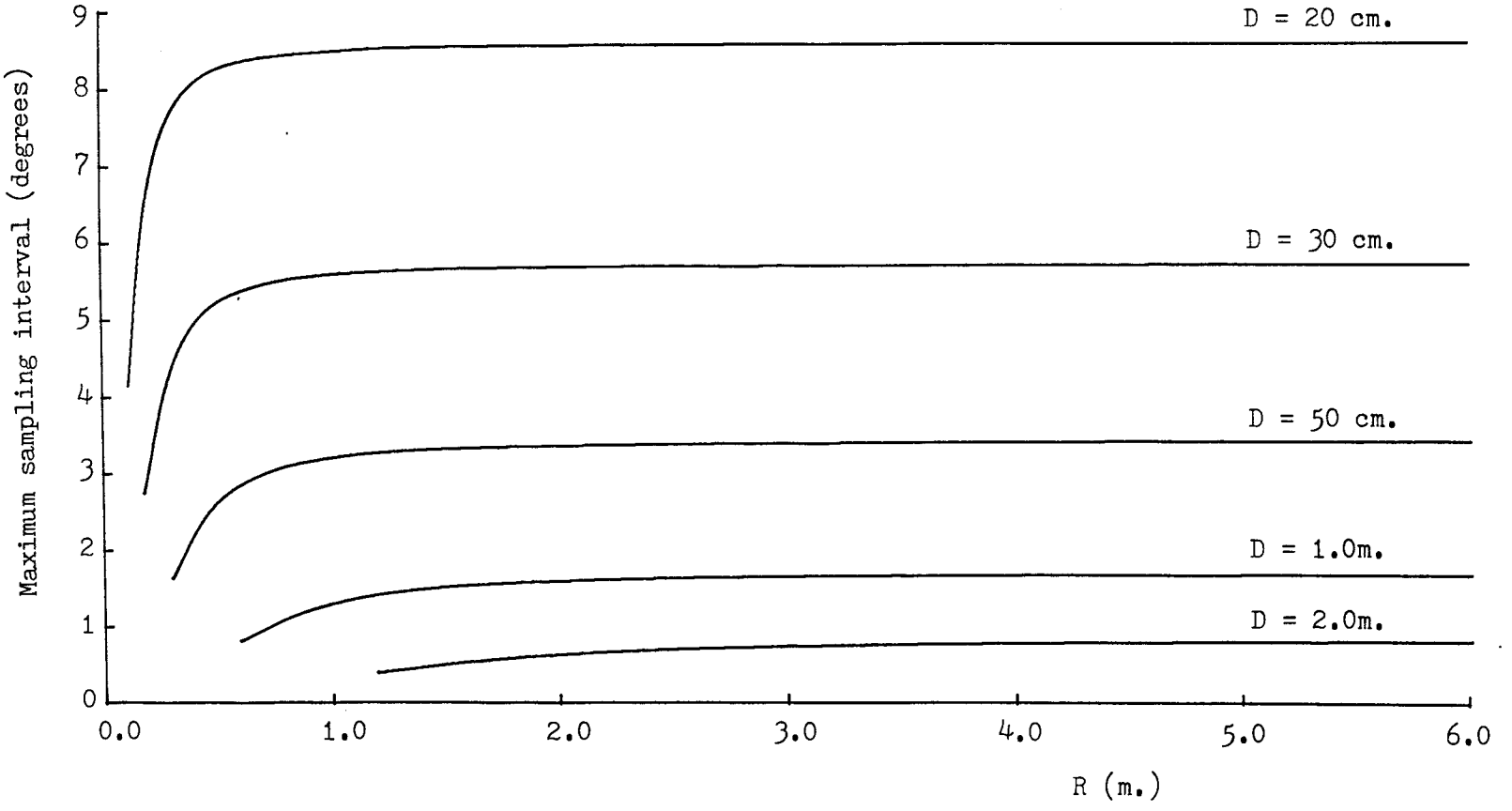

Fig. 2.7. Variation of maximum sample interval (at 10.0GHz.) with measurement radius, R, for a range of plane wave diameters.

sampling requirements for all frequencies, sizes of plane wave and measurement distances can be summarised in a single graph, Fig.2.8.

2.4 Visualisation of Field Distributions

As an aid to the understanding of the processes taking place in the formation of a plane wave from a weighting function, a computer program was developed to calculate the synthesised field distribution over a plane cut through the region containing the weighting function and forward through the plane wave. The distribution is then displayed on grey scale (or false colour) as a picture on the T.V. display system attached to the Departmental V-72 image-processing computer (see Appendix 4).

Three examples are presented in this thesis of the output from this program. The first (Fig.2.9) displays the synthesised field distribution due to a 13-point (one-dimensional) weighting function, spacing 4.16^{o}, operated at 10GHz and with a measurement range of 1.0m. The displayed range is ±1.28m in each dimension. Table 2.1 lists the correspondence between field strength and display level. The region of the weighting function is visible near the bottom of the picture and the plane wave region, specified as 30cm wide, in the centre. Towards the top of the screen, it is apparent that the plane wave distribution has broken down and regions of bifurcation etc., are apparent as the fields begin to focus into a main beam. Additionally, because of the relatively coarse sampling, two grating lobes can be seen forming on either side of the main beam. In the region

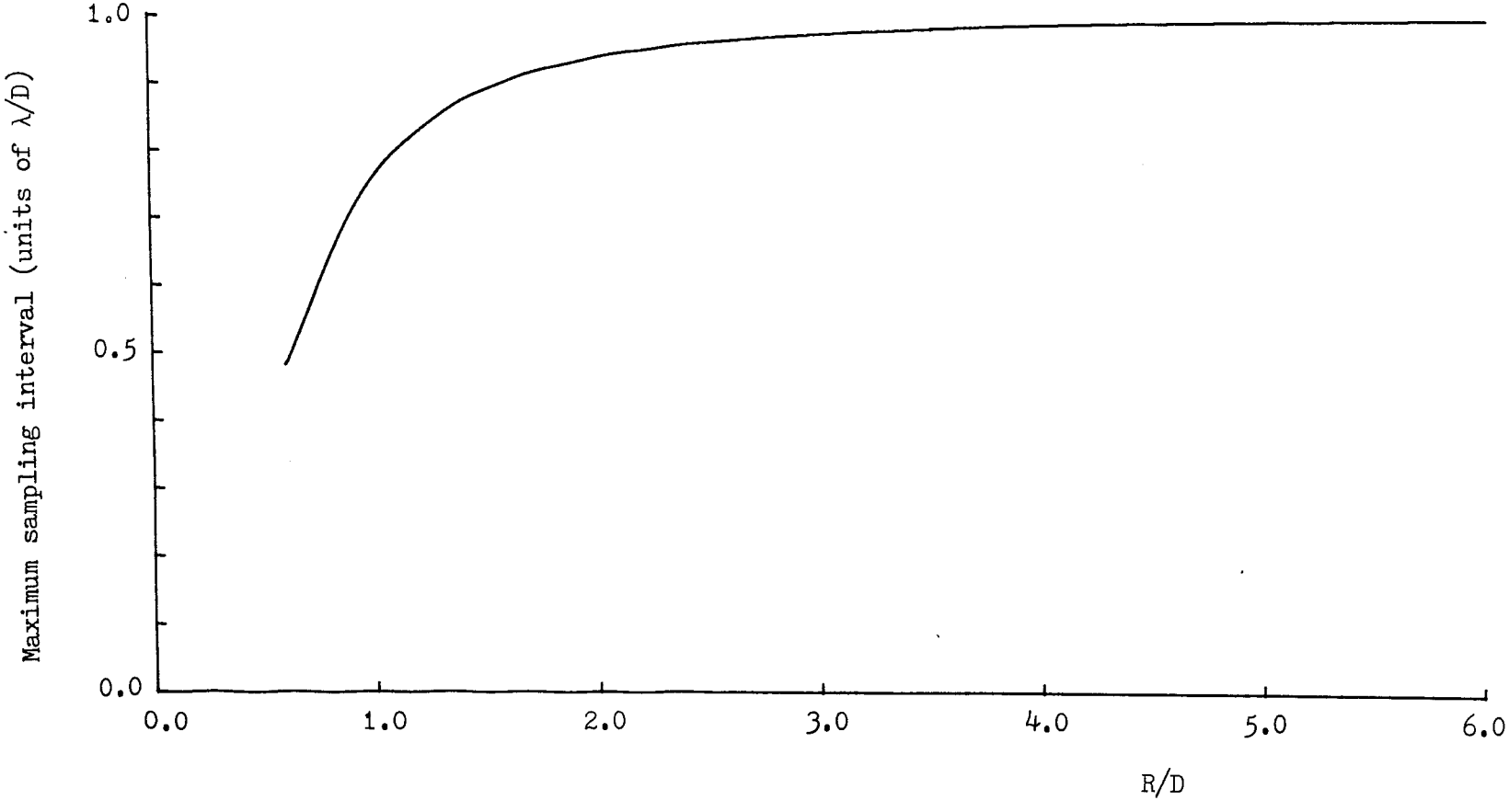

Fig. 2.8. Summary of variation of maximum sample interval with measurement radius for any antenna size at any frequency.

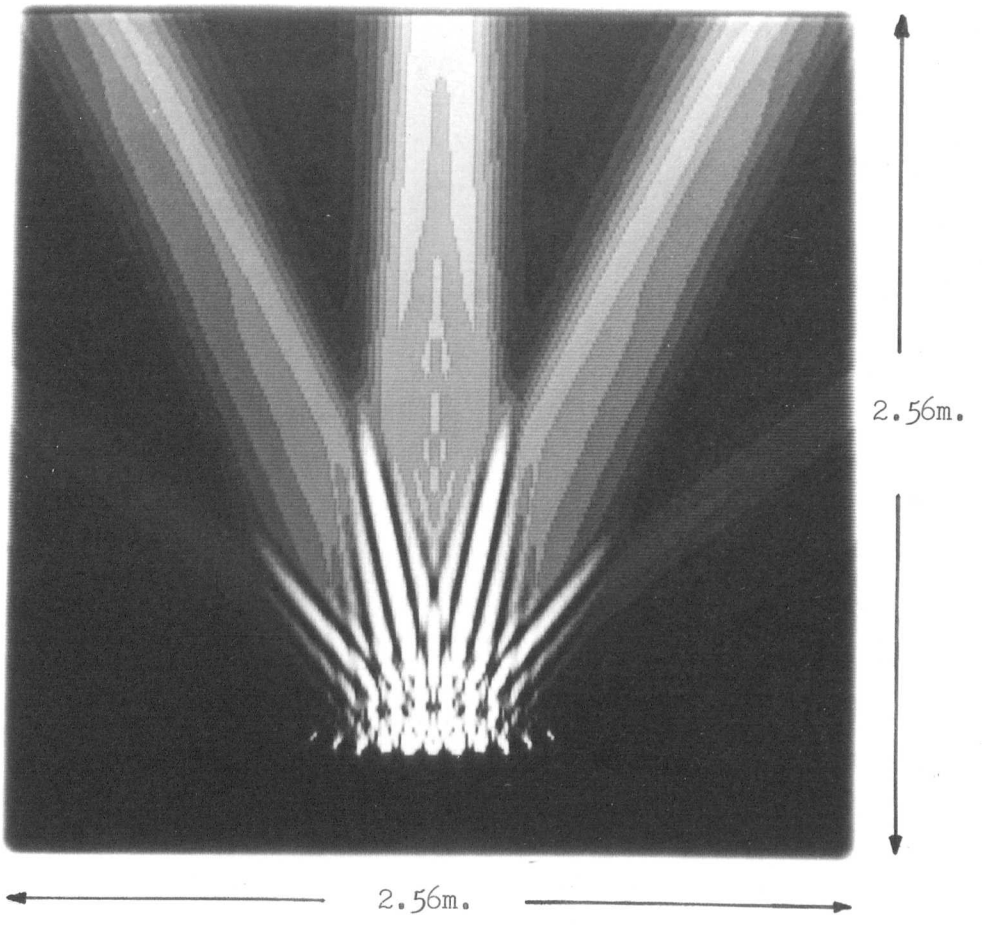

Fig. 2.9. Field distribution (linear scale, as in Table 2.1) due to 13-point weighting function, spacing 4.16°, at 10.0GHz.

Table 2.1

Correspondence between display levels and field strength for Figures 2.9 and 2.10

Display level	Field strength (normalised linear, 1.0 = desired plane wave amplitude)
0 (black)	below 0.1
1	0.2
2	0.3
3	0.4
4	0.5
5	0.6
6	0.7
7	0.8
8	0.9
9	1.0
10	1.1
11	1.2
12	1.3
13	1.4
14	1.5
15 (peak white)	above 1.5

between the weighting function and synthesised plane wave, some large ripples can be observed vanishing just at the near edges of the plane wave. This allows one to place another interpretation on the breakdown of the plane wave into high edge values for positive z : interference fringes due to the interaction of two (or more) plane waves, the required plane wave and the grating lobe(s).

The second example is for similar parameters to the above except that a 27-point weighting function was used with a 2.0^{o} sampling interval. Similar effects to those described above are observed here (Fig.2.10). Because of the reduced sampling interval, now only one grating lobe is created on either side of the main beam. The details of the significance of the different grey levels are again as in Table 2.1.

The last example of the use of this tool for visualisation of field distributions is for exactly the same parameters as example 2 except that the displayed range is reduced to ±25.6cm to show more detail of the synthesised plane wave itself (Fig.2.11). The details of the highly non-linear grey scale representation are contained in Table 2.2. It is felt that this method of displaying synthesised field distributions proves a useful aid to the understanding of the processes involved.

2.5 Two-Dimensional Experimental Results

A 30cm slotted waveguide operated at 10.143GHz was used as the test antenna for a basic verification of the process. The Rayleigh range ($2D^2/\lambda$) for this configuration is

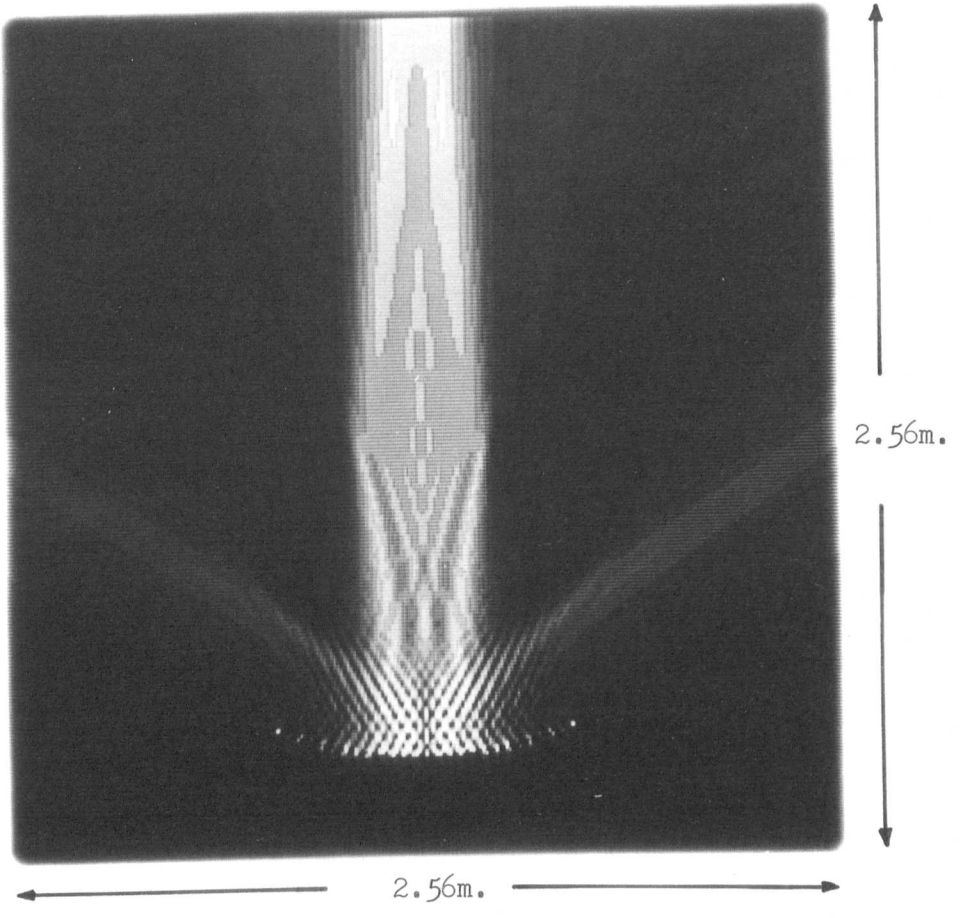

Fig. 2.10. Field distribution (linear scale, as in Table 2.1) due to 27-point weighting function, spacing 2.0°, at 10.0GHz.

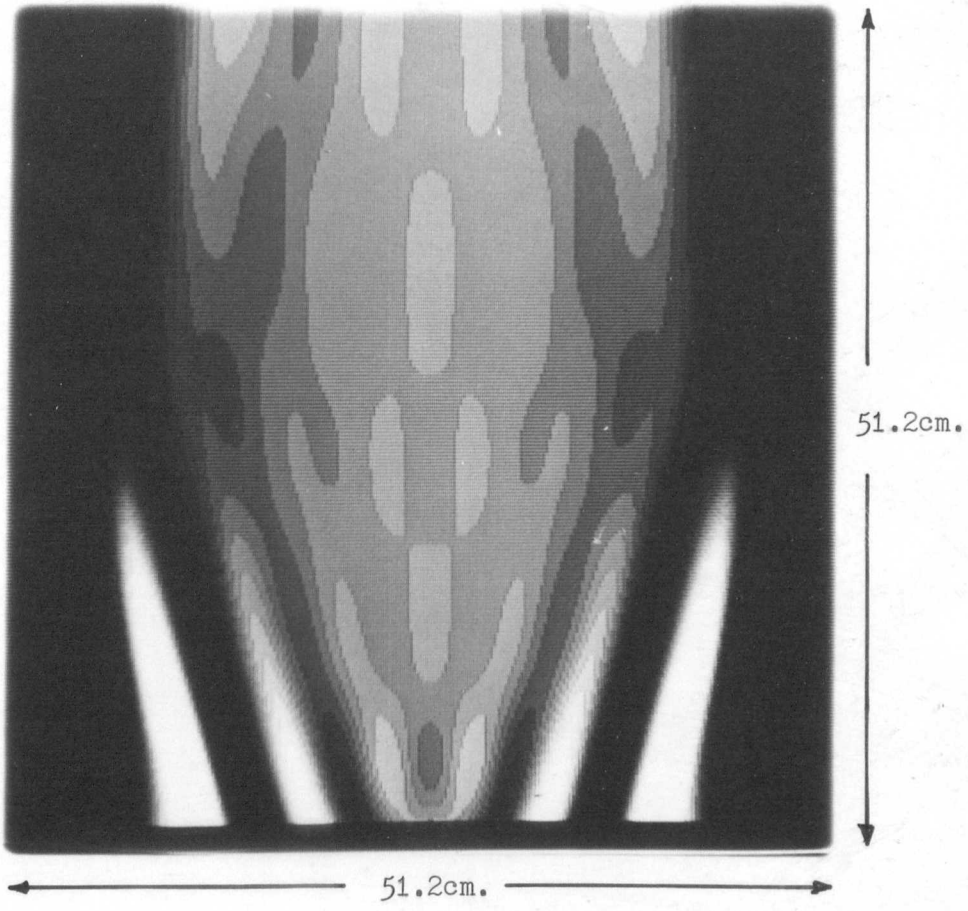

Fig. 2.11. Field distribution (expanded linear scale, as in Table 2.2) due to 27-point weighting function, spacing 2.0°, at 10.0GHz.

Table 2.2

Correspondence between display levels and field strength for Figure 2.11

Display level	Field strength (normalised linear, 1.0 = desired plane wave amplitude)
0	below 0.92
1	0.93
2	0.94
3	0.95
4	0.96
5	0.97
6	0.98
7	0.99
8	1.00
9	1.01
10	1.02
11	1.03
12	1.04
13	1.05
14	1.06
15	above 1.06

approximately 6m, and this corresponded conveniently to the length of the anechoic chamber (at that time) at the University of Sheffield antenna test range at Harpur Hill near Buxton in Derbyshire (described in detail in chapter 6). For simplicity of data processing, the antenna was assumed to be perfectly one-dimensional and it was assumed that only a single circular data scan would be necessary with processing by a one-dimensional weighting function. An inaccuracy inherent in this assumption will be mentioned shortly.

An open-ended waveguide was employed as the near-field probe for the acquisition of the data, the receiver used being a Scientific Atlanta (S.A.) model 1754 two-channel phase and amplitude instrument. The second input channel of the receiver was used for the reference signal for both phase and amplitude. The reference antenna was also formed from open-ended waveguide embedded in absorber below the test antenna. The outputs from the receiver passed via an S.A. 1822 phase meter and an S.A. 1833 amplitude ratiometer to the data logging system comprising an Argus 600 minicomputer (also responsible for control functions) and an 8-track paper-tape punch. This is illustrated diagrammatically in Fig.2.12.

Data were acquired around a full 360^{o} azimuth scan at 0.5^{o} intervals and at a variety of different measurement distances, the shortest range being 1.015m and this set of data is treated in detail here.

Initially a weighting function needed to be obtained and for this purpose, the plane wave was specified to exist over

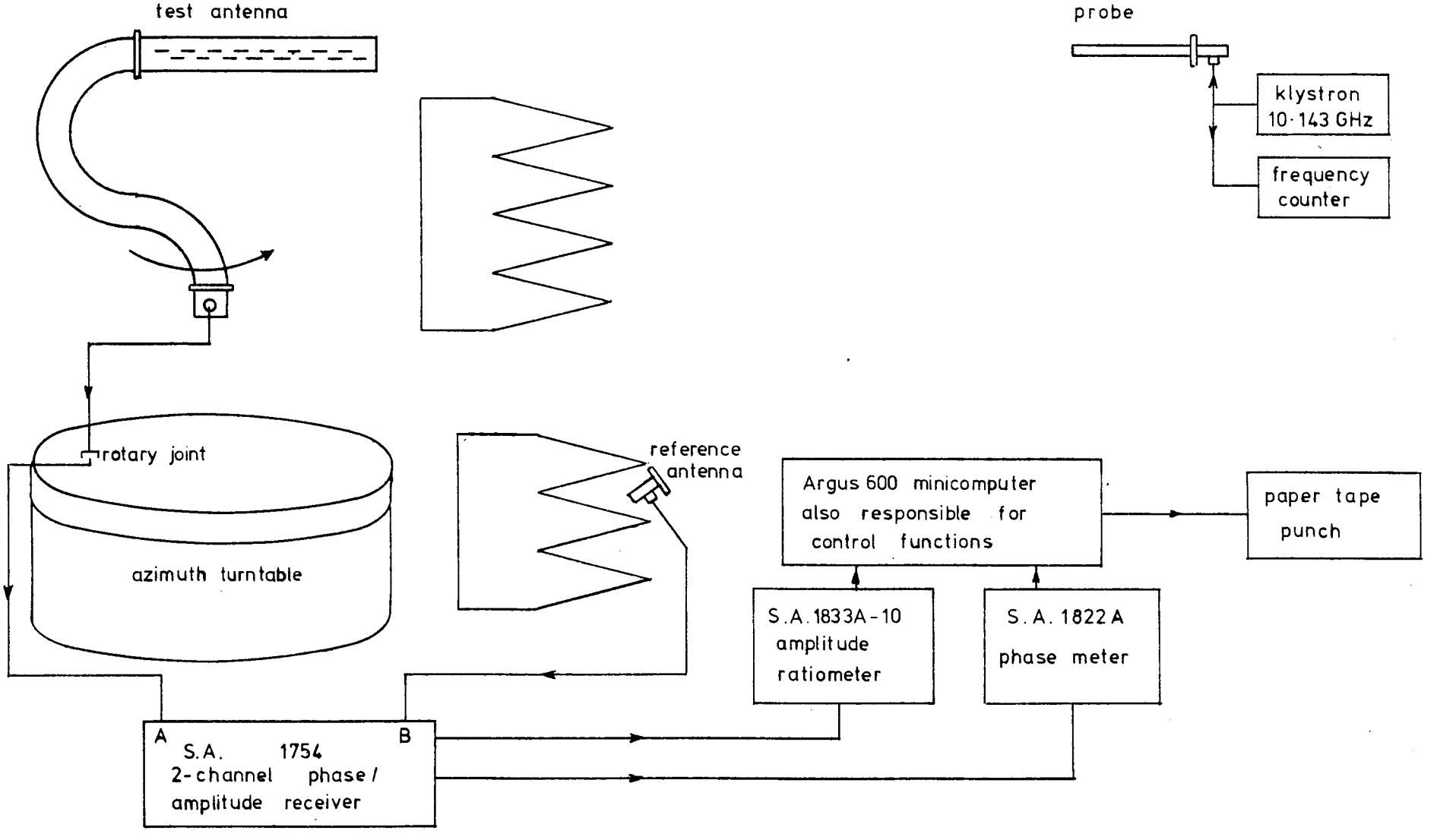

Fig. 2.12. Experimental set-up for evaluation of 30cm. slotted waveguide array.

a range of ±20cm (i.e. D = 40cm) and the weighting function consisted of 81 points spanning an angular range of $\pm 20^{o}$. This weighting function is shown in Fig.2.13. Fig.2.14 illustrates the quality of the plane wave for various values of z in the region of the test antenna. It is seen that the plane wave properties are maintained well over a sufficient depth. The worst of the ringing effects are observed to occur near the edges of the plane wave and it should be noted that, particularly for $z \neq 0$, the test antenna occupies only a central portion of the plane wave so that these peripheral regions assume little importance.

The measured near-field amplitude pattern is shown over the full 360^{o} range in Fig.2.15 and displays classical near-field defocussing effects. The predicted far-field pattern and that measured at 6m range are compared in Fig.2.16 and exhibit an encouraging similarity. Several factors may be cited as possible sources of error :

(a) The inaccuracy of the one-dimensional assumption for the antenna. While probably quite accurate for the slotted waveguide itself, the assumption breaks down for the support structure which should, strictly, be taken as part of the antenna. As much of the support structure as possible was shielded with absorber in an attempt to minimise the ill effects of this factor.

(b) The lack of probe compensation. The open-ended waveguide probe had a finite size and therefore non-uniform radiation characteristics but no compensation was incorporated for this. A scan of the probe pattern

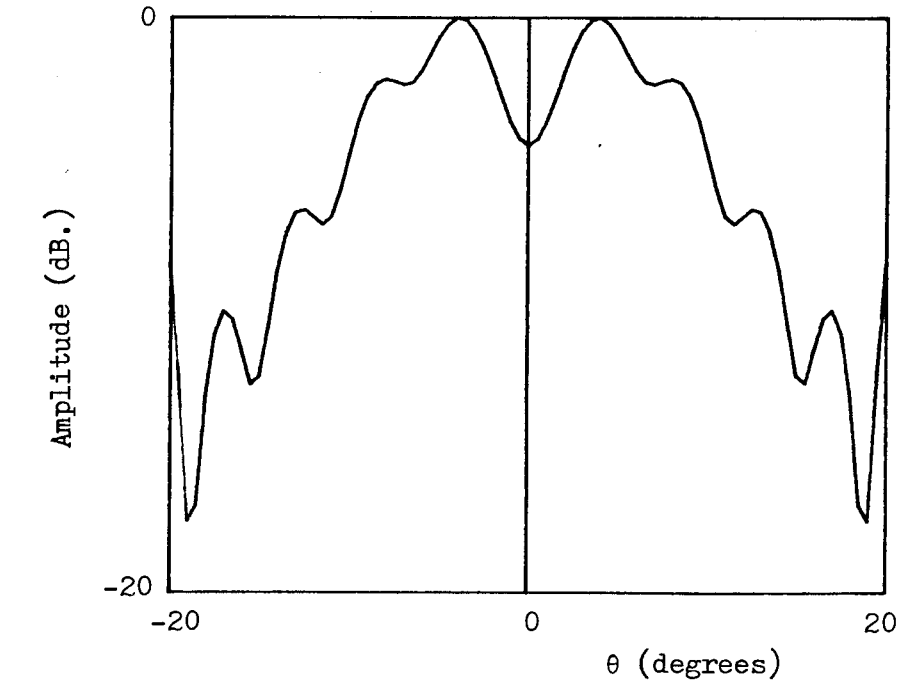

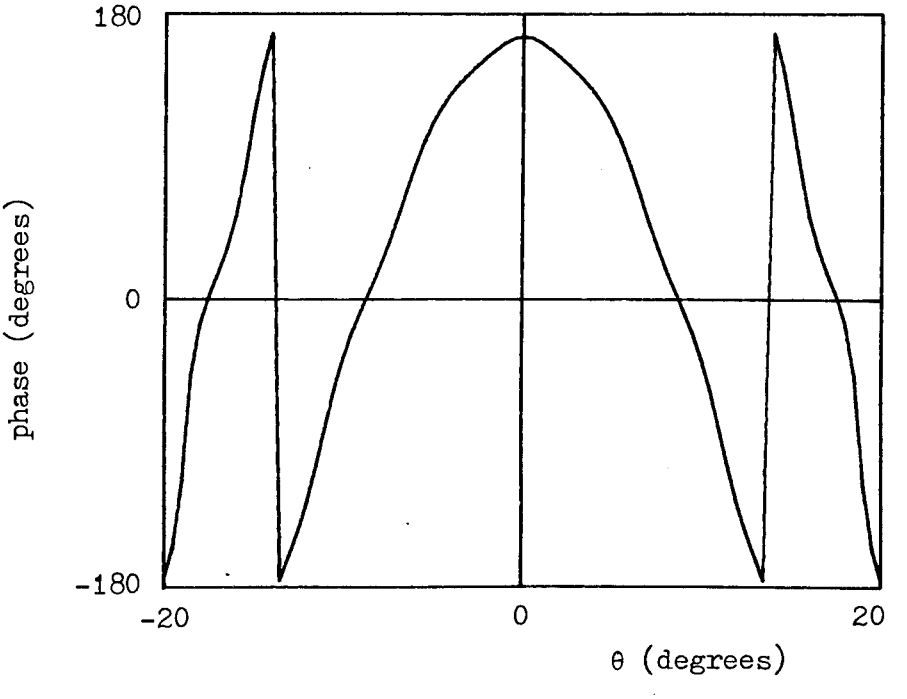

Fig. 2.13. One-dimensional weighting function used in evaluation of 30cm. slotted waveguide array.

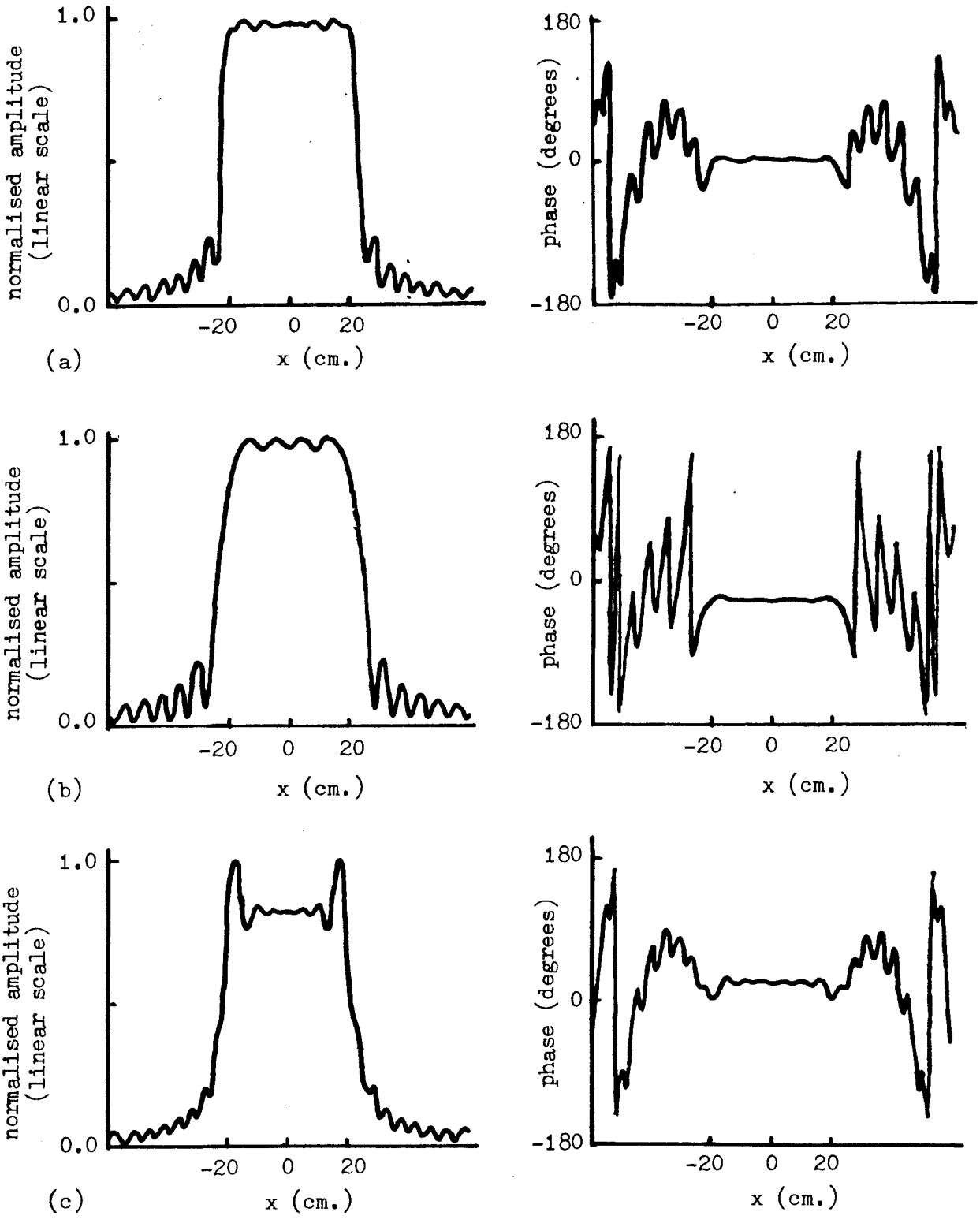

Fig. 2.14. Synthesised plane wave due to weighting function shown in Fig. 2.13; (a) z = 0, (b) z = -15cm., (c) z = +15cm.

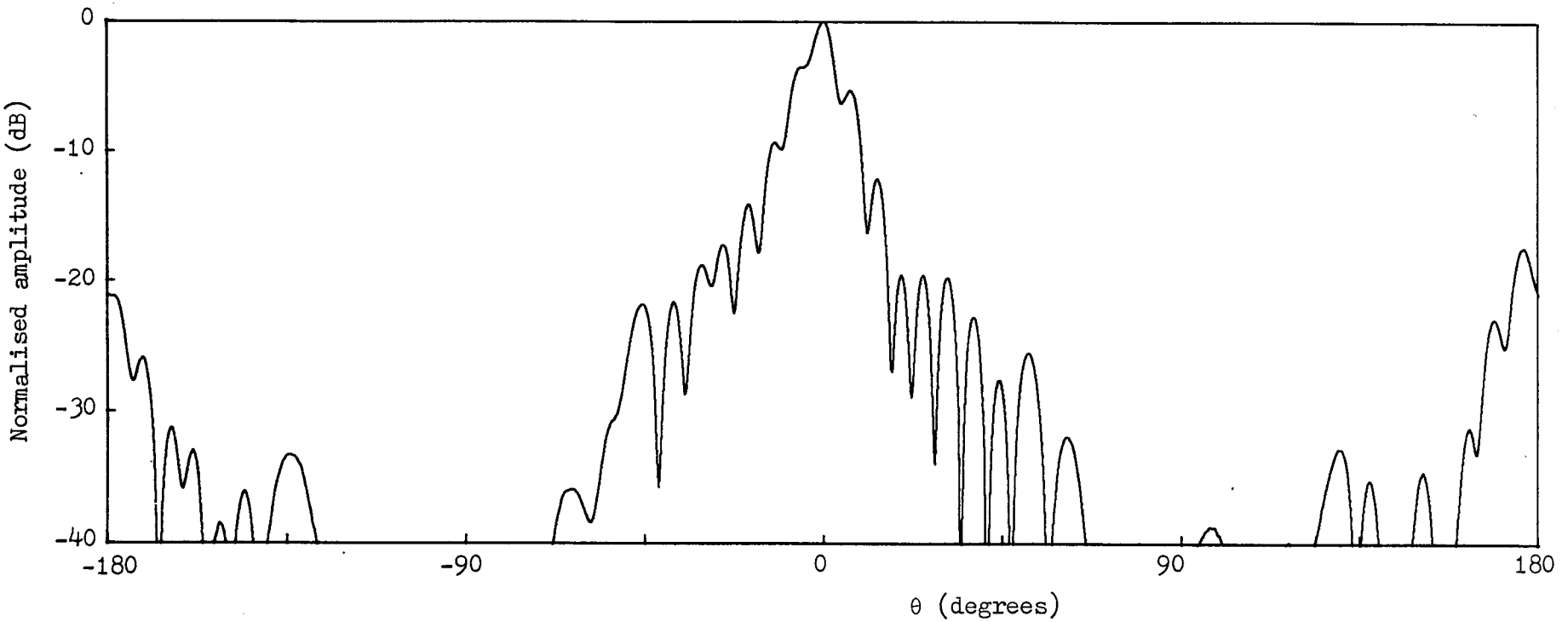

Fig. 2.15. Measured near-field amplitude pattern of 30cm. slotted waveguide array at 10.0GHz. Range 1.015m.

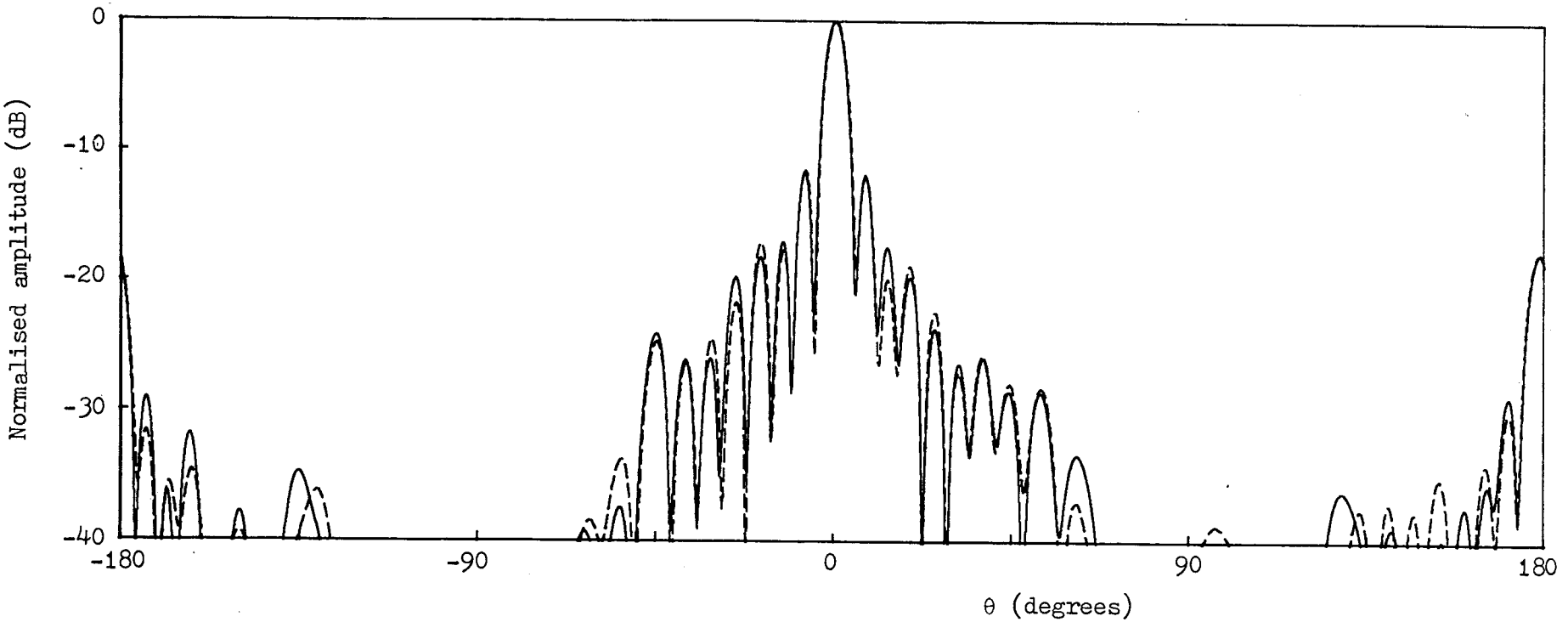

Fig. 2.16. Predicted (solid) and measured at 6m. (dashed) far-field amplitude patterns of 30cm. slotted waveguide array at 10.0GHz.

indicated that the amplitude taper over the test antenna region was a small fraction of a dB and therefore the error caused by neglecting probe compensation is probably slight.

(c) Possible discrepancies between the true far-field pattern and that occurring at a range of 6m. It is well known that certain antennas (those relying on supergain principles being particularly severe cases[28]) require a distance well in excess of the conventional $2D^2/\lambda$, to establish their true far-field patterns. In an attempt to determine whether this factor is significant in this particular case, a new weighting-function was created to synthesise a slightly spherical wave (corresponding to that due to a source at 6m range) and a prediction was performed using this (i.e. a prediction for 6m range). This is shown in Fig.2.17 and it is immediately obvious that the alterations to the predicted pattern are very slight indicating that this possible source of error is probably not important in this instance.

(d) Chamber reflections. It is expected that reflections are, in the main, at a level of -40dB or better but certain regions of the pattern separated by 180° exhibit the more noticeable errors which might indicate the effects of reflections of the main beam and back lobe from certain areas of the chamber. Such reflections may, in fact be more significant in the far-field measurements than in the near-field data since the longer measurement range implies more grazing incidence

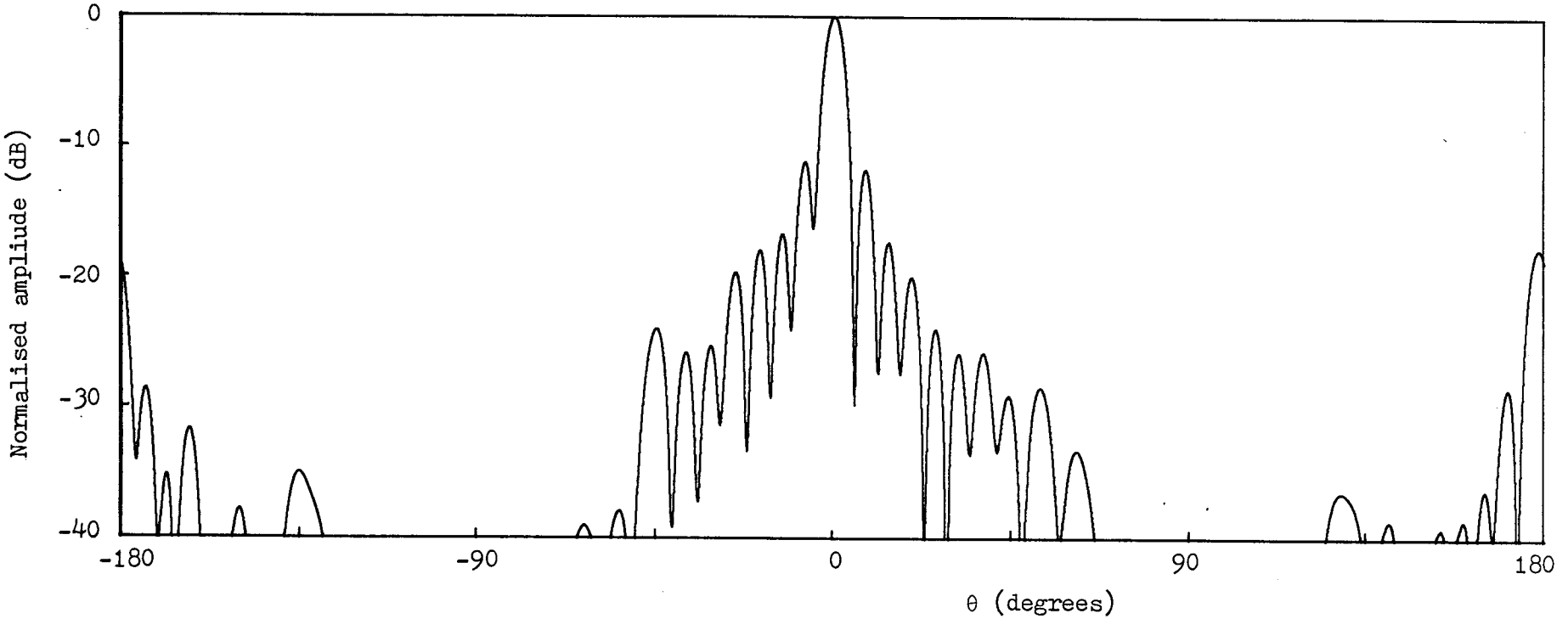

Fig. 2.17. Predicted far-field amplitude pattern of 30cm. slotted waveguide array at 10.0GHz. for a range of 6.0m.

of radiation upon the chamber walls which in turn means that the reflection levels will tend to be higher.

(e) Variation of plane wave amplitude with z. Although it is not obvious from Fig.2.14, each amplitude graph in this particular case being independently normalised, the synthesised plane wave suffered from a slight amplitude fall-off with increasing distance from the weighting function (i.e. decreasing z). This is the practical manifestation of the effect derived from the equations of section 2.2 where, using a one-dimensional weighting function, it was shown that the amplitude was proportional to $(1-z/R)^{-\frac{1}{2}}$, a cylindrical wave effect. This will be of greatest significance in the wider angle predictions ($\theta \simeq \pm 90^{o}$) whereas for predictions near to the main beam or to the back lobe, the effect will not be pronounced.

2.5.1 Conclusions From the Two-Dimensional Results

Within the limits of the two-dimensional approximation and the various errors listed (chapter 5 also covers some errors which may be of importance), it has been demonstrated that plane wave synthesis can provide a useful means of effecting a near-field/far-field transformation. Since these early results, the process has been refined rather more as regards the attainable quality of synthesised plane waves and also the move to the rather more complicated three-dimensional sampling. In the next chapter, therefore, we turn our attention to this latter aspect of the problem.

3. THREE-DIMENSIONAL PREDICTION WITH PROBE COMPENSATION USING AN ELEVATION-OVER-AZIMUTH SCANNING GEOMETRY

In Chapter 1, the sampling geometry produced by an elevation-over-azimuth scanning system was introduced; it is now necessary to formulate this geometry in detail with a view to implementing an iterative procedure, related to that encountered two-dimensionally in Chapter 2, to produce a weighting function applicable over a spherical measurement surface. The details of the iterative procedure will be covered in section 3.3.

3.1 The Approach Used

It is assumed that the radius at which the measurements are taken is in the far-field of the probe so that the radiated field can be taken to vary, in the radial direction, only as $\exp(-jkr)/r$. It is further assumed that the radiation pattern of the probe has been fully characterised (at least over the extent of the relevant solid angle about boresight) in amplitude and phase as a function of its own angular coordinates (θ_p, ϕ_p). It is convenient to assume that the probe radiation pattern has itself been measured using an elevation-over-azimuth system, although naturally, with suitable modification to the expressions, any other probe measurement geometry could equally well be accommodated.

The synthesised plane wave is built up by superposition of the components of the probe placed, in turn, at all the positions defined for the weighting function. This means that it is necessary to determine, for any particular angular position (θ_w, ϕ_w) of the probe, the field components occurring at any point Q (x, y, z) in the

plane wave region. We need, therefore, to determine what values of θ_p, ϕ_p in the probe pattern correspond to the position of point Q relative to the probe when it is at position (θ_w, ϕ_w). Initially we specify that the plane wave exists over a region of the plane z = 0 (see Fig.3.1). An offset (z_o) of the plane will be considered at a later stage.

In the elevation-over-azimuth geometry, the probe lies in the plane $\theta = \theta_w$ looking directly at the origin at all times and with what we may for convenience term its principal polarisation direction perpendicular to the plane. The relationship between θ_p and ϕ_p and θ_w, ϕ_w, x and y is not straightforward since, not only is the probe generally off-axis, but it is also twisted through two angles.

The approach used here for unravelling the complexities of the geometry is to consider a second plane, also passing through the origin, O, but rotated through two angles such that a new coordinate system (x", y", z") is formed in which the new plane is the plane z" = 0 and the probe lies on the z"-axis with its principal polarisation direction parallel to the y"-axis. The probe will still, of course, point directly towards the origin, along the z"-axis. The new configuration is illustrated in Fig.3.2. The point Q" (x", y", 0) is taken to be the projection onto the plane z" = 0, looking from the probe position, of the point Q (x, y, 0) in the original unrotated coordinate system. Being the projection looking from the probe, the point Q" in the new coordinate system must possess exactly the same angular orientation (θ_p, ϕ_p)

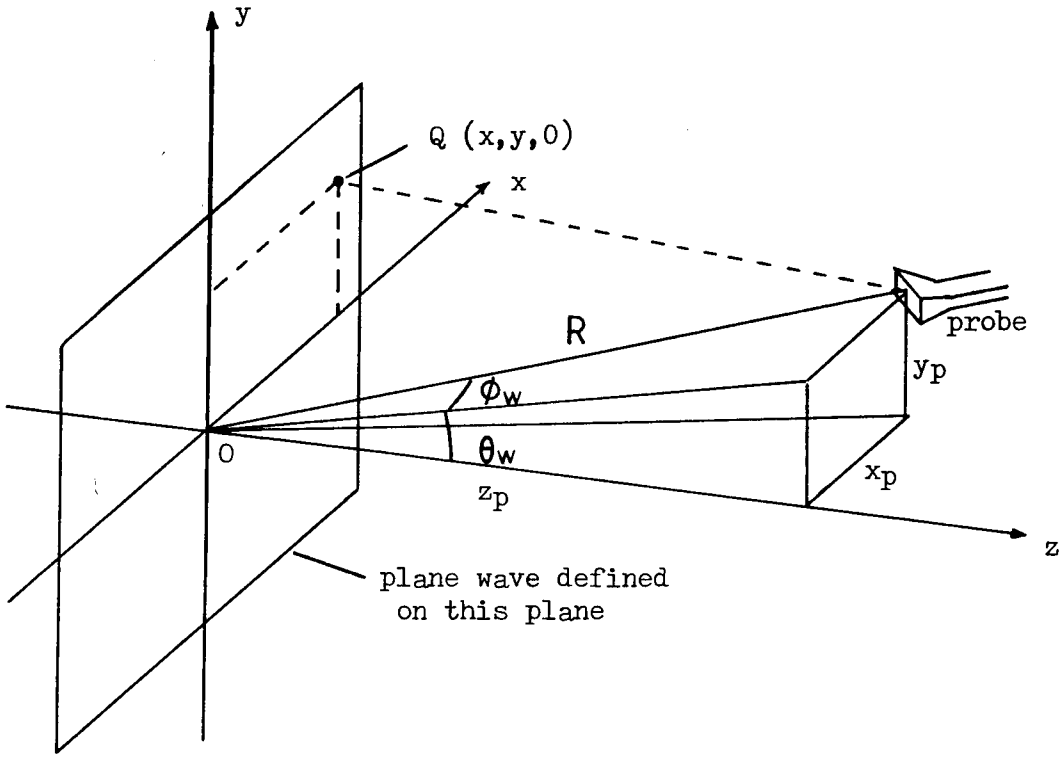

Fig. 3.1. Probe/plane-wave-point relationship for an elevation-over-azimuth scan system.

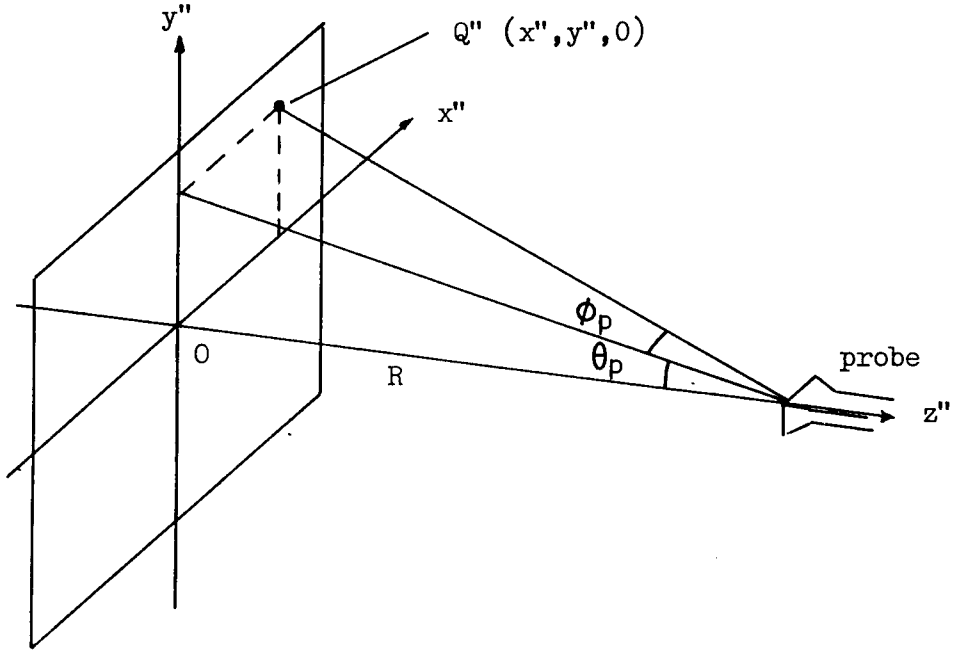

Fig. 3.2. The new x",y",z" coordinate system produced by a double rotation about the origin.

to the probe as the original point Q. The angles θ_p and ϕ_p can be related comparatively easily to x" and y" since in the x" - y" - z" coordinate system the probe lies on the z"-axis and is upright. The problem of relating θ_p and ϕ_p to x, y, θ_w and ϕ_w is effectively translated to that of relating x" and y" to x, y, θ_w and ϕ_w.

3.1.1 Rotation 1

The process of obtaining x" and y" in terms of x, y, θ_w and ϕ_w is carried out in two stages. The first stage consists of a rotation of the plane z = 0 through an angle θ_w about the x-axis to form the plane z' = 0 in the newly created x' - y' - z' coordinate system. The probe now stands upright on the plane y' = 0 as illustrated in Fig.3.3. We must now find expressions for the coordinates x' and y' of the projection, Q', of the original point Q, onto the plane z' = 0.

From Fig. 3.4 which is a view obtained looking along the x (or x') axis, we see that,

$$y' = y\ (\cos\theta_w + \sin\theta_w \tan\ (\alpha + \theta_w)) \qquad (3.1)$$

where

$$\alpha = \tan^{-1}\ (\frac{y - y_p}{z_p}) \qquad (3.2)$$

y_p and z_p being two of the Cartesian coordinates equivalent to the probe position (R, θ_w, ϕ_w), given by,

$$y_p = R\ \cos\phi_w\ \sin\theta_w \qquad (3.3)$$

and

$$z_p = R\ \cos\phi_w\ \cos\theta_w \qquad (3.4)$$

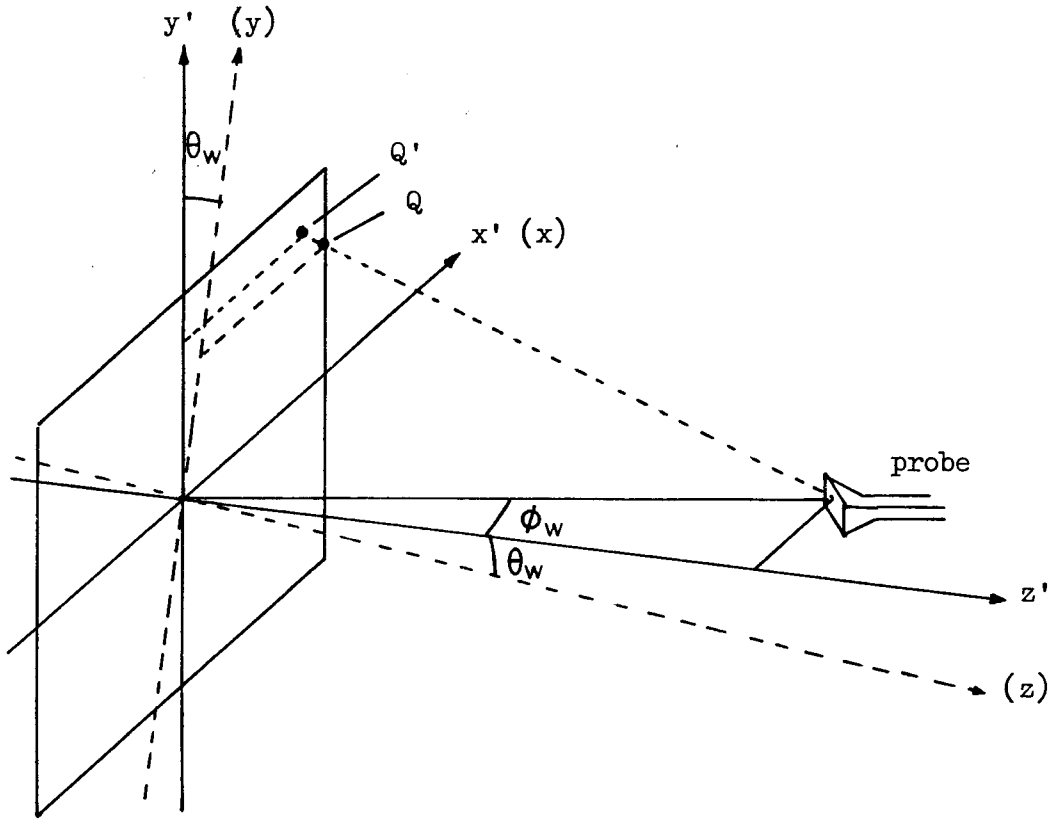

Fig. 3.3. Rotation 1 to form x',y',z' coordinate system.

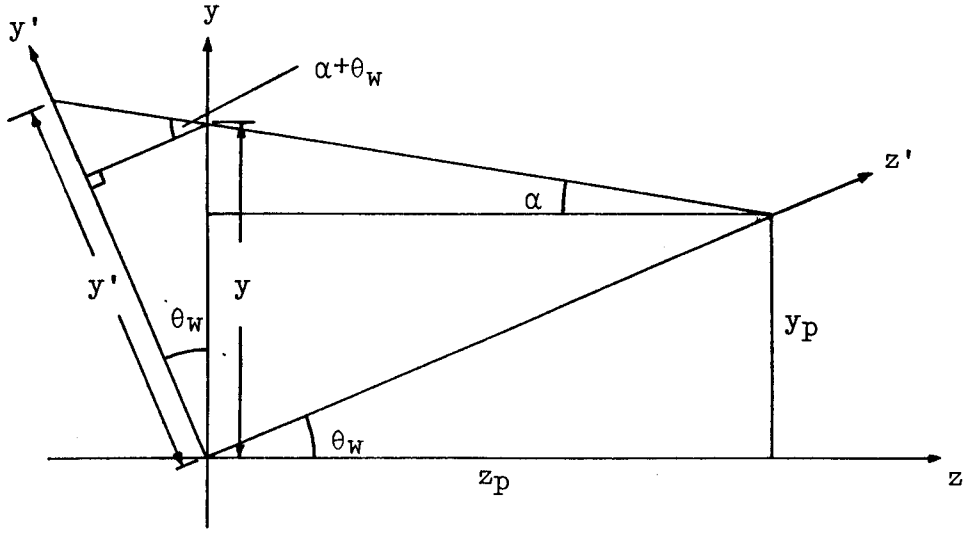

Fig. 3.4. View along x (or x') axis for first rotation.

The other Cartesian coordinate, x_p is given by,

$$x_p = R \sin\phi_w \tag{3.5}$$

and this is required in the formulation of an expression for x'. Referring to Fig. 3.5, from equivalent triangles,

$$\frac{x' - x_p}{x - x_p} = \frac{d' + d}{d} \tag{3.6}$$

which, when the appropriate substitutions are made to eliminate d and d', yields,

$$x' = x_p + (x - x_p)\left(\frac{R^2\cos^2\phi_w + y'^2}{z_p^2 + (y - y_p)^2}\right)^{\frac{1}{2}} \tag{3.7}$$

3.1.2 Rotation 2

The second rotation takes place about the y'-axis (which then becomes the y"-axis) through an angle ϕ_w, to form the plane z" = 0 in the x" - y" - z" coordinate system.

Fig. 3.6 illustrates the geometry of this rotation in some detail. It can now be shown that,

$$y'' = y'\left(1 + \frac{x' \sin\phi_w \cos\beta}{A \cos(\beta + \phi_w)}\right) \tag{3.8}$$

where, as shown in Fig. 3.6,

$$A = (y_p^2 + z_p^2)^{\frac{1}{2}} \tag{3.9}$$

and

$$\beta = \tan^{-1}\left(\frac{x' - x_p}{A}\right) \tag{3.10}$$

The change in the x-coordinate is described by,

$$x'' = x'(\cos\phi_w + \sin\phi_w \tan(\beta + \phi_w)) \tag{3.11}$$

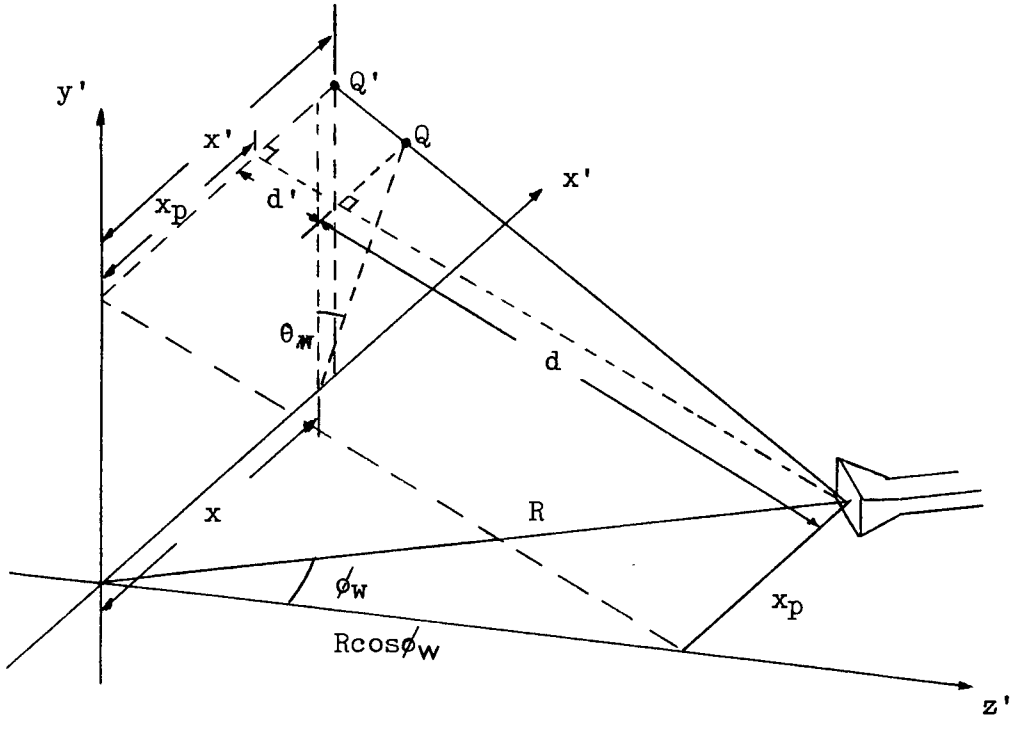

Fig. 3.5. To determine x' in x',y',z' coordinate system.

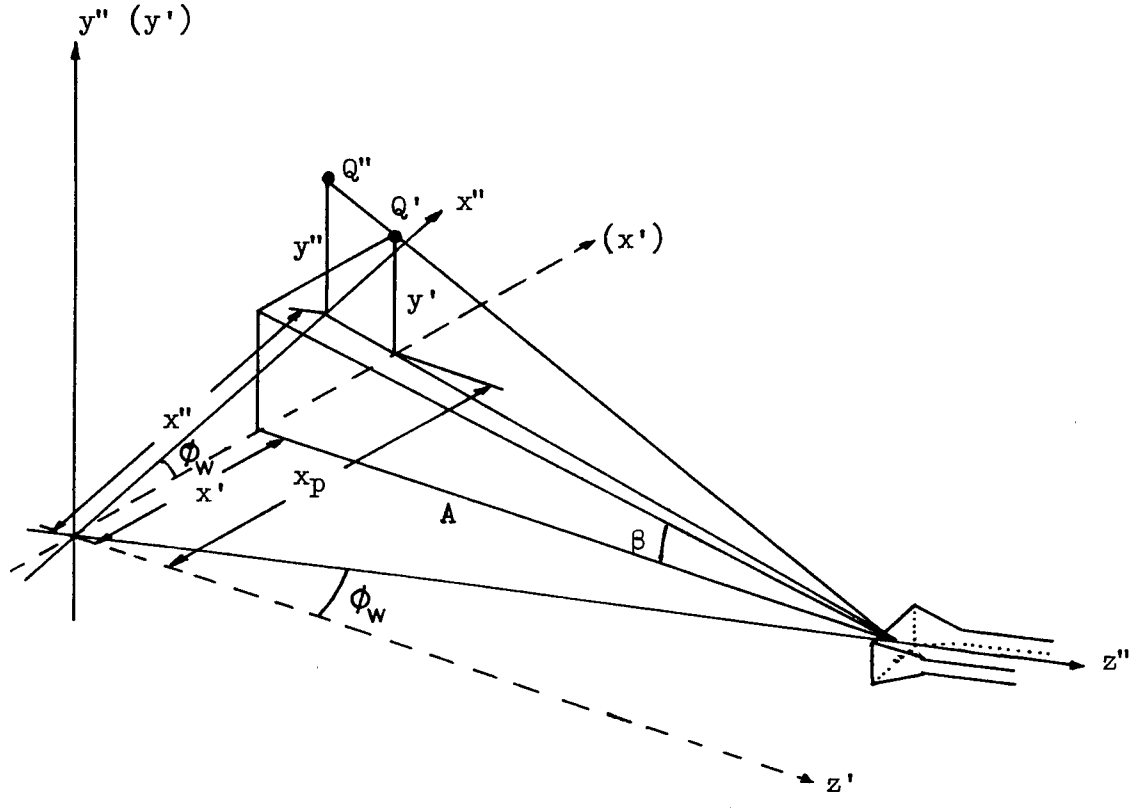

Fig. 3.6. Rotation 2 to form x",y",z" coordinate system.

3.1.3 Resulting Field Components

If we now move over to the probe coordinate system, as shown in Fig. 3.7, we can determine the angles θ_p and ϕ_p to be as follows:

$$\phi_p = \sin^{-1} \left(\frac{x''}{r_1}\right) \tag{3.12}$$

and

$$\theta_p = \tan^{-1} \left(\frac{y''}{R}\right) \tag{3.13}$$

where

$$r_1 = (x''^2 + y''^2 + R^2)^{\frac{1}{2}} \tag{3.14}$$

It is important to note, at this point, that the angle ϕ_p as defined above is not the angle actually used in the probe measurement system, as defined in Chapter 1, but is in fact its negative. The field component in the ϕ_p-direction is likewise reversed.

We now recall that, to describe fully the near-field pattern of the test antenna, it is necessary to obtain data samples with two orthogonal probe polarisations. This fact becomes of more significance in later sections but, at this stage, let it suffice to say that the analysis below applies to only a single polarisation of the probe which we may take, for convenience, to be the principal polarisation direction. It is shown in Chapter 5 that it is possible to obtain useful results utilising only a single polarisation of a suitable probe. If the appropriate components of the probe field are extracted, the following analysis is, of course, equally applicable to the secondary polarisation of the probe.

It is assumed that the radiation pattern of the probe

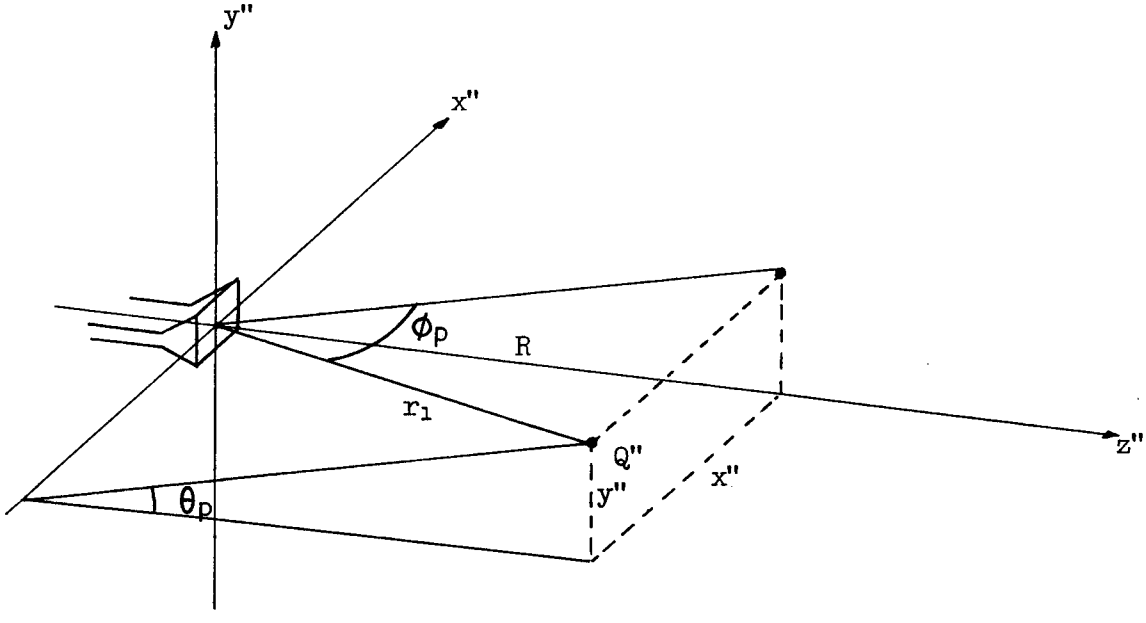

Fig. 3.7. The probe coordinate system.

has been characterised, for convenience, on an elevation over azimuth system, thus, with suitable interpolation if necessary, the components $E_{\theta p}$ and $E_{\phi p}$ will be known. It can be shown, by returning through the double rotation, that the resultant field components at the point Q in the original coordinate system are given by,

$$E_x = E_{\theta p} \sin\phi_w \sin\theta_p + E_{\phi p}(\cos\phi_w \cos\phi_p + \sin\phi_w \sin\phi_p \cos\theta_p) \quad (3.15)$$

and

$$E_y = E_{\theta p}(\cos\theta_w \cos\theta_p + \cos\phi_w \sin\theta_w \sin\theta_p) + E_{\phi p}(\cos\phi_w \sin\theta_w \sin\phi_p \cos\theta_p - \sin\phi_w \sin\theta_w \cos\phi_p - \cos\theta_w \sin\phi_p \sin\theta_p) \quad (3.16)$$

For the present, we omit the E_z component since this is not required directly for the implementation of the iteration procedure. The existence of a component in the E_z direction implies some effective propagation across the plane wave region (i.e. not in the wanted z-direction) and must therefore be associated with a perturbation of the desired plane wave component E_y and thus optimisation of the components in the plane of iteration (E_x and E_y) will automatically imply the minimisation of E_z. The coefficients characterising E_z will be given for the case of an offset plane of iteration, which is the more general case, and these can be used to derive the coefficients for the present non-offset case.

It should be noted that, for brevity, the factor $\frac{R \exp -jk(r-R)}{r}$ has been omitted from equations (3.15) and

(3.16). Here, the quantity r describes the distance from the probe at (R, θ_w, ϕ_w) to the point Q (x, y, O) and is given by,

$$r = ((x - x_p)^2 + (y - y_p)^2 + z_p^2)^{\frac{1}{2}} \qquad (3.17)$$

3.2 Introduction of z-Offset

It has been found that the synthesised plane wave tends to maintain its properties for a greater distance from the plane of iteration in a direction moving away from the weighting function region than in the direction moving towards the weighting function. In view of this, it has been found advantageous to define the plane of iteration as offset from the origin some small distance towards the weighting function region. In addition, if it is required to examine the quality of the synthesised plane wave on planes other than that passing through the origin, it is likewise necessary to introduce an offset, z_o, into the coefficients previously derived.

The two coordinate rotations which were earlier arranged to take place about the origin are now arranged to take place about the point at which the line joining the probe to the origin intersects the plane $z = z_o$. Equation (3.1) may be modified to include the offset, z_o, as follows,

$$y' = (y - z_o \tan\theta_w)(\cos\theta_w + \sin\theta_w \tan(\alpha + \theta_w)) \qquad (3.18)$$

where

$$\alpha = \tan^{-1}\left(\frac{y - y_p}{z_p - z_o}\right) \qquad (3.19)$$

the relevant diagram here being Fig. 3.8, a view looking along the x (or x') axis.

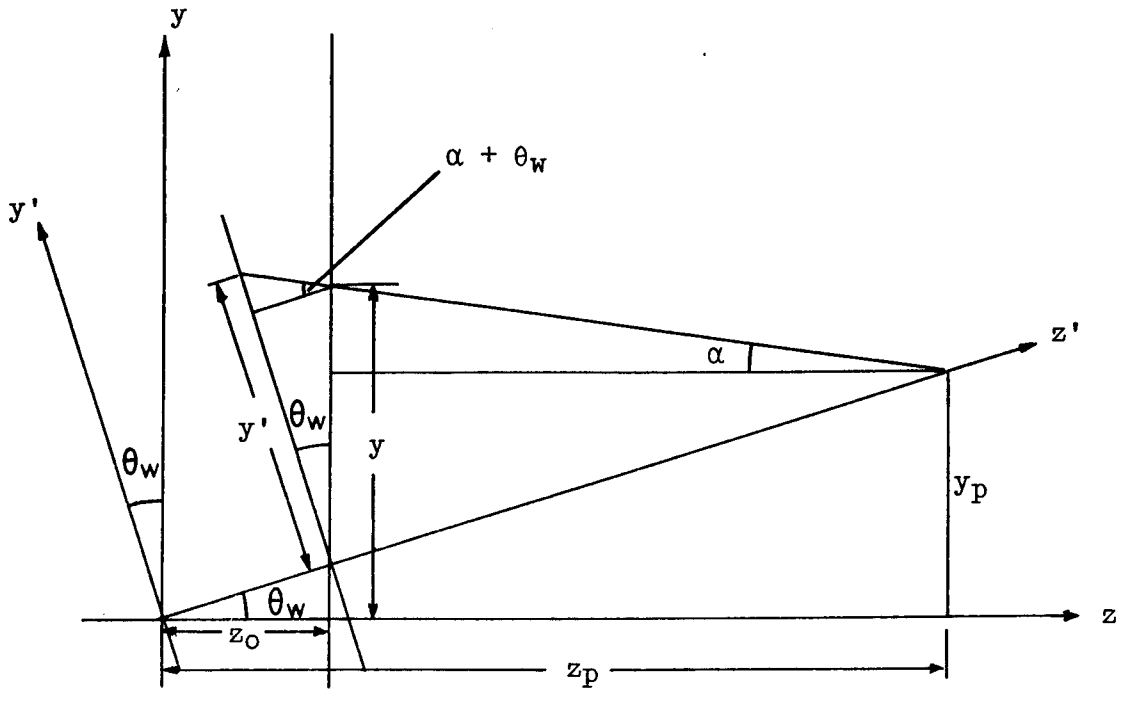

Fig. 3.8. z-offset, rotation 1, view along x (or x') axis.

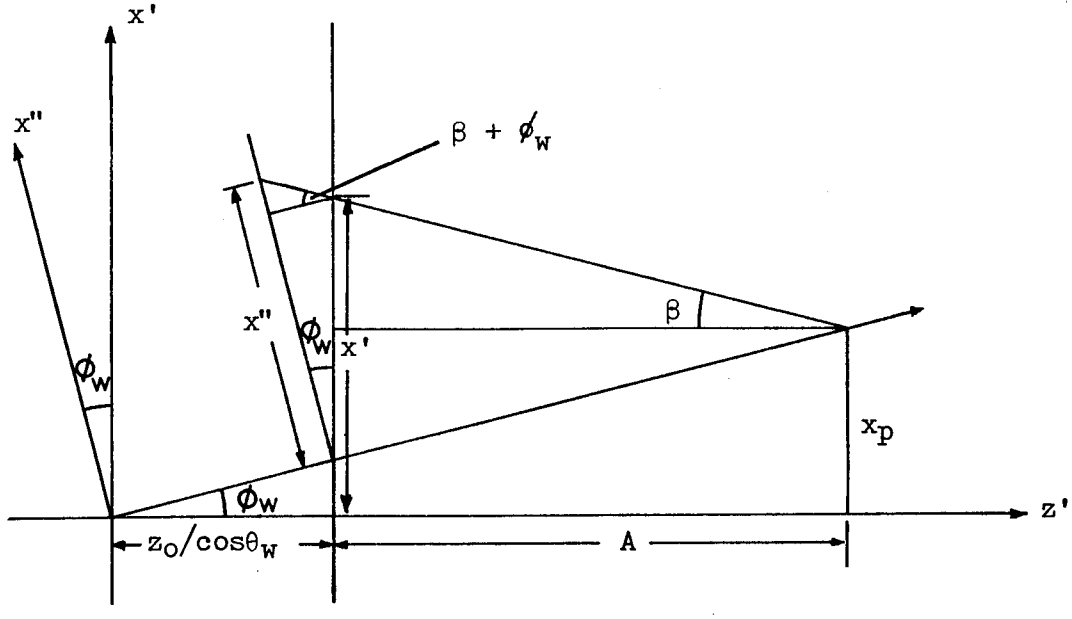

Fig. 3.9. z-offset, rotation 2, view along y' (or y") axis.

Equation (3.7) is likewise modified to read as follows,

$$x' = x_p + (x-x_p)\left(\frac{R\cos\phi_w - z_o/\cos\theta_w)^2 + y'^2}{z_p^2 + (y-y_p)^2}\right)^{\frac{1}{2}} \qquad (3.20)$$

Moving on to the second rotation, equation (3.8) for y" (repeated here for convenience) remains valid,

$$y = y'\left(1 + \frac{x' \sin\phi_w \cos\beta}{A \cos(\beta + \phi_w)}\right) \qquad (3.21)$$

where β is defined, as in equation (3.10),

$$\beta = \tan^{-1}\left(\frac{x' - x_p}{A}\right) \qquad (3.22)$$

but the value of A is slightly modified from that given in equation (3.9),

$$A = (y_p^2 + z_p^2)^{\frac{1}{2}} - z_o/\cos\theta_w \qquad (3.23)$$

For the x"-coordinate, equation (3.11) is altered to read,

$$x" = (x' - z_o \tan\phi_w/\cos\theta_w)(\cos\phi_w + \sin\phi_w \tan(\beta+\phi_w)) \qquad (3.24)$$

as may be deduced from Fig. 3.9.

3.2.1 Resulting Field Components

As in section 3.1.3, we now move over to the coordinate system used to describe the probe. The equation used for ϕ_p still remains valid,

$$\phi_p = \sin^{-1}\left(\frac{x"}{r_1}\right) \qquad (3.25)$$

but r_1 is now altered to,

$$r_1 = \left(x"^2 + y"^2 + \left(R - \frac{z_o}{\cos\theta_w \cos\phi_w}\right)^2\right)^{\frac{1}{2}} \qquad (3.26)$$

The equation for θ_p becomes,

$$\theta_p = \tan^{-1} \left(\frac{y''}{R - z_o/(\cos\theta_w \cos\phi_w)} \right) \qquad (3.27)$$

Having found the appropriate angles in the probe measurement system (and noting again the lateral inversion meaning that the value of ϕ_p shown is the negative of the actual value in the probe measurement system and the direction of $E_{\phi p}$ is reversed), the values of the two field components $E_{\theta p}$ and $E_{\phi p}$ may be obtained from the measurements. Again the factor $\frac{R \exp -jk(r-R)}{r}$ has been assumed in the above and should be included at this point bearing in mind that the value of r is now given by,

$$r = ((x-x_p)^2 + (x-y_p)^2 + (z_p-z_o)^2)^{\frac{1}{2}} \qquad (3.28)$$

For completeness, at this point, we go on to note the E_z component, although not important as regards the iteration procedure,

$$\begin{aligned} E_z = {} & E_{\theta p} (\cos\phi_w \cos\theta_w \sin\theta_p - \sin\theta_w \cos\theta_p) \\ & + E_{\phi p} (\cos\phi_w \cos\theta_w \sin\phi_p \cos\theta_p \\ & + \sin\theta_w \sin\phi_p \sin\theta_p - \sin\phi_w \cos\theta_w \cos\phi_p) \end{aligned} \qquad (3.29)$$

$\left(\frac{R \exp - jk(r - R)}{r} \text{ assumed}\right)$.

3.3 The Iteration Procedure

The preceding sections have derived, in detail, the equations relating the field distribution in the plane wave region to the angular position of the probe. This enables us to evaluate the synthesised field produced if the probe

is scanned over the spherical surface and the appropriate data samples are weighted with any desired function. We now recall that we require the synthesised field to take on the form of a linearly polarised plane wave with components,

$$E_x = 0 \tag{3.30}$$

$$E_z = 0 \tag{3.31}$$

$$E_y = \text{constant} \tag{3.32}$$

which, in turn, means that we require a weighting function which, when applied to the samples at a particular set of points defined on the spherical scan surface, gives rise as nearly as possible, to this situation. Applying the idea of reciprocity leads us to say that if we specify the desired plane wave suitably over the particular plane of interest and then integrate numerically out to the spherical surface, using coefficients identical to those obtained earlier (but with inverted exponential $\left(\frac{R \exp + jk(r-R)}{r}\right)$, an approximation to the correct weighting function may be achieved. If the angular range of this weighting function is unlimited then, as stated in section 2.2, when the set of coefficients (now with the negative exponential) are used to construct the synthesised field distribution on the same plane, a very close approximation to the desired plane wave is produced. If, however, some different z offset is introduced to examine the synthesised plane wave on a different plane, it is found that the distribution breaks down. To improve the "depth of field" of the synthesised plane wave, the angular extent of the

weighting function, $g(\theta_w,\phi_w)$, is limited. This also has the useful property of reducing the quantity of near-field data involved in any one prediction. It is now found that the synthesised plane wave exhibits somewhat reduced quality on the original plane but maintains itself much better with varying z. This property is illustrated in Appendix 3.

The quality of predictions obtainable with the "first guess" weighting function would be severely limited by the poor plane wave but this can be much improved by applying an iterative procedure. The mechanics of this are as follows. The synthesised plane wave is calculated from the "first guess" weighting function. There will be certain errors present in this field distribution and these may be extracted and propagated out again to the spherical surface in the same way as was done with the original desired plane wave distribution. This creates what may be termed an "error weighting function" which is subtracted from the "first guess" to provide a "second guess" weighting function. This, in turn, can be used to synthesise a new plane wave whose errors will be smaller than in the plane wave due to the "first guess". The process can then begin again to produce a "third guess" and so on until the process has converged to give an optimum weighting function.

3.4 Typical Parameters for the Weighting Function

It has been found that, typically, a weighting function will need to extend to between $\pm 20^{o}$ and $\pm 30^{o}$ in θ_w and ϕ_w, and will converge to produce a plane wave

of acceptable quality within 10 to 30 iterations. Originally, the weighting function region would be specified as a square matrix of points in θ_w and ϕ_w on the spherical surface but more recently it has been found advantageous, from the point of view of computing time, to specify a circular region within the square matrix of points only within which is the weighting function allowed to exist.

For the iteration procedure, the required plane wave is also specified as a matrix of points spaced at about $\lambda/2$ intervals within a circular region, slightly exceeding the dimensions of the test antenna, on the plane of iteration. It has been found to improve considerably the quality of the synthesised plane wave attainable if, initially, the desired plane wave is specified to extend a few points (typically four) beyond the edge of that actually required. These extra points are used in setting up the "first guess" weighting function but disregarded thereafter. The effect is that the ripple, particularly at the edges of the plane wave, will tend to move further out into the region of these unimportant points and the significant area of the plane wave will thus exhibit improved quality. Another facet of the behaviour of the plane wave is that it tends, in a typical situation, to be elongated in the z-direction and, as pointed out in section 2.2.2, maintains its quality better for negative z (away from the weighting function) than for positive. This has given rise to the idea of offsetting the plane of iteration from the origin of the coordinate system

and this has been implemented in the more recent software, hence the importance of formulating the relationship between plane wave components and probe position for z-offset in section 3.1. Section 2.4 includes particularly useful illustrations of field distributions in the plane wave region.

3.5 Three Dimensional Scanning

In the above, we have described the creation of a weighting function extending around part of the equatorial region of a set of points corresponding to an elevation-over-azimuth measurement geometry (or azimuth-over-elevation if everything is rotated through 90^{o}). Fig.3.10 illustrated the situation of such a weighting function positioned on a sphere of data measured on an elevation-over-azimuth system. It is immediately obvious that, to predict the $E_{\theta F}$ far-field component at any other angle, θ_F, along the principal axis, $\phi_F = 0$, the weighting function will be incremented through the data in the elevation (θ) direction and the direct positional and polarisation correspondence between data and weighting function will be maintained. If it is required, however, to produce a prediction for $\phi_F \neq 0$, the situation shown in Fig.3.11 arises where there is no longer any correspondence between measured data and weighting function. A similar sort of problem is encountered when the prediction of the $E_{\phi F}$ component is required, when the weighting function has to be rotated through 90^{o} about its centre and again the correspondence between data and weighting function is lost.

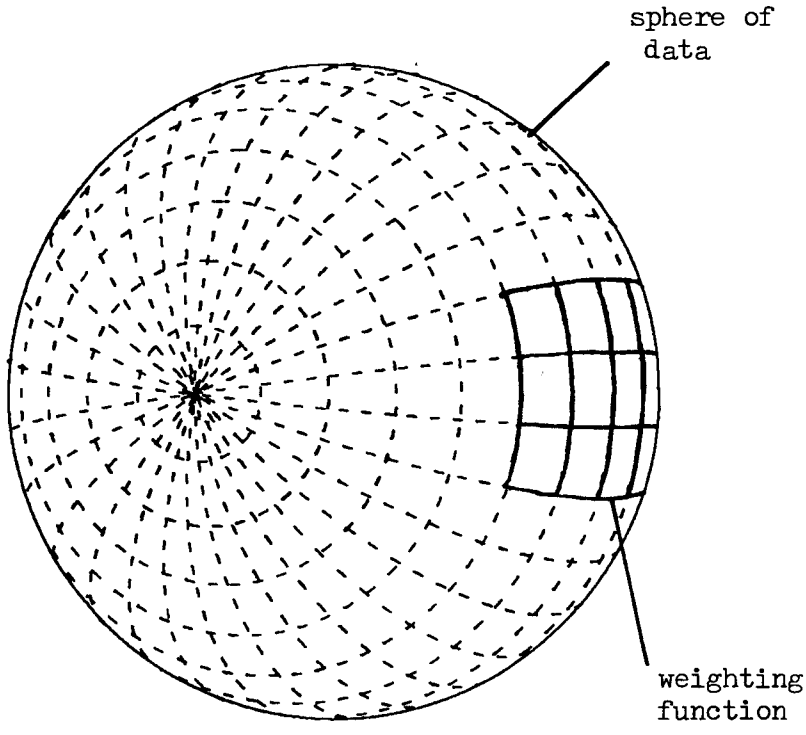

Fig. 3.10. Weighting function positioned on the principal plane.

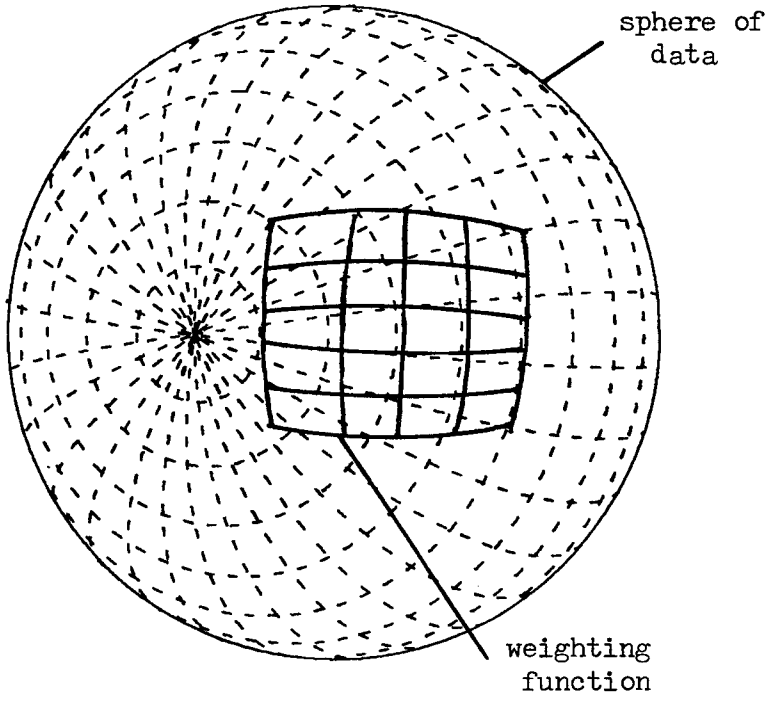

Fig. 3.11. Weighting function shifted off principal plane showing loss of direct point-for-point correspondence with data.

The straightforward solution to the problem is to interpolate the data. It will be demonstrated that the interpolation can be performed indirectly by precalculation of interpolation coefficients and combination with the known weighting function (which will then become known as the "primary" weighting function) to produce what will be termed the "composite" weighting function. It is firstly convenient to turn our attention to formulating the necessary geometrical relationships.

3.5.1 Prediction of $E_{\theta F}$ for $\phi_F \neq 0$

We consider a weighting function point at (θ_w, ϕ_w) where the centre of the weighting function has been shifted from the centre of the data set to angular position $(0, \phi_F)$. Fig. 3.12 illustrates the situation. It can then be shown that the point (θ_w, ϕ_w) in the weighting function assumes a position in the measured data given by,

$$\theta = \sin^{-1}\left((1-\sin^2\theta_w\cos^2\phi_w)^{\frac{1}{2}}\sin\left(\phi_F+\tan^{-1}\left(\frac{\tan\phi_w}{\cos\theta_w}\right)\right)\right) \qquad (3.33)$$

$$\phi = \sin^{-1}(\sin\theta_w\cos\phi_w \;/\; \cos\phi) \qquad (3.34)$$

This information enables the required near-field data to be selected/interpolated from those measured in terms of E_θ and E_ϕ, noting that the angular values may extend outside the data set limits (if the value of ϕ from equation 3.33 is $> 90^o$) so that, in an actual implementation, a check should be incorporated for this condition and the appropriate adjustments made for θ, ϕ and component direction. For application of the weighting function to the measured data, the components, E_θ and E_ϕ, should be resolved into the

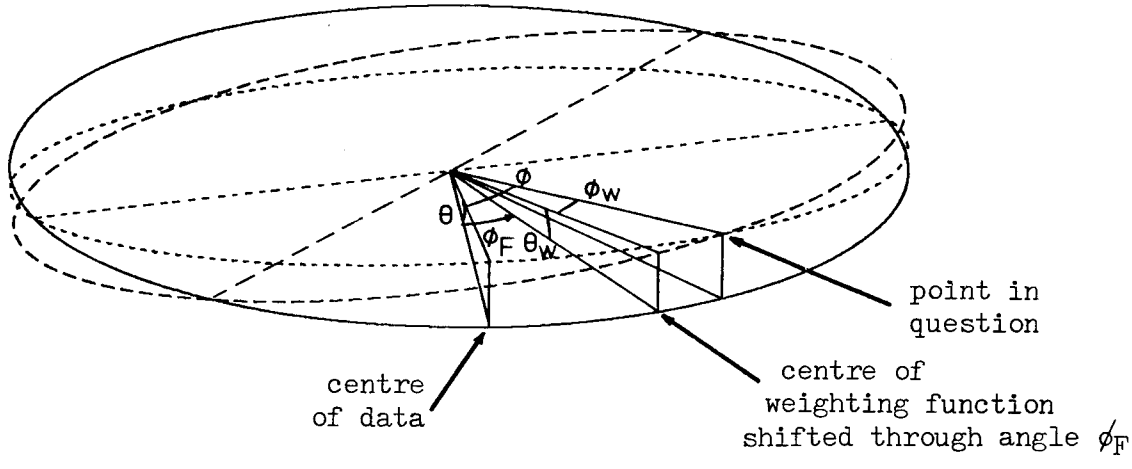

Fig. 3.12. The situation of a point in a weighting function shifted off axis.

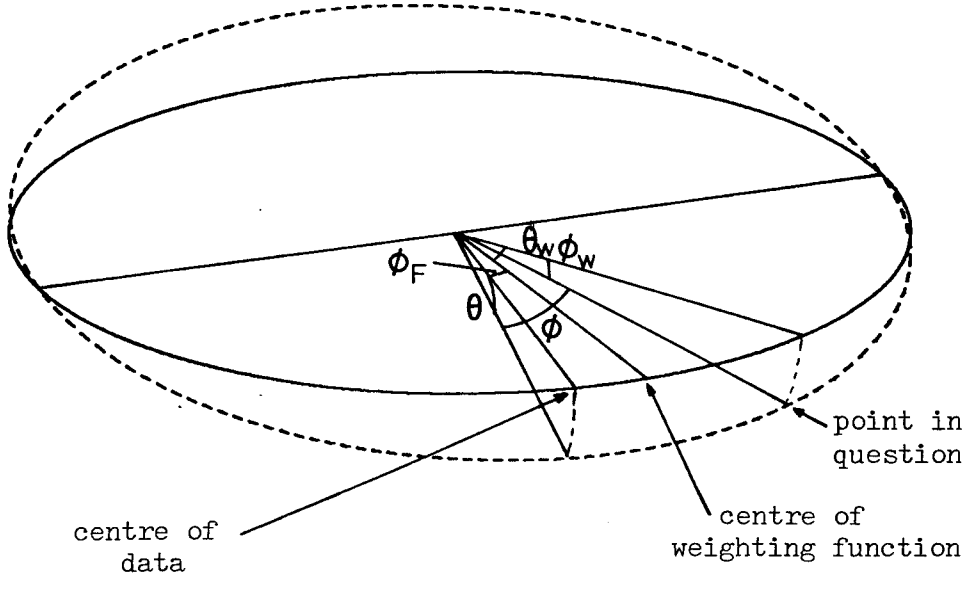

Fig. 3.13. The situation of a point in a weighting function rotated through 90°.

directions defined for the weighting function according to the following rather protracted formulae.

$$E_{\theta w} = E_{\theta}\ (\cos\theta\cos\theta_w + \sin\theta\cos\phi_F\sin\theta_w) + E_{\phi}\ (\sin\phi\sin\theta\cos\theta_w - \cos\phi\sin\phi_F\cos\theta_w - \sin\phi\cos\theta\cos\phi_F\sin\theta_w) \quad (3.35)$$

$$E_{\phi w} = E_{\theta}\ (\sin\theta(\sin\phi_F\cos\phi_w + \cos\phi_F\cos\theta_w\sin\phi_w) - \cos\theta\sin\theta_w\sin\phi_w) + E_{\phi}\ (\cos\phi(\cos\phi_F\cos\phi_w - \sin\phi_F\cos\theta_w\sin\phi_w) - \sin\phi\sin\theta\sin\theta_w\sin\phi_w - \sin\phi\cos\theta(\sin\phi_F\cos\phi_w+\cos\phi_F\cos\theta_w\sin\phi_w)) \quad (3.36)$$

The above equations facilitate evaluation of the components necessary to produce a prediction at any angle, ϕ_F, for $\theta_F = 0$. No modification is needed in the equations to predict at an angle $\theta_F \neq 0$ except that when the measured near-field data are being selected for the prediction, θ_F should be added to the value of θ obtained from equation (3.34) (but the value of θ as given by equation (3.34) should still be used in equations (3.35) and (3.36)). Again checks should be made when selecting the near-field data that the θ-range of the set is not exceeded, adjusting by $\pm 360^{o}$ if necessary to bring it back within range.

3.5.2 Prediction of $E_{\phi F}$

When the calculated weighting function is rotated through 90^{o} to predict the other (perhaps cross-polar) far-field component, $E_{\phi F}$, there again ceases to be any correspondence between the weighting function and data.

As in the above we shall consider the angular position of a point (θ_w, ϕ_w) in the weighting function (now rotated through 90°) for a prediction at $\theta_F = 0$, $\phi_F \neq 0$. The position is defined by,

$$\phi = \sin^{-1} (\cos\phi_w \sin(\phi_F + \theta_w)) \tag{3.37}$$

$$\theta = -\sin^{-1} (\sin\phi_w / \cos\phi) \tag{3.38}$$

The sense of the angles being as shown in Fig. 3.13. The components of field, resolved in the required directions for the weighting function are as follows,

$$E_{\theta w} = E_\theta \sin\theta \sin(\phi_F + \theta_w) + E_\phi(\cos\phi\cos(\phi_F+\theta_w) - \sin\phi\cos\theta\sin(\phi_F+\theta_w)) \tag{3.39}$$

$$E_{\phi w} = E_\theta(\sin\theta\cos(\phi_F+\theta_w)\sin\phi_w - \cos\theta\cos\phi_w) - E_\phi(\cos\phi\sin(\phi_F+\theta_w)\sin\phi_w + \sin\phi\sin\theta\cos\phi_w + \sin\phi\cos\theta\cos(\phi_F+\theta_w)\sin\phi_w) \tag{3.40}$$

3.6 The Composite Weighting Function

In section 3.5 it was stated that to overcome the problems caused by the nature of the scan geometry on the spherical surface, interpolation of the data could be performed. In a prototype version of a prediction (using, in fact, data obtained from a polarisation-over-azimuth system as will be discussed in Chapter 4), the data were interpolated directly but the process was found to be rather time consuming as may be forseen from the somewhat lengthy nature of the formulae involved in extracting the required field components. In a scheme designed to simplify the post-measurement processing, this is clearly undesirable and

in order to circumvent this drawback, the idea of forming a "composite weighting function" came about.

The weighting function (which to avoid confusion we shall refer to, in this section, as the "primary" weighting function) obtained by the methods described earlier is created for a particular sample geometry and interpolating it to fit the actual measured data would alter its characteristics so this is not permissible. Interpolation of the measured data, while permissible, is undesirably slow. The ideal solution would be achieved if the data could be interpolated before they were measured. Clearly, obtaining the actual interpolated data values in advance of the measurement is an absurdity, but the process embodied in the creation of the composite weighting function does allow all the work of the interpolation to be performed before the measured data are introduced.

The usual circumstance will be where near-field data are required somewhere within one of the cells of the matrix of measured data. In general, regardless of which interpolation formula is to be used, it will operate in such a way as to create a set of coefficients which, when applied to a number of the surrounding samples and the results summed, produce the required values. The next stage in the procedure would be for the results of the interpolation to be multiplied by further coefficients designed to turn the data expressed as field components in the measurement geometry into the form of field components corresponding to the weighting function geometry. They would then be multiplied by the appropriate elements of the

primary weighting function. Since the measurement geometry will be known in advance the interpolation coefficients can be calculated in advance and, exploiting the associative nature of the multiplication operations, the products of the interpolation coefficients, component resolution coefficients and primary weighting function values can likewise be precalculated. By this means, the multiplication of a primary weighting function value by a near-field component produced by the resolution of other field components, themselves resulting from interpolation from a number of actual measured samples, can be reduced to direct multiplication of these measured samples by precalculated coefficients.

The process may be taken one stage further. A matrix of measured data was utilised in the interpolation of the field components at one particular point. To interpolate the fields at a nearby point, another matrix of measured data will be used and it is likely that a number of these measured data will be the same as used for the first point. It is recognised that, within a single prediction, the remaining process will be one of summation and here, the distributive law can be invoked enabling us to say that, rather than multiplying any particular data sample by all of the appropriate precalculated coefficients individually, it is permissible to add together all these coefficients in advance and perform just one multiplication, the product then going forward into the final summation to produce the prediction.

To summarise, the composite weighting function is created by combining the primary weighting function elements with the necessary interpolation and component resolution

coefficients. The individual matrices of coefficients will overlap extensively and, where this occurs, addition of all the overlapping coefficients is performed. The end result is a composite weighting function which is entirely the result of calculations performed in advance of the measurement and acts just as if the measured data themselves were being interpolated but may be applied directly to the measured data without any further interpolation processing. As such the composite weighting function is independent of the measured data and may be applied to whatever test antenna is being measured, assuming, of course, that the measurement parameters are commensurate with those incorporated into the composite weighting function.

Such a composite weighting function could be stored in the form of an array equal in size to the whole of the measured data but since most of the stored values would be zero and furthermore, a separate weighting function is required for each value of ϕ_F (in the present geometry) and for each polarisation of prediction, this would seem rather wasteful. It is much more useful to store the composite weighting function in the form of groups of two complex numbers (being the coefficients for the two polarisations of measured data) together with two integers defining the measured data to which the coefficients are to be applied.

3.7 Interpolation Schemes

A brief investigation has been performed into the properties of a number of common interpolation formulae. The different schemes assessed were as follows:

(a) Fourier interpolation.

(b) Lagrange interpolation.

(c) The Newton forward difference method.

(d) Everett's formula.

(e) Bassel's formula.

(which are variously described in references[29][30][31]). In each case a four-point interpolation formula was used. The test function was a sine wave of unit amplitude. In each case a wide range of sample spacings was tried. For each sample spacing, the interpolation was performed with a large number of different sets of four points spread across one period of the function and for each set of four points used, the point of interpolation was varied within the central interval. In this way it was hoped to obtain a statistically meaningful set of results.

For each individual interpolation method, maximum deviation from the correct function and r.m.s. deviation have been plotted as a function of sample spacing and the results form Figures 3.14 to 3.23. On each graph a dotted line has been inserted to indicate the Nyquist sampling interval and the error at that point. Fourier interpolation (Figures 3.14 and 3.15) exhibits the interesting property of the error oscillating from very small values to peaks of, in the case of four-point interpolation, about 0.2 (maximum-error graph), in the region within the Nyquist sampling rate. It has been found (although not illustrated here) that increasing the number of points used in the interpolation brings about an increase in the number of lobes within this region while decreasing their size and

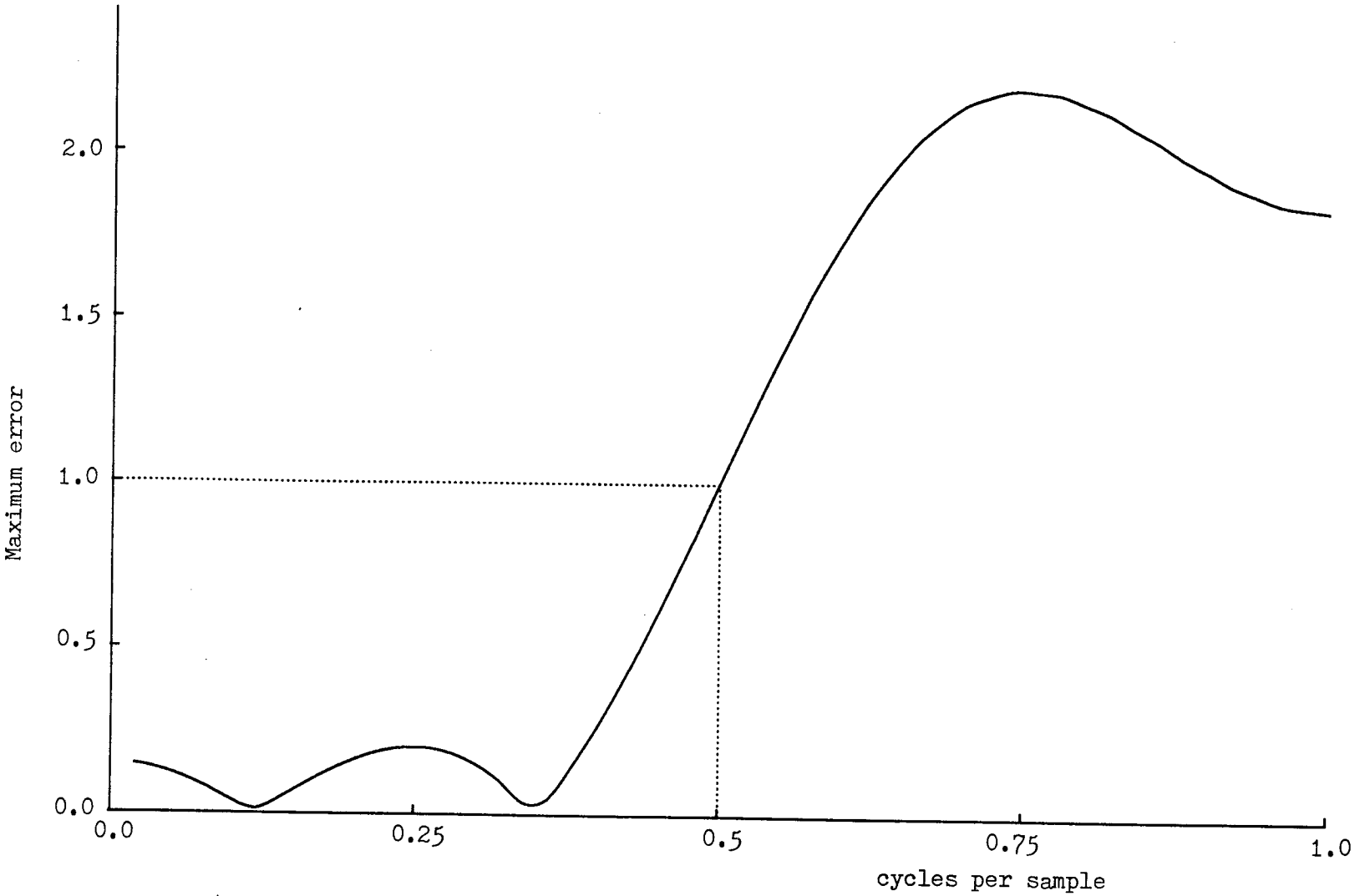

Fig. 3.14. Maximum error due to 4-point Fourier interpolation of a sinusoid (amplitude 1.0): variation with sample spacing.

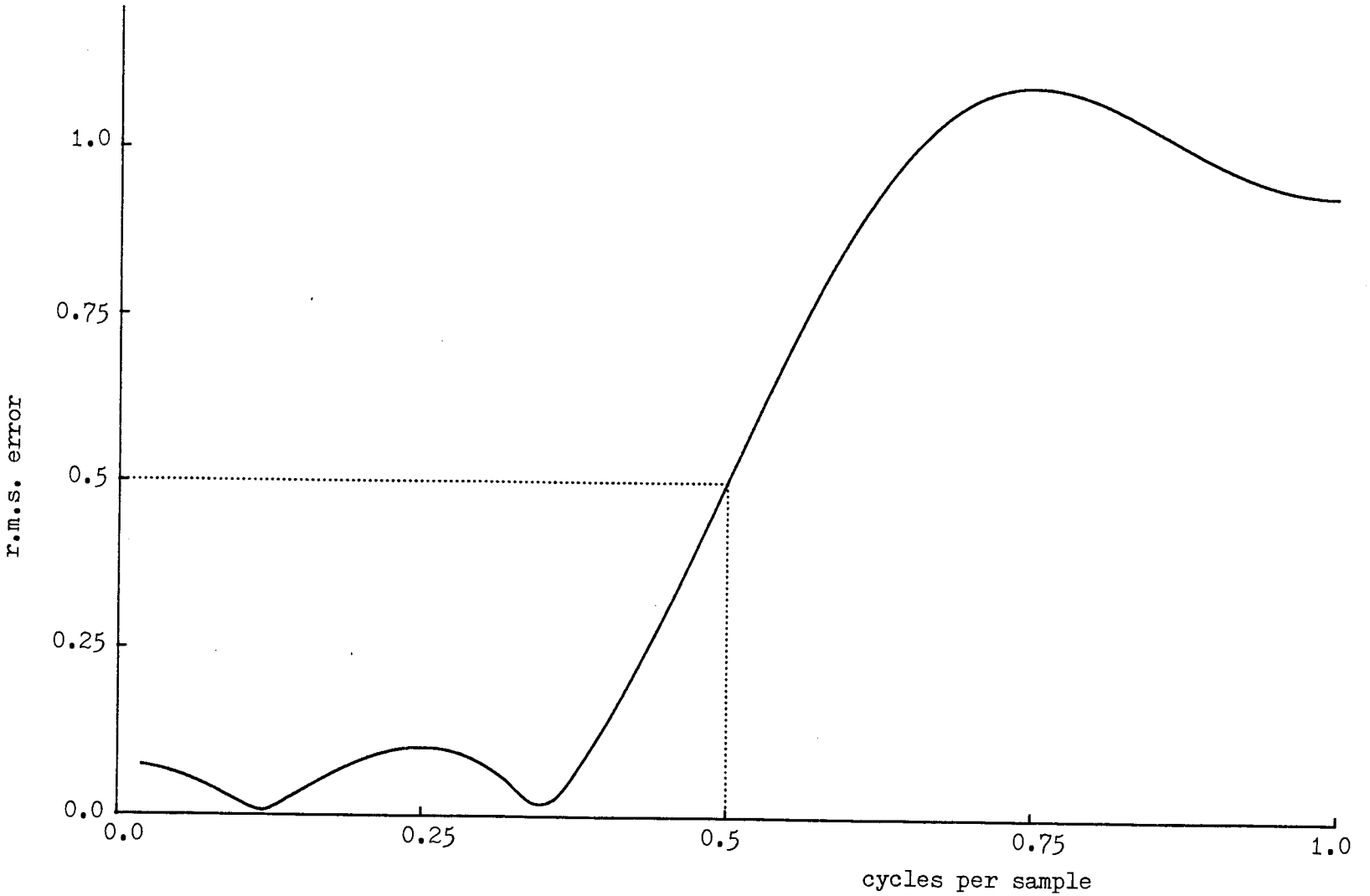

Fig. 3.15. R.m.s. error due to 4-point Fourier interpolation of a sinusoid (amplitude 1.0): variation with sample spacing.

steepening the rise of the error as the sampling rate passes through the Nyquist value. Another interesting point is that for Fourier interpolation, as opposed to the other interpolation schemes considered, the error does not fall to zero as the sampling interval tends to zero. It is easy to show that the maximum error for the four-point scheme will become equal to 0.15117 as the sampling interval tends to zero. The corresponding values for even numbers of points between 2 and 64 have been calculated and are listed in Table 3.1.

Lagrange four-point interpolation (Figures 3.16 and 3.17) exhibits better low-spacing performance than the four-point Fourier method but there is an area nearer the Nyquist rate in which Fourier interpolation is considerably better. This might suggest that, when interpolating near-field data with a sampling rate not much better than the classical sampling criterion, Fourier interpolation should be used but two other points should also be considered:

i) Fourier interpolation involves sine and cosine functions and so can become time consuming.

ii) Many microwave antennas will have tapered illumination functions meaning that the amplitudes of the higher spatial frequencies are relatively low. Most of the energy will be in the lower spatial frequencies in which the Lagrange scheme wins out.

The Newton forward difference scheme (Figures 3.18 and 3.19) displays good accuracy for small sampling intervals but rapidly worsens as the sampling becomes more coarse and

Table 3.1

Maximum error in interpolating a unit-amplitude sine function with Fourier interpolation at zero sampling interval: variation with number of data values used.

No.of points	Max.error (rounded to 4 d.p.)
2	0.2732
4	0.1512
6	0.1035
8	0.0784
10	0.0631
12	0.0527
14	0.0452
16	0.0396
18	0.0353
20	0.0318
22	0.0289
24	0.0265
26	0.0244
28	0.0227
30	0.0212
32	0.0199
34	0.0187
36	0.0177
38	0.0167
40	0.0159
42	0.0151
44	0.0145
46	0.0138
48	0.0133
50	0.0127
52	0.0122
54	0.0118
56	0.0114
58	0.0110
60	0.0106
62	0.0103
64	0.0099

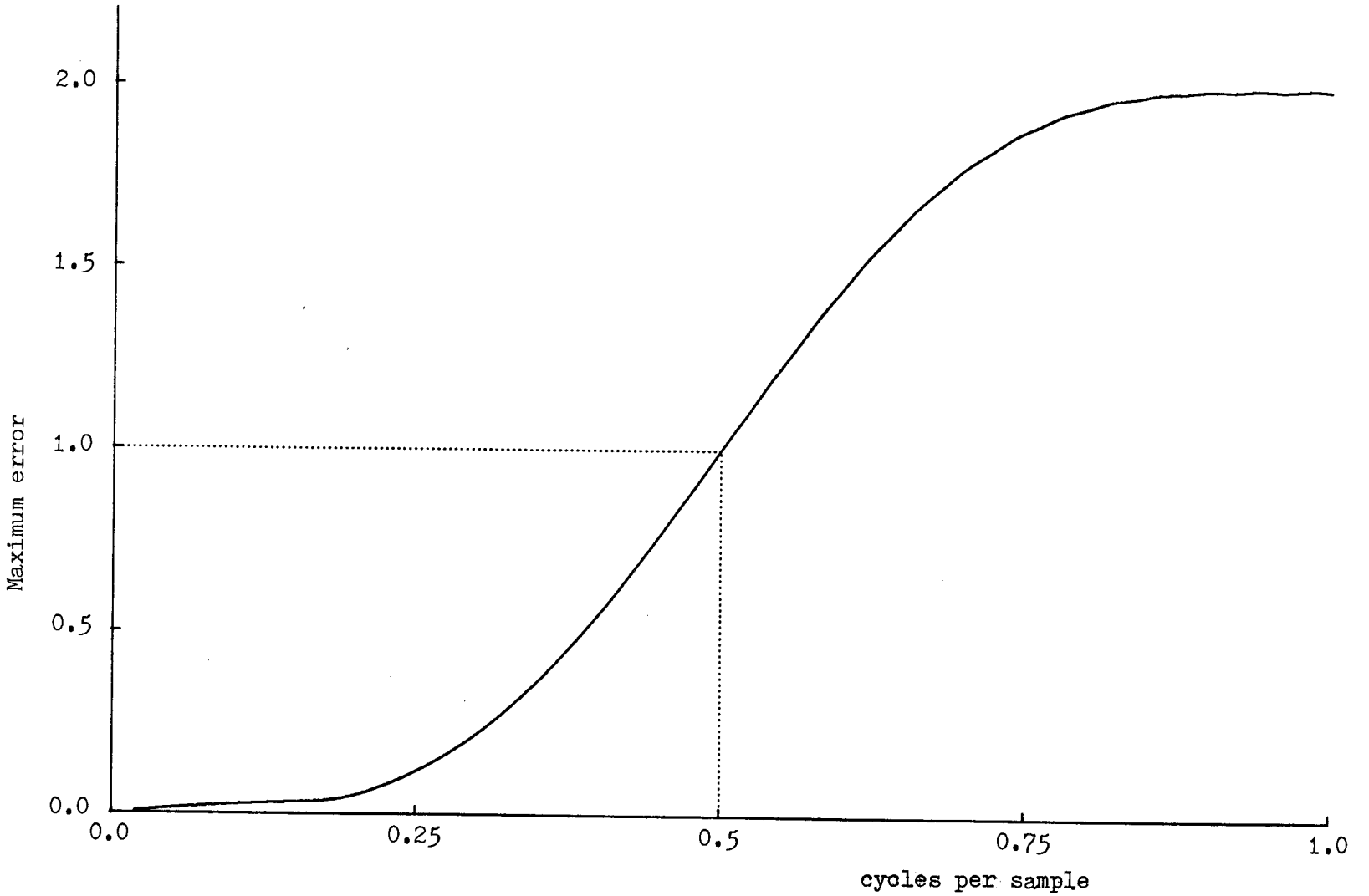

Fig. 3.16. Maximum errors due to 4-point Lagrange interpolation of a sinusoid (amplitude 1.0): variation with sample spacing.

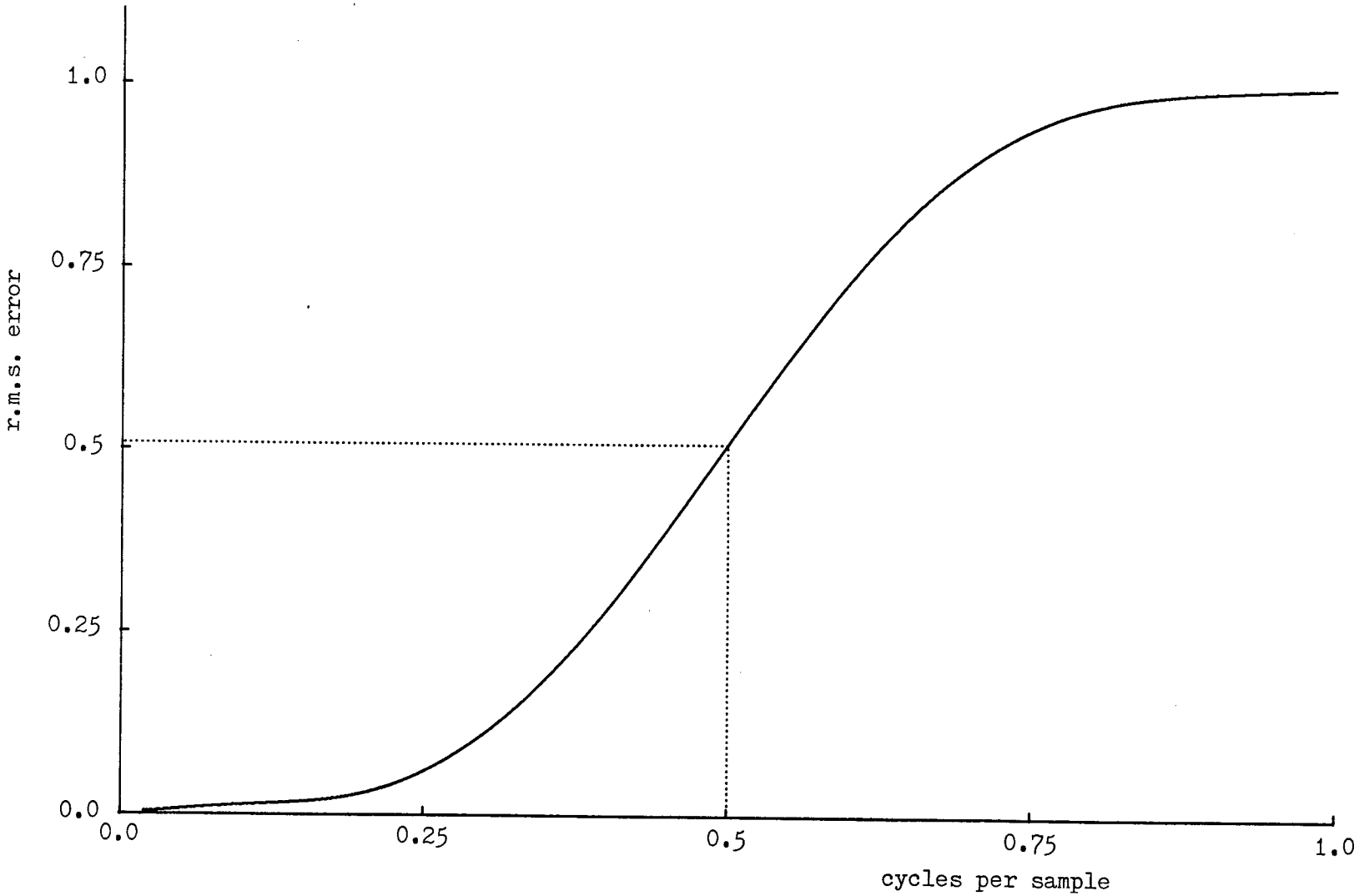

Fig. 3.17. R.m.s. errors due to 4-point Lagrange interpolation of a sinusoid (amplitude 1.0): variation with sample spacing.

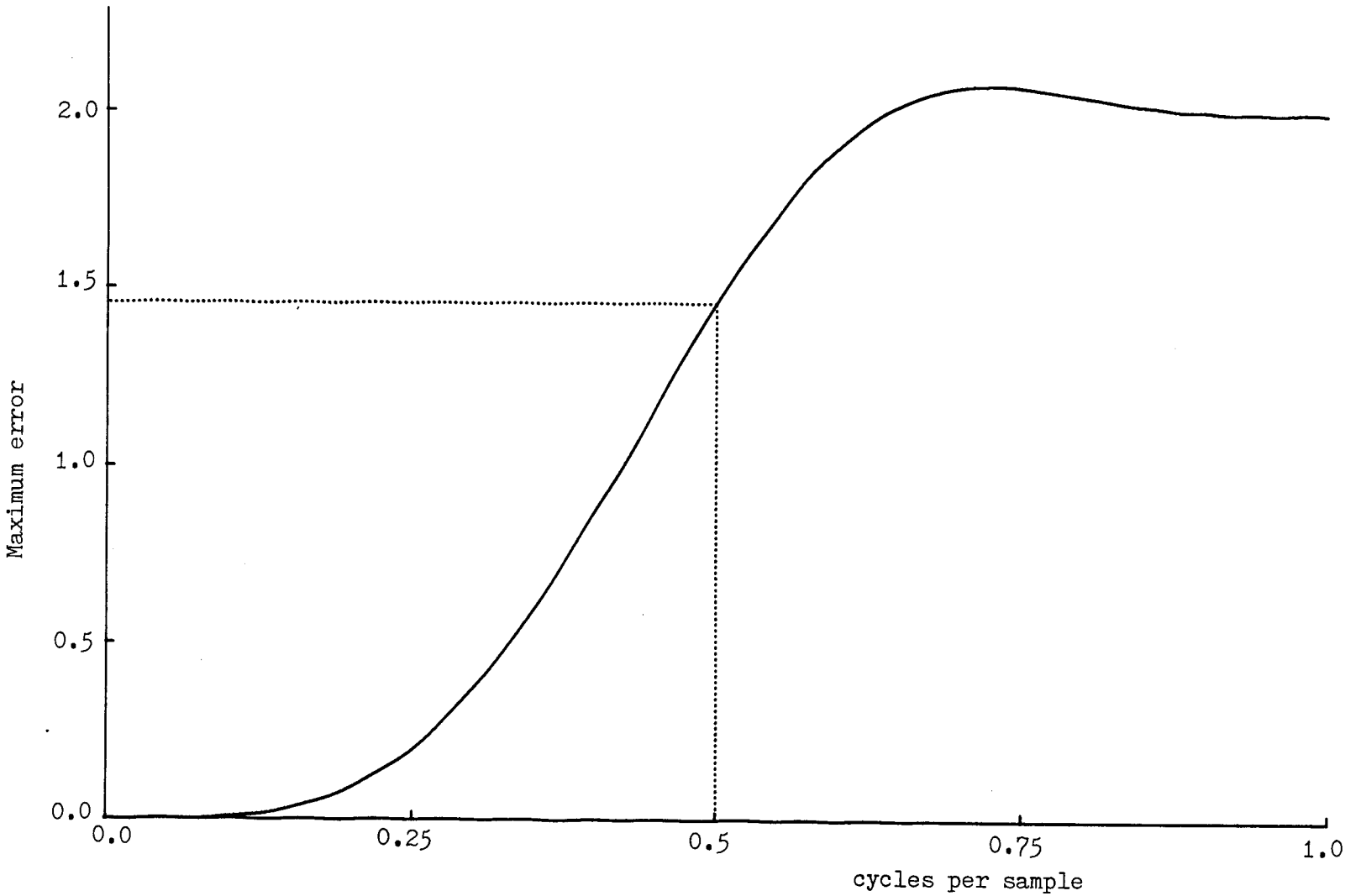

Fig. 3.18. Maximum error due to 4-point Newton forward-difference interpolation of a sinusoid (amplitude 1.0): variation with sample spacing.

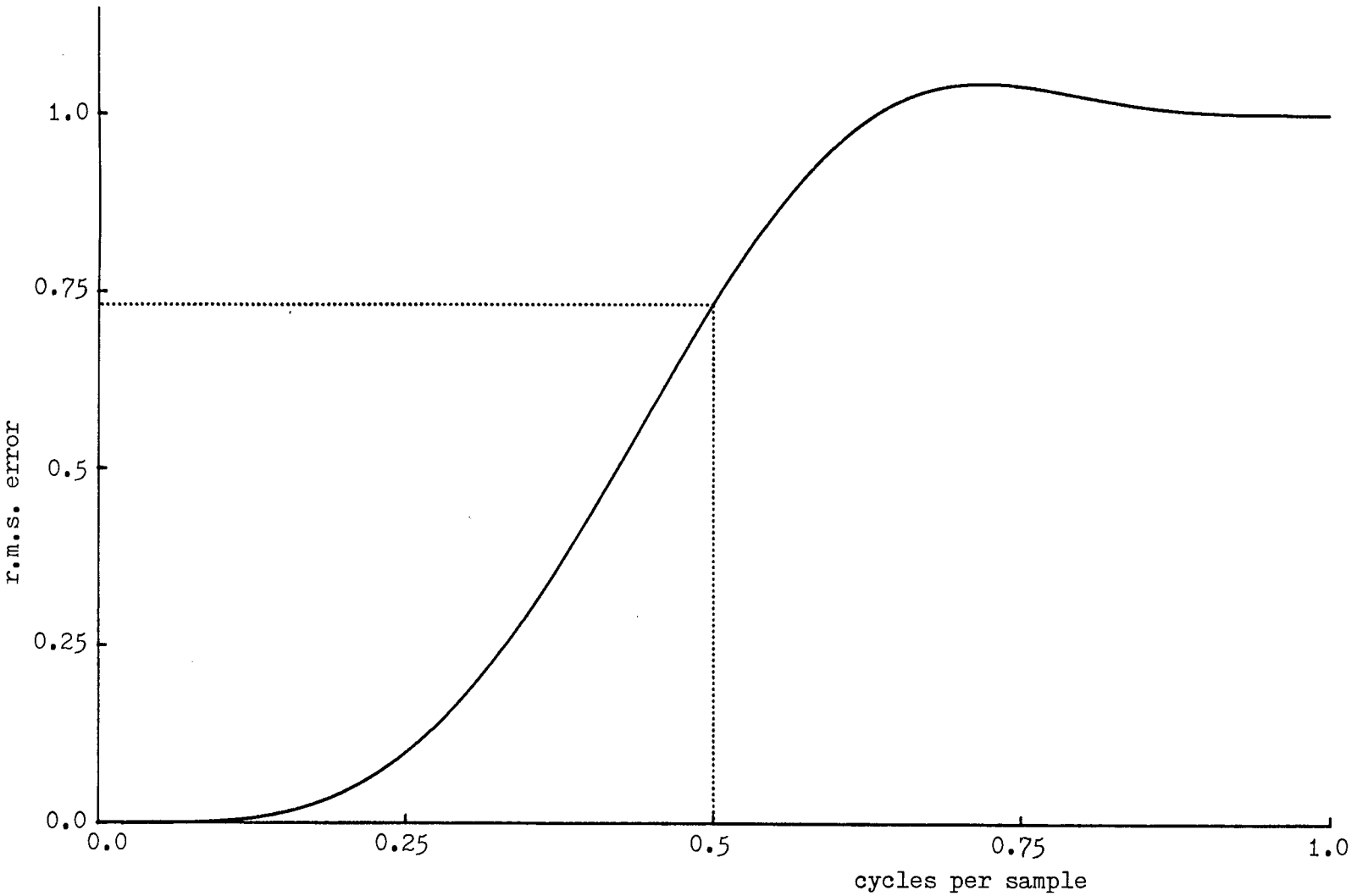

Fig. 3.19. R.m.s. error due to 4-point Newton forward-difference interpolation of a sinusoid (amplitude 1.0): variation with sample spacing.

is therefore probably less acceptable.

Everett's interpolation formula (Figures 3.20 and 3.21) exhibits the low-spacing accuracy of the Newton method but becomes virtually identical to the Lagrange formula at the larger sampling intervals. For this region it probably just has the advantage over the Lagrange method.

The final method examined was the Bessel interpolation formula (Figures 3.22 and 3.23). While the accuracy at very small sample spacings is good, the rise in the error starts to occur relatively early and for this reason, it would seem that this approach can be rejected.

In conclusion, it may be said that, from the point of view of overall accuracy, there is probably little to choose between the Lagrange four-point, Everett four-point and Fourier four-point methods with Everett possibly just marginally superior to Lagrange.

Fourier four-point interpolation, however, involves the calculation of sine and cosine functions which, unfortunately, makes it rather slow in comparison with the others.

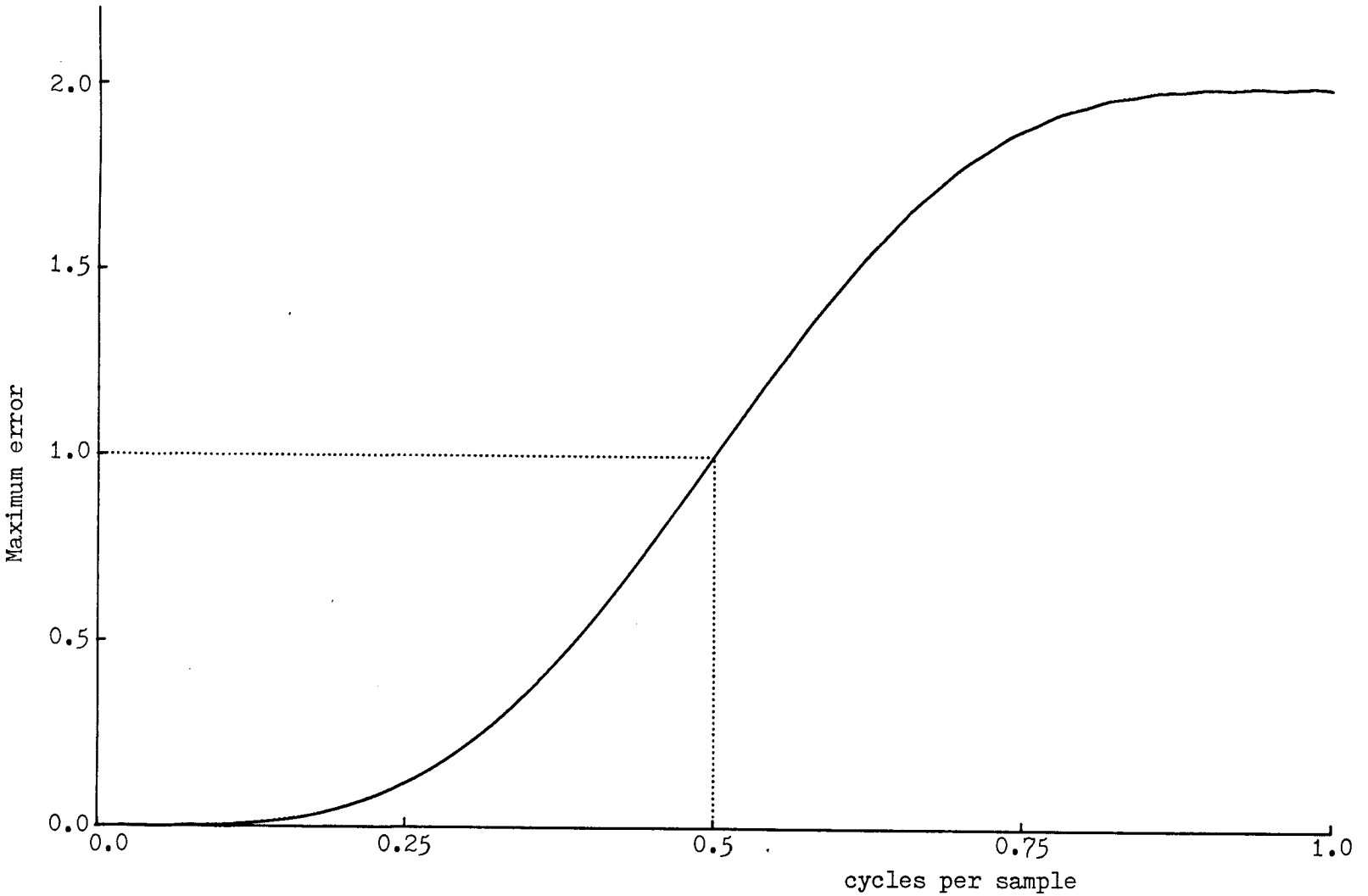

Fig. 3.20. Maximum error due to 4-point Everett interpolation of a sinusoid (amplitude 1.0): variation with sample spacing.

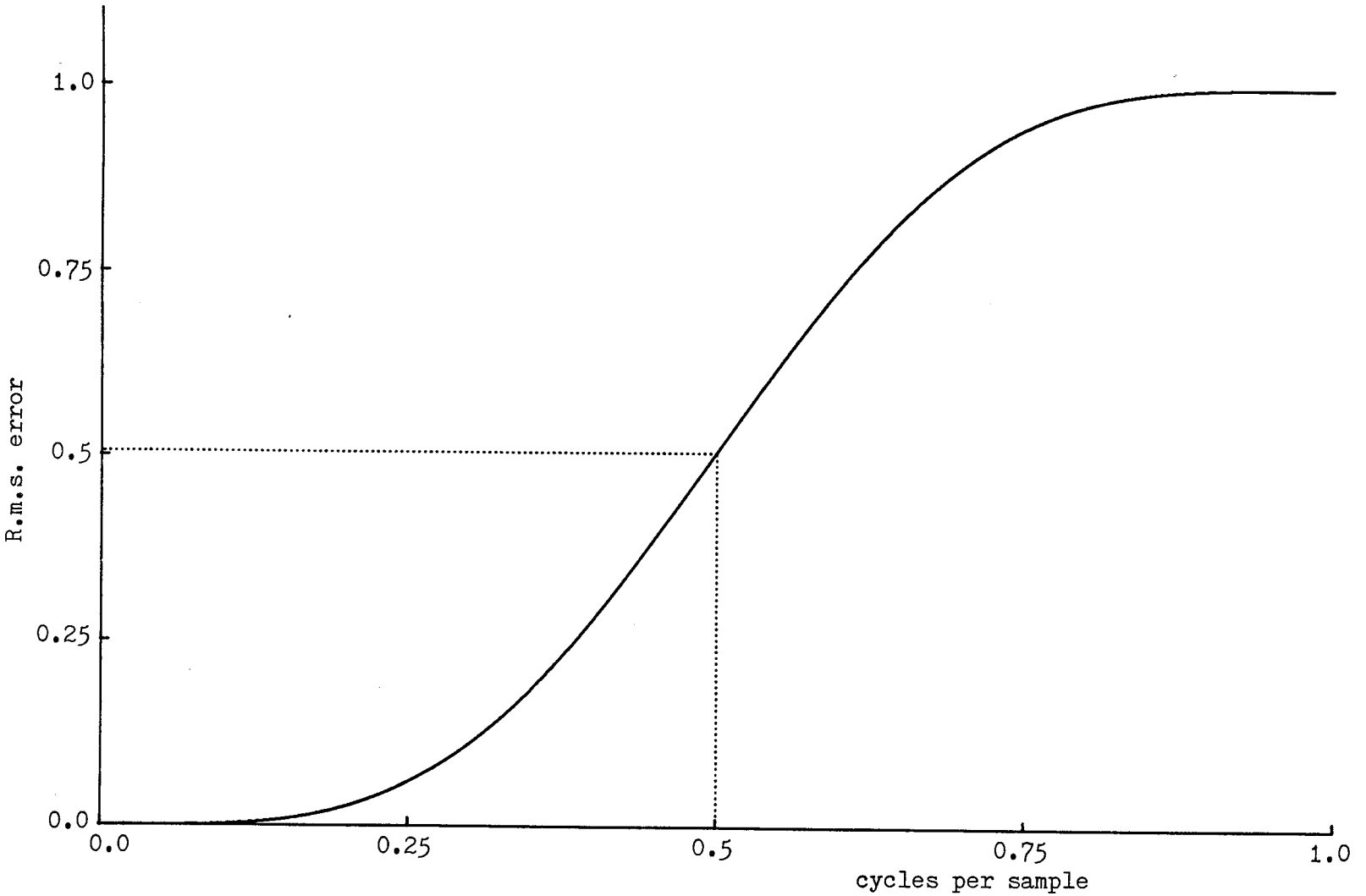

Fig. 3.21. R.m.s. error due to 4-point Everett interpolation of a sinusoid (amplitude 1.0): variation with sample spacing.

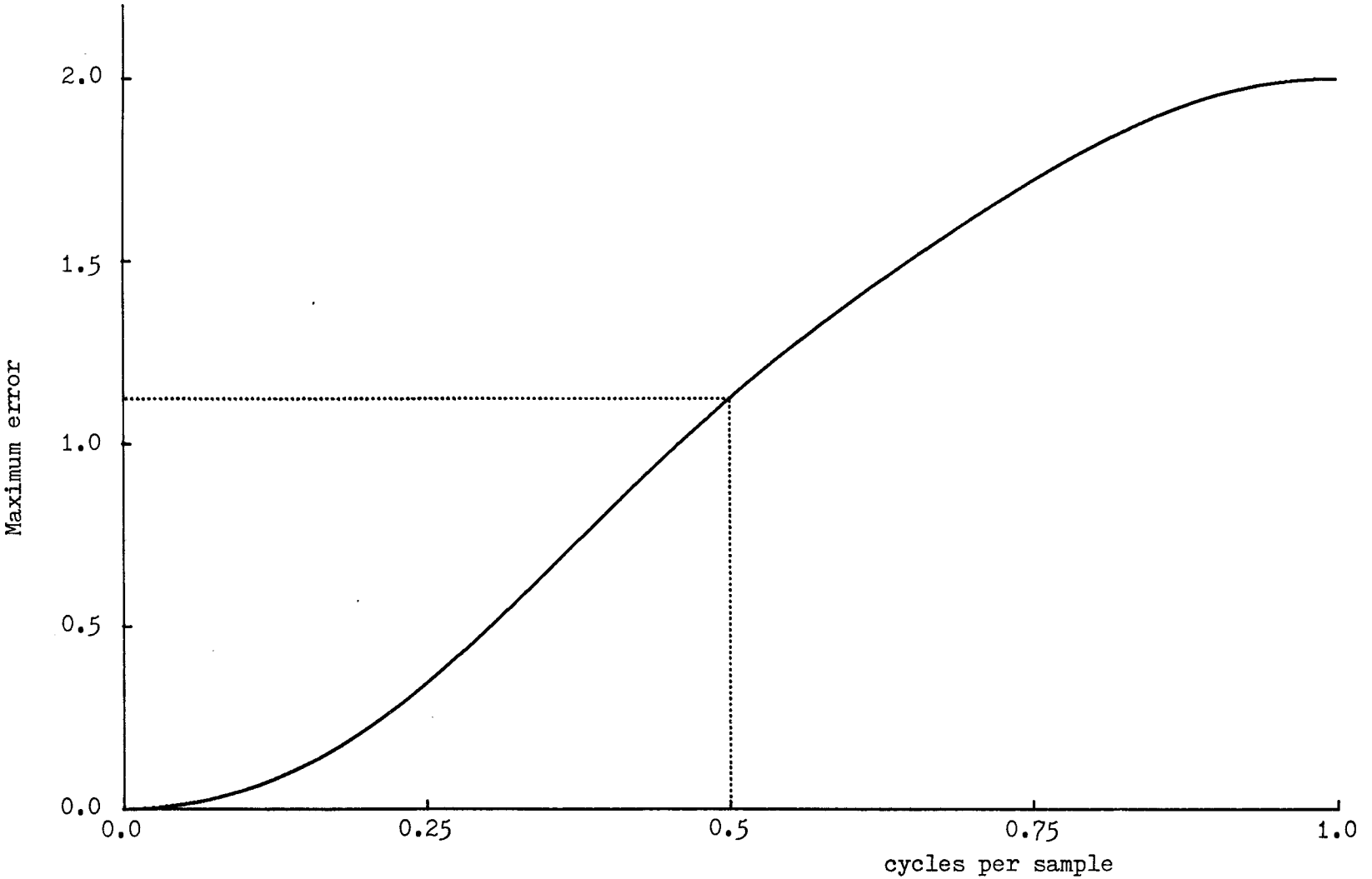

Fig. 3.22. Maximum error due to 4-point Bessel interpolation of a sinusoid (amplitude 1.0): variation with sample spacing.

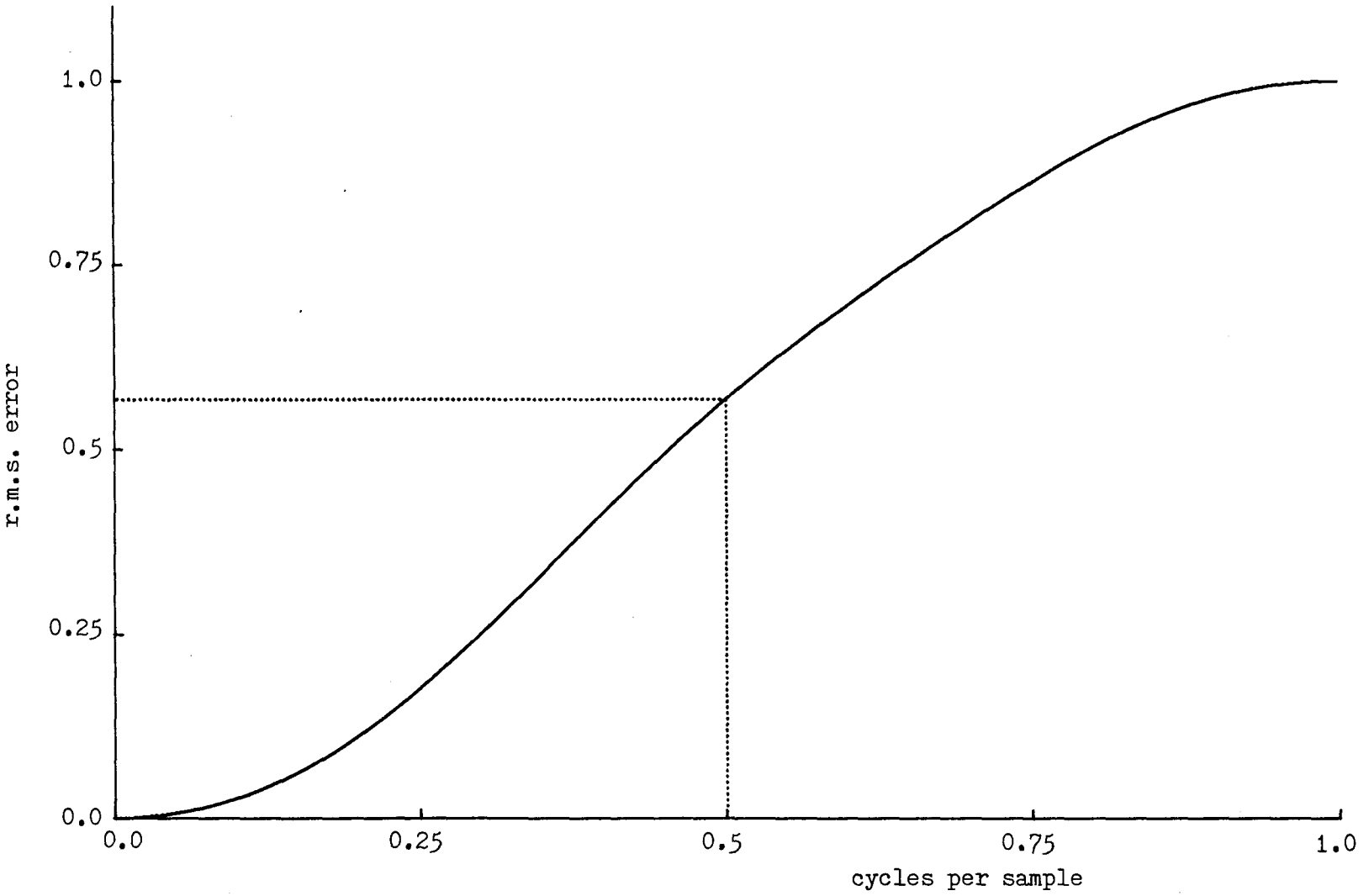

Fig. 3.23. R.m.s. error due to 4-point Bessel interpolation of a sinusoid (amplitude 1.0): variation with sample spacing.

4. THREE-DIMENSIONAL PREDICTION WITH PROBE COMPENSATION USING A POLARISATION-OVER-AZIMUTH SCANNING DEVICE

The polarisation-over-azimuth scanning geometry is one which has come very much into favour in recent years for antenna test facilities, the major reason being that, as described in Chapter 1 when the geometry was introduced, the support structure can be kept further away from the front of the test antenna. It is useful, therefore, to consider the details of this type of system, in a way similar to that in Chapter 3 for the elevation-over-azimuth system, with a view to implementing an iterative procedure for the weighting function. A further advantage embodied in this type of scan is that circular symmetry is applicable. In Chapter 3 it was seen that, as a precursor to the iterative procedure, it was required to determine the coefficients defining the field components at each specified point in the plane wave region due to the probe placed at each of the points of the weighting function. In the earlier case, this meant the creation of a separate set of four coefficients for every possible combination of weighting function point and plane wave point (the factor of four reflecting the need to relate two plane wave components, E_x and E_y, to two probe polarisations). It is clear from Fig. 4.1 that if the desired plane wave field distribution is defined in terms of polar components E_{rpw} and $E_{\theta pw}$;

$$E_{rpw} = \sin\theta_{pw} \tag{4.1}$$

$$E_{\theta pw} = \cos\theta_{pw} \tag{4.2}$$

(assigning unit amplitude to the plane wave, zero phase to both components) and the synthesised plane wave is also

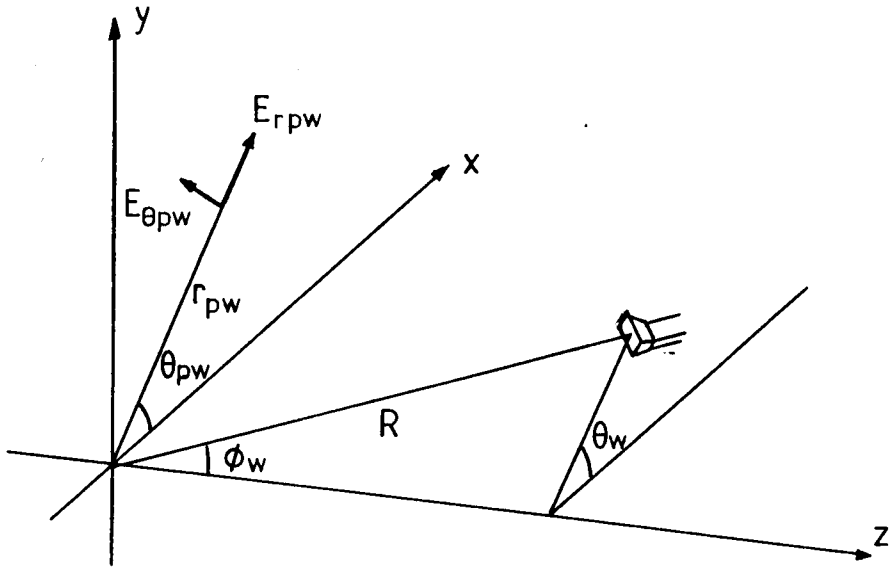

Fig. 4.1. Probe and plane wave for polarisation-over-azimuth geometry.

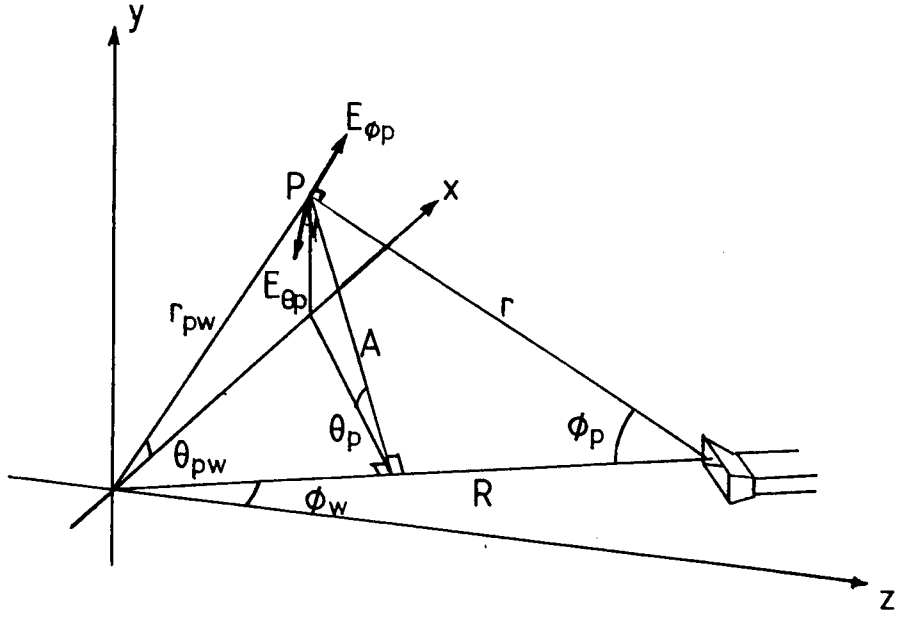

Fig. 4.2. Relationship between probe and plane wave point, for θ_w set to zero.

calculated in this form, then the coefficients relating these field components at point (r_{pw1}, θ_{pw1}) in the plane of iteration to the probe at point (θ_{w1}, ϕ_{w1}) in the weighting function may equally well be used to relate the fields at $(r_{pw1}, \theta_{pw1} + \Delta\theta)$ to the probe at $(\theta_{w1} + \Delta\theta, \phi_{w1})$. This means that it is only necessary to calculate the coefficients relating the field components at all the plane wave points to the probe when positioned at those weighting function points lying along a single radial line. For simplicity, we may consider the particular radial line to be the line $\theta_w = 0$ so that the situation depicted in Fig. 4.2 is the one to investigate.

4.1 The Coefficients

Let us assume that the probe itself has been characterised on a polarisation-over-azimuth scan system so that, to determine the probe fields at P (the point r_{pw}, θ_{pw}) due to the probe at angular position ϕ_w (along the line $\theta_w = 0$), it is necessary to formulate the angles θ_p and ϕ_p in the probe measurement coordinate system corresponding to the line from the probe to P. From Fig. 4.2, it can be ascertained that the first of these angles, θ_p, is given by,

$$\theta_p = \tan^{-1} (\tan\phi_{pw}/\cos\phi_w) \qquad (4.3)$$

and the other, ϕ_p, by,

$$\phi_p = \sin^{-1} (A/r) \qquad (4.4)$$

where

$$A = rpw\ (1-\cos^2\theta_{pw}\ \sin^2\phi_w)^{\frac{1}{2}} \qquad (4.5)$$

and

$$r = (r_{pw}^2 + R^2 - 2r_{pw}R\cos\theta_{pw} \sin \phi_w)^{\frac{1}{2}} \quad (4.6)$$

These angular coordinates, θ_p and ϕ_p, enable us to extract the correct probe field components from the probe calibration data. It is important to note here that the coordinate ϕ_p, as given above, is that actually used in the polarisation over azimuth system when the probe pattern was measured but there is a lateral inversion which means that the value of θ_p is not quite the θ-coordinate used in measuring the probe. It is in fact defined by,

$$\theta_p = \pi - \theta_{pm} \quad (4.7)$$

where θ_{pm} is the θ-coordinate relevant to the actual probe measurement system. This should be borne in mind when the probe field information is included in an implemented system. The direction of the θ_p field component, $E_{\theta p}$, as used below, is in the same direction as defined in the probe measurement system (see Fig. 4.3).

4.1.1 Field Components

Let us determine the x and y components of field (these are the only components which contribute to $E_{\theta pw}$ and E_{rpw}) due firstly to field component $E_{\theta p}$,

$$E_{x1} = E_{\theta p} \sin\theta_p \cos\phi_w \quad (4.8)$$

$$E_{y1} = -E_{\theta p} \cos\theta_p \quad (4.9)$$

The components due to $E_{\phi p}$ are

$$E_{x2} = E_{\phi p} \cos \alpha \cos(\beta - \phi_w) \quad (4.10)$$

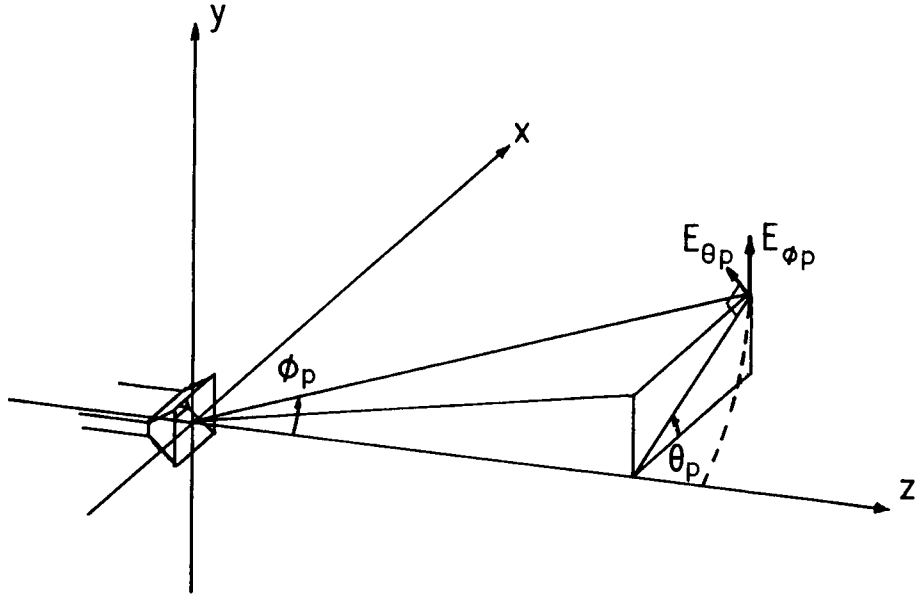

Fig. 4.3. Geometry of the probe measurement system.

$$E_{y_2} = E_{\phi p} \sin \alpha \tag{4.11}$$

where

$$\alpha = \sin^{-1} (\sin\theta_p \cos\phi_p) \tag{4.12}$$

and

$$\beta = \sin^{-1} \left(\frac{\sin\phi_p}{\cos\alpha}\right) \tag{4.13}$$

Equation (4.12) implies that

$$\cos \alpha = (1 - \sin^2\theta_p \cos^2\phi_p)^{\frac{1}{2}} \tag{4.14}$$

Combining the above components into E_x and E_y and then resolving into the desired polar components yields,

$$E_{rpw} = E_x \cos\theta_{pw} + E_y \sin\theta_{pw} \tag{4.15}$$

and

$$E_{\theta pw} = -E_x \sin\theta_{pw} + E_y \cos\theta_{pw} \tag{4.16}$$

where

$$E_x = E_{\theta p} \sin\theta_p \cos\phi_w + E_{\phi p} (\cos\theta_p \cos\phi_p \cos\phi_w + \sin\phi_p \sin\phi_w) \tag{4.17}$$

and

$$E_y = -E_{\theta p} \cos\theta_p + E_{\phi p} \sin\theta_p \cos\phi_p \tag{4.18}$$

In the definition of the field components above, the variation of amplitude and phase due to varying distance, $\frac{R \exp -jk(r-R)}{r}$ has been assumed.

4.2 z-Offset

As in Chapter 3, we now proceed to consider the effect upon the above of introducing a z-offset, z_o, to the plane of iteration. It is not important to modify the speci-

fied plane wave distribution as this will merely introduce a constant phase offset into the predictions which does not affect the relative phase distribution. The situation is illustrated in Fig. 4.4.

The distance from the probe to point P is adjusted from that given in equation (4.6) to read,

$$r = (r_{pw}^2 + R^2 - 2Rr_{pw} \cos\theta_{pw} \sin\phi_w + z_o^2 - 2Rz_o \cos\phi_w)^{\frac{1}{2}} \quad (4.19)$$

Equation (4.3) for θ_p is modified as follows,

$$\theta_p = \tan^{-1} \left(\frac{r_{pw} \sin\theta_{pw}}{r_{pw} \cos\theta_{pw} \cos\phi_w - z_o \sin\phi_w}\right) \quad (4.20)$$

The equation (4.4) for ϕ_p can remain unaltered,

$$\phi_p = \sin^{-1} (A/r) \quad (4.21)$$

but in this case A is modified:

$$A = (r_{pw}^2 \sin^2\theta_{pw} + (r_{pw} \cos\theta_{pw} \cos\phi_w - z_o \sin\phi_w)^2)^{\frac{1}{2}} \quad (4.22)$$

r is as given in equation (4.22).

Using these modified values of θ_p, ϕ_p and r, the field components in the plane wave region may be evaluated as in equations (4.8) to (4.18).

4.3 The Iteration Procedure

The relevant ideas for producing a weighting function, given the necessary coefficients, are identical to those for the elevation-over-azimuth scheme in section 3.3 and need not be repeated here. It is merely noted that the result is a weighting function which when applied to measured data at

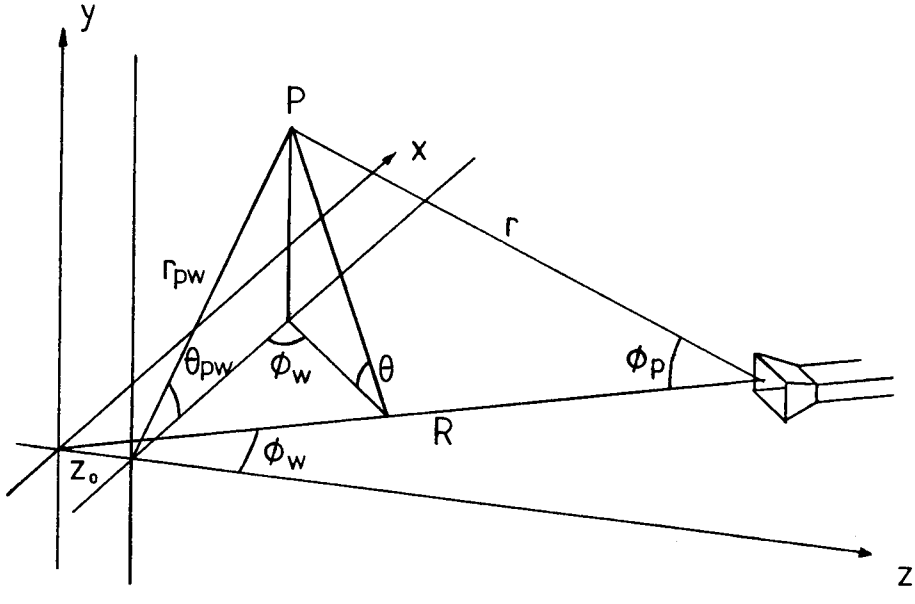

Fig. 4.4. Relationship between probe and plane wave point with plane wave z-offset.

the correct points on the spherical surface and of the correct polarisations enables a linearly polarised plane wave of the form of equations (4.1) and (4.2) to be synthesised in the plane of iteration. By virtue of the depth of field effects discussed in Chapters 2 and 3, the plane wave field distribution will, in fact, encompass a volume large enough to enclose the test antenna positioned at any desired angle.

4.3.1 Timing Difficulties

The procedure used to generate a weighting function, developed on a polarisation-over-azimuth type of coordinate system, has been outlined. It was stated early in the chapter that for the creation of the coefficients used in weighting function generation, circular symmetry could be applied to reduce the amount of computer time consumed. Unfortunately, the same argument does not apply to the iteration procedure itself since, although the number of coefficients used is reduced, these coefficients still have to be applied at all points around the weighting function. Because of the high density of points around the boresight pole of the polarisation-over-azimuth system, it was found that the iteration time was prohibitively increased and so, although ideas have been considered for some form of data thinning, it was considered advisable to return to the elevation-over-azimuth weighting function generation scheme.

4.4 Application of an Elevation-Over-Azimuth Weighting Function

This chapter is concerned with processing of data obtained with a polarisation-over-azimuth scan system. So far, we have thus considered a weighting function generated in the same coordinate system. There is no reason, however,

why a weighting function generated by the means described in Chapter 3 cannot be applied to data obtained on a polarisation-over-azimuth system. It is simply a matter of generating a composite weighting function using equations for data selection, interpolation and component resolution designed for the correct measurement geometry.

4.4.1 Prediction of $E_{\phi F}$

The situation here is illustrated in Fig. 4.5. In this case, it is convenient to consider the prediction of the $E_{\phi F}$ far-field component along the radial arm $\theta_F = 90^o$ (i.e. the centre of the weighting function will move outwards from the boresight pole along the radial line $\theta = 90^o$). We define firstly the angles θ and ϕ in the near-field data set corresponding to the weighting function point (θ_w, ϕ_w) when the function is centred at boresight ($\phi = 0$) for a prediction at $\phi_F = 0$. These angles are,

$$\theta = \tan^{-1} \left(\frac{\sin\theta_w}{\tan\phi_w}\right) \tag{4.23}$$

$$\phi = \tan^{-1} \left(\frac{(1 - \cos^2\phi_w \cos^2\theta_w)^{\frac{1}{2}}}{\cos\phi_w \cos\theta_w}\right) \tag{4.24}$$

These angular coordinates enable the calculation of the polar field components, E_θ and E_ϕ at the appropriate point and it is now necessary to resolve these into directions corresponding to those defined for the weighting function;

$$E_{\theta w} = E_\theta \cos\theta \cos\theta_w + E_\phi (\cos\phi \sin\theta \cos\theta_w + \sin\phi \sin\theta_w) \tag{4.25}$$

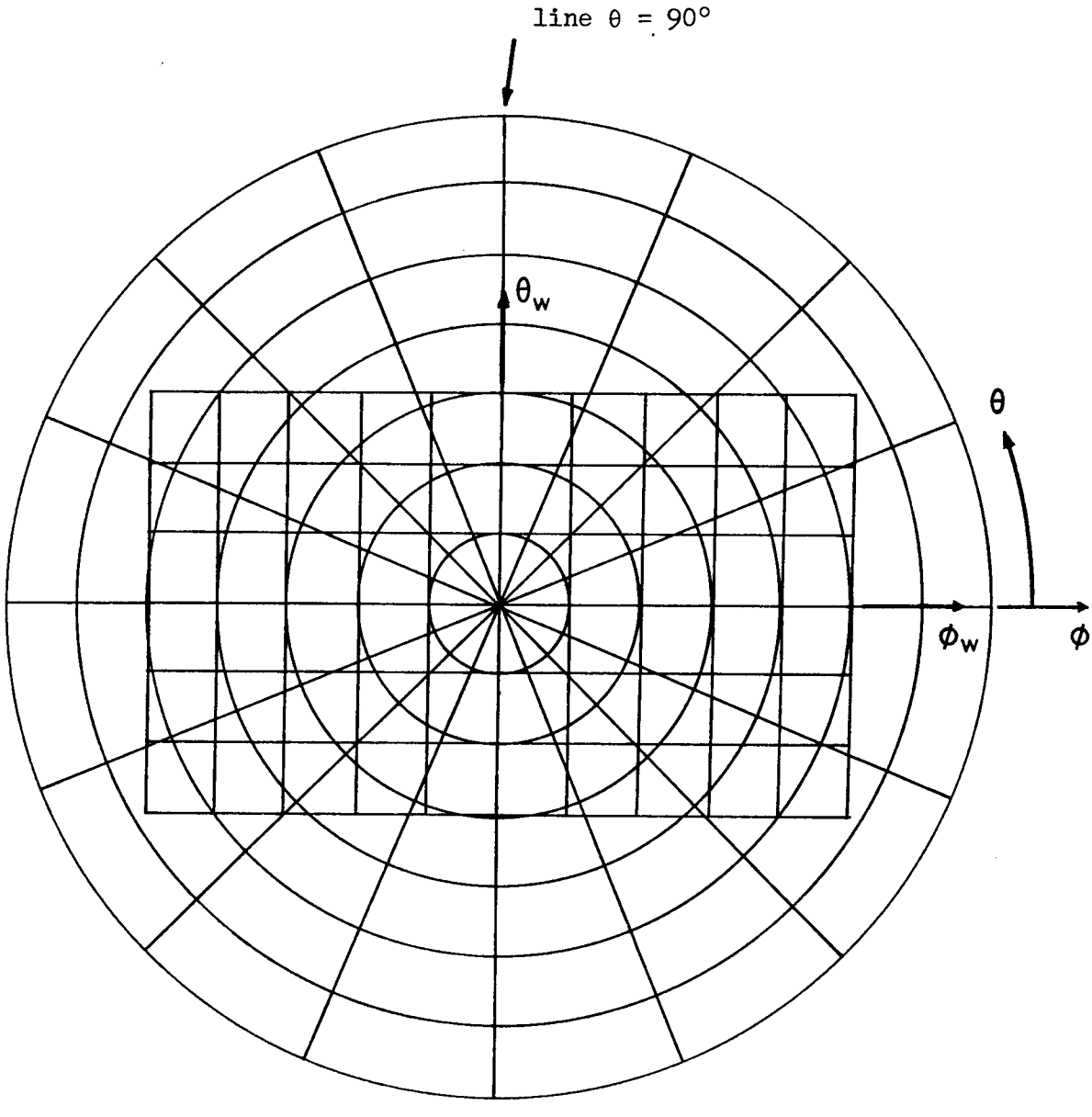

Fig. 4.5. Elevation-over-azimuth weighting function superimposed upon polarisation-over-azimuth data sphere.

and

$$E_{\phi w} = E_{\theta} (\sin\theta \cos\phi_w - \cos\theta \sin\theta_w \sin\phi_w) + E_{\phi} (\cos\phi \cos\theta \cos\phi_w - \cos\phi \sin\theta \sin\theta_w \sin\phi_w + \cos\theta_w \sin\phi_w) \quad (4.26)$$

Equations (4.25) and (4.26) enable field components, which can be used with the weighting function, to be derived, from those data values produced by interpolation of the actual measured near-field data. The combination of the interpolation coefficients, determined on the basis of the known measurement geometry and the values of θ and ϕ from equations (4.23) and (4.24), and the component resolution coefficients of equations (4.25) and (4.26) enables a composite weighting function to be found for the prediction at $\phi_F = 0$. For prediction at any $\phi_F \neq 0$, it is merely necessary to add this value of ϕ_F to the value of θ_w to be used in equations (4.23) to (4.26). Such a modification enables the far-field component $E_{\phi F}$ to be evaluated at any point along the line $\theta_F = 90^o$. The circular symmetry of the data set may be exploited to enable us to say that no further modifications to equations (4.23) to (4.26) are needed to produce a prediction at any other angle $\theta_F \neq 90^o$. It is simply necessary to add the value $\theta_F - 90^o$ to the value of θ from equation (4.25) when selecting the near-field data to be used for the prediction (but the value of θ should be left unchanged for all other purposes).

Before moving over to the prediction of the other coordinate of the far-field, two points should be noted with regard to the above. The first of these is that the

value of θ required in the polar system should be restricted to anywhere within $\pm 180^{o}$ whereas the value given in equation (4.23) will, if implemented directly as given, produce angles only within the range $\pm 90^{o}$ (if the normal principal value definition applies). In the FORTRAN language, this can be overcome by use of the ATAN2 function in the form, ATAN2 ($\sin\theta_w \cos\phi_w$, $\sin\phi_w$) which will put the angle θ into the correct quadrant. The second point is that, as usual, care should be taken that the angles used are not allowed to go out of the range of the data, and if so then adjustment of the values of θ and/or ϕ is made (as necessary) to bring the values back within range.

4.4.2 Prediction of $E_{\theta F}$

It is convenient for the prediction of the second far-field component to consider the elevation-over-azimuth-defined primary weighting function, as formulated in equations (4.23) to (4.26) (for the boresight prediction), to be slid off boresight with its centre moving along the line $\theta = 0$ thus producing predictions of $E_{\theta F}$ for $\theta_F = 0$. The angular positions assumed by a weighting function point when the prediction is at ϕ_F are,

$$\theta = \tan^{-1} \left(\frac{\sin\theta'}{\cos\theta' \cos\phi_F + \sin\phi_F/\tan\phi'}\right) \qquad (4.27)$$

and

$$\phi = \cos^{-1} \left(\cos\phi'\cos\phi_F - \sin\phi'\cos\theta'\sin\phi_F\right) \qquad (4.28)$$

where θ' and ϕ' are the values of θ and ϕ resulting from equations (4.23) and (4.24). It is now necessary to find the modified equations for the component resolution at that point.

These are,

$$E_{\theta w} = E_{\phi} (\cos\phi\sin\theta\cos\theta_w - \cos^2\phi\cos\theta\sin\theta_w + \sin\phi\cos\phi_F\sin\theta_w) + E_{\theta} (\cos\theta\cos\theta_w + \sin\theta\cos\phi\sin\theta_w) \quad (4.29)$$

and

$$E_{\phi w} = E_{\phi} (\cos\phi\cos\theta\cos\phi_F\cos\phi_w + \sin\phi\sin\phi_F\cos\phi_w - \cos\phi\sin\theta\sin\theta_w\sin\phi_w - \cos\phi\cos\theta\sin\phi_F\cos\theta_w\sin\phi_w + \sin\phi\cos\phi_F\cos\theta_w\sin\phi_w) + E_{\theta} (-\sin\theta\cos\phi_F\cos\phi_w - \cos\theta\sin\theta_w\sin\phi_w + \sin\theta\sin\phi_F\cos\theta_w\sin\phi_w) \quad (4.30)$$

where θ and ϕ are as in equations (4.27) and (4.28)

Again, to produce a far-field prediction at any other angle $\theta_F \neq 0$, it is not necessary to modify equations (4.27) to (4.30) in any way. It is merely necessary to add θ_F to the value of θ from equation (4.27) when the actual measured data are being selected for the prediction.

It should be pointed out again that the value of θ from equation (4.27) will, when implemented computationally, produce the principal value in the range $\pm 90^{\circ}$. To expand this to the full $\pm 180^{\circ}$ range it is convenient to examine the value of θ' (which is the result of equation (4.23)). If the sign of θ' is the same as that of tan θ then the principal value should be selected. Otherwise the other possible quadrant should be used. The usual care should be taken to modify the angular-coordinates appropriately if the permissible range is exceeded at any point in the process.

5. PROBE COMPENSATION EFFECTS AND ERROR ANALYSIS

In the earlier chapters of this thesis, the process of near-field/far-field transformation by plane wave synthesis has been described and various aspects have been considered without, in general, a detailed examination of the errors likely to be involved. When the two-dimensional experiment (evaluation of a slotted waveguide array) was described in Chapter 2, some of the practical errors likely to be present were listed and, in Chapter 3, there was included a consideration of a number of possible interpolation schemes and the levels of errors which might be introduced at various sampling rates. In Chapter 6, a practical prediction will be presented with a discussion of the particular errors present in that instance. It will be useful, however, to present a more general investigation of some of the problems liable to be encountered and in particular, of errors resulting from the processing and of the effects of probe compensation. This latter aspect is looked at in the next section.

5.1 Probe Compensation

Previous chapters have shown how the characteristics of the measurement probe are incorporated into the procedure at the stage of generating the weighting function and it has been pointed out that the probe compensation adds no extra work to the prediction process itself. In this section, the effects of the non-inclusion of probe compensation upon the plane wave are illustrated together with some indication of the sorts of errors likely to be introduced thereby. In

addition, a computational simulation is presented of the prediction of a principal plane cut of the far-field pattern from an array of dipoles. This provides further illustration of probe compensation in action.

5.1.1 Effects upon the Synthesised Plane Wave

As an investigation of the effects upon the synthesised plane wave of incorrect probe compensation, a weighting function was generated (using the usual one-dimensional approximation) for the following parameters. The frequency specified was 10GHz and a 102cm plane wave was specified initially (69 points at 1.5cm spacing). The measurement range was chosen to be 2.0m and a weighting function was generated consisting of 59 points with 0.8^{o} spacing. A wide-beam probe (half-power beamwidth of 90^{o}) was assumed.

The weighting function resulting from the iterative process is shown in Fig. 5.1 with the synthesised plane wave on the plane z = 0 appearing as Fig. 5.2. Very uniform amplitude, and phase barely distinguishable from the zero axis, are features of the plane wave. For the time being, we pass over Figures 5.3 and 5.4, since the significance of these will require a little explanation, and move on to show the effect upon the synthesised plane wave of using, in the unmodified weighting function, a probe with a beamwidth different from that for which the function was designed. In the first case a probe with a slightly narrower beamwidth (3dB beamwidth of 75^{o}) is used and the synthesised plane wave is shown as Fig.5.5.

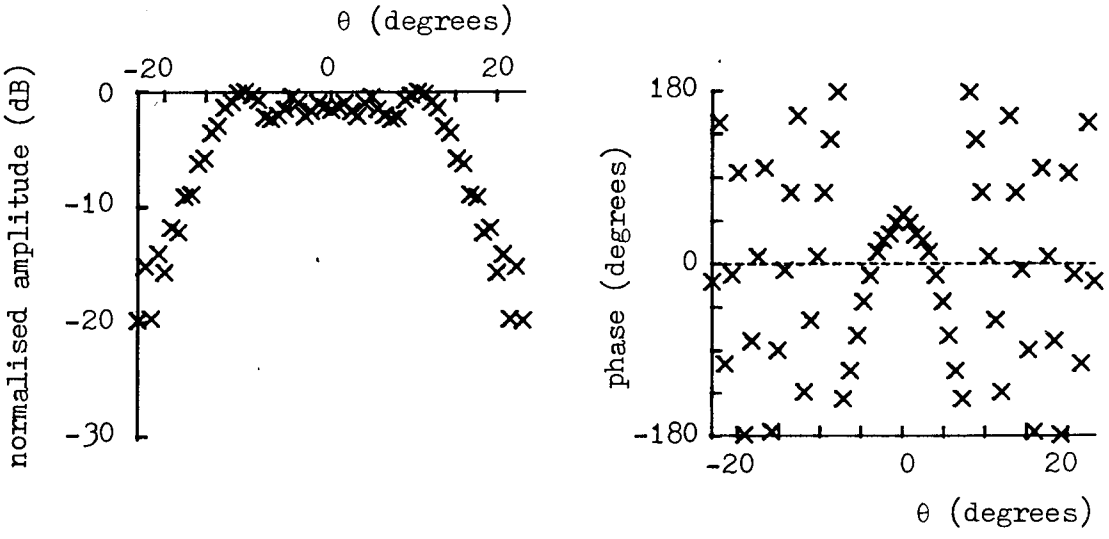

Fig. 5.1. 59-point weighting function designed to synthesise 1.02m. plane wave, at 10.0GHz., using a probe with 90° 3dB beamwidth, at 2.0m. measurement radius.

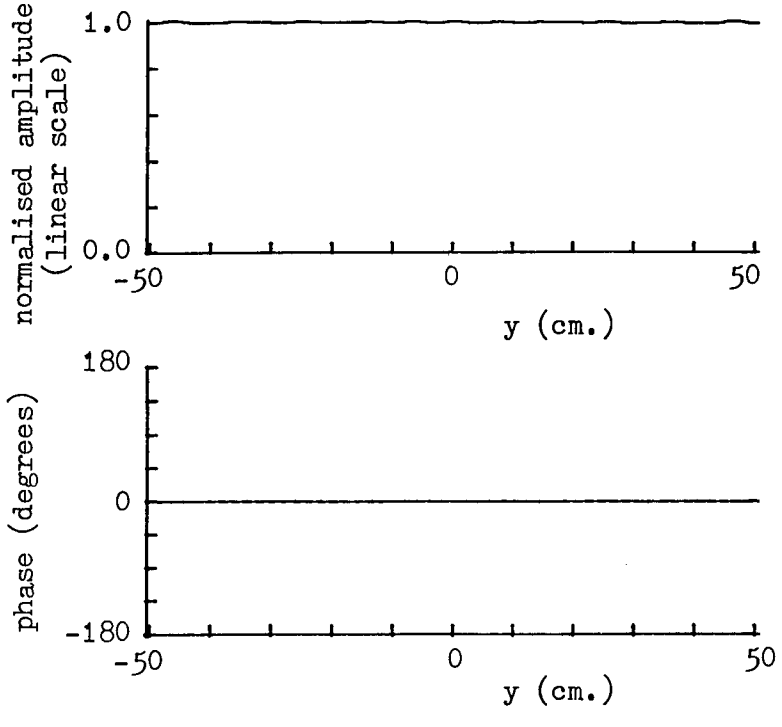

Fig. 5.2. Synthesised plane wave due to weighting function of Fig. 5.1, using correct probe.

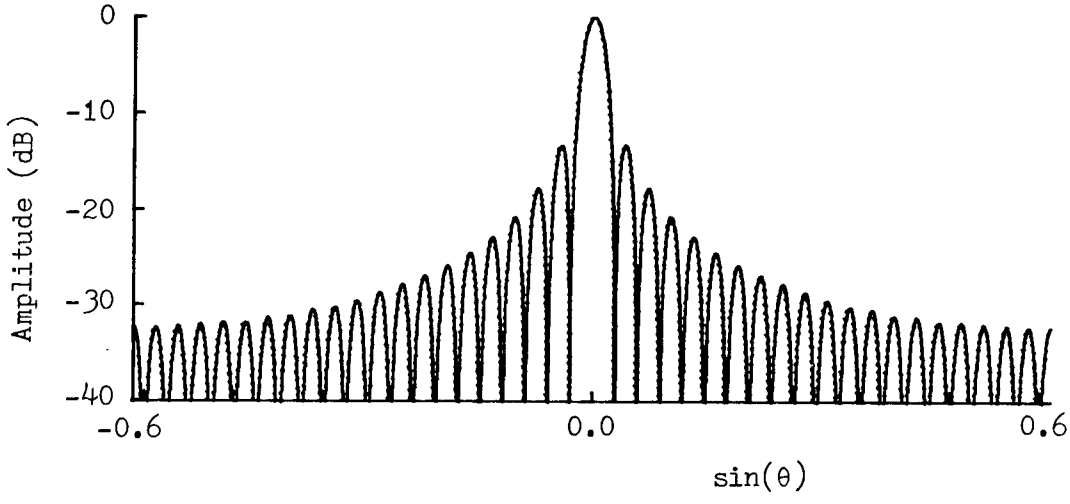

Fig. 5.3. Fourier transform of synthesised plane wave shown in Fig. 5.2 (solid) compared with ideal (dotted).

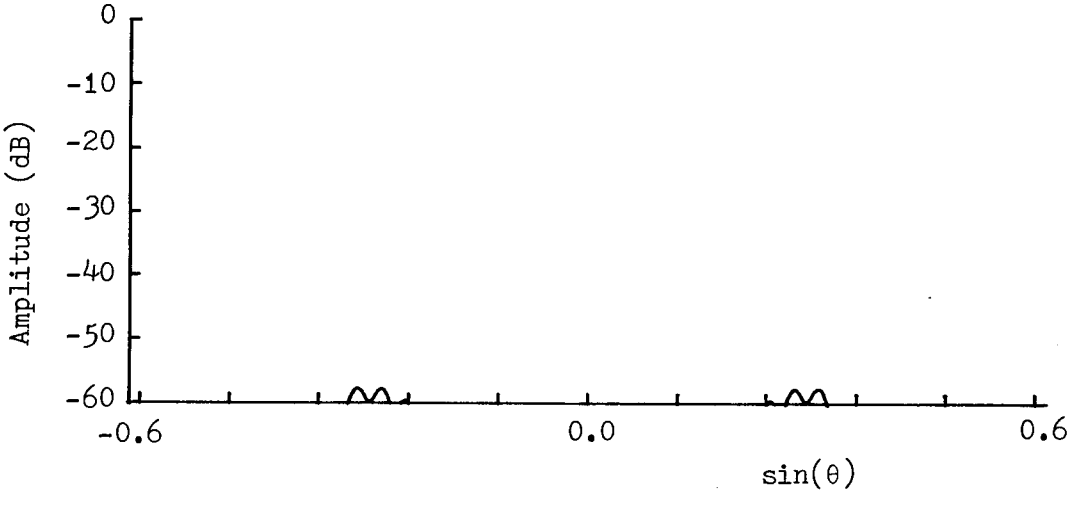

Fig. 5.4. Fourier transform of non-ideal residual of plane wave shown in Fig. 5.2 illustrating effective spurious far-field sources.

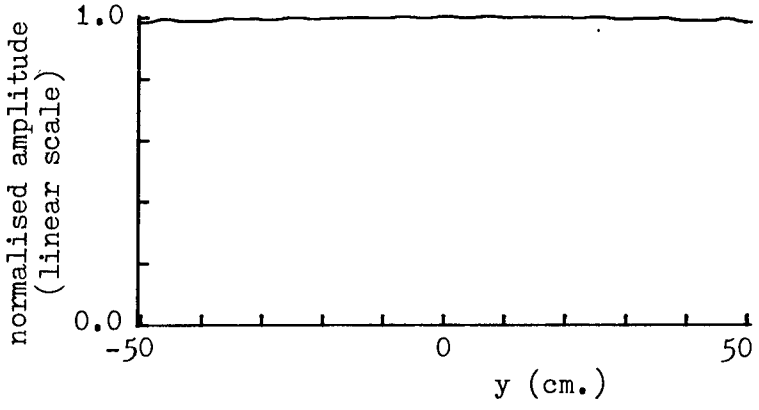

Fig. 5.5. Synthesised plane wave due to weighting function of Fig. 5.1 but using probe with 3dB beamwidth of 75°.

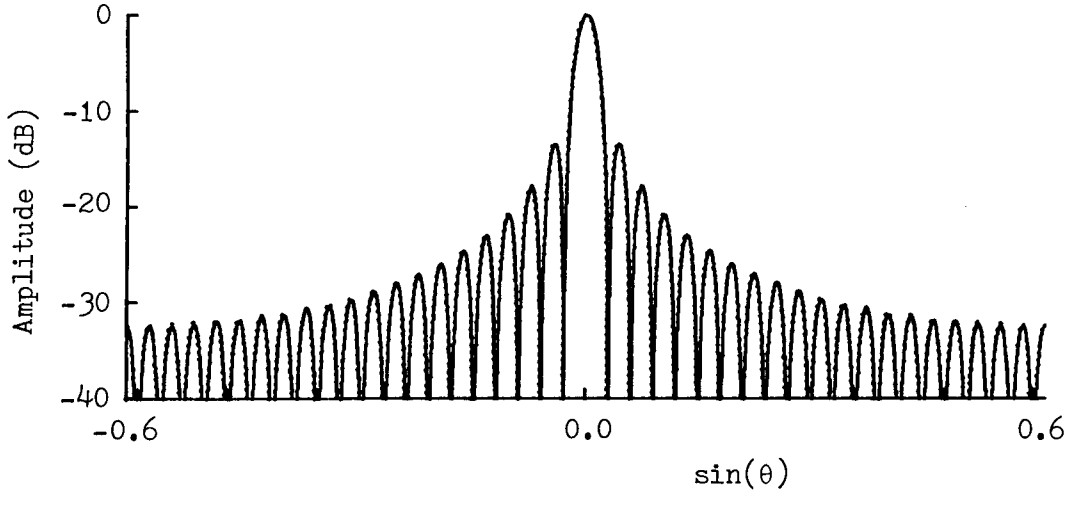

Fig. 5.6. Fourier transform of synthesised plane wave shown in Fig. 5.5 (solid) compared with ideal (dotted).

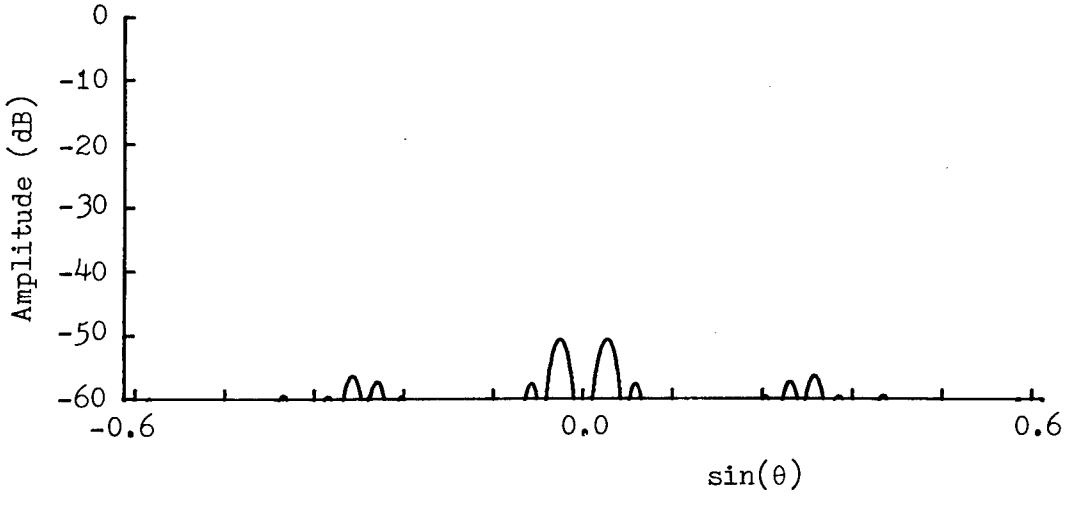

Fig. 5.7. Fourier transform of non-ideal residual of plane wave shown in Fig. 5.5 illustrating effective spurious far-field sources.

The phase (not shown) is substantially unaltered by the use of a different probe but the amplitude is slightly tapered. A much more drastic taper is introduced, as illustrated in Fig. 5.8, when a probe with a 3dB beam-width of only 25° is introduced into the same weighting function although again, the phase of the plane wave (not shown) remains virtually unaltered.

Probe compensation can be carried out for the narrower beam probes and for the case of the medium-beam probe, the resulting weighting function is shown as Fig.5.11 with the synthesised plane wave as Fig. 5.12. If the weighting function is compared with the earlier one (Fig.5.1) it will be discovered that it is very difficult to detect any difference between the two. Nevertheless, the slight improvement in the synthesised plane wave is quite discernible. For the narrow-beam probe, the weighting function is shown as Fig. 5.15 with the resulting synthesised plane wave as Fig. 5.16. The modifications to the weighting function in this case are noticeable and the removal of the taper in the plane wave amplitude has been achieved. It should be noted that it would not prove possible to carry out probe compensation if the probe pattern had a null in the region of interest but, of course, it is extremely unlikely that one would attempt to use such a probe.

5.1.2 Fourier Transform Analysis

We now move on to explain the significance of those graphs which have been passed-over in the above. The plane wave synthesis technique, as should now be clear, is

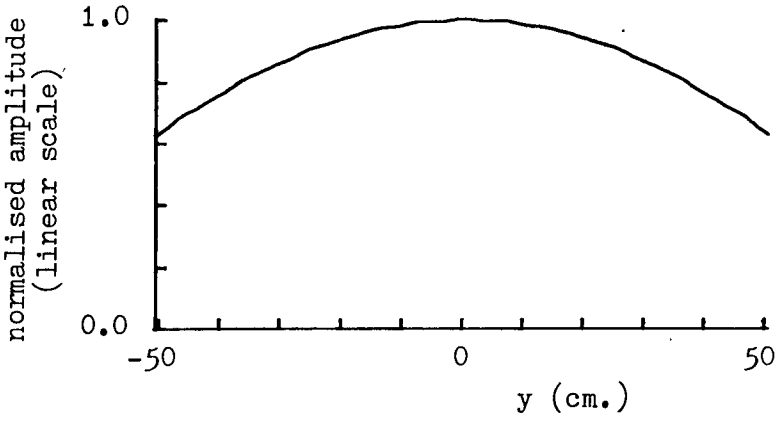

Fig. 5.8. Synthesised plane wave due to weighting function of Fig. 5.1 but using probe with 3dB beamwidth of 25°.

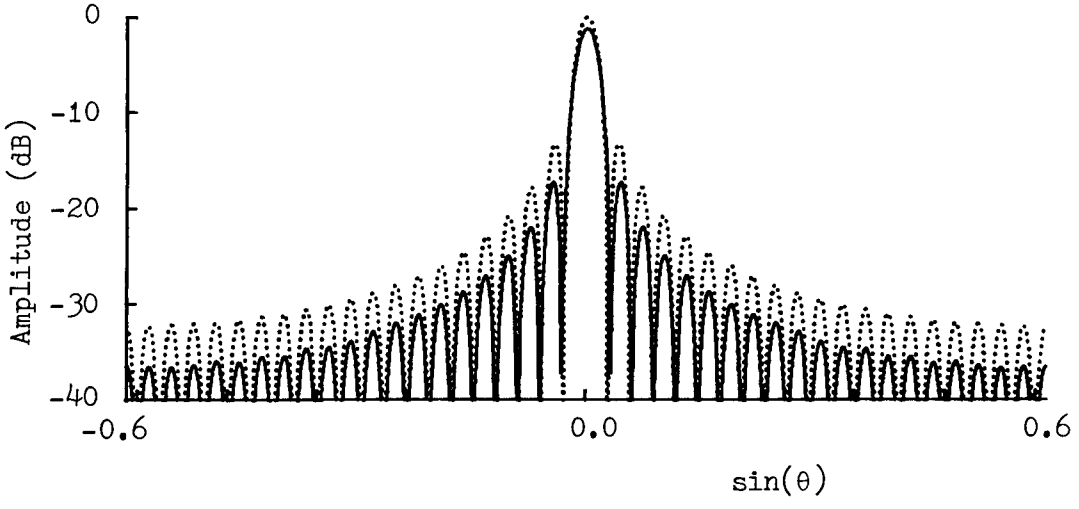

Fig. 5.9. Fourier transform of synthesised plane wave shown in Fig. 5.8 (solid) compared with ideal (dotted).

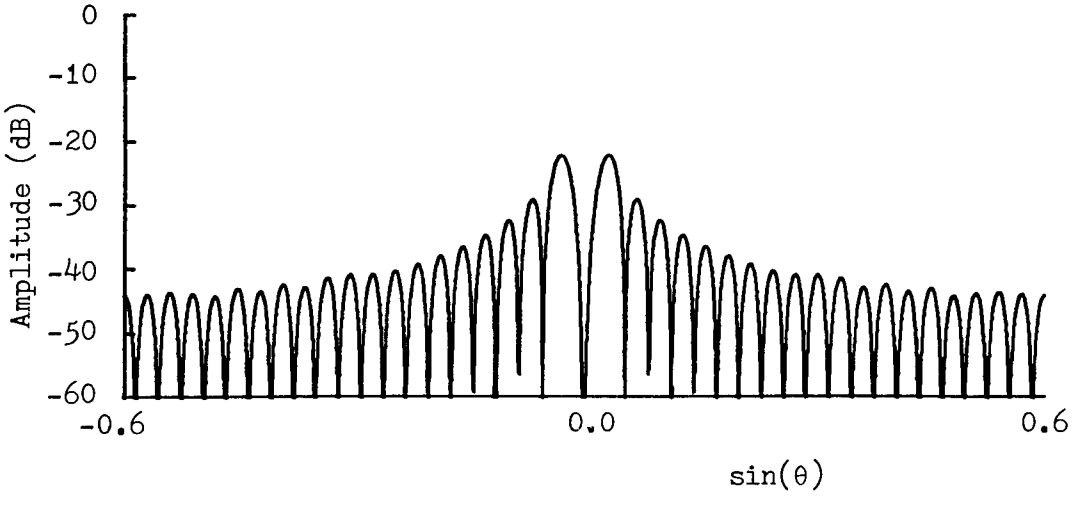

Fig. 5.10. Fourier transform of non-ideal residual of plane wave shown in Fig. 5.8 illustrating high level of effective spurious far-field sources.

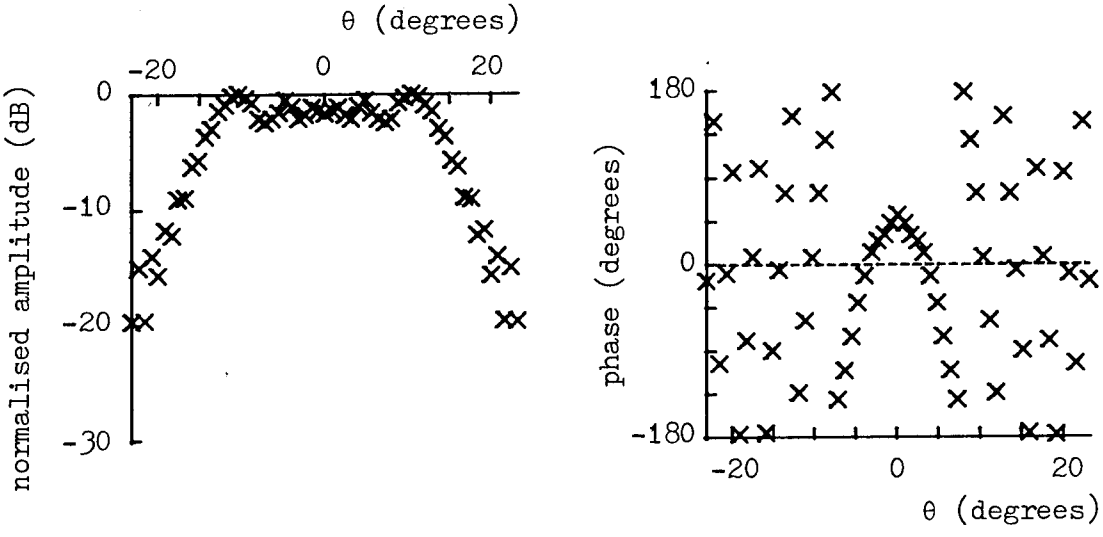

Fig. 5.11. Weighting function for the same parameters as that of Fig. 5.1 but designed for use with a probe having 75° 3dB beamwidth.

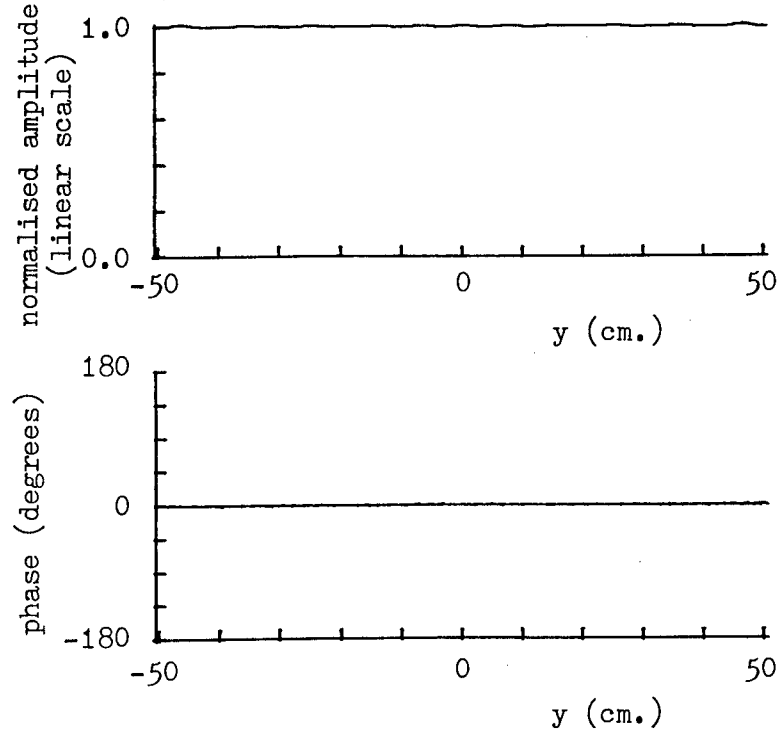

Fig. 5.12. Synthesised plane wave due to weighting function of Fig. 5.11 using correct probe.

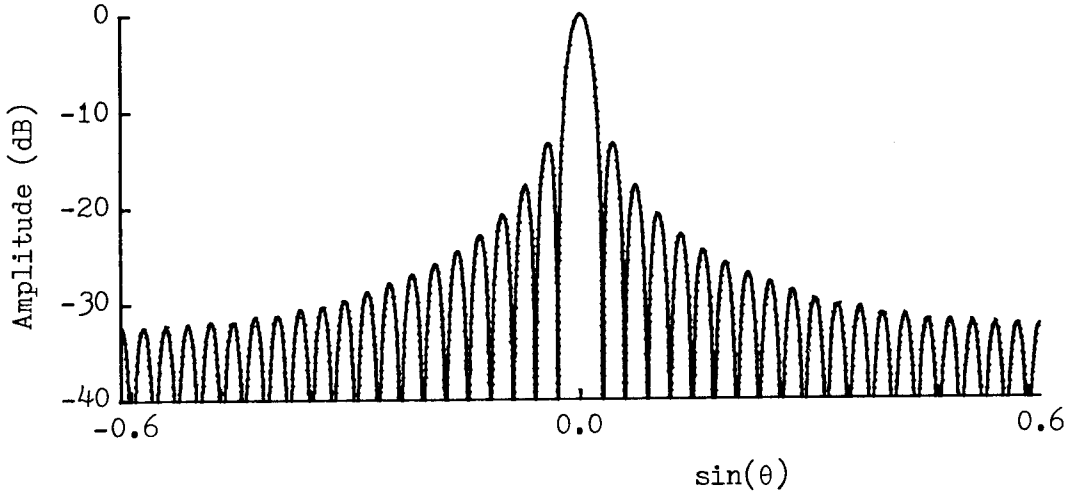

Fig. 5.13. Fourier transform of synthesised plane wave shown in Fig. 5.12 (solid) compared with ideal (dotted).

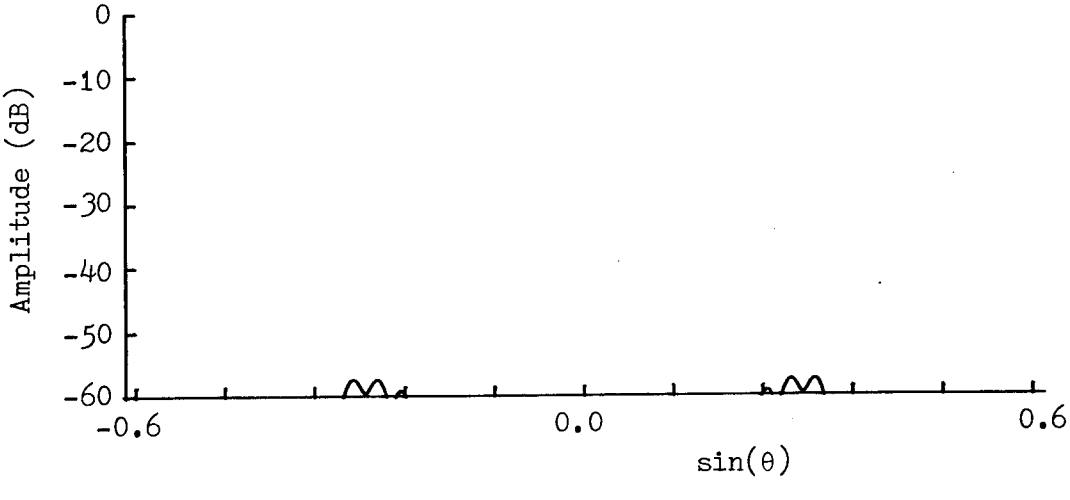

Fig. 5.14. Fourier transform of non-ideal residual of plane wave shown in Fig. 5.12 illustrating effective spurious far-field sources.

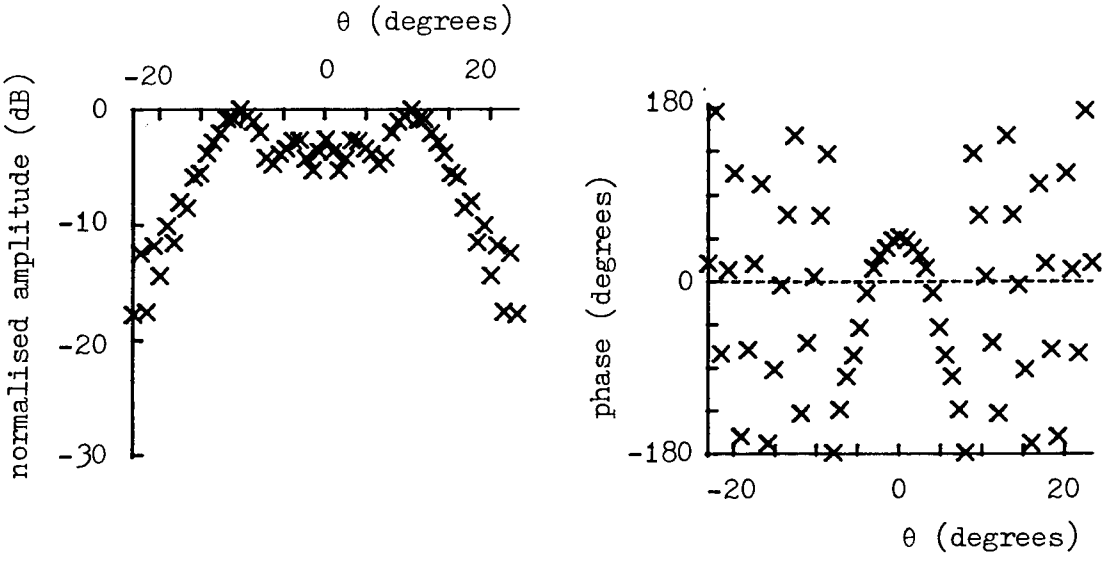

Fig. 5.15. Weighting function for the same parameters as that of Fig. 5.1 but designed for use with a probe having 25° 3dB beamwidth.

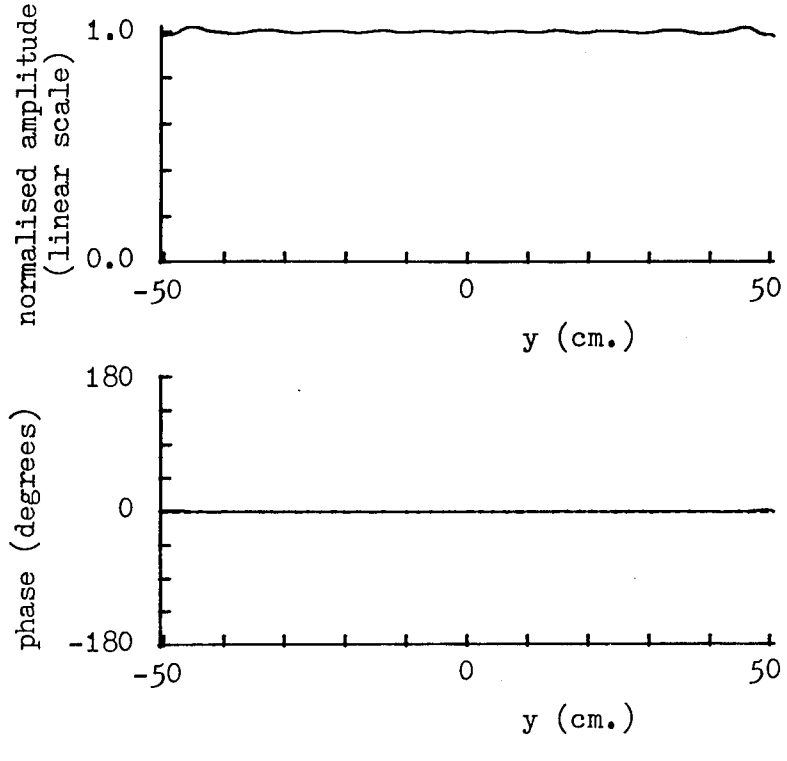

Fig. 5.16. Synthesised plane wave due to weighting function of Fig. 5.15 using correct probe.

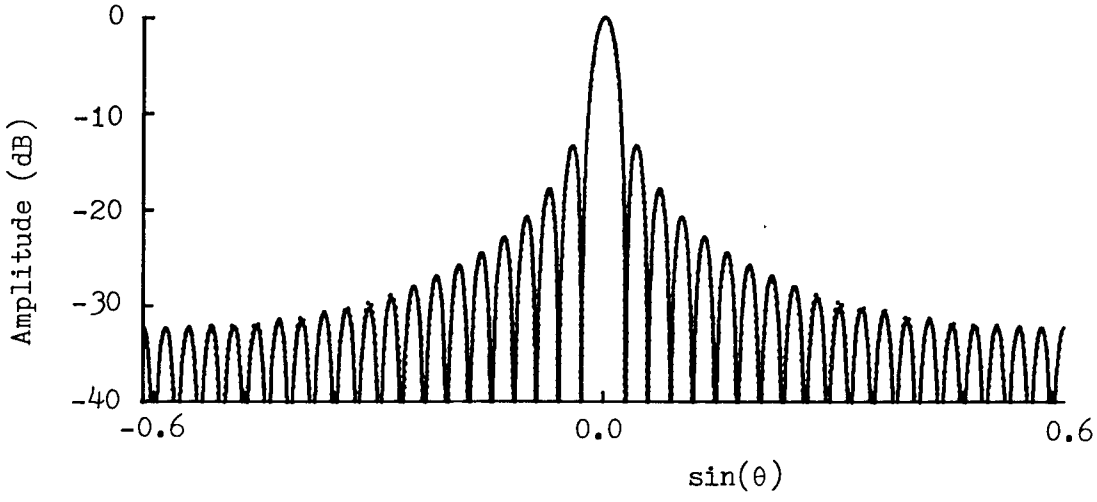

Fig. 5.17. Fourier transform of synthesised plane wave shown in Fig. 5.16 (solid) compared with ideal (dotted).

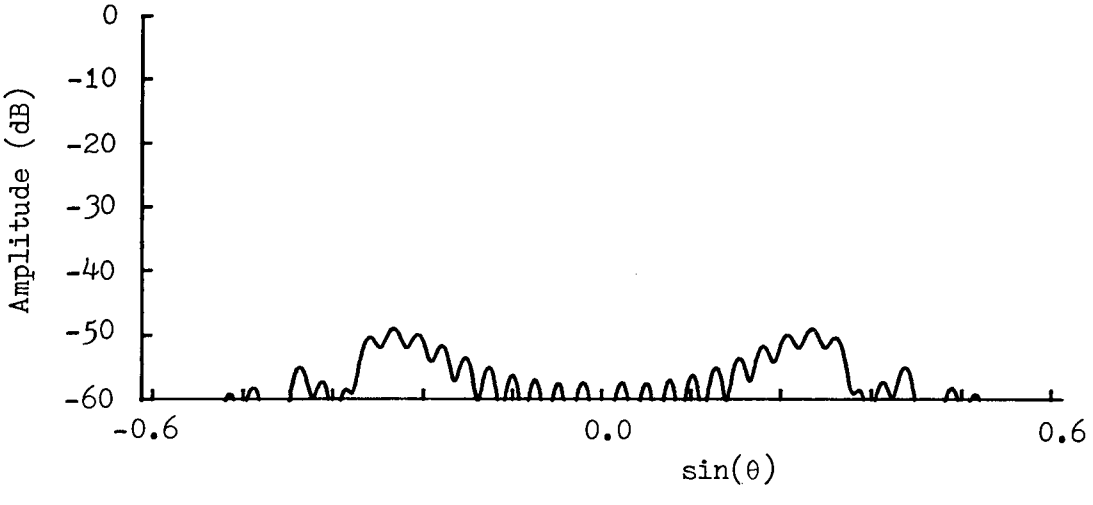

Fig. 5.18. Fourier transform of non-ideal residual of plane wave shown in Fig. 5.16 illustrating effective spurious far-field sources.

dependent upon an attempt to simulate the conditions of direct far-field measurement by computational manipulation of the near-field data. When the synthesised plane wave is examined closely it is seen that it consists in the major part of the ideal uniform plane wave, which is what would be produced by the ideal far-field source. In addition, however, there will be present some deviation from the perfect plane wave; amplitude or phase ripple, or, as has been seen above, taper. Such deviations can be thought of as being the product of interference from other spurious far-field sources.

The effective far-field source distribution can be obtained simply by Fourier transforming the synthesised plane wave distribution. The ideal plane wave component will appear not as a point-source but, because of the limited size of the plane wave, as a sinc ($\sin a\theta/a\theta$) function. The other spurious far-field sources will be present in the form of deviations from this function. Thus Fig. 5.3 shows the Fourier transform of the synthesised plane wave of Fig. 5.2. In addition, the Fourier transform of the ideal plane wave is plotted for comparison as a dotted curve and in this particular case the two curves are indistinguishable from one another confirming that the plane wave is of very good quality.

It is possible to take this reasoning one step further and to argue that, if the mean value of the synthesised plane wave is subtracted from all of the plane wave elements, the residue comprises the results of the

spurious sources alone. The Fourier transformation will then yield the positions and sizes of the spurious effective sources. This process has been carried out for the plane wave of Fig. 5.2 and the resulting spurious source distribution is shown as Fig. 5.4. Again, the quality of the synthesised plane wave is confirmed by the fact that there are only two very small incursions of the spurious far-field distribution into the 60dB range displayed. It should be noted that the full Fourier transform array is displayed here (the transform was effected by means of an FFT algorithm) and in certain instances part of the displayed transform will be for imaginary values of θ, i.e. in the invisible region. In this particular case the edge of the visible region is at about the point where the spurious source appears in Fig.5.4. The appearance of a spurious source at a particular angle means that, as the prediction moves off boresight, the main beam of the test antenna will pass from the area of the ideal far-field source through the spurious source so that the prediction at this angle will consist, in fact of the required far-field prediction plus the main beam distribution of the pattern attenuated by whatever is the level of the spurious source below 0dB. The occurrence of the spurious sources in the above example at $\theta \simeq \pm 90^{o}$ and at a level of almost -60dB indicates that the pattern prediction at $\theta_F \simeq \pm 90^{o}$ will be subject to a possible error equivalent to 60dB below the main beam (assuming that the test antenna is aligned with its main beam at the zero angular coordinate.

A similar Fourier transformation analysis was carried out for the case of the medium-beam probe, the two

diagrams forming Figs. 5.6 and 5.7. Again, very little deviation of the plane wave Fourier transform from the ideal are visible but in this case, the Fourier transform of the residual after subtraction of the ideal plane wave indicates the appearance of two further spurious effective sources at $\theta \simeq \pm 5^{o}$ and at a level of about -50dB. In this case, therefore, the worst effects of the non-ideal quality of the synthesised plane wave would appear a few degrees either side of boresight.

For the narrow-beam probe, the Fourier transform of the synthesised plane wave (Fig. 5.9) shows considerable differences from the ideal and this is reflected in Fig.5.10 showing the Fourier transform of the non-ideal residue. In this case, the spurious far-field sources reach a level of -20dB confirming the unacceptability of this plane wave taper for most practical purposes.

After probe compensation for the medium-beam probe (as appeared in Fig. 5.12) the taper was removed from the synthesised plane wave and Figs. 5.13 and 5.14 confirm that the spurious far-field source level has once more been reduced to almost -60dB. On the other hand, the narrow-beam probe proves a more difficult case to correct since the probe-compensated plane wave (as seen in Fig. 5.16) still has some residual ripple and although its Fourier transform differs from the ideal apparently in only minor ways (Fig. 5.17), the spurious source distribution revealed when the non-ideal residual is transformed (Fig. 5.18) does extend above the -50dB mark. More iterations (in this case the iteration was terminated after 45) would probably effect some additional improvement.

5.1.3 A Simulation

An array of vertically polarised half-wave dipoles was modelled computationally as a further investigation of probe compensation in action. A frequency of 10GHz was used and the array was specified to be 11 elements wide by 21 elements high with $\lambda/2$ spacing in both directions. "Measured" near-field data were computed over a band of 13 points, angular spacing 3.6^{o}, extending along the elevation (E-plane) principal axis at a range of 1.0m. Only one polarisation of data was used. From these simulated near-field measurements a principal plane pattern was predicted (over a 90^{o} range, symmetry applying for the other quadrants). The true far-field was evaluated analytically and used as a comparison for the prediction.

In Fig. 5.19 is shown a comparison of the prediction of the far-field pattern using a probe with a cosinusoidal main beam, 3dB beam width of 90^{o}, and the true far-field. Good accuracy is observed over most of the pattern down to the -60dB level. Using the same weighting function, a prediction was performed using the data which would be measured with a probe having only a 12^{o} 3dB beamwidth and the prediction is compared with the true far-field in Fig. 5.20. A significant lowering of the predicted sidelobe levels together with shifting of the nulls is apparent. When probe compensation for the directive probe was performed the predicted pattern changed to that shown in Fig. 5.21 (compared again with the true far-field). Virtually all of the pattern shows a marked improvement over the uncompensated case. Errors are still present in

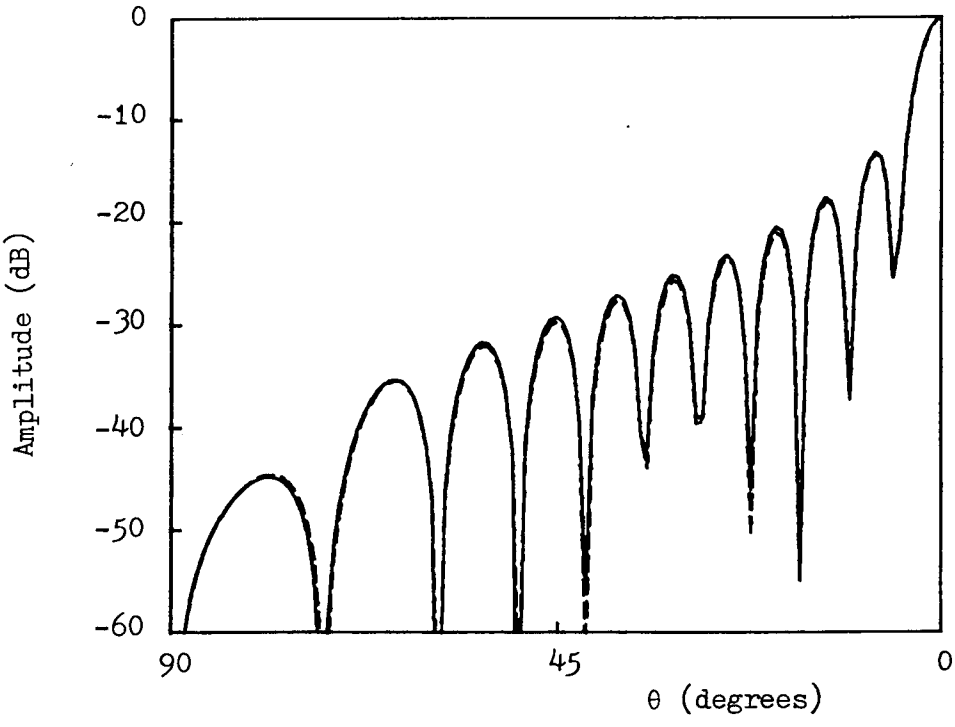

Fig. 5.19. Far-field pattern (over one quadrant - symmetry applies) of dipole array. E-plane cut predicted using wide-beam probe (solid) compared with true pattern (dashed).

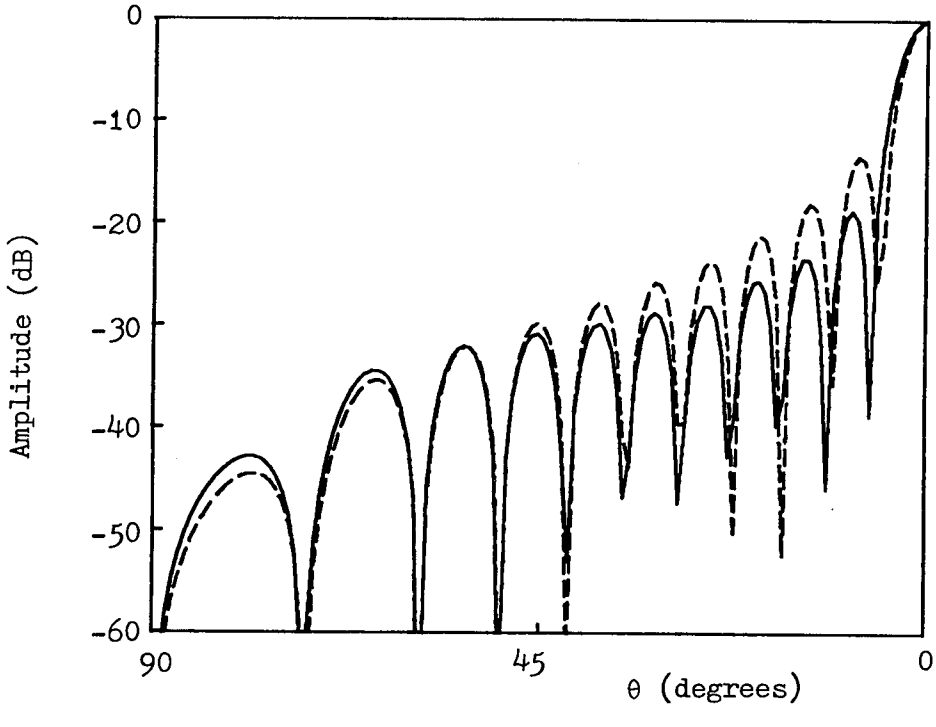

Fig. 5.20. Far-field pattern of dipole array. E-plane cut predicted using narrow beam probe, uncompensated (solid) compared with true pattern (dashed).

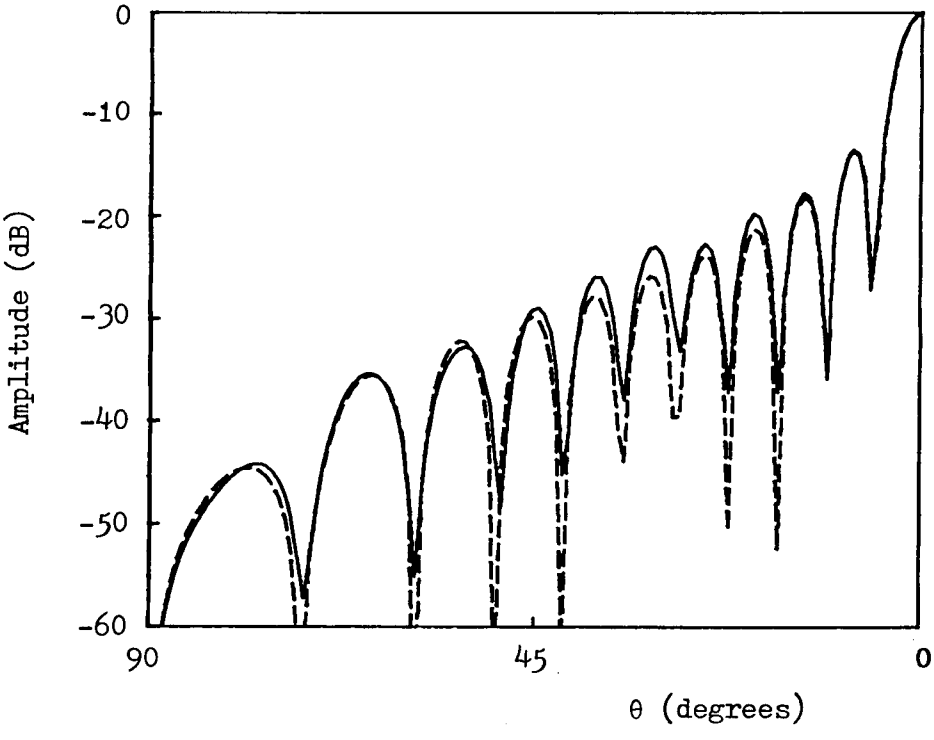

Fig. 5.21. Far-field pattern of dipole array. E-plane cut predicted using narrow-beam probe, compensated (solid) compared with true pattern (dashed).

places but it will be realised that this is a far more directive probe than is likely to be used in a practical measurement system. It should also be noted that this simulation indicates that it is possible to obtain useful results using only one polarisation of near-field data given the right circumstances although, in general, both polarisations of the near-field will be required.

5.2 Effects of Measurement Errors

A useful summary of some of the types of errors liable to be found in a practical measurement system is given by Joy [32]. Although this is intended to apply particularly to the planar scan geometry, most of the errors are applicable to any measurement system. A brief analysis has been carried out of the sorts of effects which these errors might introduce and certain other effects, also. This is mentioned in section 5.2.2. Firstly an investigation of a particular type of random noise introduction is presented.

5.2.1 Level-Independent Random Noise

The effect of random noise in the measured near-field data when multiplied by the weighting function can be thought of as essentially similar to ideal data being processed by a weighting function containing random errors. In this particular investigation, normally distributed random noise of a specified amplitude standard deviation, random phase, was introduced into the weighting function and the resulting errors in the plane wave and its Fourier transforms were observed. There was no attempt to link this

to a particular set of near-field data but the noise values were multiplied by the appropriate weighting function element before being added to it (i.e. the noise was weighted in the same way as would be done with the actual measured data). The reasoning behind this might be thought of as follows. As the test antenna is scanned, its main beam region will pass around the walls of the anechoic chamber (assuming that the measurement is taking place within such a chamber). There will be some reflections which will appear as noise at a certain level within the data and will thus be weighted along with the desired data. Thus the weighted noise will appear as the unwanted ripple superimposed upon the synthesised plane wave. A similar argument can be applied for any random noise appearing in the data (such as receiver noise, etc.)

In this test a 50cm plane wave was specified at 10GHz with a measurement range of 1.0m. A 29-point (one-dimensional) weighting function was used with 2.5^{o} spacing. The synthesised plane wave with its Fourier transform and the transform of the non-ideal residual are shown in Figs. 5.22, 5.23 and 5.24. Very little deviation from the ideal is detectable in the synthesised plane wave and Fig.5.24 shows that the effective spurious far-field sources are at a level of better than -70dB. If noise is introduced at a standard deviation of -40dB into the data, the effective synthesised plane wave begins to show a little ripple (Fig. 5.25) and although little discrepancy is visible, in Fig. 5.26, between the Fourier transform of the plane wave and that of the ideal, a spurious far-field effective

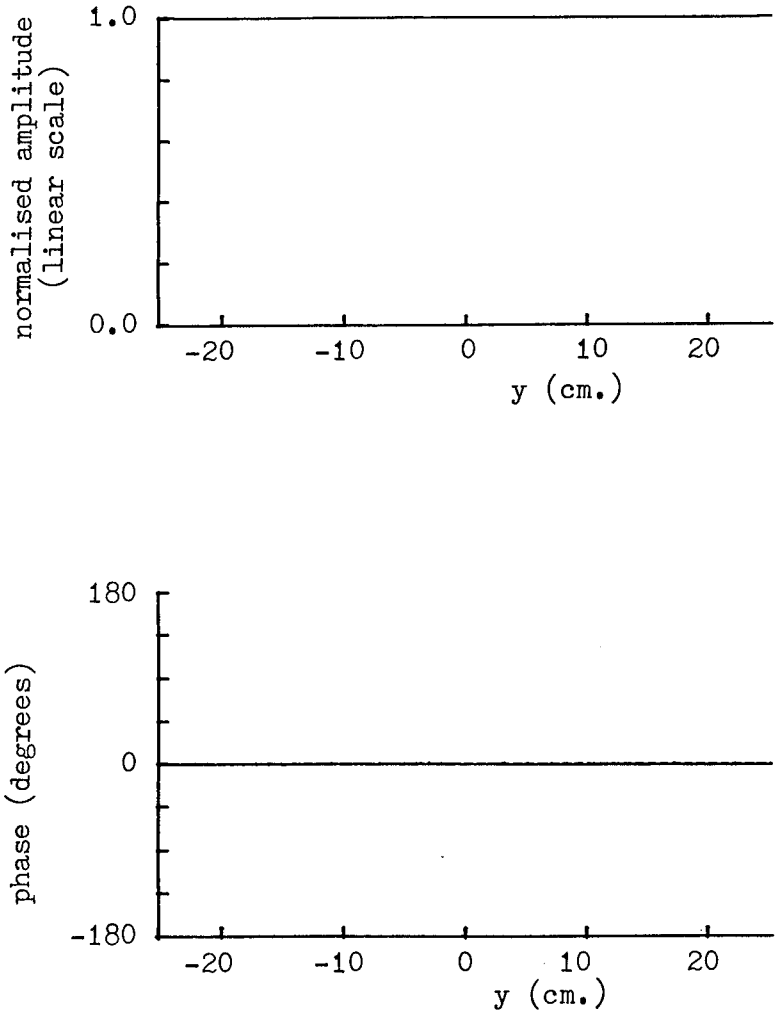

Fig. 5.22. Synthesised plane wave due to 29-point weighting function with no introduced noise.

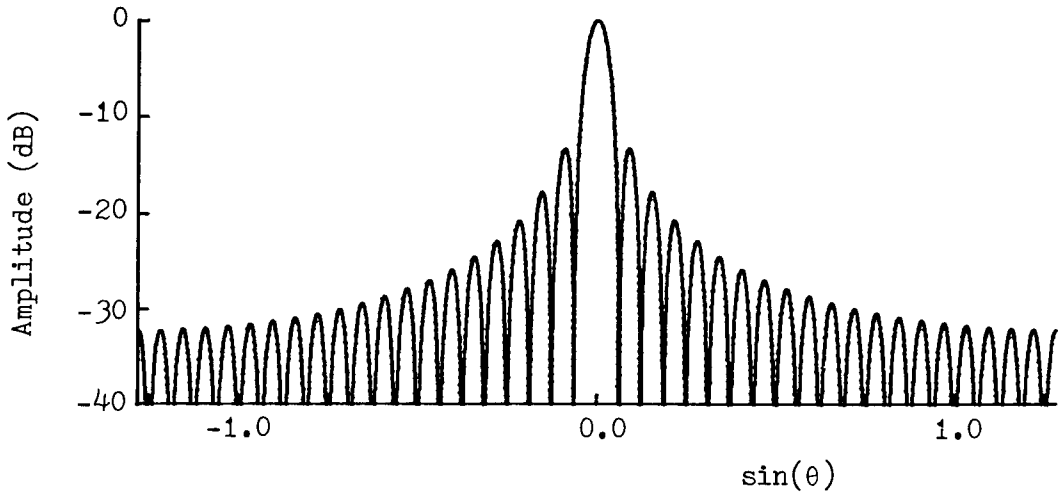

Fig. 5.23. Fourier transform of synthesised plane wave shown in Fig. 5.22 (solid) compared with ideal (dotted).

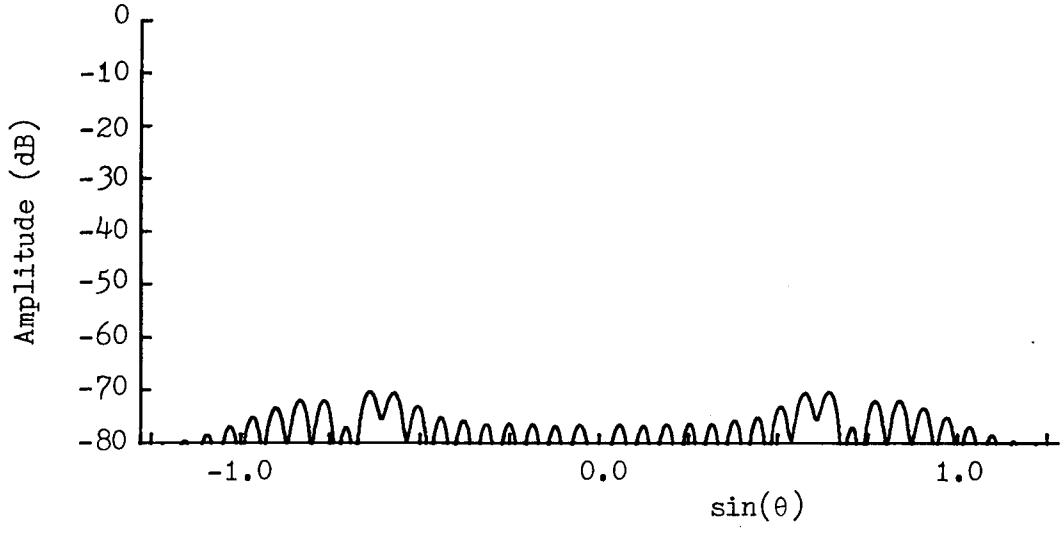

Fig. 5.24. Fourier transform of non-ideal residue of synthesised plane wave shown in Fig. 5.22.

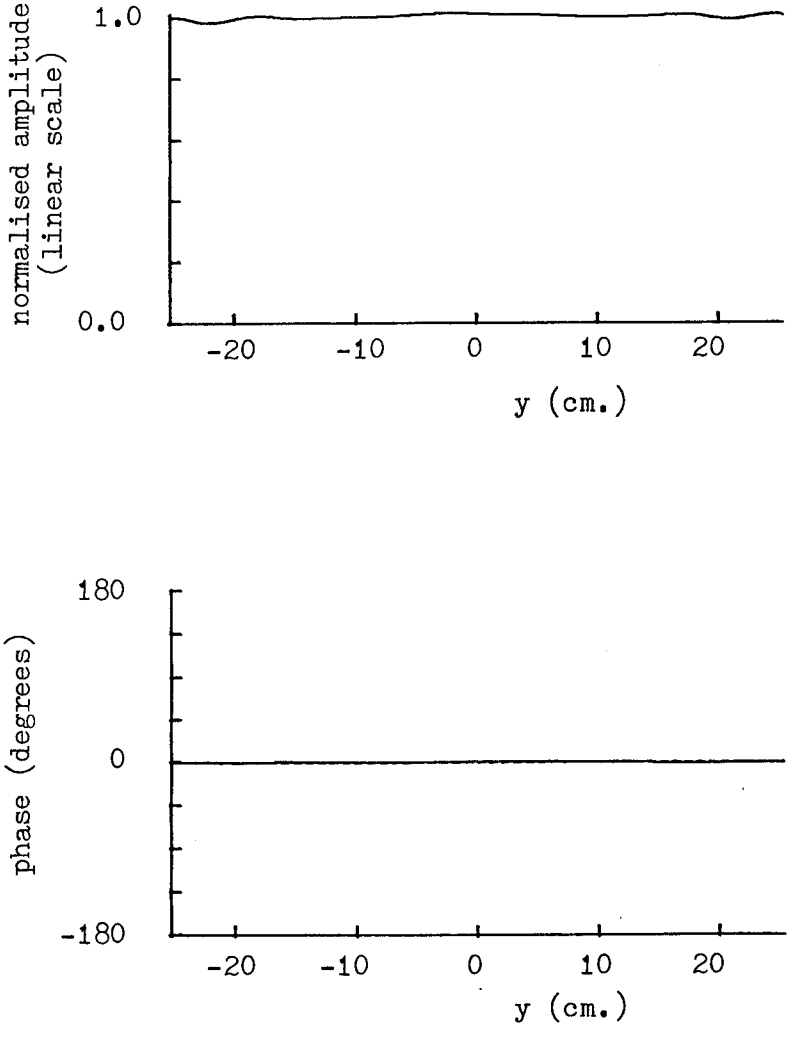

Fig. 5.25. Synthesised plane wave due to 29-point weighting function with normally distributed random noise added at a level of -40dB.

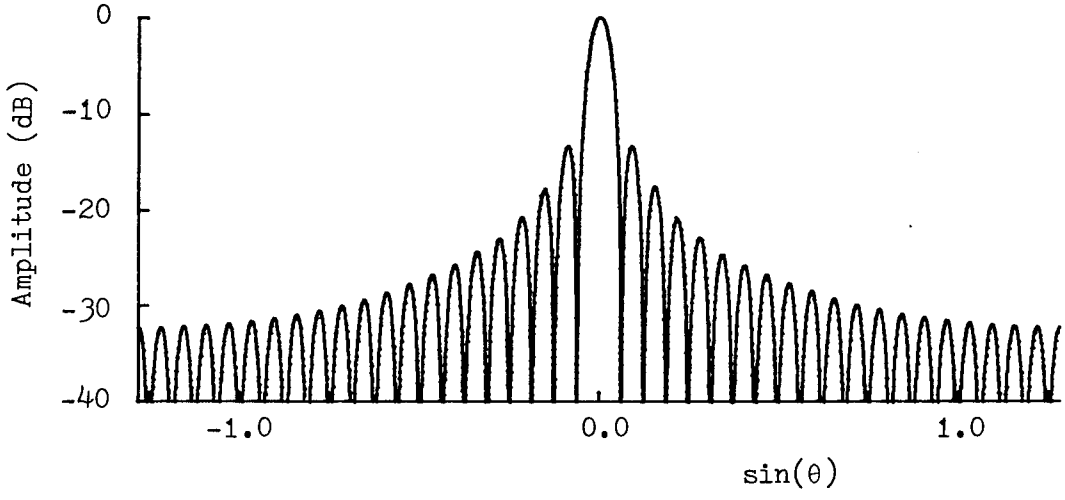

Fig. 5.26. Fourier transform of synthesised plane wave shown in Fig. 5.25 (solid) compared with ideal (dotted).

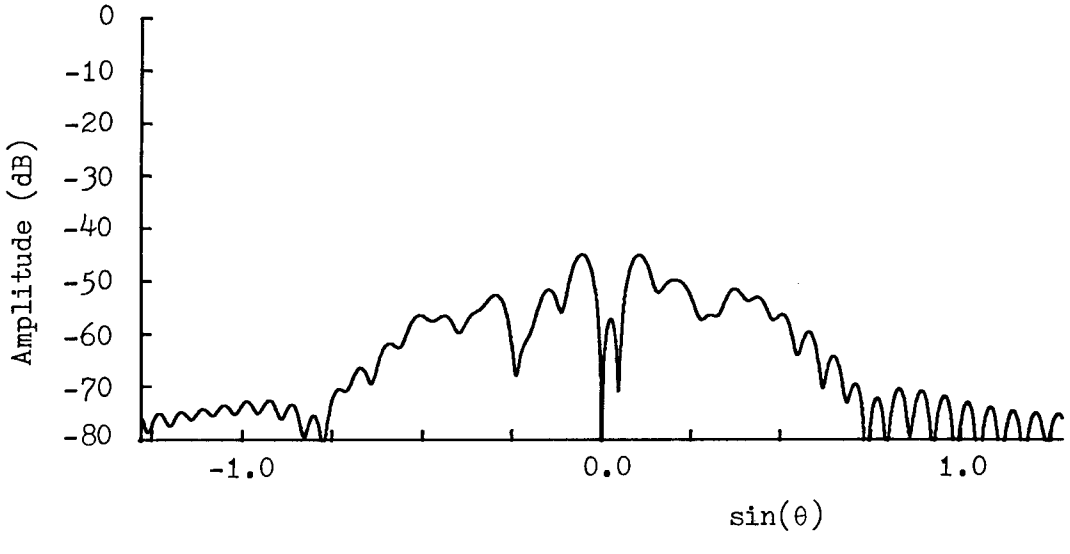

Fig. 5.27. Fourier transform of non-ideal residue of synthesised plane wave shown in Fig. 5.25.

source level of about -45dB is apparent in Fig. 5.27.

When the noise level is increased to -30dB, the synthesised plane wave, displayed in Fig. 5.28, has a Fourier transform (Fig. 5.29) which possesses considerably more deviation from the ideal and the spurious far-field source level (Fig. 5.30) has risen to above -35dB. Continuing the trend, if the measured noise level is increased to -20dB, the synthesised plane wave (Fig.5.31) exhibits severe ripple, its Fourier transform (Fig. 5.32) now deviates markedly from the ideal and the spurious far-field source distribution (Fig. 5.33) has risen by another 10dB. Clearly this latter case would be of little value for measuring any antenna but the earlier cases (-30dB and particularly -40dB noise) might be usable in the right circumstances dependent upon the antenna being measured and the accuracy required.

5.2.2 Non-Ideal Probe

It may be the case that the dual polarised probe (assuming that such a device is in use) does not possess perfect orthogonality of polarisation. A technique for extracting correctly polarised data from a non-ideal probe has been formulated by Bach et al [33] and this technique can be used to correct for this type of error.

5.2.3 Other Measurement Errors

Under this heading are included the other types of error which might occur on the R.F. side of the system, but we do not cover the various mechanical errors which can occur. These will be mentioned shortly. A number of simulations have been performed [34], using a scalar approach,

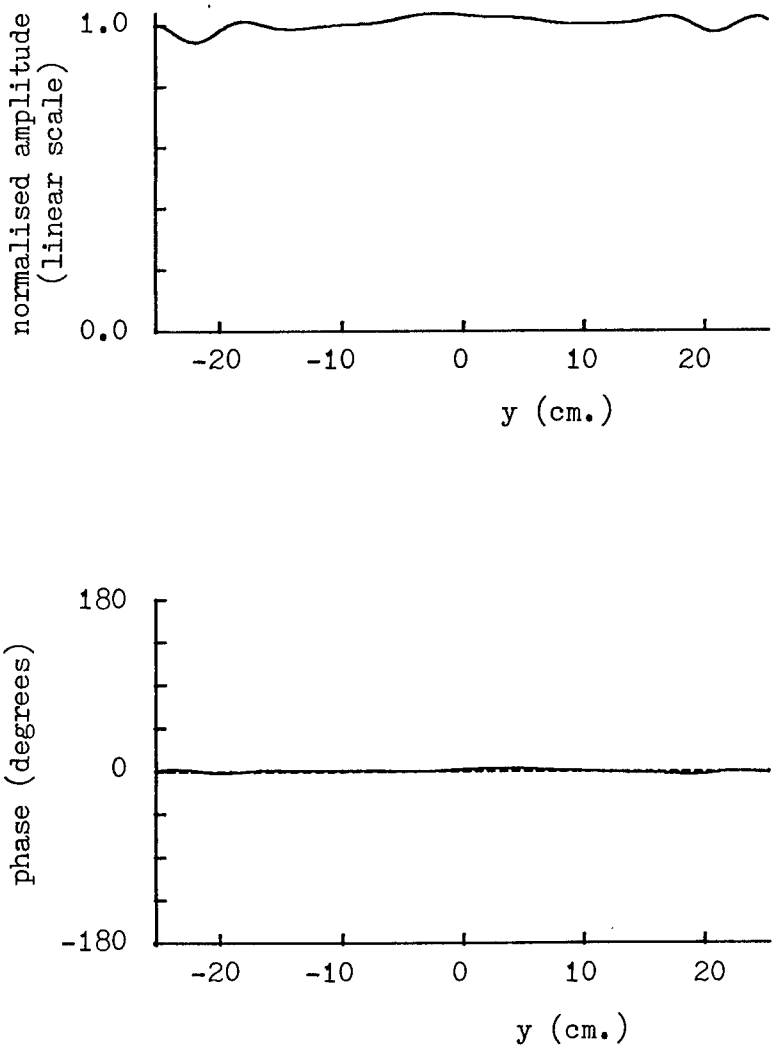

Fig. 5.28. Synthesised plane wave due to 29-point weighting function with normally distributed random noise added at a level of -30dB.

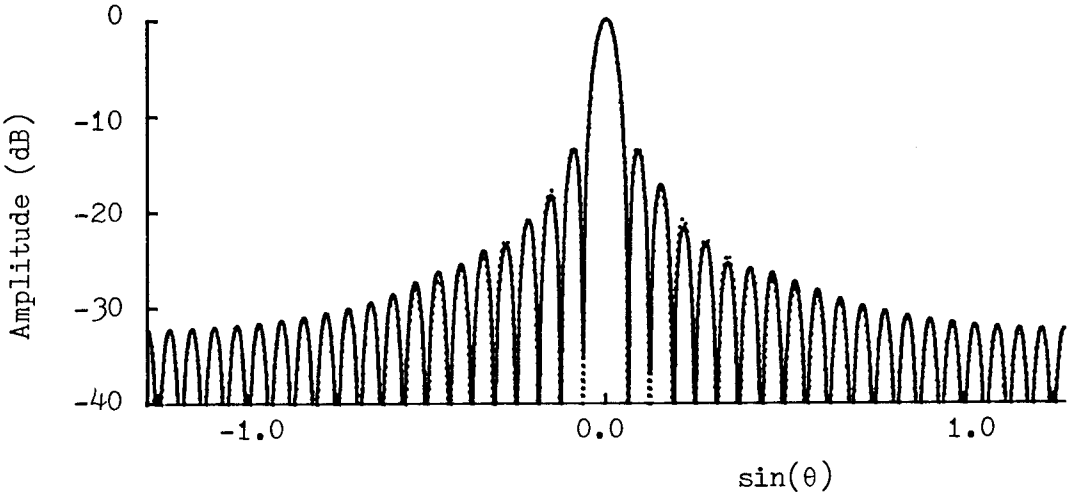

Fig. 5.29. Fourier transform of synthesised plane wave shown in Fig. 5.28 (solid) compared with ideal (dotted).

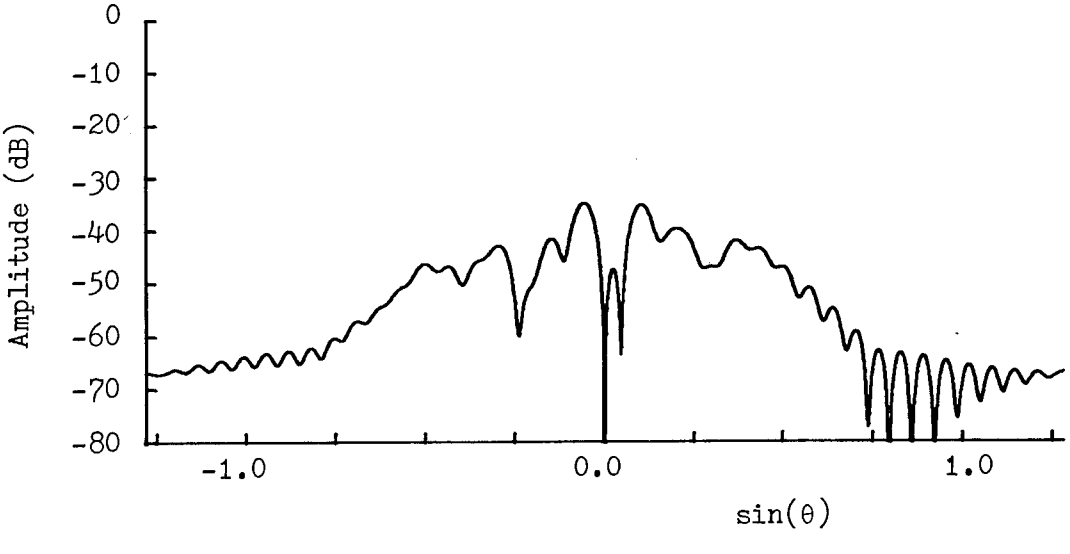

Fig. 5.30. Fourier transform of non-ideal residue of synthesised plane wave shown in Fig. 5.28.

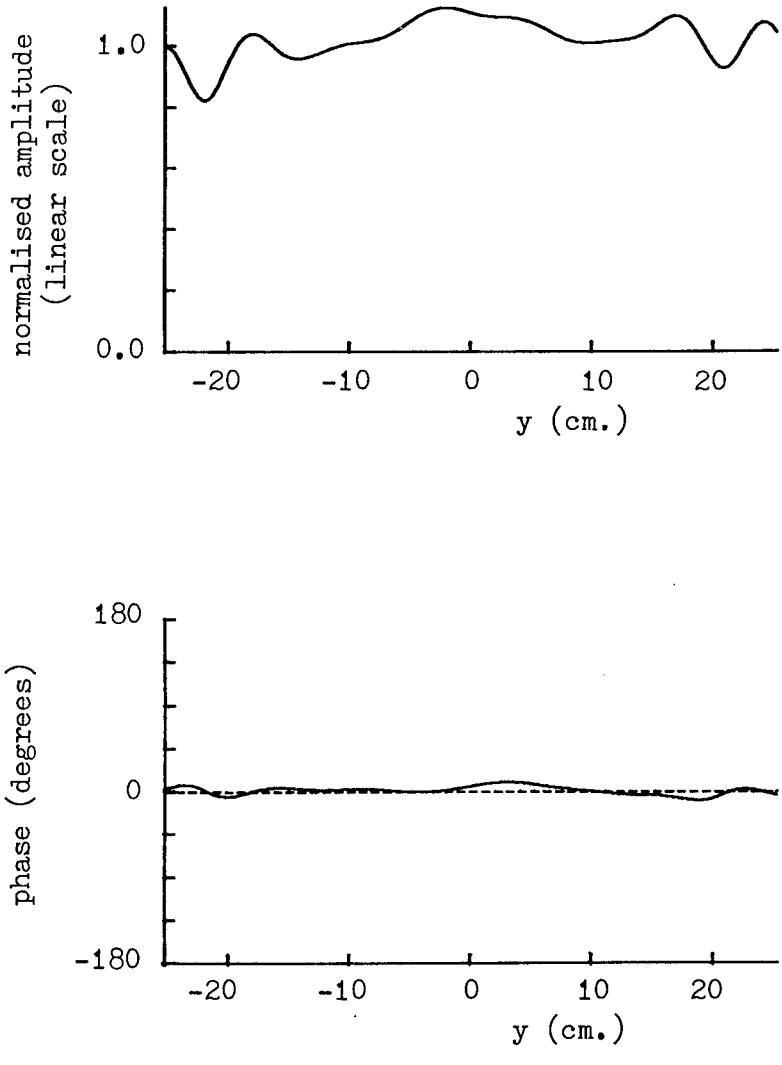

Fig. 5.31. Synthesised plane wave due to 29-point weighting function with normally distributed random noise added at a level of -20dB.

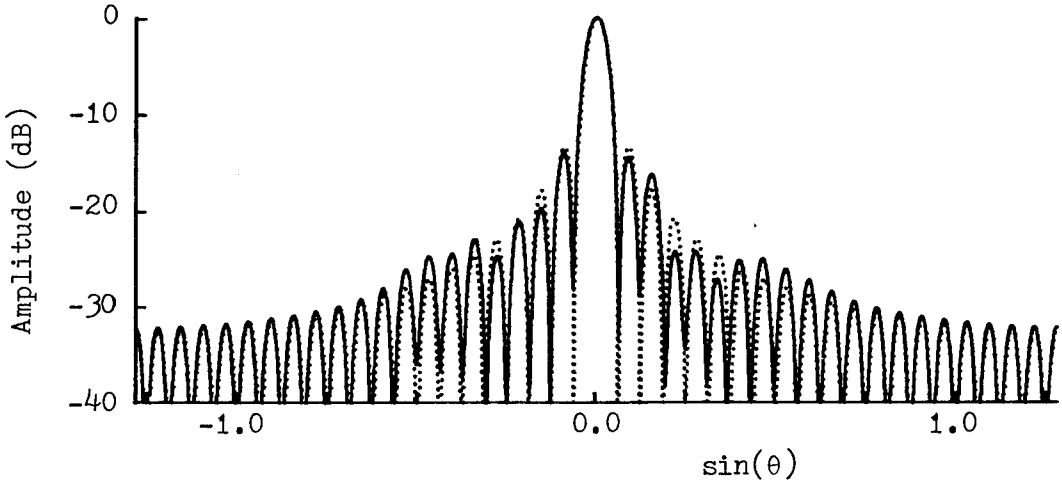

Fig. 5.32. Fourier transform of synthesised plane wave shown in Fig. 5.31 (solid) compared with ideal (dotted).

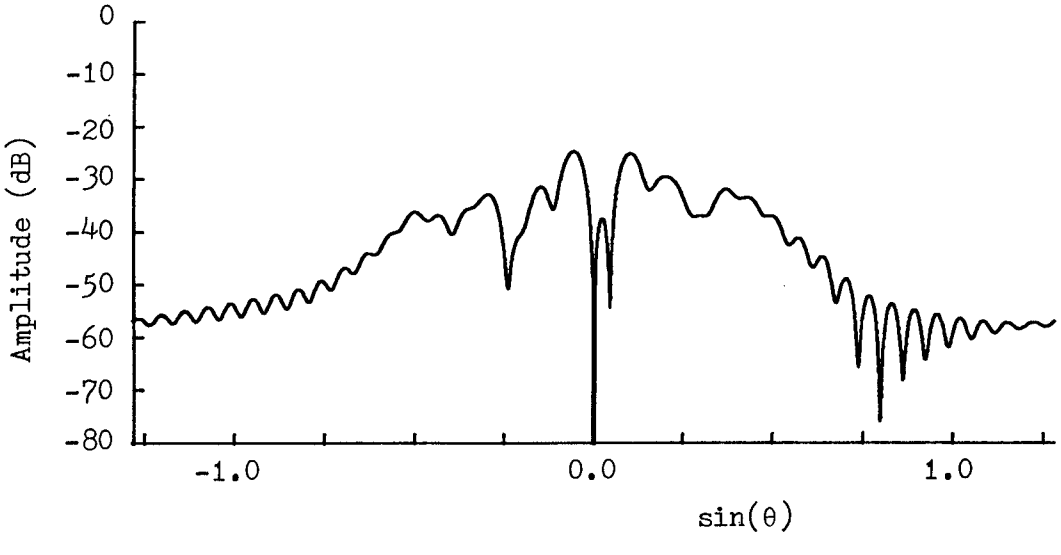

Fig. 5.33. Fourier transform of non-ideal residue of synthesised plane wave shown in Fig. 5.31.

of various measurement errors which can occur in a practical system and the results are summarised briefly here.

The simulation was of an X-band 10λ antenna and one of the investigations involved uniform illumination of the antenna and simultaneous introduction of the errors numbered 1 to 10 of those listed by Joy [32] at the levels suggested as the maximum allowable. The most noticeable effect due to the presence of the errors was a change in the level of some of the sidelobes, for instance an error of 0.5dB in a sidelobe at -27dB. When the errors introduced were increased by a factor of 5, the resulting errors in the prediction were much more severe with the 0.5dB error now appearing in the first (-12dB) sidelobes. Inner nulls were filled to about -35dB and some null positions were shifted by up to 0.5^{o}. Similar results were observed when the above errors (not multiplied by 5) were introduced into the near-field of an antenna with a tapered illumination. When the antenna was illuminated in a monopulse configuration, rather more significant errors were observed, typically 1dB at -25dB.

The other type of error investigated was quantisation error. Near-field phase quantisation was tried at 10^{o} intervals, 30^{o} intervals and 60^{o} intervals. The 10^{o} quantisation introduced little discernible error. Under 30^{o} quantisation some error was observable, perhaps 0.4dB in the first sidelobes and some filling of inner nulls. The 60^{o} quantisation introduced much greater error, almost 1.5dB in the first sidelobe, filled inner nulls (to -25dB) and

null shifts of up to about 1^{o}. The amplitude quantisation was at 100 levels, linear. The errors produced in this latter case were of similar magnitude to those due to the errors from Joy (0.5dB at -27dB).

5.2.4 Mechanical Errors

A useful investigation of the different types of mechanical errors likely to be present in a spherical near-field measurement system is given by Jensen [35] and it is believed that the effects due to a prediction by the plane wave synthesis technique will be broadly similar. The general effects of some types of error are listed below. These are discussed as they apply to a polarisation-over-azimuth system. Clearly the application to another type of scanning system will in some cases be different.

(a) Probe position. Position error as regards the azimuth direction of the scanning system will be equivalent to an error in the setting up of the azimuth zero position and will be discussed under that heading. It will be shown later in this chapter that measurement distance error and frequency error are to some extent equivalent and so that too is covered no further here. The remaining inaccuracy possible is that the height of the probe will not be the same as the height of the centre of rotation. The result of this will be, as shown in Fig. 5.34, that the fields are measured around scans at slightly incorrect ϕ values (the discrepancy decreasing as ϕ increases to become zero at $\phi = 90^{o}$), slightly incorrect θ values (again decreasing as ϕ increases to a minimum of $\tan^{-1}$ (h/R) where h is the probe height error) and at these angles the polarisation

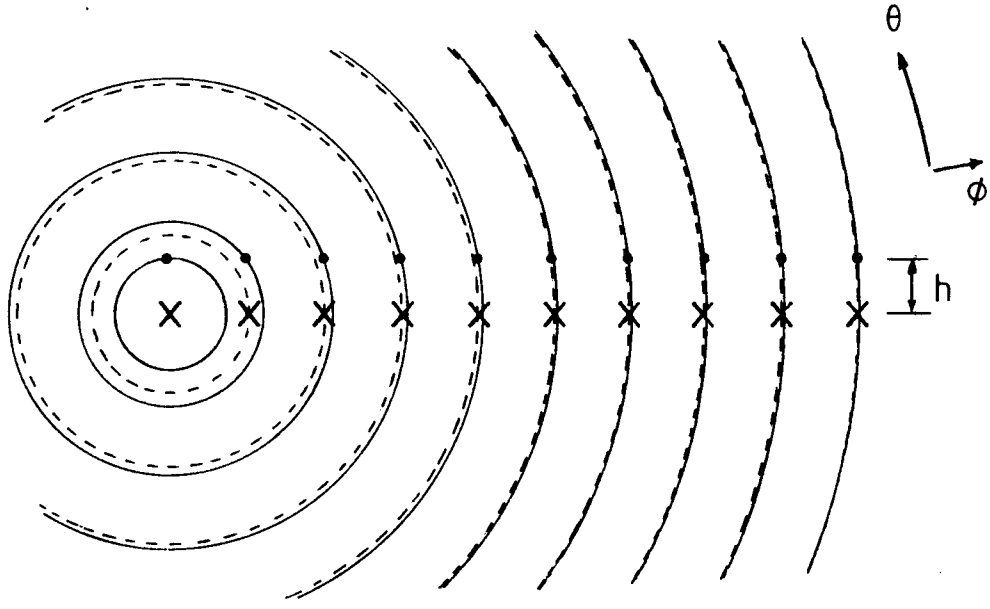

X - Desired scan start position.

• - Actual scan start position, displaced by height error, h, from that desired.

Fig. 5.34. Effect of probe height error on resultant scan geometry for polarisation-over-azimuth system. The dashed lines show the desired scan positions and the solid lines show the actual scans.

will not be quite accurate.

(b) Probe pointing. If the pointing of the probe is not correct the effect will be as if a slightly incorrect probe had been used. Section 5.1 may be consulted for further demonstration of the possible effects.

(c) Probe polarisation. This will be particularly relevant where cross-polar patterns are being predicted. If the polarisation is not correct then a small amount (proportional to sin Ω where Ω is the polarisation error) of the co-polar will appear also.

(d) Azimuth axis verticality. If the azimuth axis is not truly vertical the polarisation axis, although it may start horizontal, will not remain so and therefore effects similar to probe height error will appear.

(e) Polarisation positioner axis horizontality. Again the effects will be broadly similar to probe height error.

(f) Intersection of positioner axes. If the axes of the two positioners do not intersect accurately the measurement surface will not be a sphere (as shown in Fig. 5.35) but will in fact be the surface of rotation created by rotation of a circular arc which is not half of the desired circle.

(g) Azimuth zero setting. An error in this setting will add a constant ϕ error. One pole of the data set (boresight or rear boresight) will be omitted from the scan while the other will be overlapped.

(h) Sample position errors. There will be small over-shoots on the positions at which data are taken. In the system used at the University of Sheffield antenna test

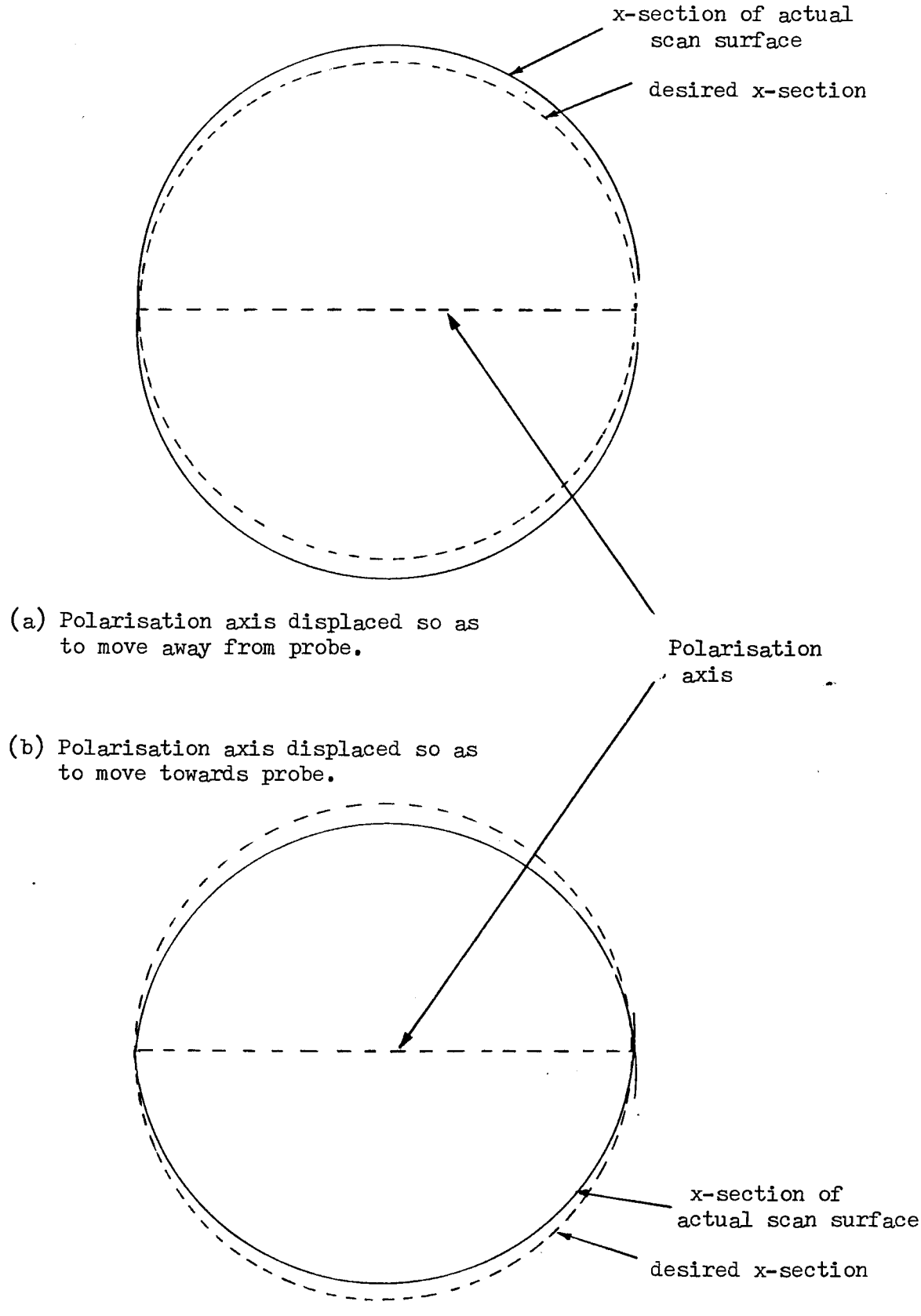

Fig. 5.35. Effect upon scan surface, for polarisation-over-azimuth system, of non-coincidence of positioner axes.

site the scans of data are taken in polarisation and between scans, the azimuth incrementation is performed relatively slowly so that the error in this latter coordinate should be slight. In the polarisation coordinate (θ), there will be some error introduced by the finite sample time and this will appear as a slight offset in θ_F of the prediction direction. There will, of course, be a slight smearing effect over the integration time and, if the sample interval is not an exact multiple of 0.01^{o} (the resolution of the equipment being used) there will be a small quantisation error. Of course, if the angular indication from the equipment is not accurate then this will be an additional error.

5.3 Weighting Function Edge Effects

In a way similar to that encountered with the compact range [36], it is found that one of the most serious sources of ripple in the synthesised plane wave is due to the discontinuity found at the edge of the near-field weighting function. This is displayed clearly by the three graphs comprising Fig. 5.36. These consist of the synthesised plane wave (amplitude only), its Fourier transform and the transform of the ripple component of the plane wave (the spurious far-field source distribution) due to a 17-point weighting function, angular spacing 3^{o}, at a measurement range of 1.0m. The frequency used was 10GHz. The synthesised plane wave has a substantial amount of ripple. This diagram corresponds to the "first guess" weighting function before any iteration and was chosen specifically for its large ripple component. The

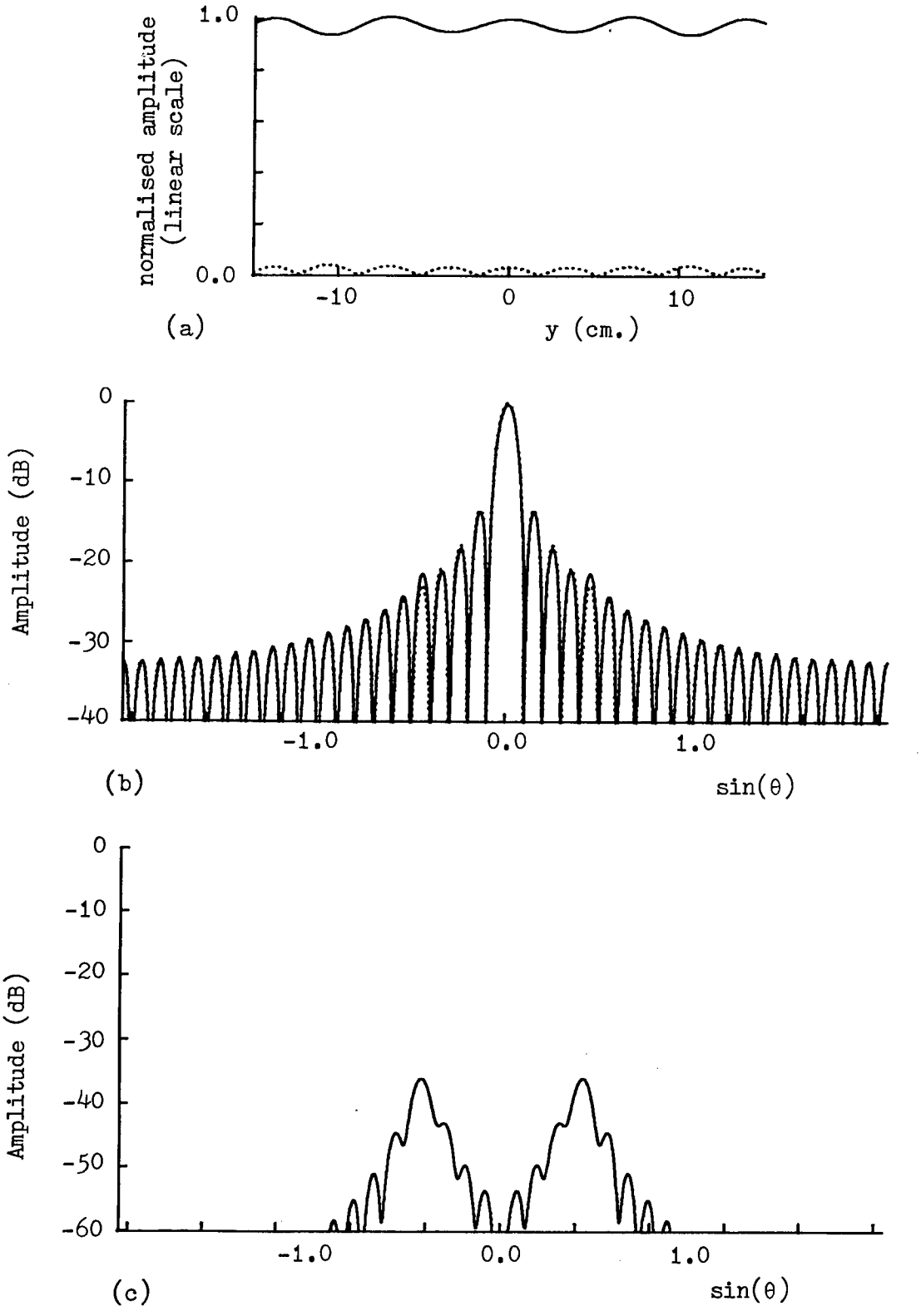

Fig. 5.36. (a) 30cm. synthesised plane wave amplitude (solid) with amplitude of non-ideal residue shown as dotted. First guess, before iteration. (b) Fourier transform of plane wave (solid) compared with ideal (dotted). (c) Fourier transform of non-ideal residue of plane wave.

amplitude of the ripple component of the plane wave is shown as the dotted line on this graph. The Fourier transform shows its worst deviations from the ideal in the fourth sidelobe and this is even more apparent in the graph showing the Fourier transform of the non-ideal parts of the plane wave. The peak values of the spurious far-field sources appear just outside the x-axis scale-ticks corresponding to $\sin^{-1} 0.4$ (which is 23.5^{o}) and from the figures above it may be realised that the weighting function extends to $\pm 24^{o}$ thus the source of the ripple in the synthesised plane wave corresponds exactly with the edge of the weighting function. The peak level of the spurious effective far-field sources is at -35dB.

After two cycles of the iterative procedure the ripple in the synthesised plane wave has visibly reduced and this is confirmed by the fact that the spurious far-field sources have reduced to -42dB, this being displayed in Fig. 5.37. Another three iterations see the spurious source level down to -45dB (Fig. 5.38). By iteration 30, the spurious far-field source level has fallen to -51dB (Fig. 5.39) and the reduction in the ripple continues so that finally by iteration 80 the peak level is at -63dB (Fig. 5.40).

It appears from this that under certain circumstances, edge discontinuity of the weighting functions can be the principal source of synthesised plane wave deviation from the ideal. The application of the usual iterative process reduces the ripple (and the corresponding spurious effective far-field source level). In a relatively coarsely sampled

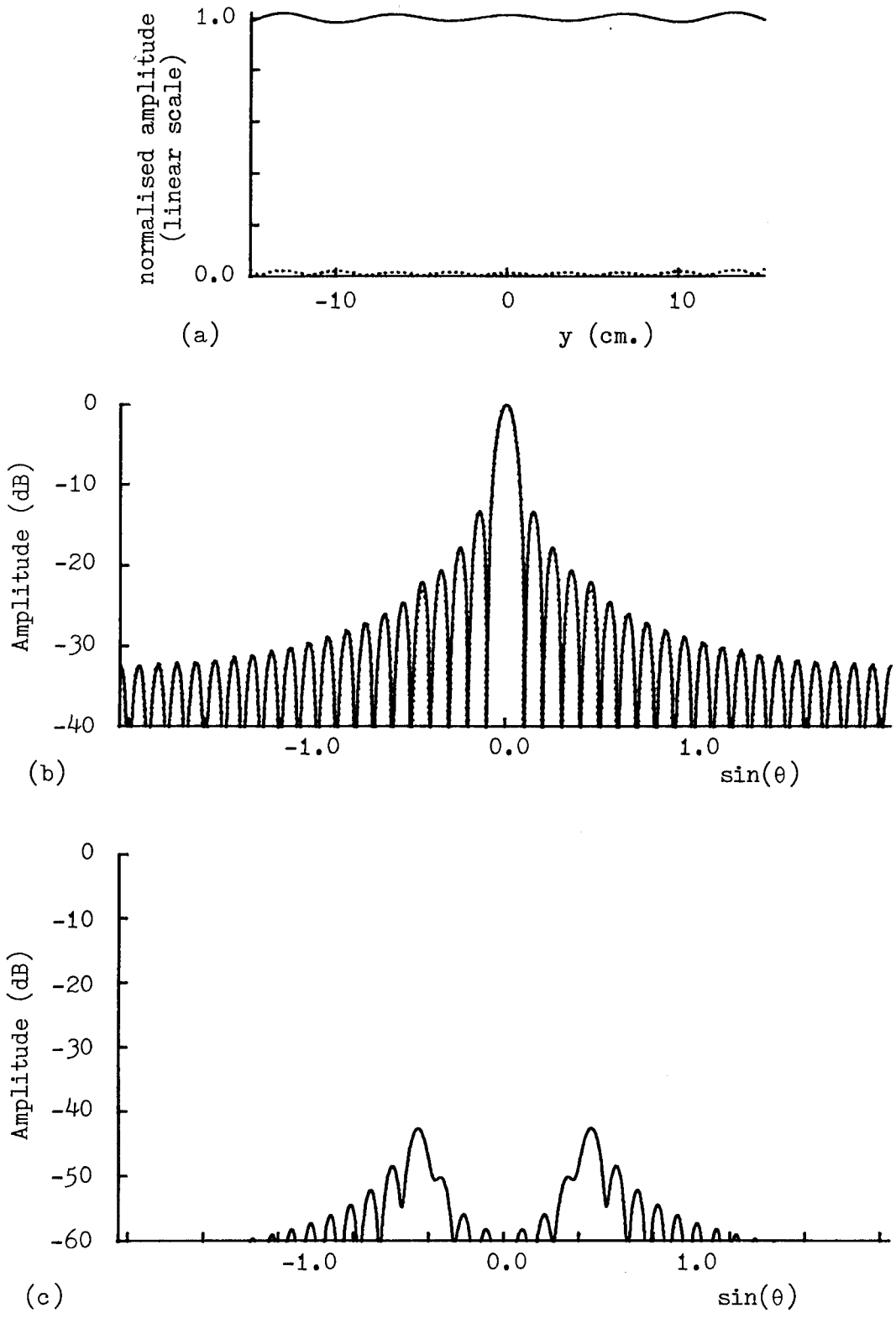

Fig. 5.37. (a) 30cm. synthesised plane wave amplitude (solid) with amplitude of non-ideal residue shown as dotted. Before iteration 3. (b) Fourier transform of plane wave (solid) compared with ideal (dotted). (c) Fourier transform of non-ideal residue of plane wave.

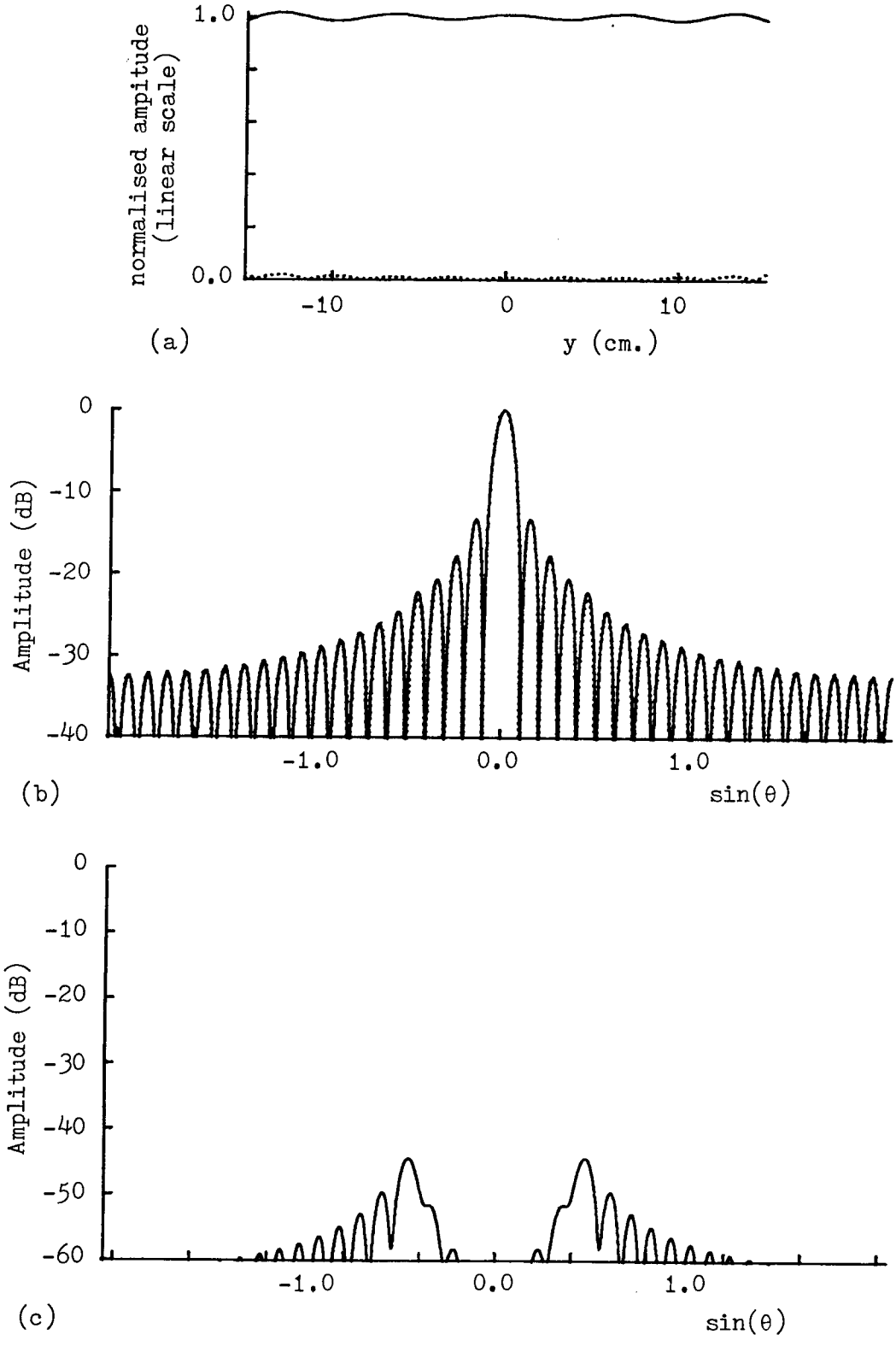

Fig. 5.38. (a) 30cm. synthesised plane wave amplitude (solid) with amplitude of non-ideal residue shown as dotted. Before iteration 6. (b) Fourier transform of plane wave (solid) compared with ideal (dotted). (c) Fourier transform of non-ideal residue of plane wave.

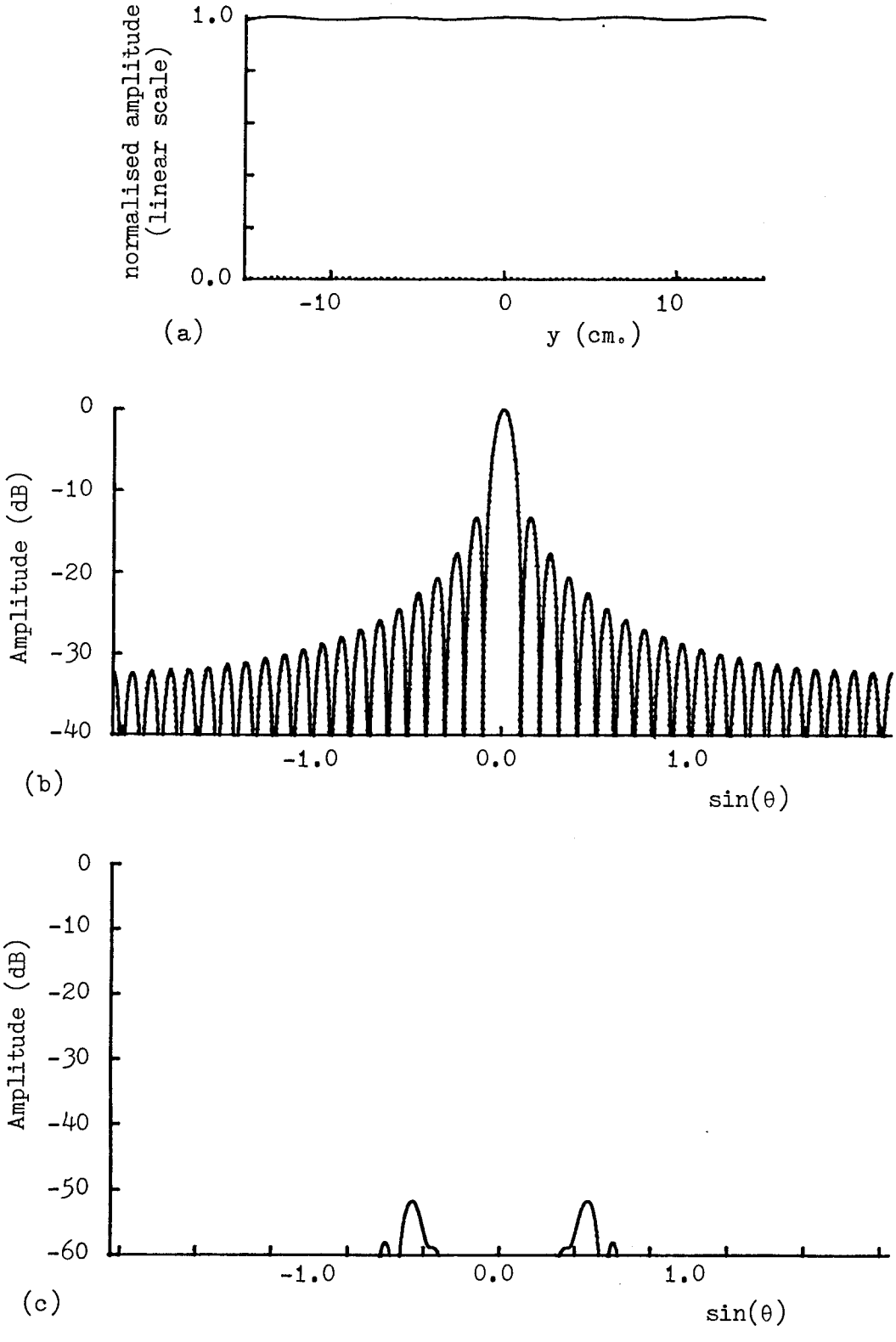

Fig. 5.39. (a) 30cm. synthesised plane wave amplitude (solid) with amplitude of non-ideal residue shown as dotted. Before iteration 30. (b) Fourier transform of plane wave (solid) compared with ideal (dotted). (c) Fourier transform of non-ideal residue of plane wave.

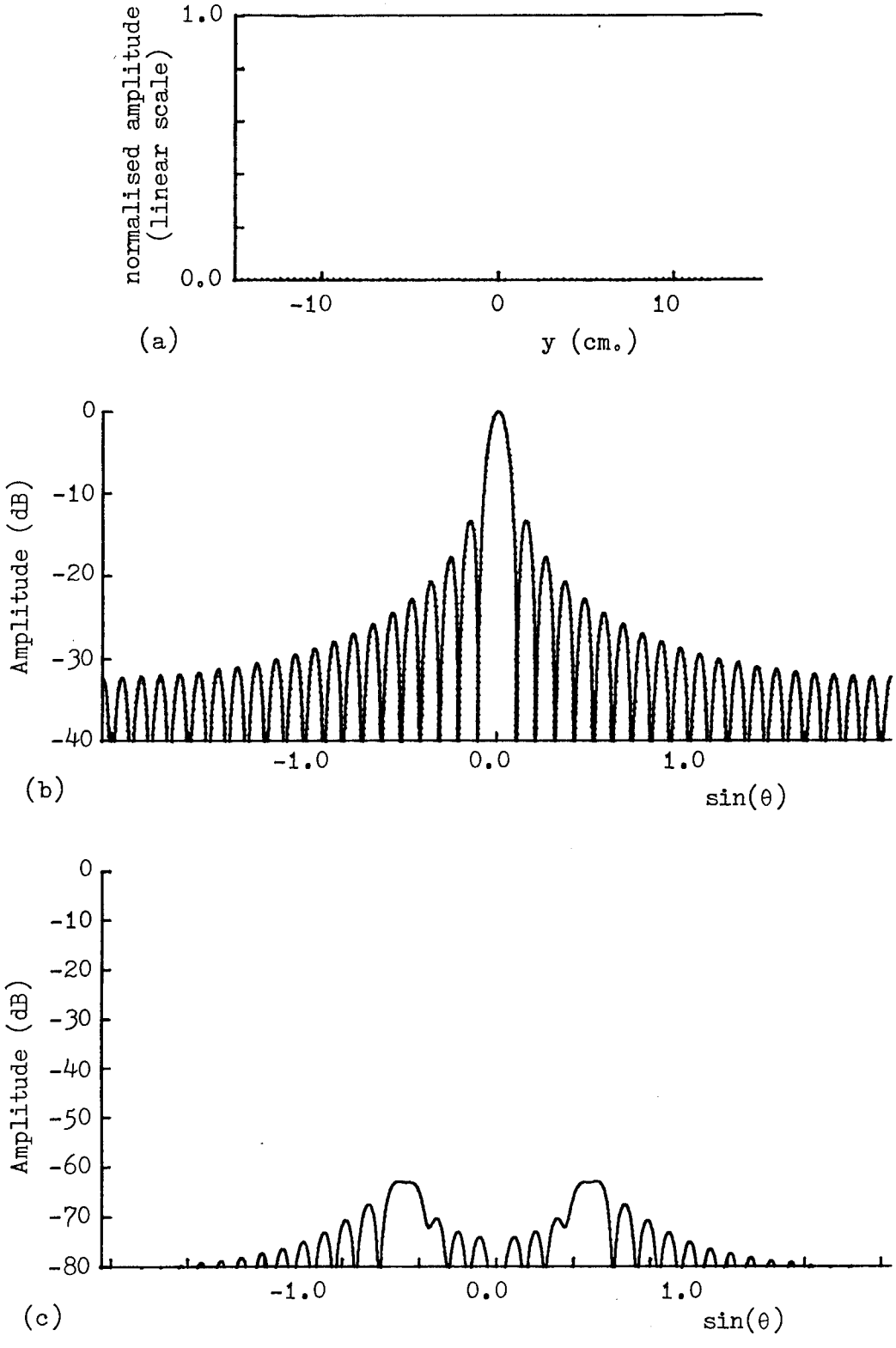

Fig. 5.40. (a) 30cm. synthesised plane wave amplitude (solid) with amplitude of non-ideal residue shown as dotted. Before iteration 80. (b) Fourier transform of plane wave (solid) compared with ideal (dotted). (c) Fourier transform of non-ideal residue of plane wave - note 80dB range compared with 60dB range of earlier figures.

weighting function, it is believed that the convergence of the iteration towards the optimum weighting function will be slower because of the relatively fewer degrees of freedom available for removing the edge effects.

5.4 Frequency Tolerance of the Weighting Function

The synthesised plane wave, over 50cm, due to a 29-point weighting function, spacing 2.5^{o}, measurement range 1.0m, frequency 10GHz, has already been shown as Fig. 5.22. The weighting function is, however, not restricted to use at exactly the frequency for which it was designed. To determine the frequency band over which the weighting function might be usable, the plane wave was examined with the same weighting function used at a range of frequencies. The different frequencies together with a summary of the effects upon the synthesised plane wave are as follows:

(a) 9.5GHz (Fig. 5.41)

Little effect on plane wave amplitude but a slight phase curvature is introduced.

(b) 9.5GHz (Fig. 5.42)

Effects as for (a) but slightly more pronounced.

(c) 9.0GHz (Fig. 5.43)

Still little effect on plane wave amplitude but greater phase curvature.

(d) 10.2GHz (Fig. 5.44)

Effects of a similar order to those in (a) but inverted phase curvature.

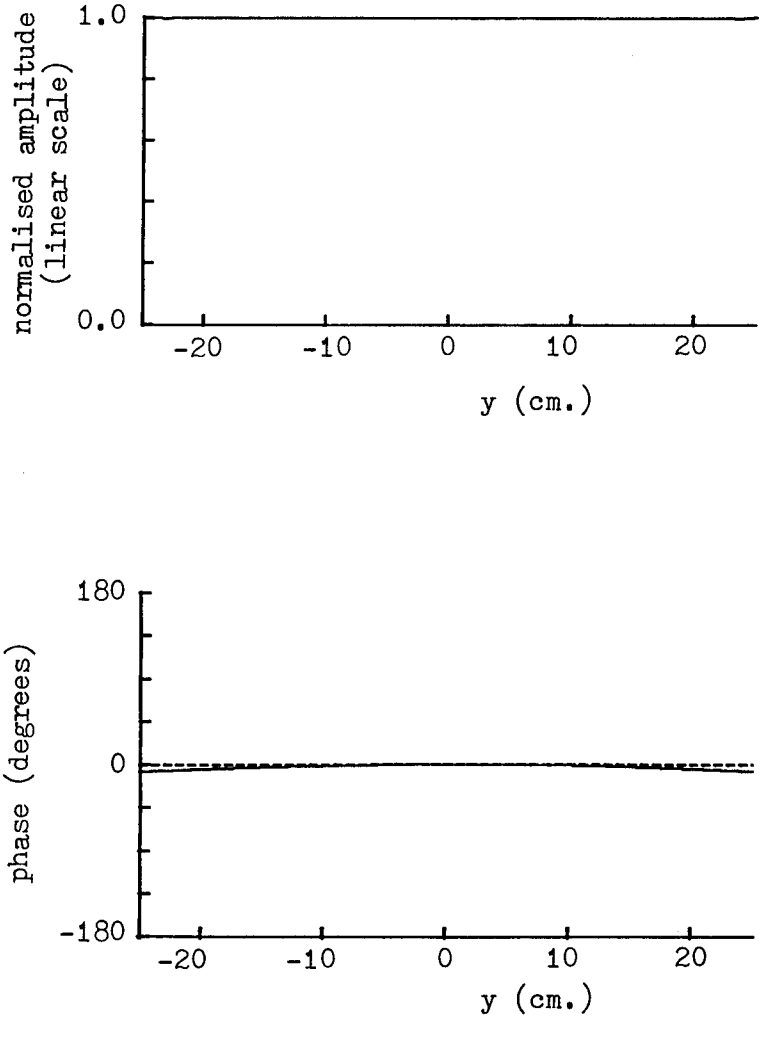

Fig. 5.41. Synthesised plane wave due to 29-point weighting function (as Fig. 5.22) but at the incorrect frequency of 9.8GHz.

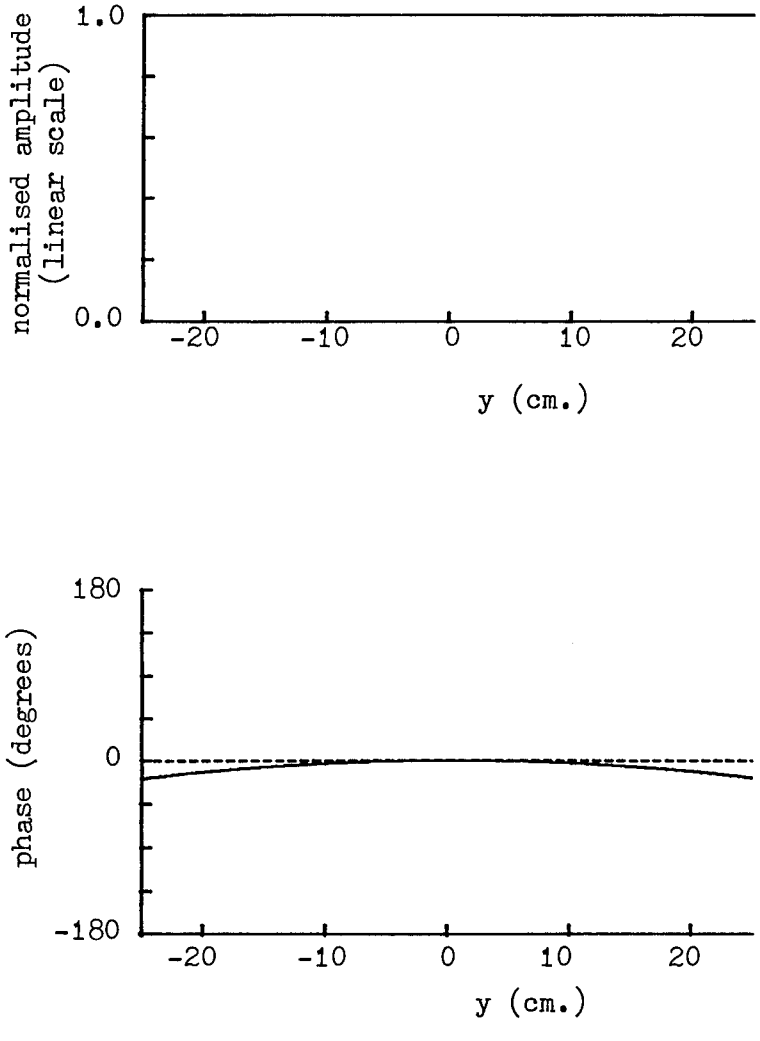

Fig. 5.42. Synthesised plane wave due to 29-point weighting function but at the incorrect frequency of 9.5GHz.

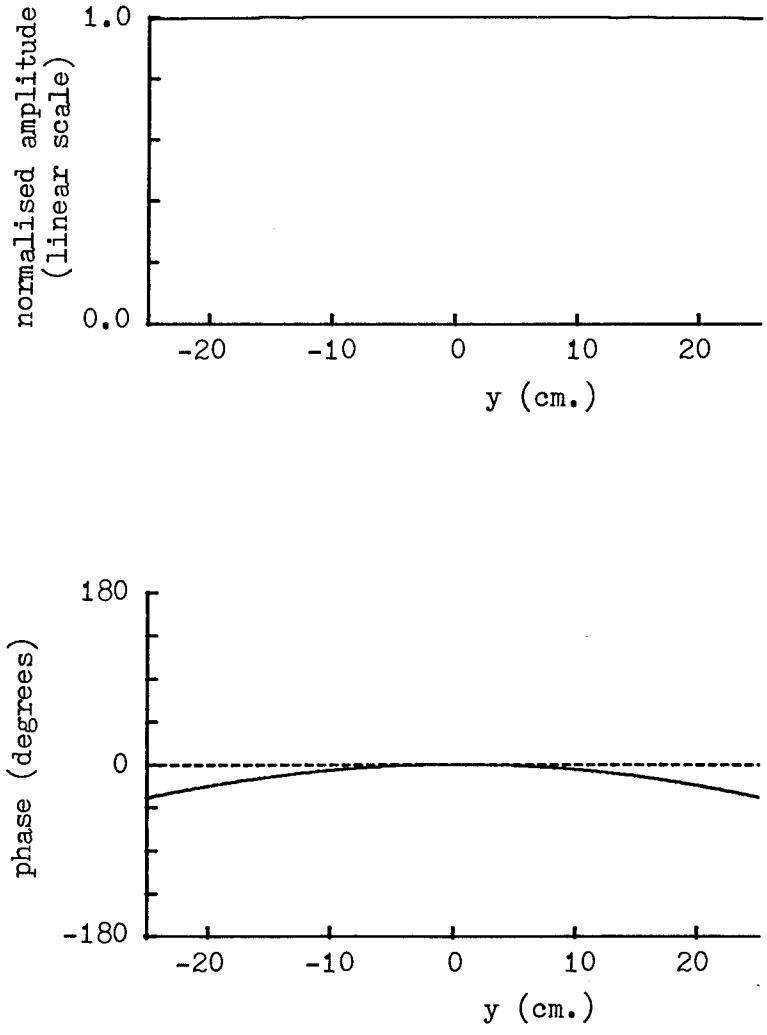

Fig. 5.43. Synthesised plane wave due to 29-point weighting function but at the incorrect frequency of 9.0GHz.

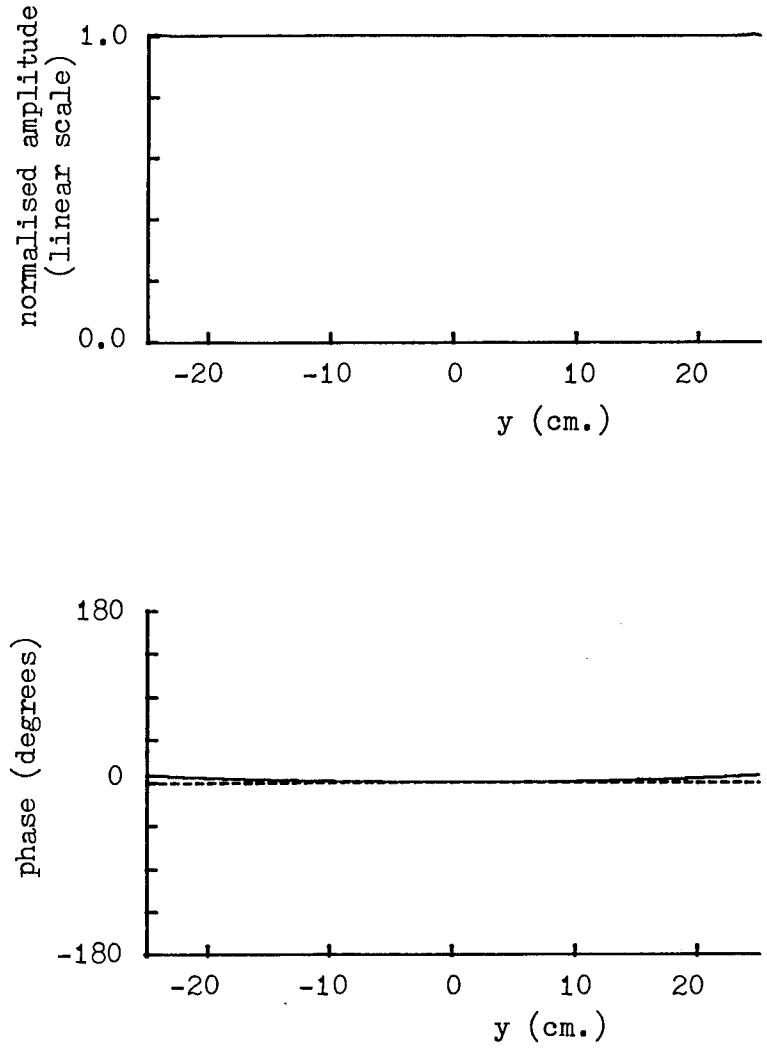

Fig. 5.44. Synthesised plane wave due to 29-point weighting function but at the incorrect frequency of 10.2GHz.

(e) 10.5GHz (Fig. 5.45)

Increased phase curvature.

(f) 11.0GHz (Fig. 5.46)

Effects more severe than (e) and the phase curvature is slightly greater than observed in (c).

The classical Rayleigh range ($2D^2/\lambda$) criterion for far-field measurement is defined as the distance at which the edge phase taper reaches 22.5^{o} for a boresight measurement. It is possible to calculate an equivalent measurement range for the edge phase taper in each of the above cases and this can then be compared with the Rayleigh range. The edge phase tapers and equivalent measurement ranges in each case are listed in Table 5.1. From examination of these values and comparison with the Rayleigh range of 16.8m, it may be concluded that the same weighting function may be used over a frequency range of approximately 1GHz yielding a synthesised plane wave at least as good as (and generally considerably better than) that produced by a point source radiator at the Rayleigh range.

5.5 Range/Wavelength Scaling

It is possible to extend the range of usage of a given weighting function by scaling all the linear dimensions (measurement range, width of synthesised plane wave, etc.) in proportion to the wavelength. This is easy to demonstrate graphically. The synthesised plane wave as shown in Fig.5.22 is displayed on a wider scale in Fig. 5.47. When the frequency (alone) was altered to 12.5GHz, as shown in Fig. 5.48, the phase, in particular, of the plane wave

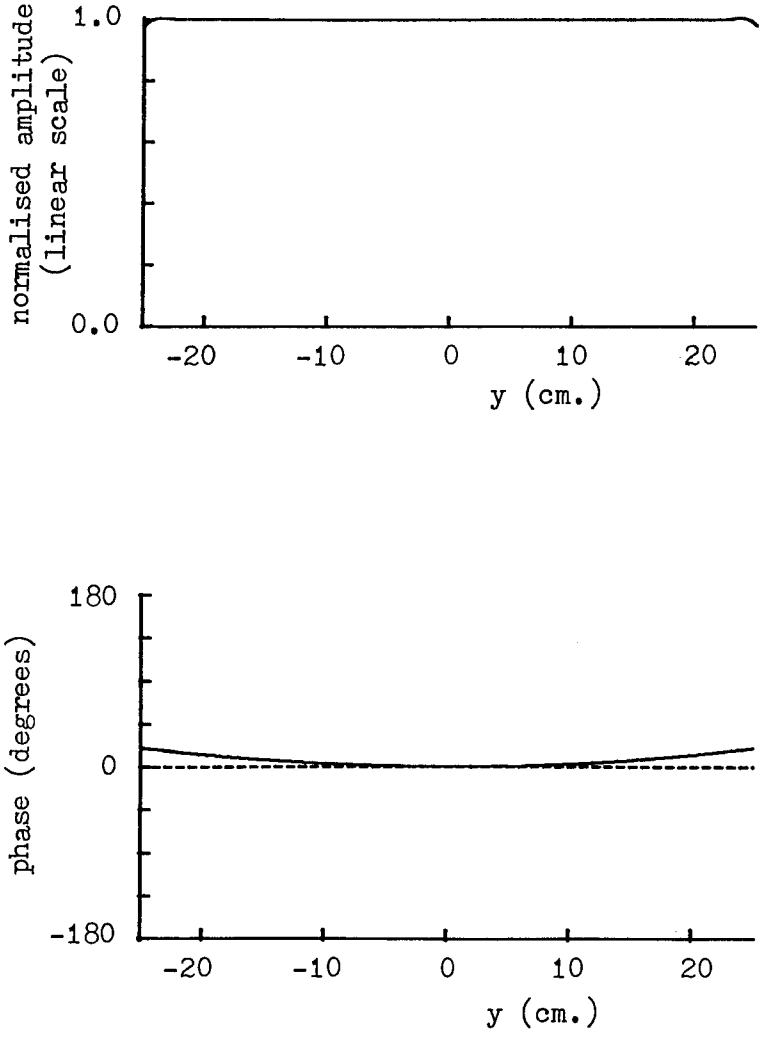

Fig. 5.45. Synthesised plane wave due to 29-point weighting function but at the incorrect frequency of 10.5GHz.

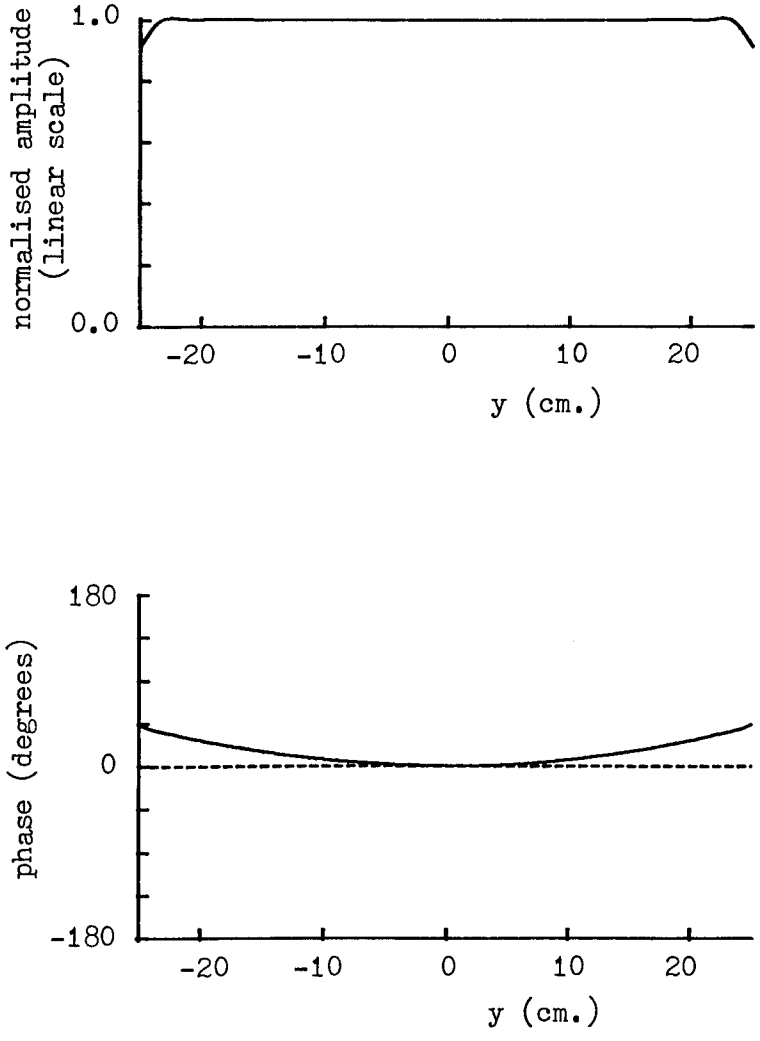

Fig. 5.46. Synthesised plane wave due to 29-point weighting function but at the incorrect frequency of 11.0GHz.

Table 5.1

Edge phase taper and equivalent measurement range for plane wave due to weighting function used at a range of frequencies

f(GHz)	Edge phase taper (degrees)	Equivalent R
9.0	36.0	10.4m
9.5	19.5	19.2m
9.8	6.0	62.5m
10.0	0.0	∞
10.2	10.5	35.7m
10.5	25.5	14.7m
11.0	48.0	7.8m

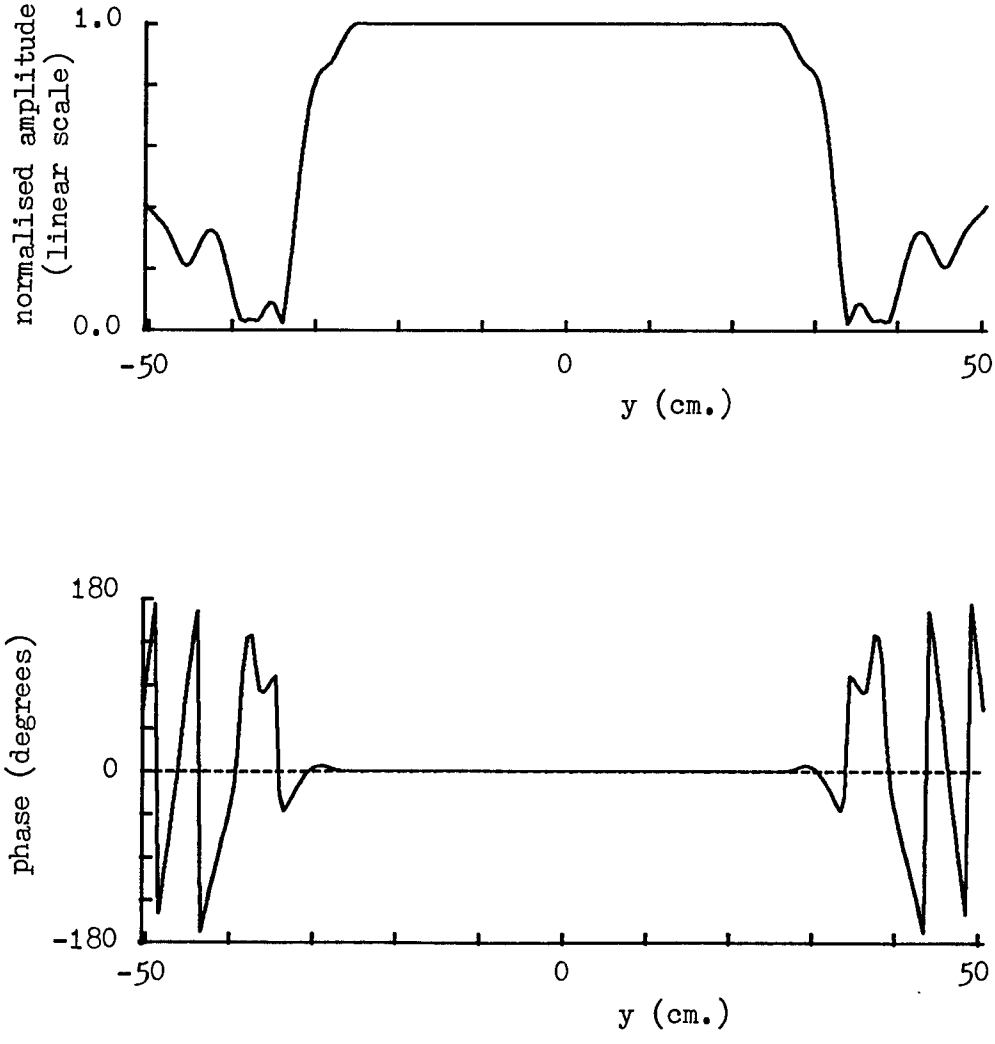

Fig. 5.47. Synthesised plane wave due to 29-point weighting function (as Fig. 5.22 but displayed over a wider area).

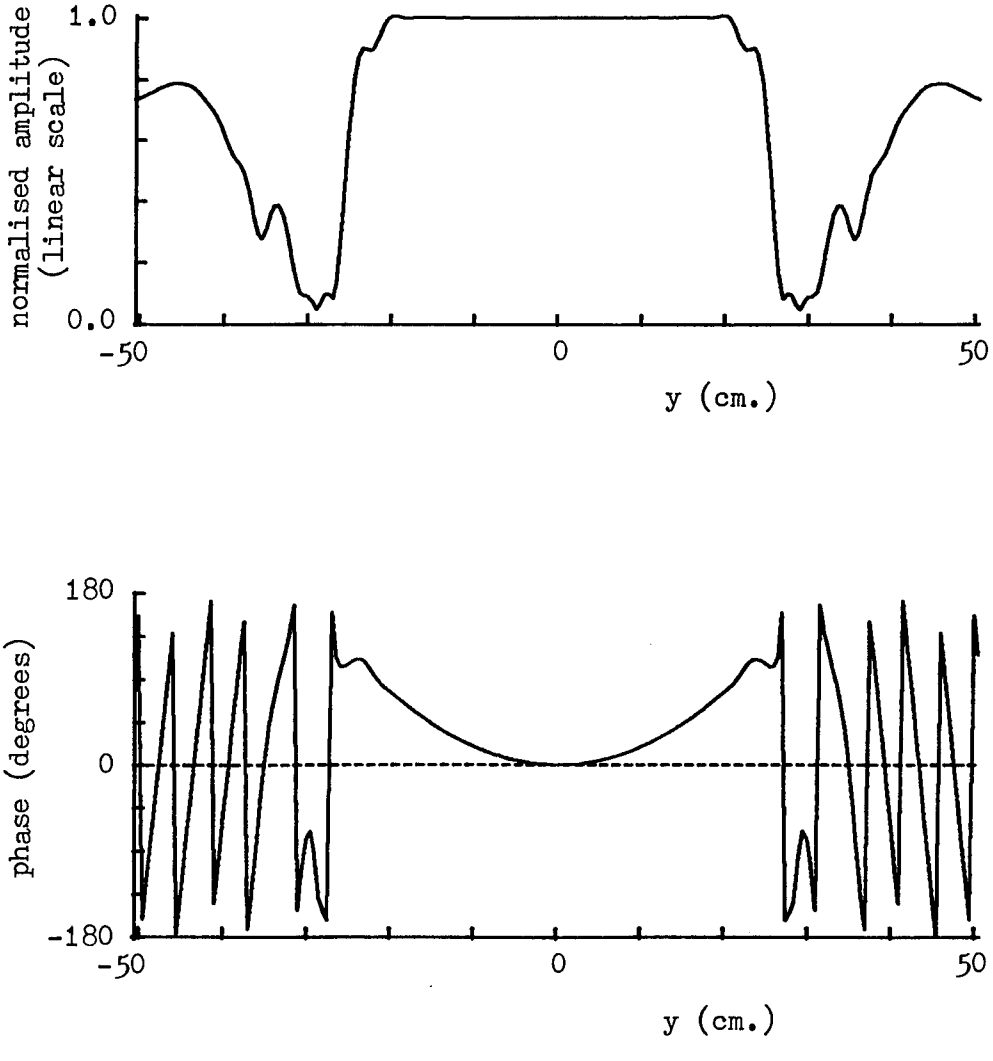

Fig. 5.48. Synthesised plane wave due to 29-point weighting function but at the incorrect frequency of 12.5GHz.

acquired a pronounced curvature. By scaling down the measurement range to 80cm, the plane wave quality, shown in Fig. 5.49, was restored (the change in amplitude and the phase offset are merely due to the way the probe was initially defined and to the fact that no new normalisation was carried out). As an extreme example, the frequency was changed to 20GHz and Fig. 5.50 indicates that the plane wave had broken down badly particularly in phase. A reduction of the measurement range to 50cm, however, restored the plane wave quality over, now, a 25cm area (Fig. 5.51). Lastly the frequency was reduced to 5GHz whereupon the synthesised plane wave was seen to exhibit a significant taper and, again, phase breakdown (Fig. 5.52) but a move to 2m measurement range once again restored the quality (Fig. 5.53).

It should be noted that the above scaling process depends on the characteristics of the measurement probe not altering in any significant way under the frequency change. Certain types of probe, for instance some scalar feeds, have the useful property of not changing their radiation patterns over restricted frequency ranges so that this might be feasible in such a case. Otherwise, a practical measurement facility might consider having a number of scale-model probes for use at different frequencies but, whatever the method used, the end result must be the maintenance of the probe's radiation characteristics. If this can be achieved then there is no theoretical reason why the bandwidth of a given weighting function cannot be regarded as effectively infinite.

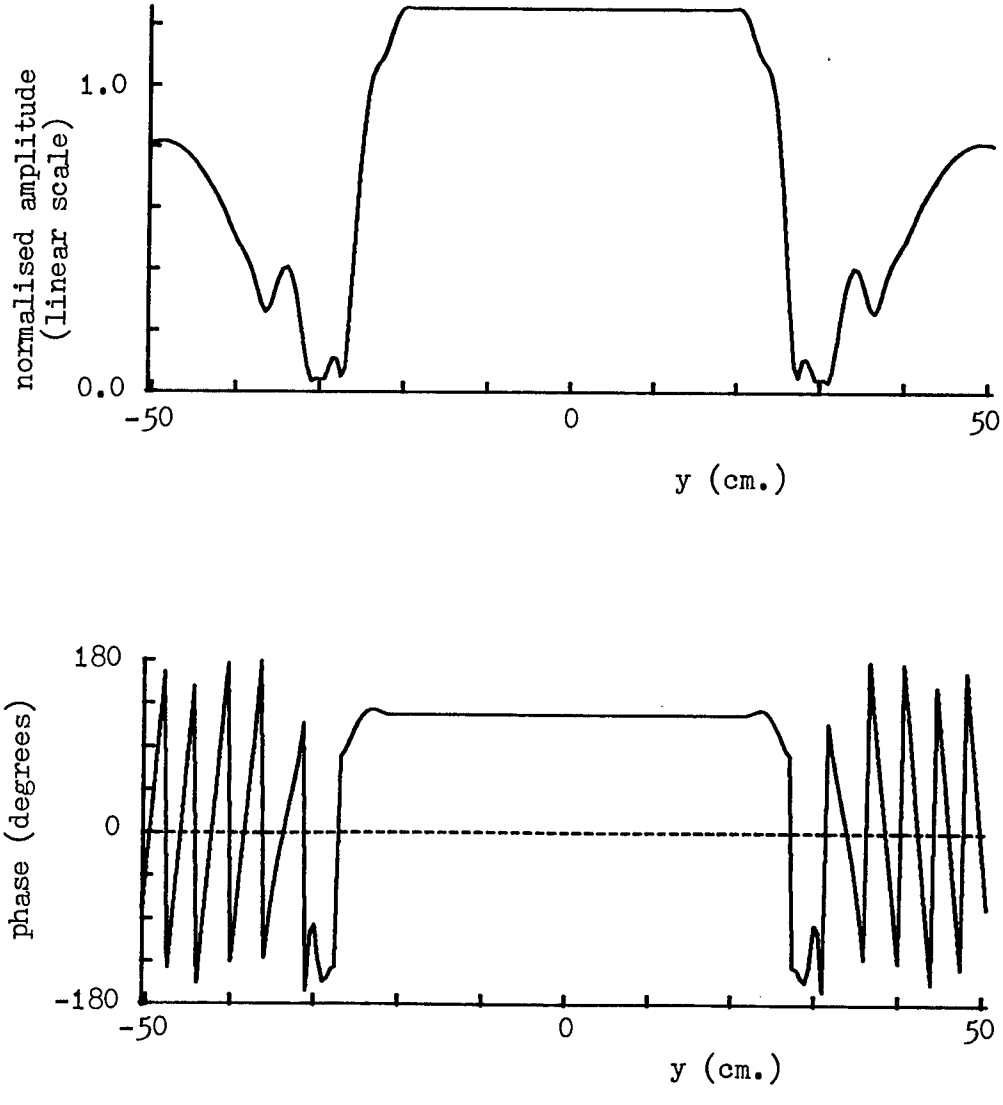

Fig. 5.49. Synthesised plane wave due to 29-point weighting function at the incorrect frequency of 12.5GHz. but with the measurement radius scaled in proportion to λ (to 80cm.).

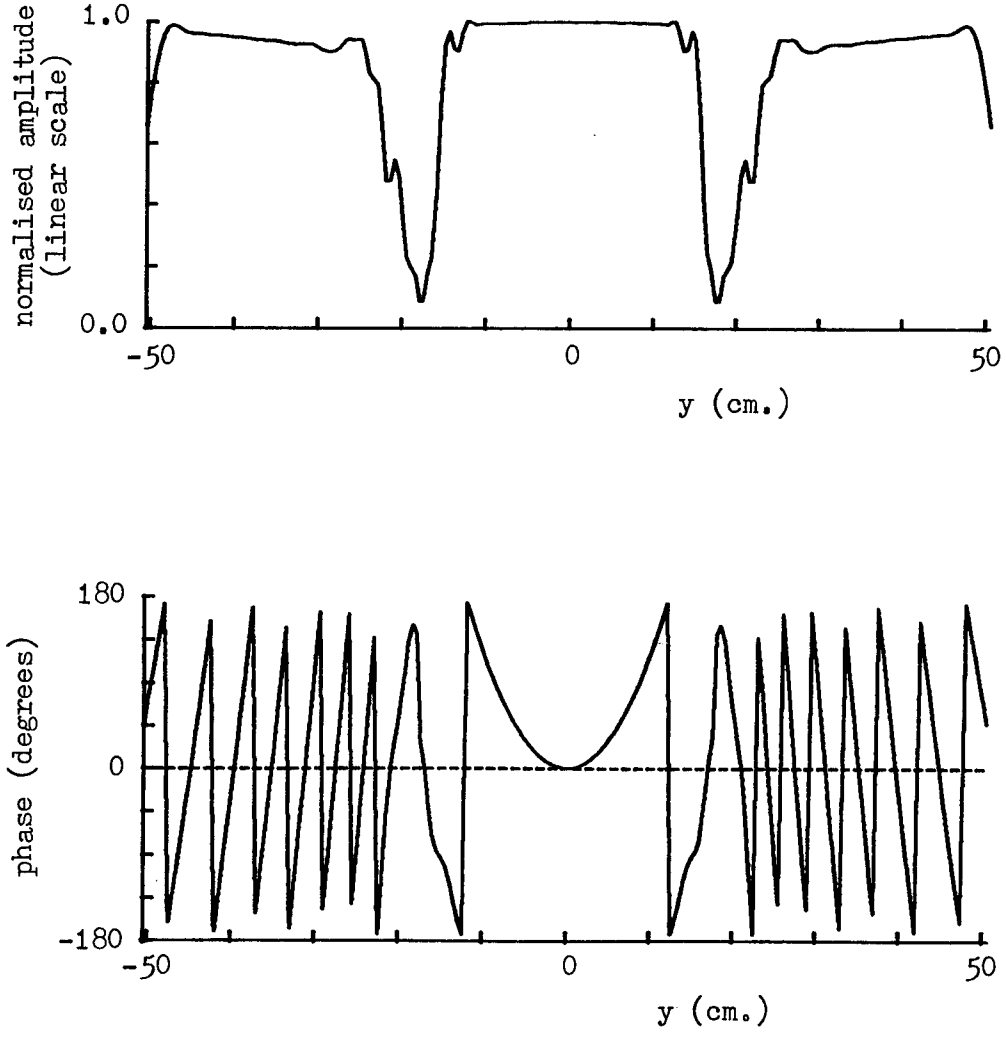

Fig. 5.50. Synthesised plane wave due to 29-point weighting function but at the incorrect frequency of 20.0GHz.

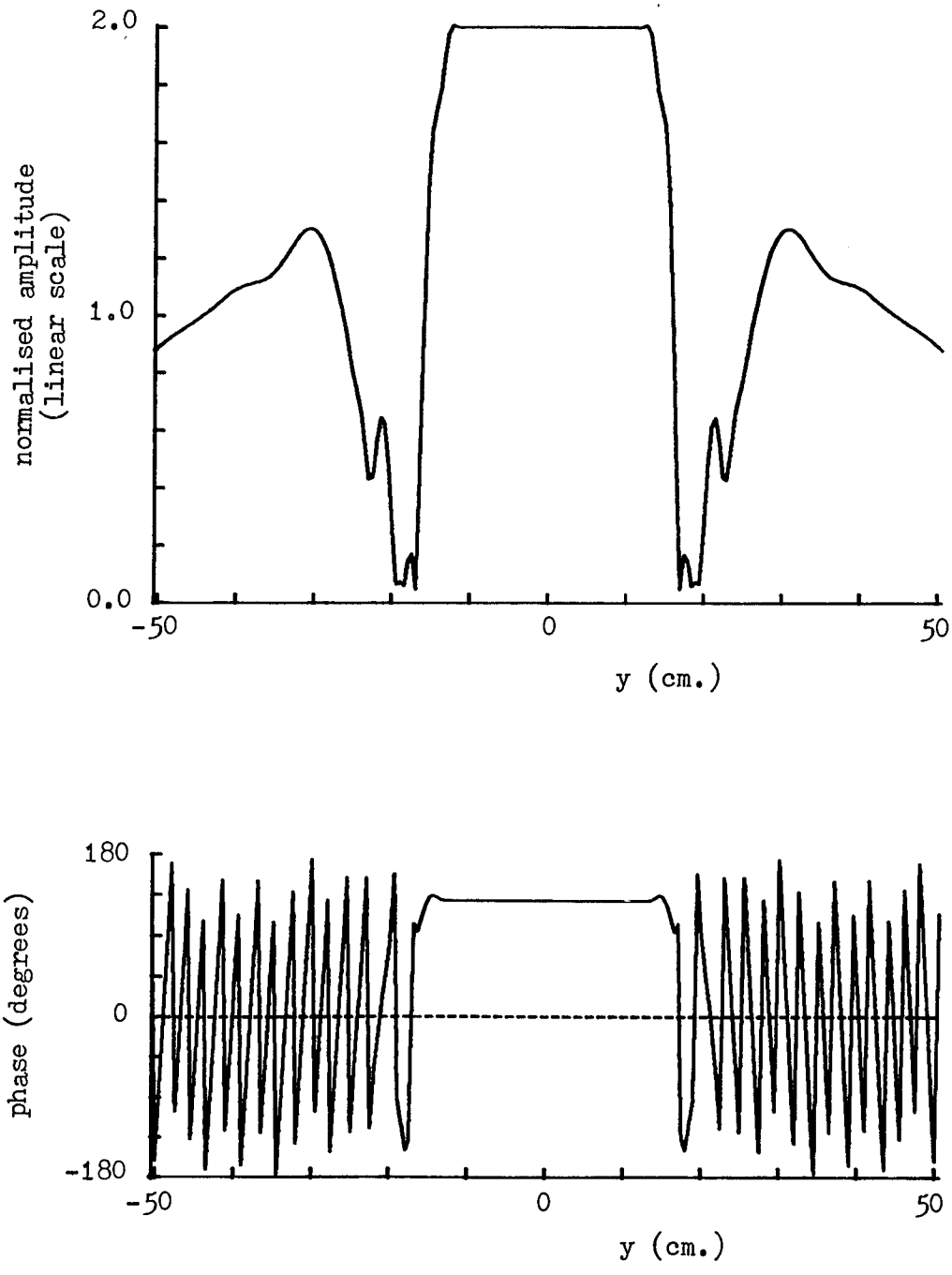

Fig. 5.51. Synthesised plane wave due to 29-point weighting function at the incorrect frequency of 20.0GHz. but with the measurement radius scaled in proportion to λ (to 50cm.).

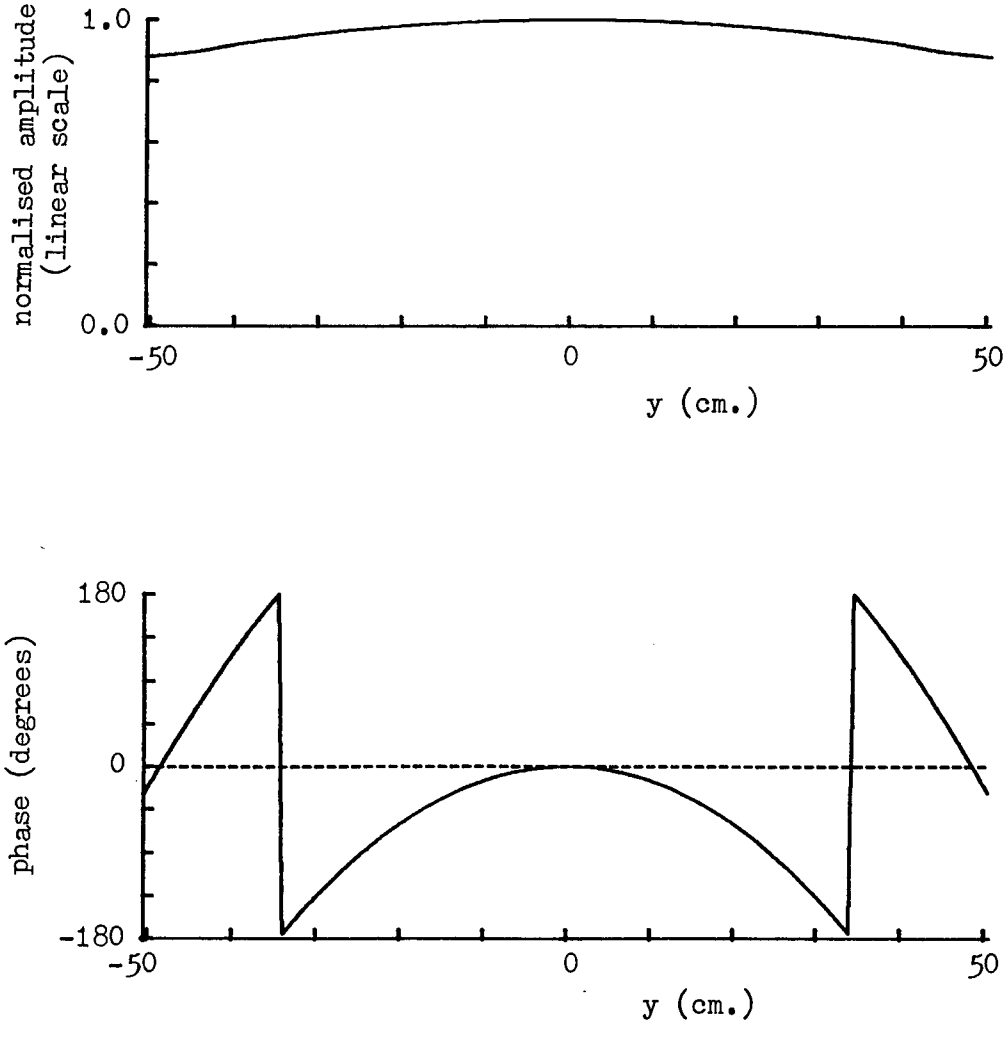

Fig. 5.52. Synthesised plane wave due to 29-point weighting function but at the incorrect frequency of 5.0GHz.

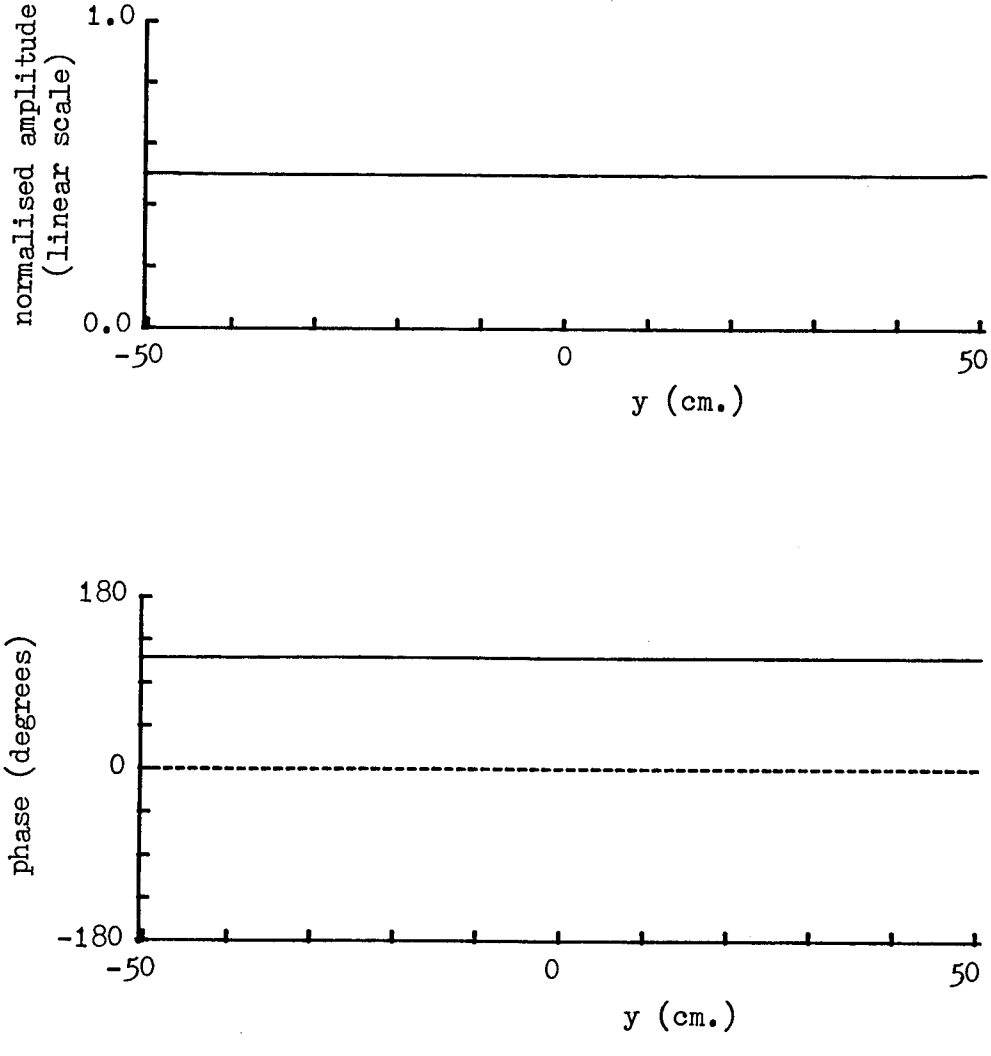

Fig. 5.53. Synthesised plane wave due to 29-point weighting function at the incorrect frequency of 5.0GHz. but with the measurement radius scaled in proportion to λ (to 2.0m.).

6. THREE-DIMENSIONAL VERIFICATION

To verify the technique in its full three-dimensional configuration a 45cm reflector antenna was evaluated at X-band and this chapter is concerned primarily with describing the experiments and the results. Before carrying out the experiments, however, it was necessary to set up the measurement equipment in the anechoic chamber at the University of Sheffield antenna test range and the details of this are discussed first.

6.1 Antenna Test Range and Equipment

The Departmental antenna test range is located on a fairly rugged site at Harpur Hill near Buxton in Derbyshire about 30 miles from Sheffield. The site is quite elevated and remote so that interference from terrestrial sources is at a relatively low level. There are a number of possible measurement ranges available, the longest of these being across a valley to a distant hillside on which a transmitter may be located at a distance of up to 3 miles from the Departmental buildings, antenna tower, etc. Within the site, various ranges are available (using hillside locations, etc.) of up to about 150m and one of particular relevance gives a measurement range of approximately 30m. This range stretches between the roof of the main Departmental bunker and a metal tower at a similar height (about 12ft above ground level) built originally to support a fairly heavy duty Scientific Atlanta (S.A.) elevation over azimuth positioner system (not used for these experiments). This was the range used for the far-field measurements of the 45cm reflector.

The near-field measurements on the antenna were performed in a small radio-anechoic chamber located inside the main bunker (along with the control room). The chamber is about 8m in length and is of square cross-section tapering from about 2.5m square at the positioner end to about 60cm square. The chamber is lined with Plessey absorbing materials types AF20 to AF24 along the sides and type AF50 on the large rear wall. A small azimuth turntable (S.A. type 5103) was originally mounted on a pair of steel rails allowing 1m longitudinal adjustment within the quiet zone.

For the present measurement programme various new items of equipment were purchased and others designed and built in-house. To obtain the complete spherical scan capability another positioner was required to mount over the existing azimuth turntable. To fulfil this requirement an S.A. type 56060 polarisation positioner was chosen. A rigid mounting unit was then designed to hold the polarisation positioner on the azimuth turntable. The design was complicated by the 90kg load limit on the azimuth turntable but a suitably rigid construction was achieved. This may be seen in Fig. 6.1.

Related to the rigidity of the system, it was also found that the existing support rails were too flexible and these were replaced with a new structure of heavy duty steel beams bolted to the floor and cemented in place.

On the probe side, a scalar feed had recently been constructed within the Department, for use at 11.7GHz in another project and it was decided that this would form a suitable device with a smoothly varying and therefore easily defined radiation pattern. In addition it possessed the desirable attribute of circular symmetry. Behind the probe,

Fig. 6.1. The positioning system showing azimuth positioner, positioner tower, polarisation positioner and 45cm. reflector antenna mounted in place.

some equipment for selecting one of two orthogonal probe polarisations was required. For this purpose, an Andrew Antennas model 64100A-107 dual polarised circular to rectangular waveguide transition was selected. This item has a specified frequency bandwidth of 10.7GHz to 11.7GHz.

In order to switch between the two ports of the waveguide transition, an R.F. switch was necessary and the Hewlett Packard 33311B coaxial switch was considered suitable with bandwidth from D.C. to 18GHz, very high port-to-port isolation (typically in excess of 100dB at X-band) and with the particularly useful property of internal termination of the ungated R.F. port in 50Ω to avoid mismatch and consequent reflection problems. The probe was selected to be the transmitting antenna and the microwave source used was a Gunn diode delivering approximately 10mW at a frequency of 11.7GHz. Fig. 6.2 shows the probe with dual polarised transition behind it and the microwave switch is just visible on the photograph. A cable reference was taken to the receiver from the Gunn diode via a directional coupler.

Careful setting and alignment of the mechanical subsystem was, of course, a prerequisite to acquiring the data and this will be outlined a little later. Next, however, is given a brief description of the parts of the data acquisition and control subsystems held within the control room of the test facility.

Basic control of the S.A. positioners was by means of two model 4111 position controllers. These are essentially manual control devices but some in-house modifications meant that a remote drive on/off control function could be exercised

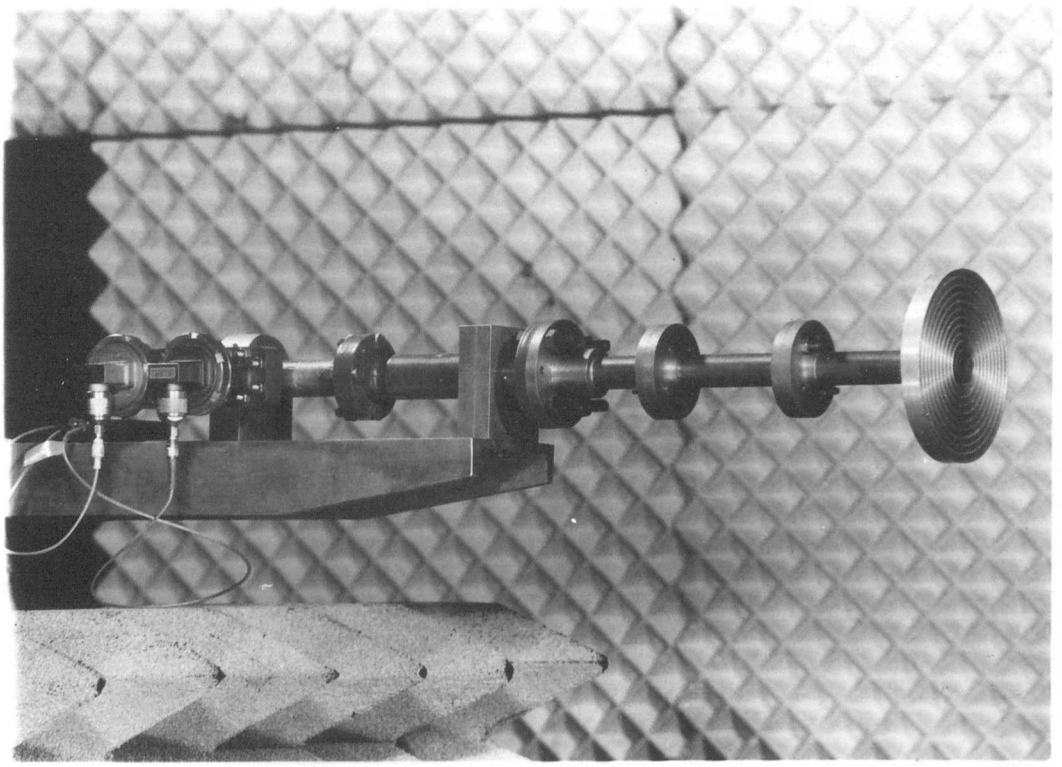

Fig. 6.2. The probe assembly before coating in absorber. The scalar feed probe is on the right, the dual polarised waveguide transition towards the left and the coaxial microwave switch is just visible on the extreme left.

from a purpose built remote control unit commanded by a Ferranti Argus 600 minicomputer, a very basic machine with only 2k-bytes of memory and a very limited instruction set. The position information was derived from an S.A.1842A synchro-to-digital position indicator connected, again under computer control, to the selected positioner (only one positioner can be operated at any one time).

In addition to scan control, the Argus minicomputer controlled the data acquisition. The polarisation of the data was selected by the computer via a locally designed and built drive unit for the Hewlett Packard R.F. switch. This unit incorporated the appropriate logic functions for computer control together with the drive circuitry for the switch and an electromechanical counter to keep a tally of the total number of switching operations performed. For the far-field measurements, this was later slightly modified to incorporate a "drive boost" facility to enable the switch to be driven through in excess of 100m of cable.

The receiver used was an S.A.1754 two-channel phase and amplitude receiver (one signal channel plus reference channel) and the preliminary scans taken to verify the operation of the R.F. and mechanical aspects of the system were recorded on an S.A.1523 (rectangular) chart recorder. For the data scans themselves, the analogue signals from the receiver were converted to digital form by an S.A.1833A amplitude ratiometer and an S.A.1822A phasemeter (to a resolution of 0.1dB and 0.1^{o}) and output onto punched paper tape by the Argus 600.

6.2 System Alignment

It is important that the system should be set-up mechanically as accurately as possible to enable good quality data to be obtained. This has various aspects:

(a) Probe position and pointing accuracy.

The probe should point accurately towards the origin of the coordinate system (the centre of rotation). It should be at the same height as the polarisation axis and the distance from the probe to the centre of rotation should be known.

(b) Orientation and intersection of positioner axes.

The axis of the azimuth turntable should be truly vertical, the axis of the polarisation turntable should be truly horizontal and the two axes should intersect accurately in space.

(c) Positioner pointing accuracy.

The system should be set up so that, when the azimuth positioner is set at 0^{o}, the axis of the polarisation positioner should be pointing at the centre of the probe.

The effects of these mechanical errors have been discussed to some extent in Chapter 5. Here, the methods used to avoid the errors are detailed.

For the setting-up procedure, five main items of equipment were used:

(1) A sensitive spirit level.

(2) A sharply pointed rod in a mounting device with a 4-screw fine lateral adjustment mechanism. The mounting device should have a base suitable for clamping onto the azimuth turntable (or similar surface) so that it can point along the vertical

azimuth axis with the polarisation positioner mounting unit in place. The length should be adjustable.

(3) Another sharply pointed rod in similar adjustable mounting unit with mounting holes suitable, this time, for the polarisation turntable to enable the rod to point along the horizontal polarisation axis. Spacers should be provided to hold the base approximately 2cm off the turntable. An angled viewing hole (approximately 1cm diameter) should be drilled in the base plate for a purpose which will be described below.

(4) A flat plate bearing a finely scribed cross at its centre with mounting holes suitable for the polarisation turntable.

(5) A precision optical level with fairly high magnification and crossed hair sights.

For the last item, a Sokkisha B1-C precision automatic level with 32x magnification (see Fig. 6.3) was purchased. Sensitive spirit levels were already available within the Department and the other devices were manufactured in the Departmental workshop.

6.2.1 The Alignment Procedure

The details of the procedure for setting-up the mechanical alignment of the system (which should be already assembled) are as follows:

(a) Ensure that the axis of the azimuth turntable is vertical. This is achieved by placing the sensitive spirit level on the turntable which is then set in motion. The mounting screws on the turntable base are adjusted until the bubble in the level remains stationary as the turntable rotates. It should

Fig. 6.3. The optical level used for system alignment.

be emphasised that the bubble does not have to be centred in the level (and in general will not be so) since the adjustment for a vertical turntable axis does not imply that the turntable face is exactly horizontal.

(b) Set the scribed cross of the metal plate to be on the axis of the polarisation positioner. The plate is mounted on the polarisation turntable which is then rotated. The centre of the scribed cross is viewed through the optical level (lined-up on the crossed hairs) and its position on the turntable adjusted until the centre of the cross appears to remain fixed in space as the turntable rotates.

(c) Set up the first of the pointed rods vertically so that the tip is on the axis of the azimuth turntable. The pointer is mounted approximately above the centre of the turntable and its length is adjusted so that its point is as nearly as possible level with (or fractionally below) the axis of the polarisation positioner. The pointer is then laterally adjusted until its tip appears fixed in space when viewed through the optical level.

(d) Set the tip of the second pointer on the axis of the polarisation positioner. The second pointer is mounted at the centre of the polarisation turntable over the scribed plate (using the spacers). The length is adjusted so that the point is almost coincident with the azimuth axis pointer. At this stage, it may be found that the length of the latter was set too great or too little. If so, this may be corrected but it will then be necessary to return to step (c) to check its lateral setting. The polarisation positioner is then set in motion (cautiously at first, lest the two points should

collide and damage one another - care should be taken for this possibility in the following two steps also) and the lateral position of the second pointer is adjusted in a similar manner to step (c) so that the tip lies on the polarisation axis. Fig. 6.4 illustrates this stage.

(e) Make the polarisation axis horizontal. This is the point at which the viewing hole in the base plate of the second pointer comes into play. The azimuth and polarisation positioners are rotated into such positions that the cross on the scribed plate is visible (careful lighting arrangements may be necessary at this point) through the viewing hole. The optical level is carefully adjusted to be at the same height as the centre of the cross and then panned horizontally to look at the polarisation axis pointer. The mounting screws of the polarisation positioner are adjusted to bring the tip of the pointer up to the same height. This adjustment may have changed the height of the scribed cross so that the procedure should be repeated several times until the tip of the pointer and the cross are at the same height.

(f) Make the axes intersect in space. The azimuth turn-table is rotated so that the polarisation axis pointer is viewed end-on. The position of the polarisation positioner is adjusted in the transverse direction until the tips of the two pointers almost coincide. If the two pointers are not close enough (or are so close that they are likely to touch) the length of one or both of the pointers may have to be adjusted in which case a return should be made to step (c) or (d), depending on which pointer(s) has been adjusted. Otherwise, when the transverse position of the

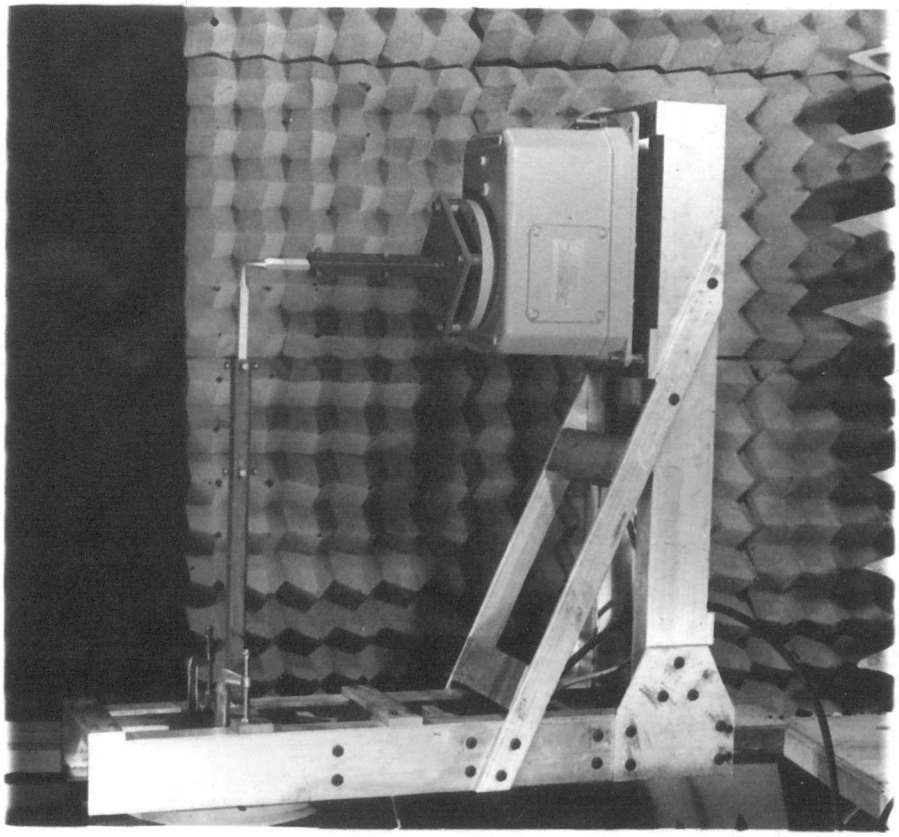

Fig. 6.4. The positioning system with alignment pointers in place.

polarisation positioner has been adjusted as precisely as possible (the polarisation axis pointer should appear vertically above the azimuth axis pointer), the other adjustments from step (e) should be re-checked and this procedure should be repeated until no further adjustment is required. If the distance between the pointer tips is 0.5mm, for example, and the vertical can be judged to an accuracy of 5^{o} (considerably better accuracy than this is to be expected) then the error introduced by this will be less than 0.05mm.

(g) Set up the probe height and horizontal. In many probe mounting systems, it is likely that the central line (in height) of the probe will be defined by the joining lines of the clamps. If not then a datum line should be marked out in advance. Whatever line is used, this should be adjusted to be horizontal and at the same height as the centre of rotation by the same panning technique as used in step (e).

(h) Set the probe azimuth. Again, the central line of the probe in the longitudinal direction may be obvious or it may be necessary to mark this out on the mounting bracket (front and back). Using whichever method is convenient, the centre of rotation is viewed from the end of the chamber and the probe pointing adjusted in azimuth until looking along the same line. If the probe azimuth adjustment mechanism cannot be guaranteed to give an accurate azimuth sweep, it may be necessary to return to step (g) to check the probe height and horizontal.

(i) The azimuth pointing of the scanning system is finely adjusted. The optical level is set up looking from behind the probe (as left by step h) along its axis to the centre of rotation. The polarisation axis pointer is removed and the azimuth zero is set up at the point where the centre of the scribed cross on the plate beneath lines up with the probe.

(j) The probe is inserted in the mounting bracket and its longitudinal position finely adjusted (it is assumed that the coarse setting up of the distance will have been done when the probe mounting system was originally positioned) to give the required measurement distance.

(k) All alignment equipment is removed and the scan may proceed.

It is anticipated that with the use of the technique described and the equipment presently being employed, setting accuracies of 0.1mm or better can be achieved.

6.2.2 The Test Antenna

The antenna under test was a 45cm diameter aluminium focal-plane reflector fed from what has been described as a "splash-plate" feed[37] which is similar to but much simpler than the feed described by Silver[38] and from the appearance of the data, has a somewhat mediocre performance. The antenna was mounted onto the polarisation turntable by four aluminium arms holding the dish at the perimeter. Additional support was supplied by the cable attached to the rear of the feed via the harmonic mixer. The test antenna is shown set up ready for scanning in Fig. 6.5.

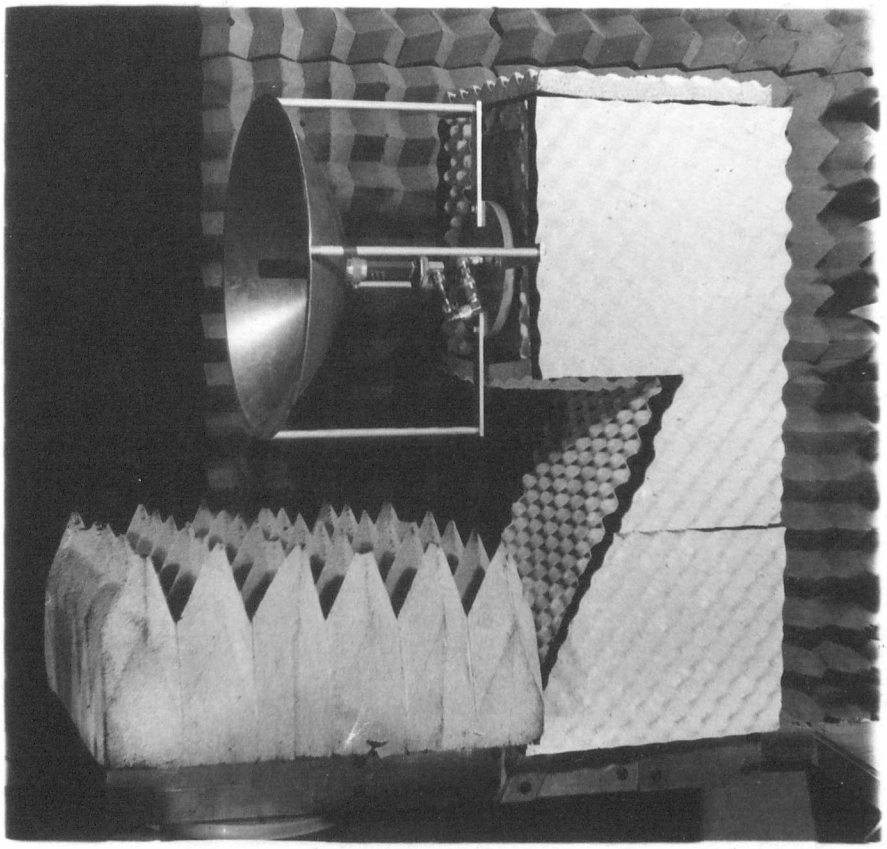

Fig. 6.5. The positioning system set up ready for a scan.

6.3 The Scans Performed

Three usable sets of data were obtained for the 45cm reflector. The first was a near-field set in the anechoic chamber at a measurement range of 1.1m. The scan consisted of a full hemisphere of data at 1.5^{o} intervals in both co-ordinates with 2 polarisations of data, amplitude and phase, at each point making a total of 29280 samples of amplitude and phase data. The time for the set was a little over four hours, thus the mean sampling rate was approximately 2 samples per second. The time includes, however, periods advancing (slowly) between individual scans when no sampling was taking place. The sampling rate was, in fact, a little under 2 samples per second for the region within 45^{o} of boresight and increased to nearly 2.5 per second for the region beyond 45^{o}.

The scan started from boresight (azimuth set to 0^{o}) and a full 360^{o} sweep of the polarisation positioner took place with sampling at 1.5^{o} intervals using probe polarisation 1. The polarisation scan was then repeated using probe polarisation 2. At this point, the setting of the azimuth turntable was incremented by 1.5^{o} and two further polarisation scans were performed. This process was repeated until the azimuth turntable was at 90^{o}.

In addition to the above scan (which will be termed the "main" scan) a number of calibration scans were performed. The purpose of these was firstly to obtain some indication of the repeatability of the results and therefore of the quality. Secondly, if any long term drift were found to be present in the main scan, it might be possible at least to attempt to calibrate it out. The calibration scans took the form of a set of cuts taken radially from boresight at 45^{o} intervals

of test antenna polarisation with both probe polarisations. Since each of these cuts was taken over a short period of time any slow drift occurring would show up minimally in the calibration scan but if it were compared with the corresponding cut extracted from the main scan, the slow drift present there would appear as a varying discrepancy across the cut.

The second set of data was another near-field set taken, this time, at a range of 1.5645m. The parameters of the main scan and the accompanying calibration scans are exactly as for the 1.1m set.

For a comparison with the near-field predictions, the remaining data were taken in the far-field on an outdoor 30m range as described in section 6.1. In this case the outer limit of the scans was 70.5^{o} but otherwise the parameters were the same thus indicating a total of 23040 sample points. The equipment for these outdoor measurements was set up with the probe (source) on the metal tower and the test antenna and positioners (taken from the anechoic chamber) set up on the bunker roof. This arrangement was chosen so that, as the scan progressed away from boresight, the test antenna would turn in azimuth to look away across a wide valley thus, it was hoped, avoiding the worst of the ground reflection problems. In addition, a wall of absorber was placed on the ground between the probe and the test antenna at the approximate specular reflection points.

In each case it was found to be of significant value to take preliminary scans in the form of two boresight scans of the polarisation positioner, one with each probe polarisation.

The results of these scans were logged on the chart recorder for immediate examination. The expected pattern in this case would be (a) cosinusuidal in form and (b) identical for each probe polarisation apart from a 90^{o} angular shift. Any significant variation in the first case would be looked upon with suspicion (dependant upon the nature of the antenna, for a paraboloidal reflector the cosinusoidal form might be expected to be quite good) while in the second instance any difference (apart from constant amplitude and/or phase shifts) would certainly indicate problems. Severe cable faults in both near and far-field systems were revealed in this way and corrected.

Figs. 6.6 to 6.11 are examples of the measured data showing H-plane co- and cross-polar cuts for each of the data sets (comparing main and calibration scans in each case). These are the raw data before any drift correction or independent normalisation and display the effects of quite severe drift, particularly in the case of the far-field set. The sources of the drift are discussed at a later stage but it is noted here that before using the near-field data for predictions of the far-field, they were corrected as far as possible for the amplitude and phase drift present. It is interesting to note that in the case of the 1.1m data set, the amplitude and phase drifted equally (about 0.9dB and 45^{o}) for both probe polarisations. In the data set obtained at 1.5645m, on the other hand, while the phase drift was similar (about 30^{o}) for both probe polarisations, only one polarisation exhibited any serious amplitude drift (2dB). This point will also be covered later.

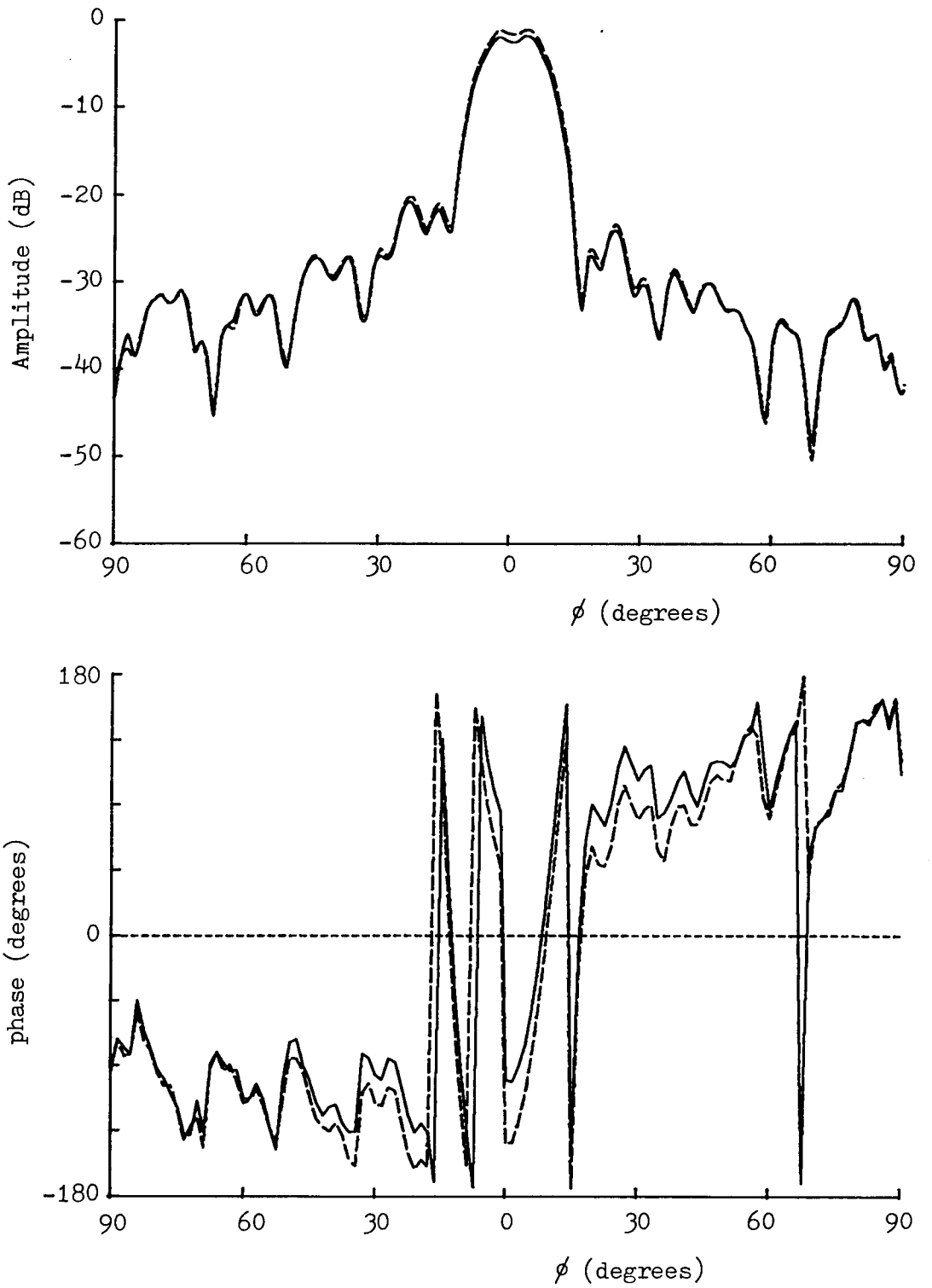

Fig. 6.6. Measured near-field H-plane co-polar data. Main scan is shown as solid and calibration scan as dashed. These data are for R = 1.1m.

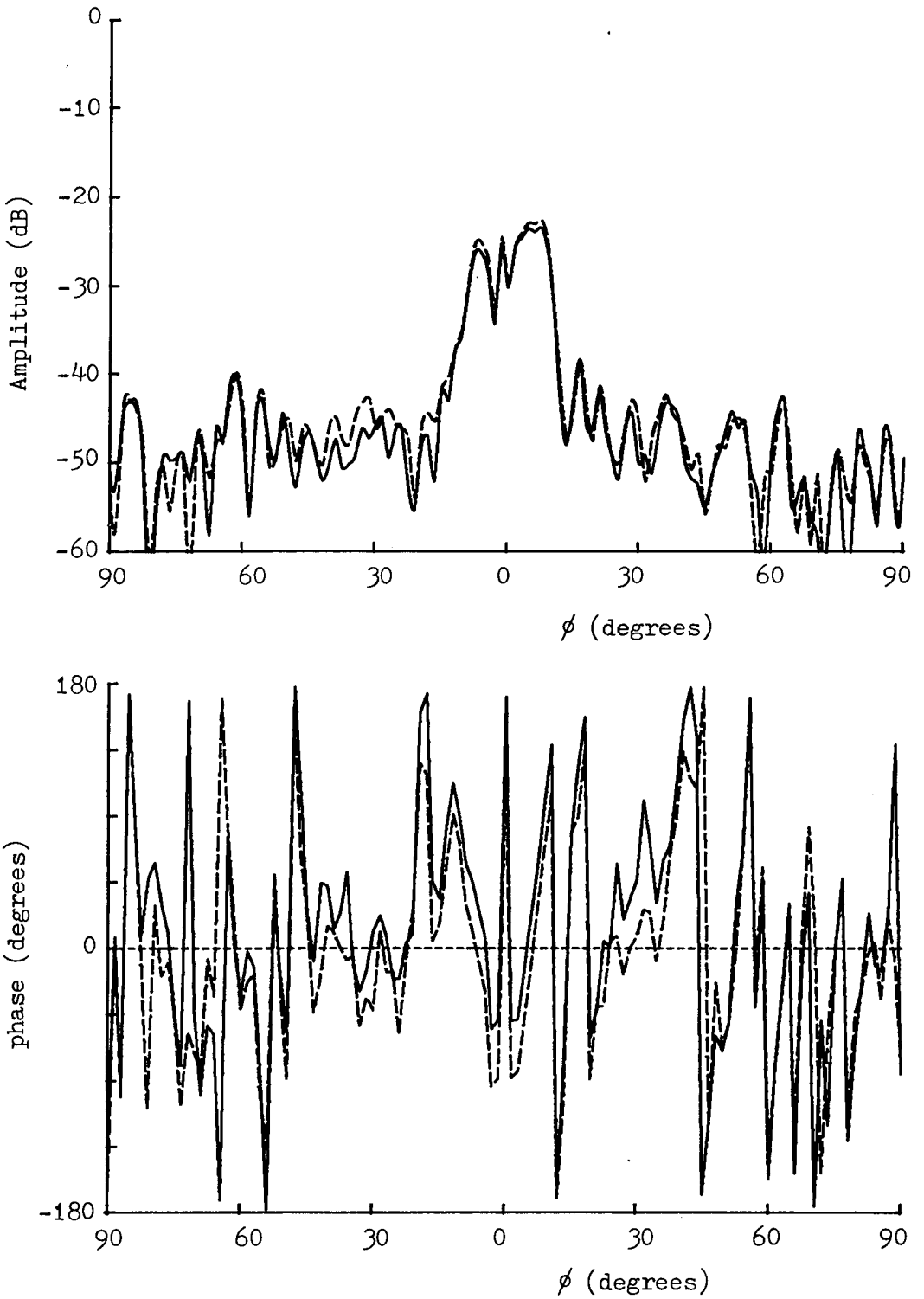

Fig. 6.7. Measured near-field H-plane cross-polar data. Main scan is shown as solid and calibration scan as dashed. These data are for R = 1.1m.

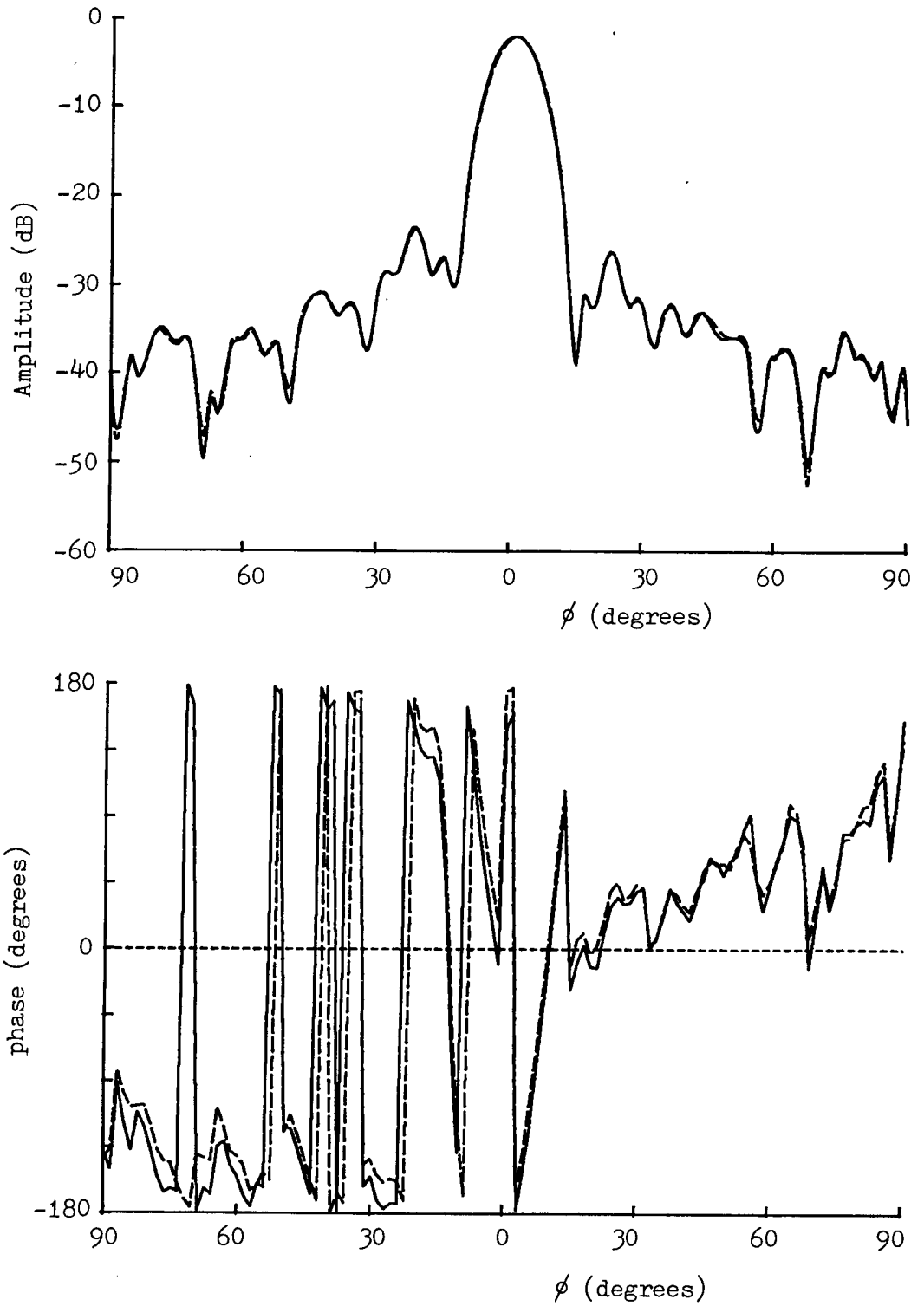

Fig. 6.8. Measured near-field H-plane co-polar data. Main scan is shown as solid and calibration scan as dashed. These data are for R = 1.5645m.

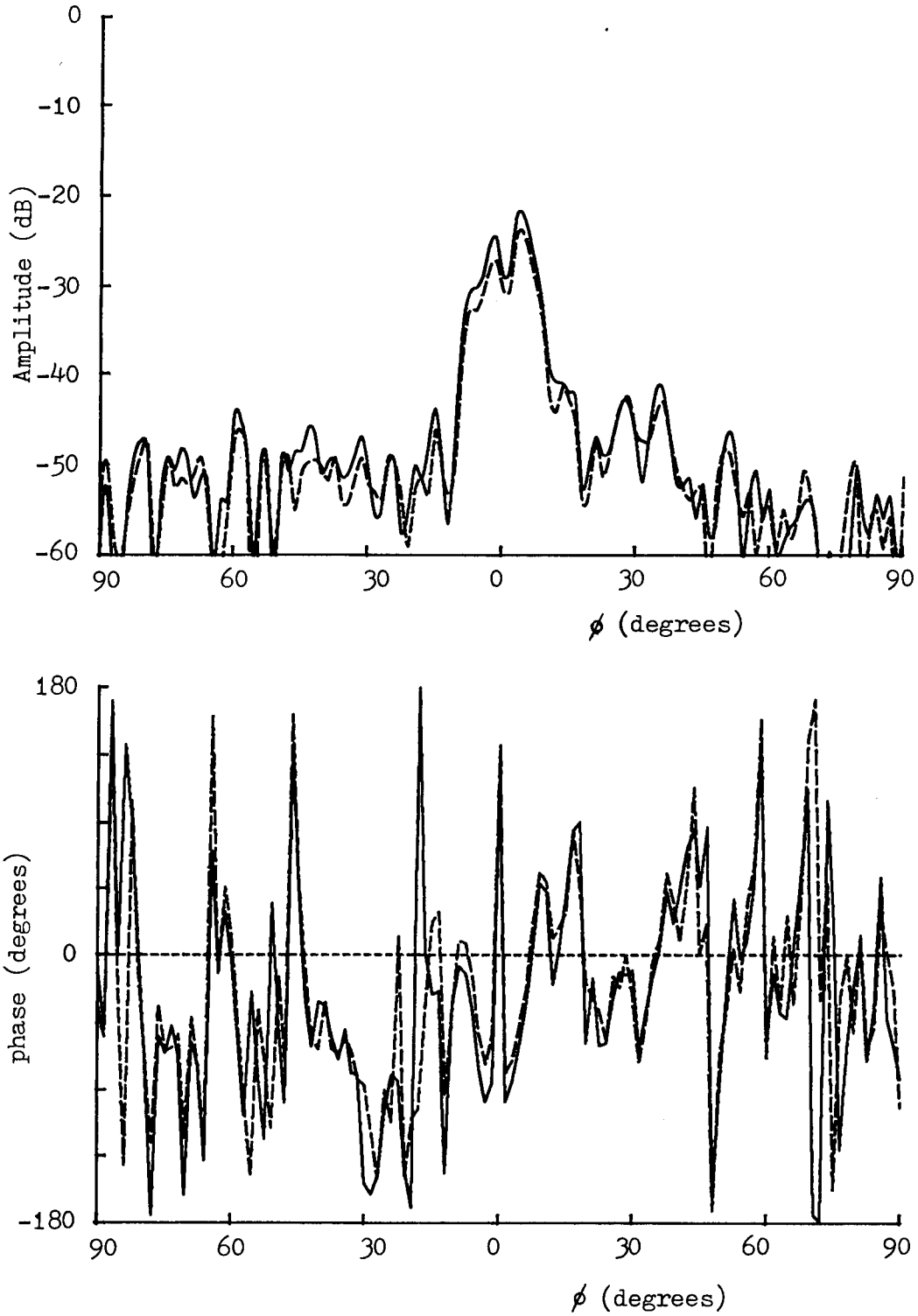

Fig. 6.9. Measured near-field H-plane cross-polar data. Main scan is shown as solid and calibration scan as dashed. These data are for R = 1.5645m.

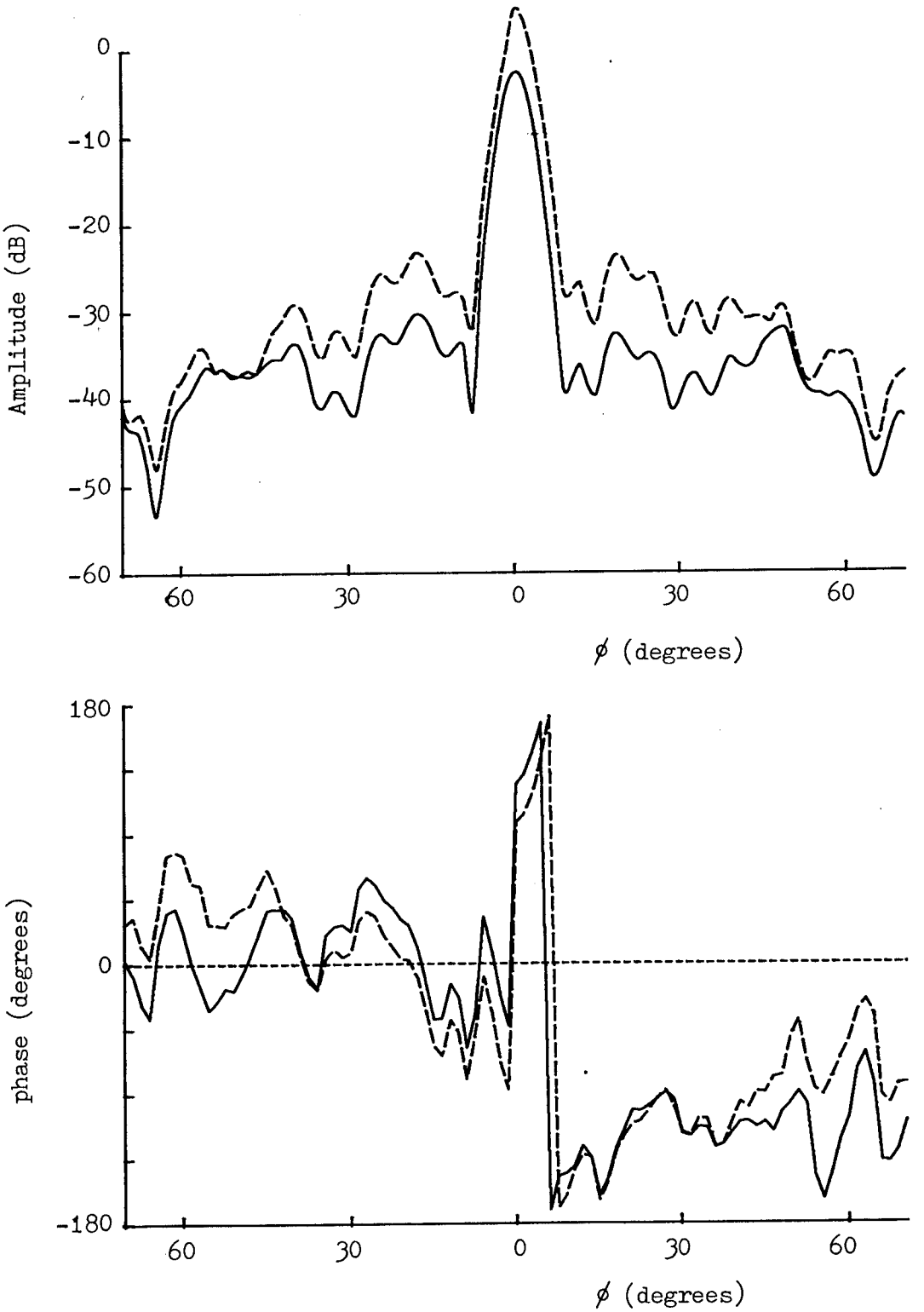

Fig. 6.10. Measured far-field H-plane co-polar data. Main scan is shown as solid and calibration scan as dashed. The apparently unusual shape of the calibration scan main beam is because, due to the severe drift, the two halves of the calibration scan (taken separately) did not meet at boresight.

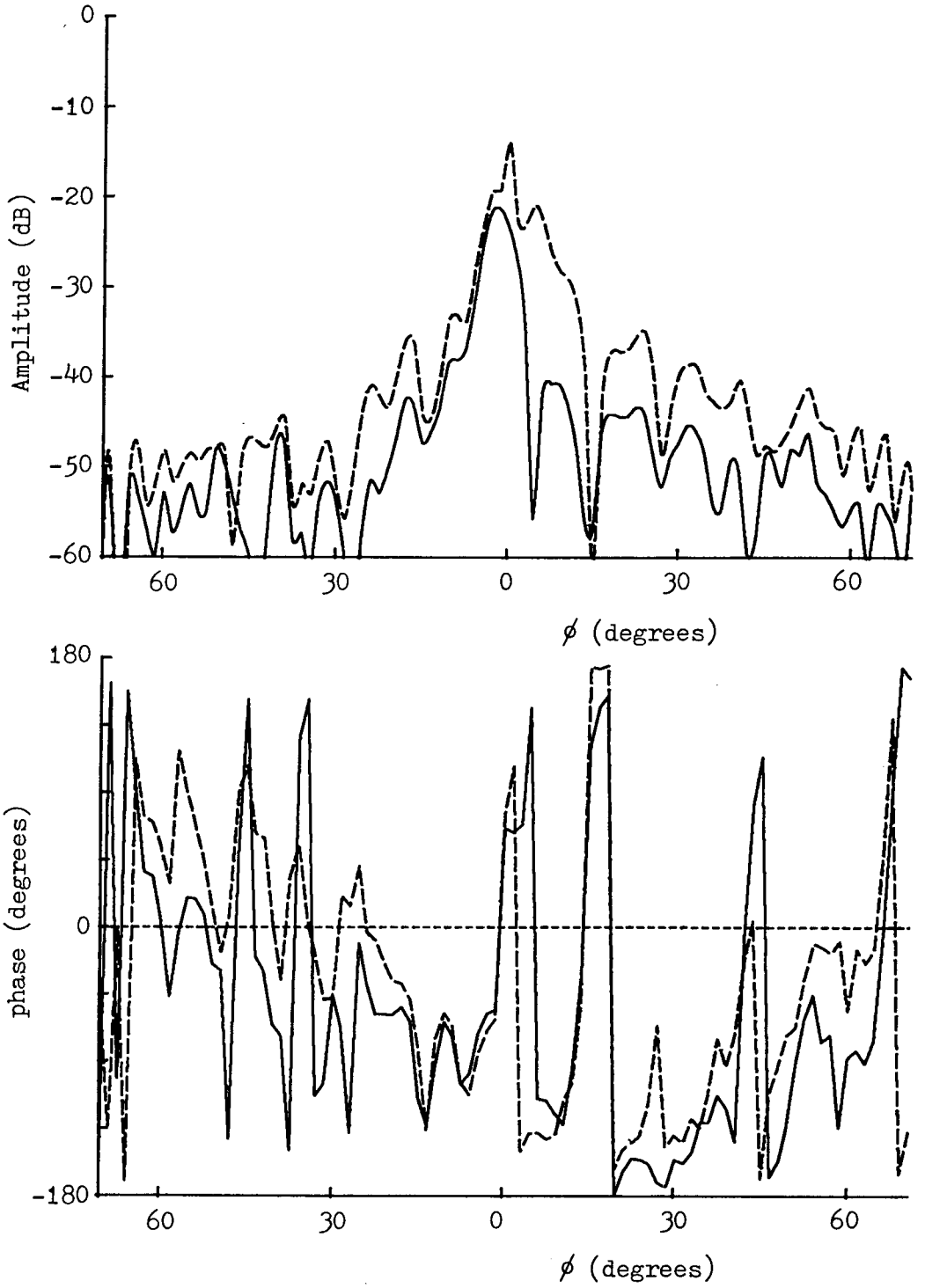

Fig. 6.11. Measured far-field H-plane cross-polar data. Main scan is shown as solid and calibration scan as dashed.

6.4 Far-field Predictions

Earlier chapters (in particular Chapter 3) have included details of the creation of a primary weighting function including the iterative optimisation and the method of converting it into a composite weighting function possibly for a different geometry (Chapter 4). The first of these two operations requires a fairly powerful computer and so, to date, one of the CDC 7600 machines at the University of Manchester Regional Computing Centre has been used. For the antenna size under test here, it has been found that a CPU time of typically 4 minutes has been required to achieve a primary weighting function. These data are then transferred via a data-link to Sheffield for use locally.

Prototype far-field prediction software was written for the main University ICL 1906S computer and an earlier set of data (not described in this thesis) was processed by this means. This early version did not create a separate composite weighting function but interpolated the measured data directly.

The more recently developed software has been used on the Departmental Varian (now Sperry Univac) V-72 image processing computer. This machine is described in detail in Appendix 4. The software developed, to date, for processing the data is described in Appendix 5.

The first set of data to be processed was that obtained with the 1.1m measurement range. The E-plane co-polar and H-plane cross-polar patterns were predicted. Because of the differences between the measured E-plane

co-polar main and calibration scans (the normalised curves of E-plane co-polar measured far-field patterns are shown as Fig. 6.12) it has proved useful to compare the prediction with both of these and so Figs. 6.13 and 6.14 compare the predicted E-plane co-polar pattern with the measured main scan data and the calibration scan data. In the former, a slow drift of quite severe proportions is observed in the area well away from boresight.

The H-plane cross-polar main and calibration measured patterns (Fig. 6.15) display significant differences in places particularly in the region between boresight and 15^{o}. In Figs. 6.16 and 6.17, the prediction from 1.1m data of this pattern cut is compared again with the measured and calibration scans. It will be noticed that there are quite substantial discrepancies but in general the predicted cross-polar pattern is at a lower level than the measured. The possible reasons for this will be discussed later in the chapter. Some similarity in the broad side-lobe structure is discernible.

Moving on to the predictions from the 1.56m data, Figs. 6.18 and 6.19 display comparisons between the prediction of the E-plane co-polar pattern and the measured main and calibration scan data. It seems that within the area less severely affected by the drift encountered during the far-field measurements, the comparison between the prediction and the measured main scan data is the superior. Again, some likely reasons for this will be discussed in the next section.

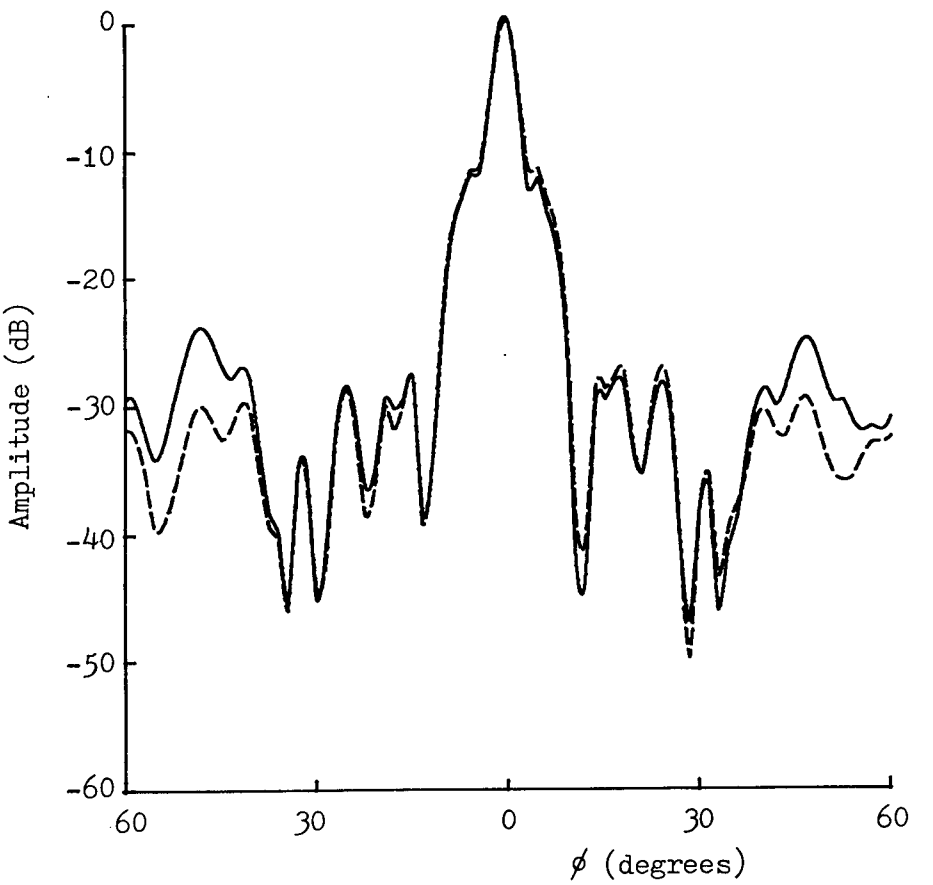

Fig. 6.12. Normalised measured far-field E-plane co-polar amplitude pattern. Main scan is shown as solid and calibration scan as dashed.

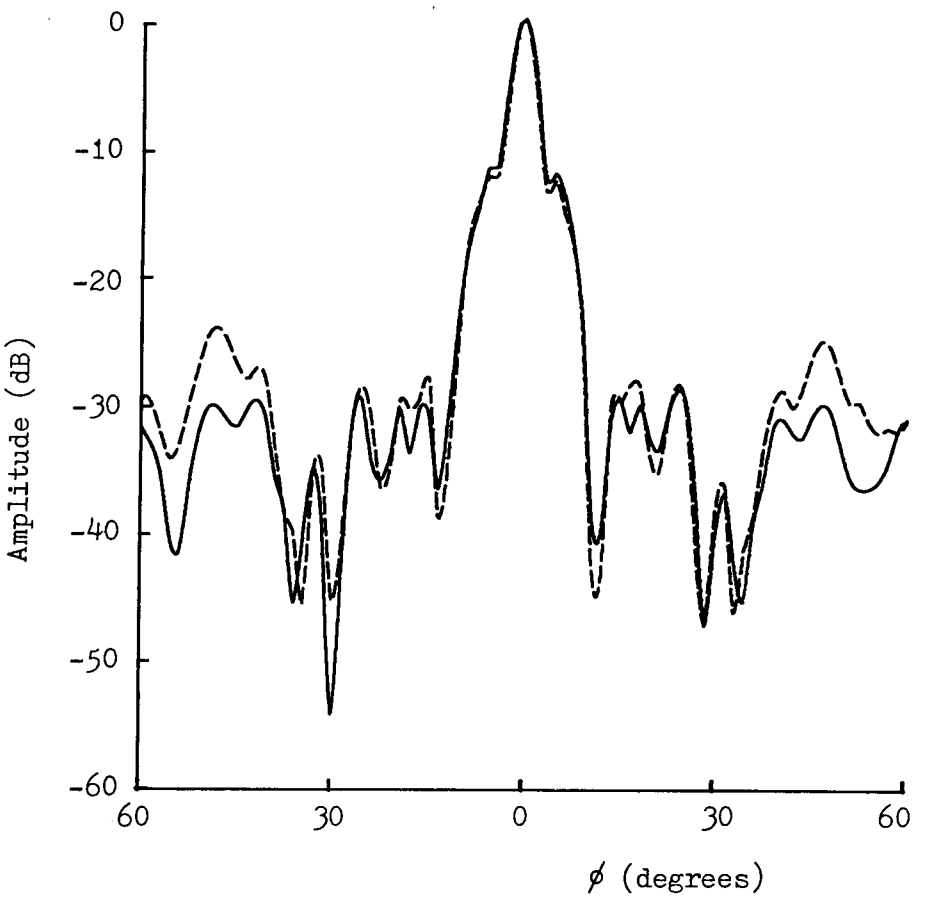

Fig. 6.13. E-plane far-field amplitude patterns, co-polar. Solid curve is predicted from 1.1m. near-field data and dashed curve is measured main scan.

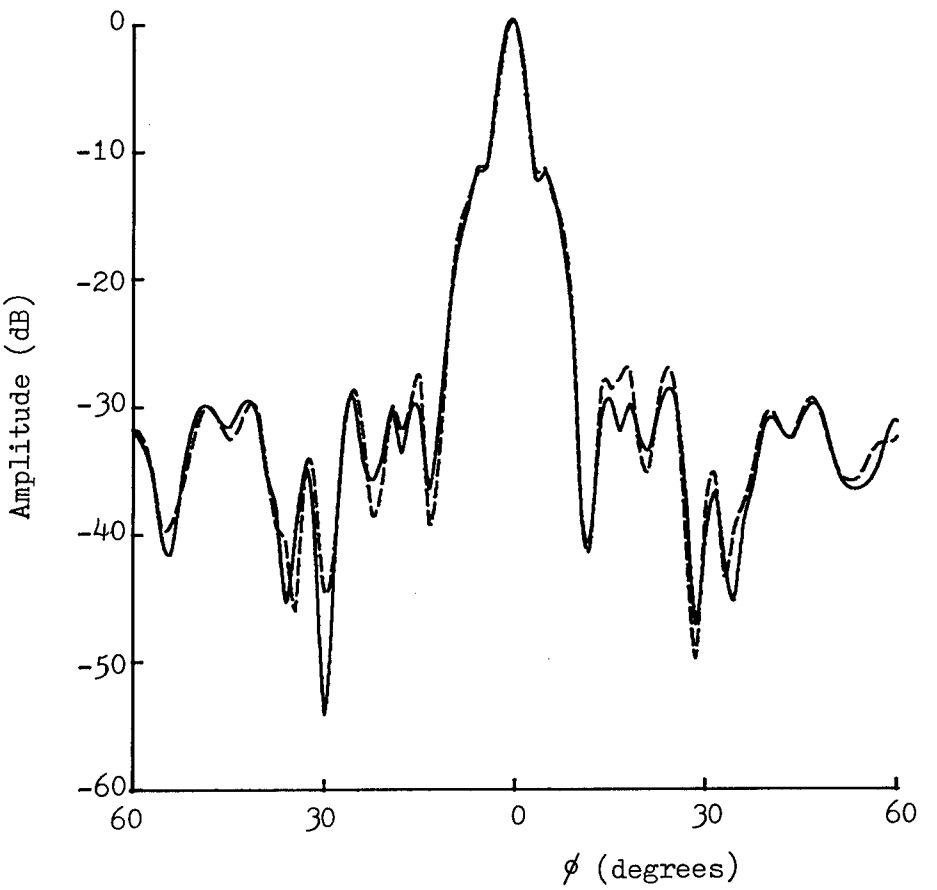

Fig. 6.14. E-plane far-field amplitude patterns, co-polar. Solid curve is predicted from 1.1m. near-field data and dashed curve is measured calibration scan.

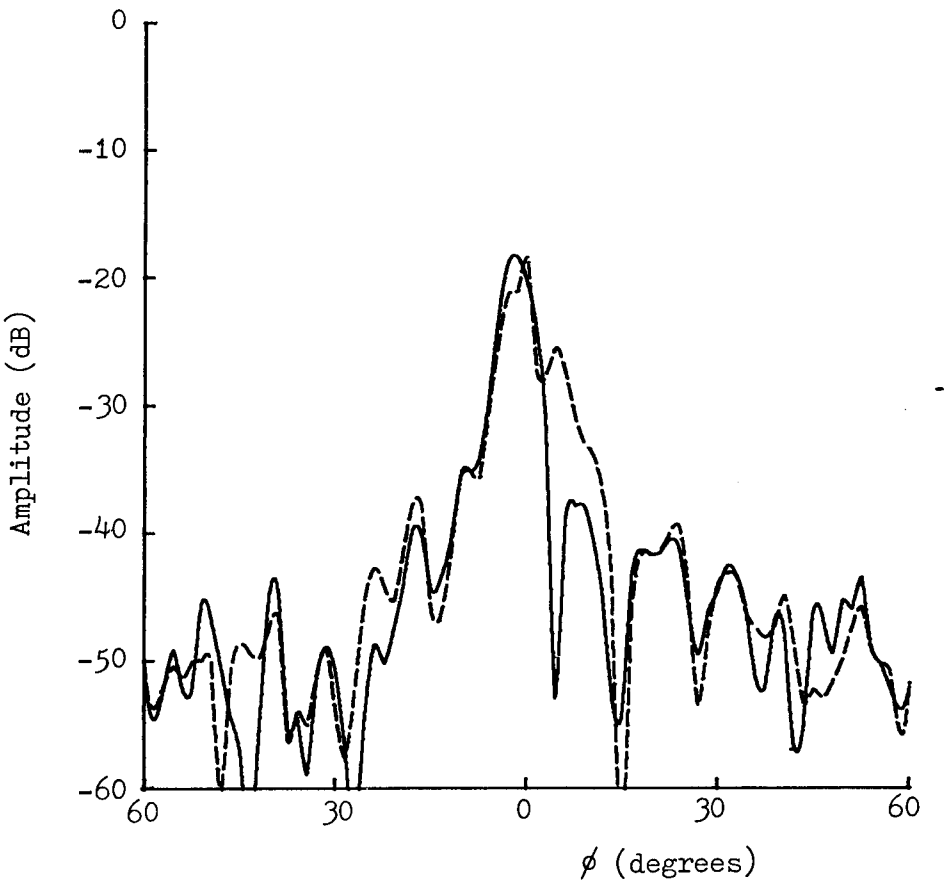

Fig. 6.15. Normalised measured far-field H-plane cross-polar amplitude pattern. Main scan is shown as solid and calibration scan as dashed.

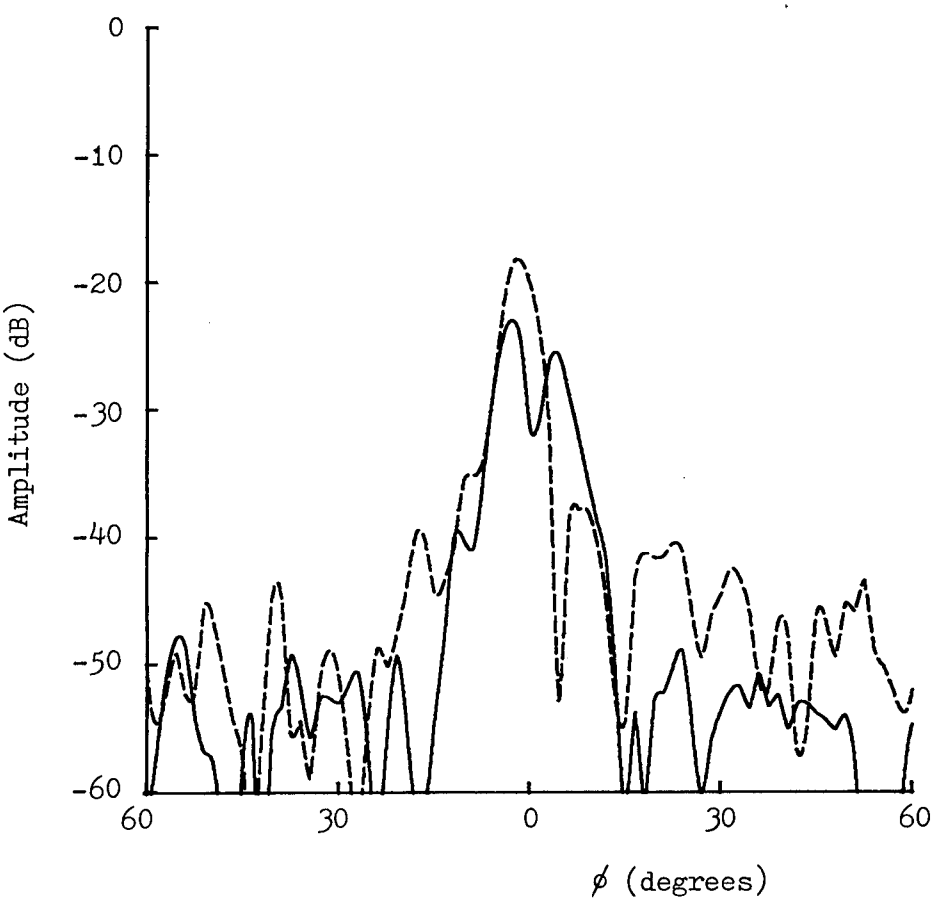

Fig. 6.16. H-plane far-field amplitude patterns, cross-polar. Solid curve is predicted from 1.1m. near-field data and dashed curve is measured main scan.

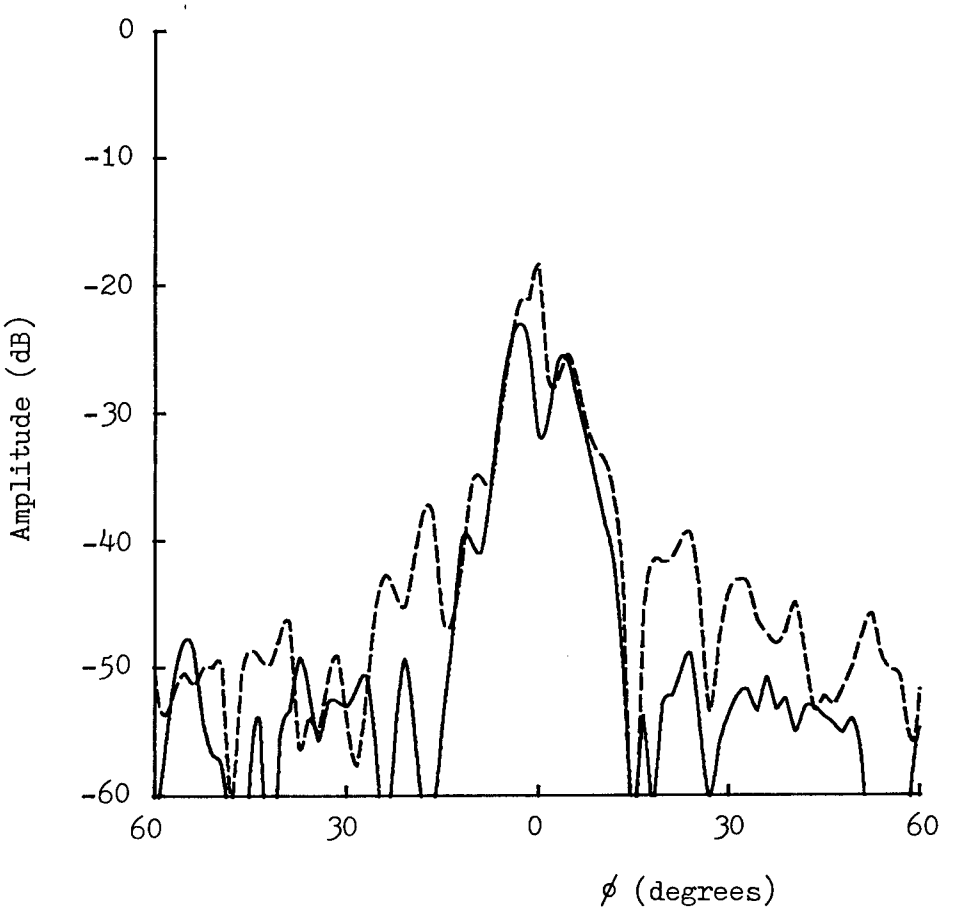

Fig. 6.17. H-plane far-field amplitude patterns, cross-polar. Solid curve is predicted from 1.1m. near-field data and dashed curve is measured calibration scan.

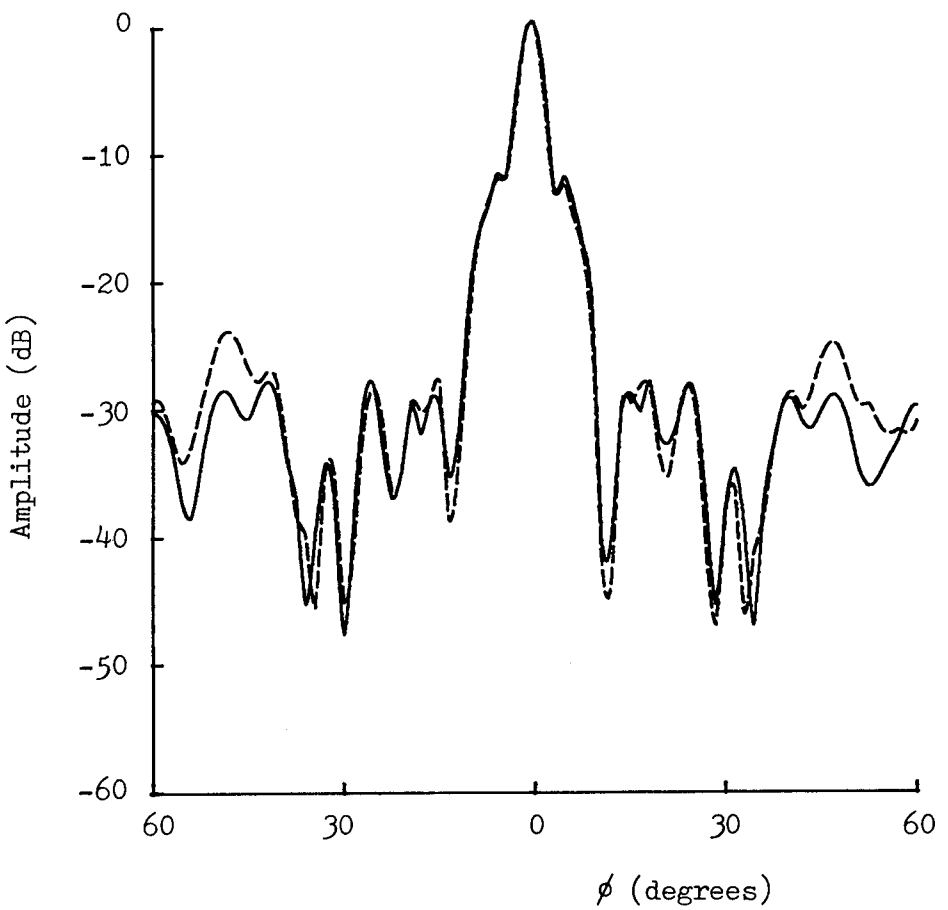

Fig. 6.18. E-plane far-field amplitude patterns, co-polar. Solid curve is predicted from 1.5645m. near-field data and dashed curve is measured main scan.

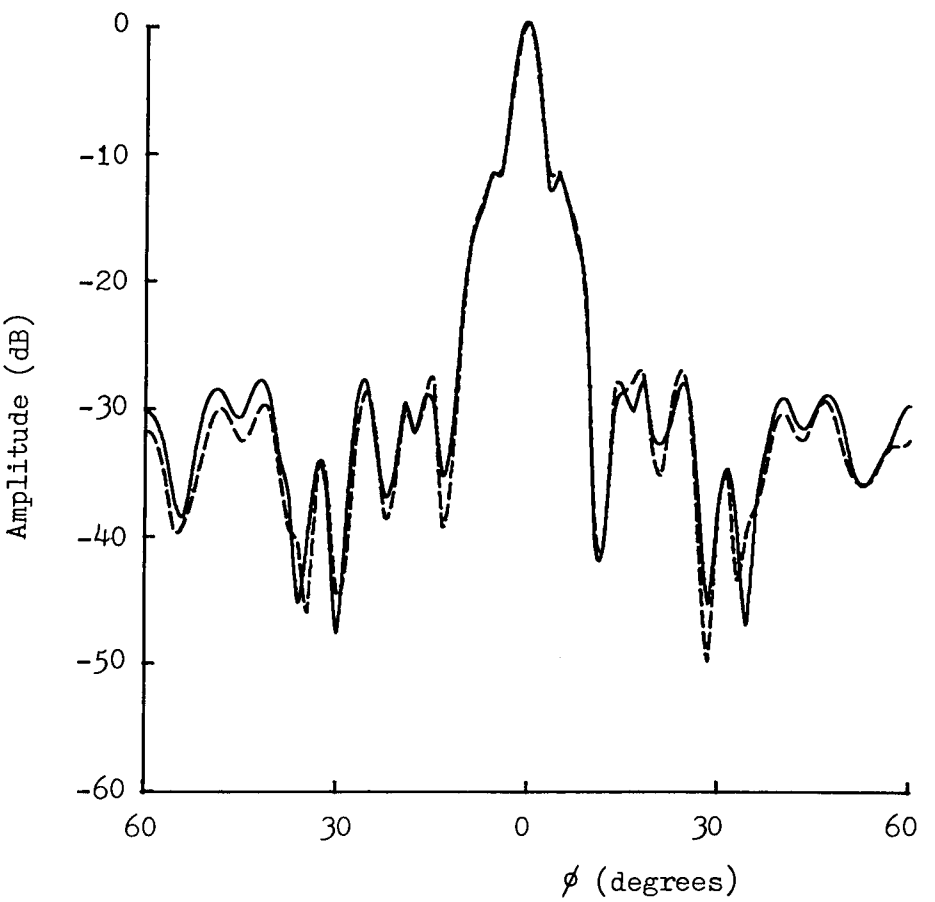

Fig. 6.19. E-plane far-field amplitude patterns, co-polar. Solid curve is predicted from 1.5645m. near-field data and dashed curve is measured calibration scan.

The remaining prediction presented here is the H-plane cross-polar pattern predicted from the 1.56m data (Figs. 6.20 and 6.21). In general, the agreement with the measured far-field is better in this case than in the prediction from 1.1m data. It is rather difficult to make a decision as to which of the two measured far-fields (main or calibration scan) agrees best with the prediction except for the region $0 < \phi < 15^{o}$ where the comparison with the calibration scan is clearly the better.

Before embarking upon a discussion of the possible sources of errors two more comparisons might prove to be of value. These are between the predictions of the E-plane co-polar (Fig. 6.22) and H-plane cross-polar (Fig. 6.23) patterns obtained from the two different sets of near-field data. Apart from some level shifts, the overall agreement in the main pattern shape for both cuts is very encouraging.

6.5 Pattern Discrepancies

The sources of discrepancies between the far-field predicted and measured patterns may be assigned to three broad areas; (a) errors in the measured near-field data, (b) errors in the measured far-field, (c) errors introduced by the processing. Some of the possible sources of errors observed in the data for the 45 reflector are investigated below as they fall into these areas. The reader is also referred to Chapter 5 where the topic of processing errors is covered more generally (rather than specifically as applied in the present measurements).

In the measured near-field data, some element of frequency drift is believed to be present. Although the

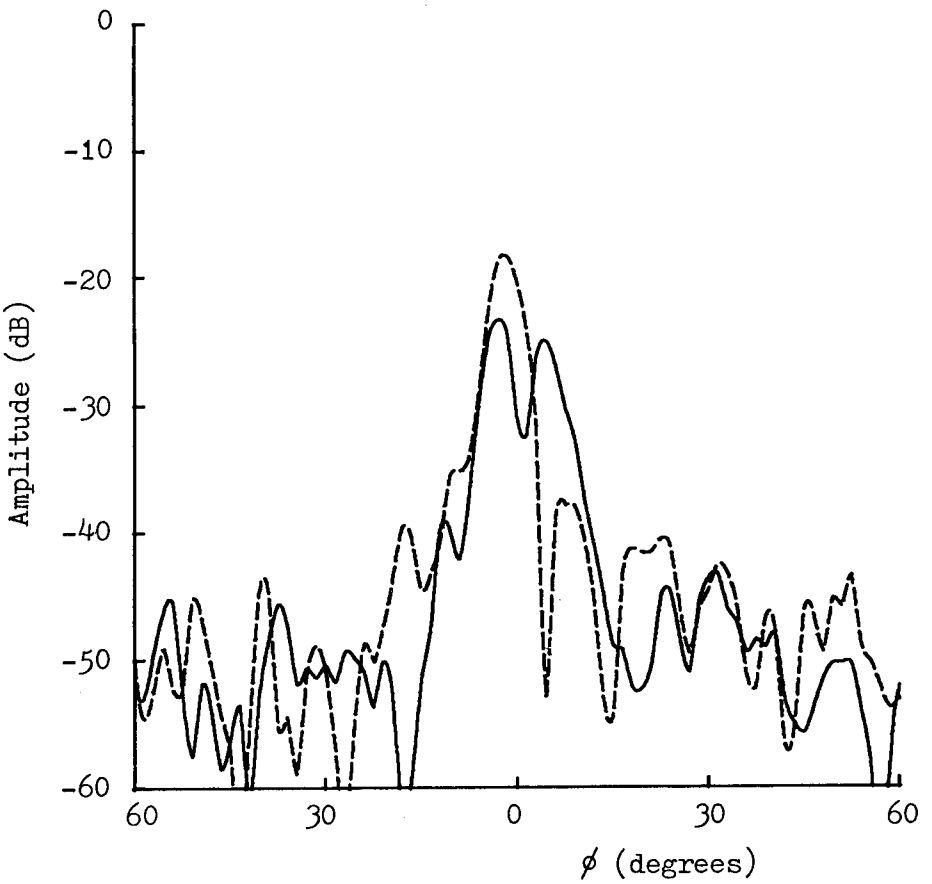

Fig. 6.20. H-plane far-field amplitude patterns, cross-polar. Solid curve is predicted from 1.5645m. near-field data and dashed curve is measured main scan.

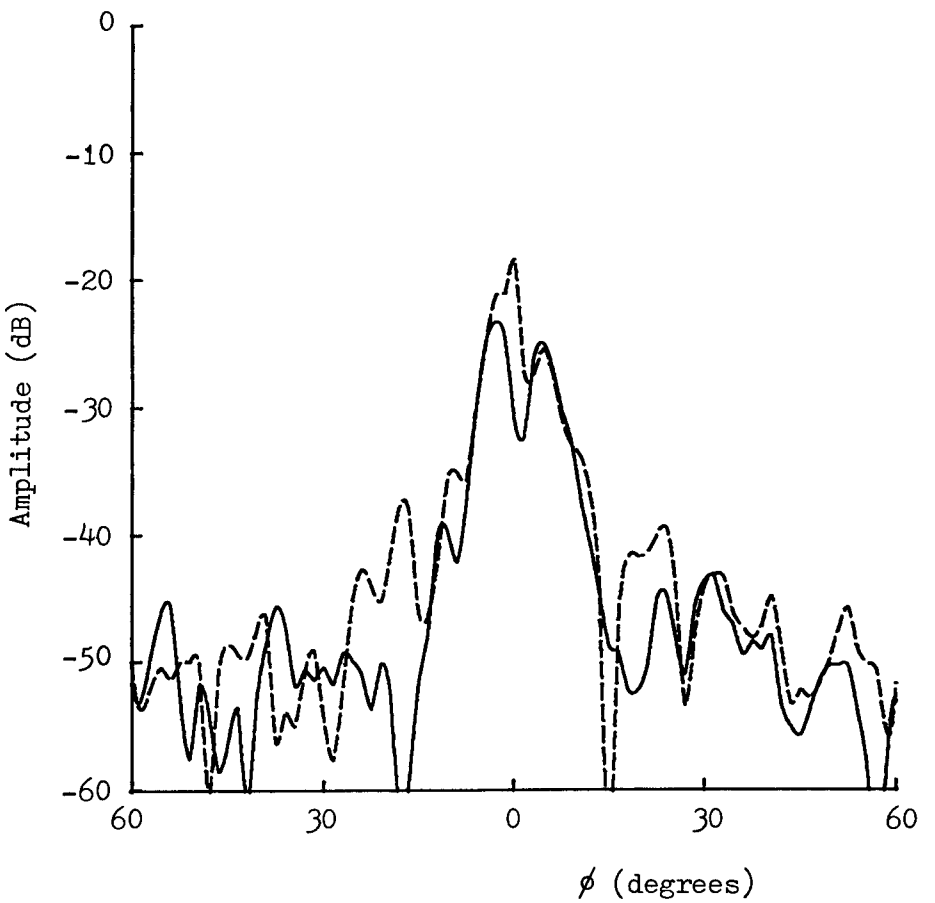

Fig. 6.21. H-plane far-field amplitude patterns, cross-polar. Solid curve is predicted from 1.5645m. near-field data and dashed curve is measured calibration scan.

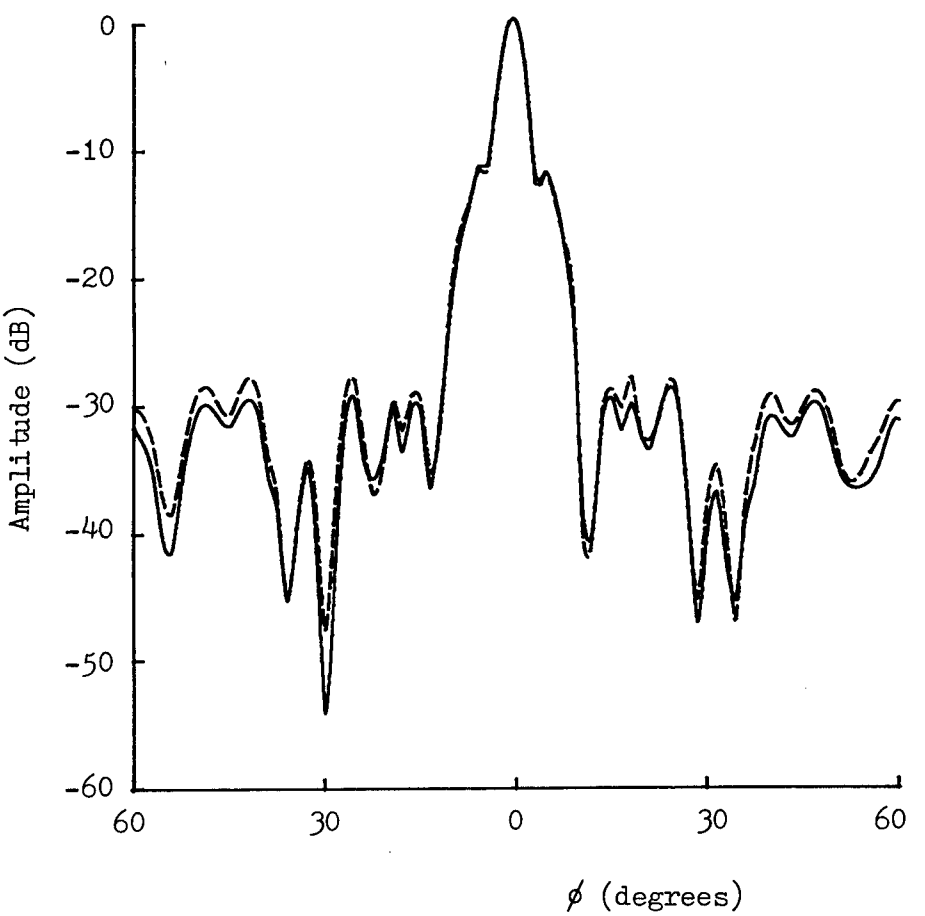

Fig. 6.22. Predicted E-plane co-polar amplitude patterns. Solid curve shows prediction from 1.1m. near-field data and dashed shows prediction from 1.5645m. near-field data.

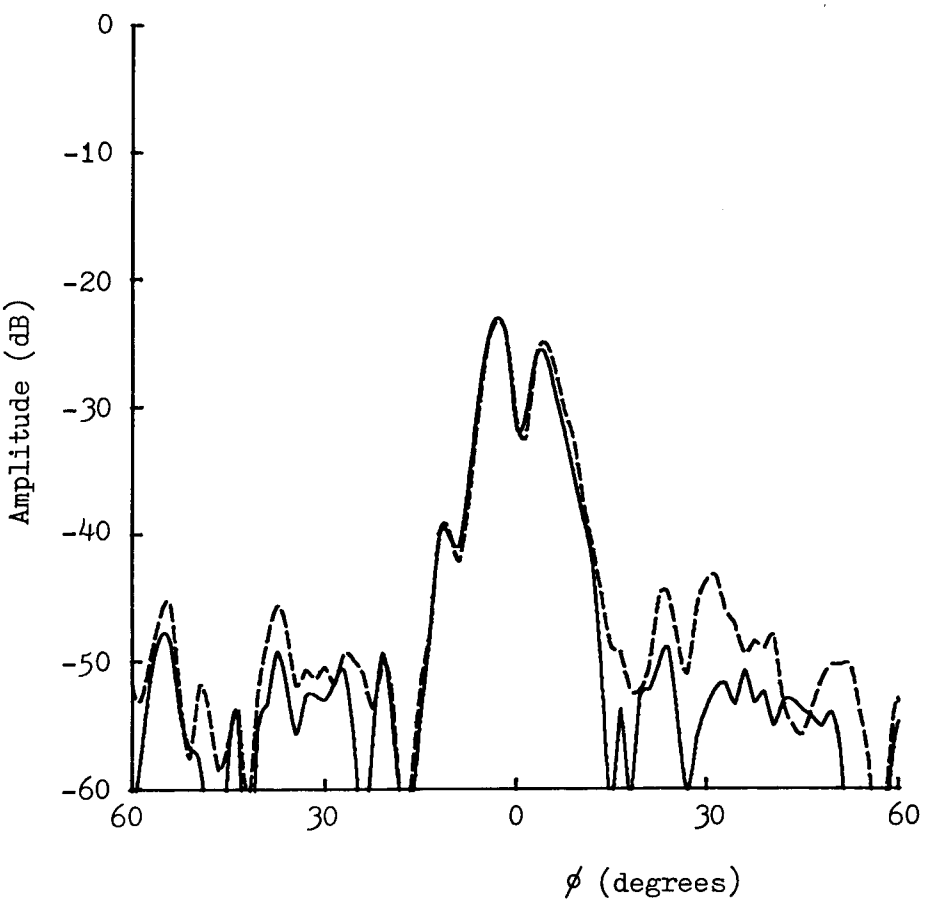

Fig. 6.23. Predicted H-plane cross-polar amplitude patterns. Solid curve shows prediction from 1.1m. near-field data and dashed shows prediction from 1.5645m. near-field data.

usual efforts were made to equalise the electrical path lengths of the signal and reference channels, there was almost certainly a difference between the two. In the presence of a drift in the measurement frequency, such a path length difference is manifested as a phase drift. The measurement frequency was nominally 11.7GHz but it is now believed that the Gunn diode source used was probably not sufficiently stable to provide really accurate results. In the first set of near-field data, a drift of up to 45^{o} in phase was observed. If the approximate formula,

$$\Delta\psi = 2\pi N\frac{\Delta f}{f} \qquad (6.1)$$

is applied, where f = test frequency, Δf = frequency change, N = electrical path difference in wavelengths and $\Delta\psi$ = relative phase change, and a possible path length difference of 30λ is assumed, this would indicate the serious frequency drift of 48MHz. This is based, of course, on the assumption that all of the phase drift is due to the combination of frequency drift and electrical path difference. This will not, in fact, be the case. In the practical system there will be other sources of drift. The attenuation of cables will vary with frequency as may the characteristics of the harmonic mixers used. A likely cause of drift will be temperature variation and this leads us to consider other factors not directly related to frequency. The behaviour of hardware items such as the directional coupler may vary with temperature but probably much more significant will be temperature sensitivity of the mixers. One other significant point may be expansion effects on the mechanical parts causing

the alignment of the system to vary although tests have indicated that this is probably not occurring to a large extent here.

The phase drift in the second set of near-field data was rather less (approximately 30^{o}) but in this set, another effect becomes apparent: differential amplitude drift between the two probe polarisation channels. It is suspected that a possible cause of this is that the frequency drifted above 11.7GHz which is the specified upper limit for operation of the dual polarised waveguide transition. The first (unaffected) port of the device is coupled directly into the circular waveguide but the second port (the one exhibiting the drift) is via a pin-twist in the circular waveguide and this is likely to be the frequency sensitive component.

Apart from the possible distortion of the hardware with temperature, it is believed that using the setting-up techniques described, errors associated with system static misalignment are not significant. The other source of positioning errors will be the fact that the equipment is in motion during the sample. The sample command is issued by the control computer at the moment that the specified angle is reached but there is a finite integration time involved with obtaining the sample which means that there will be a smearing effect over the area from the required sample position to some position beyond this, dependent upon the integration period and the scan speed. At the scan speed of 3^{o} per second and with an integration time of 10 ms (the value used) the smearing effect will extend over 0.03^{o}. At a region of constant field, this will

introduce no error while if there is a linear amplitude gradient equivalent to 20dB per degree the effective amplitude error will be of the order of 0.1dB. It is to be expected that amplitude gradients exceeding this value will be fairly rare so that it is felt that a scan speed of 2 samples per second with 1.5^{o} sampling interval will be satisfactory. In spite of this, it is noticeable that, in both near-field scans, there is a slight increase in the discrepancies between main scan and calibration scan data in the region beyond 45^{o} from boresight where the speed of scanning was increased slightly. This will also be associated, however, with the fact that this region is one of lower sidelobes where the signal to noise ratio might be expected to be worse. Since the apparent speed-dependent errors seem to be of a magnitude no greater than the inherent noise, they are probably of no greater significance. It is recognised that it would not be desirable to increase the speed much beyond the level of 2.5 samples per second.

Chamber reflections may be of some significance, but it is anticipated that since the experiments were set up in the best part of the chamber, the effects are probably quite small.

As mentioned previously, the far-field measurement set up too was designed to minimise range reflections but inevitably, these will be present to some extent. Any effects of these will, however, be totally masked by the much more significant error introduced by the severe temperature drift. The far-field measurements extended into the early hours of the morning by which time the temperature

had dropped markedly. Over a period of about 30 minutes, it was possible to observe the amplitude of the reference channel fall by over 10dB due to a combination of falling source level and almost certainly extreme temperature drift in the mixers. The effects are quite apparent in the graphs of raw far-field data (Figs. 6.10 and 6.11).

One other measurement error is particularly relevant to the predictions of the cross-polar pattern. Because of the height to which the probe had to be raised to bring it level with the test antenna, it became very difficult to set up the polarisation with any degree of confidence. The measured cross-polar level is particularly sensitive to polarisation error (e.g. at boresight, a polarisation setting error of 3^{o} means that the measured pattern will be effectively the cross-polar level added to the co-polar level attenuated by 25dB) so that the discrepancies between the H-plane cross-polar predicted and measured far-field patterns could well be attributable in a large part to polarisation error setting. It should also be recognised that the pattern along the cross-polar null is likely to be relatively sensitive to frequency difference. Indeed, the measured near-field is also likely to be affected comparatively severely by the frequency changes.

The quality of the synthesised plane waves for the 1.1m and 1.56m weighting functions are illustrated with a single co-polar cut of each in Figs. 6.24 and 6.25. It is clear that the quality of the latter is better and this is largely attributable to the fact that the former was allowed to undergo only seven cycles of the iterative

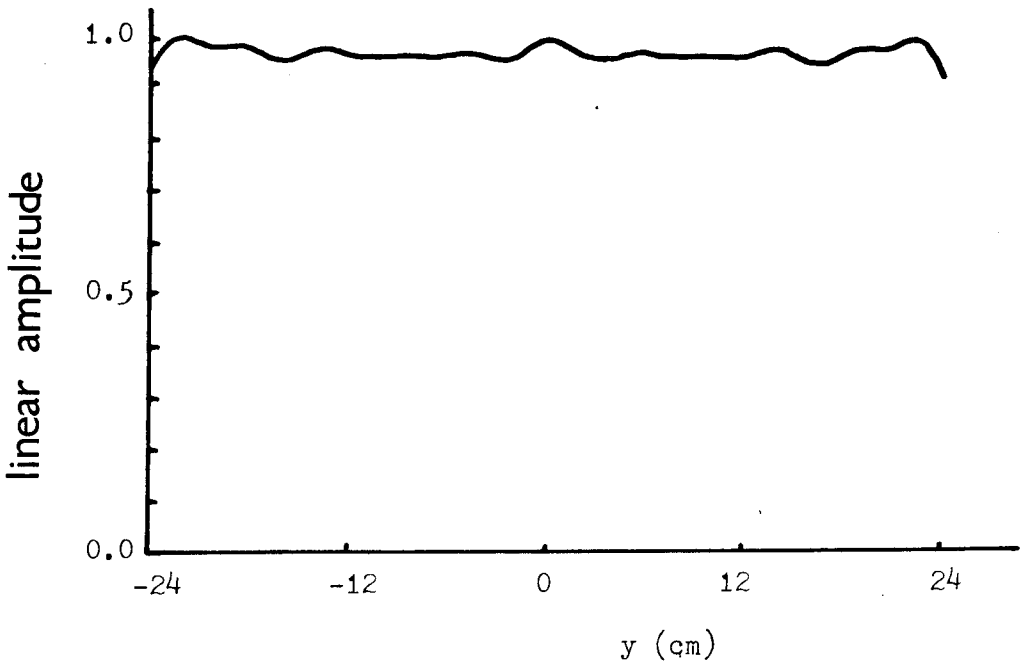

Fig. 6.24. Central cut of synthesised plane wave, co-polar, due to weighting function at 1.1m.

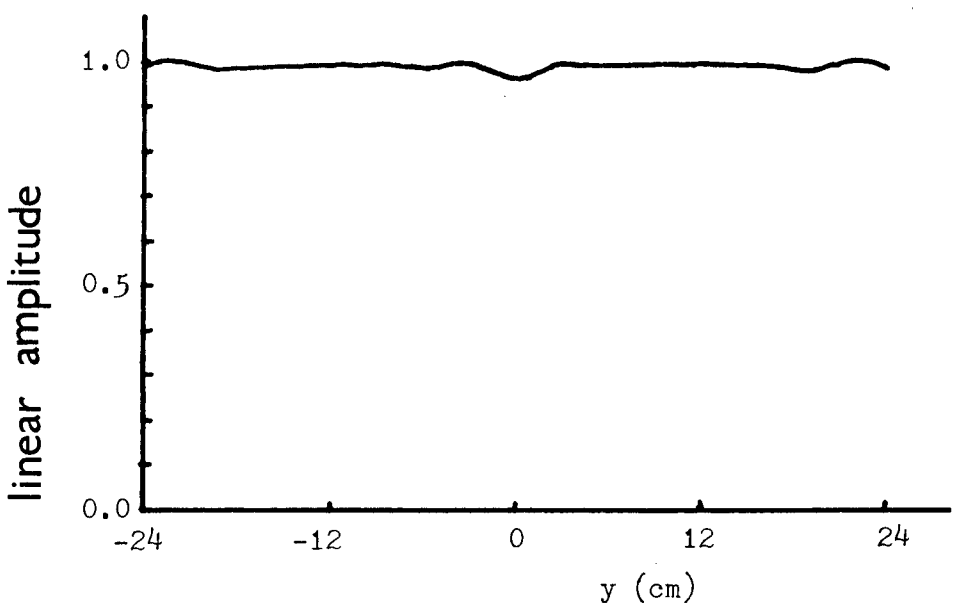

Fig. 6.25. Central cut of synthesised plane wave, co-polar, due to weighting function at 1.5645m.

process whereas the latter was allowed twelve. Treating the ripple in the 1.1m synthesised plane wave in the manner described in Chapter 5 would suggest a spurious far-field source at approximately 16.5^{o} from the desired source with the harmonics of the ripple appearing as sources at 35^{o} and at 58^{o}. It is interesting to note that some of the worst discrepancies between the measured and predicted patterns occur at these angles. For the 1.56m plane wave, the ripple is generally at a rather lower level and indeed the far-field discrepancies at the above angles also seem overall to be rather less.

Particularly interesting as regards two other possible error sources is Fig. 6.22 which compares the two predictions of the E-plane co-polar pattern. In the region outside the main beam, the shapes of the two predictions are very similar but the prediction from the 1.1m data is at a consistently lower level than that from the 1.56m data. There are various possible sources for such an error for which one candidate must be the slow drift which took place. In view, however, of the attempt at calibrating out the drift it was felt that the residual drift effects would probably not be manifested in this fashion. Another possible source which was considered was a slight misalignment between azimuth zero and the position of the probe. This would result in one prediction of the pattern passing near the peak of the main beam while the other might miss the beam peak slightly. Under normalisation, this would appear as a shift of the sidelobe level. This argument may be rejected as defining a serious contributor to the errors when the figures are calculated which

indicate that, at the very least, the probe would have to be displaced by several millimeters to produce the sort of effects present.

Another examination of the synthesised plane waves (Figs. 6.24 and 6.25) gives us a clue as to what might produce this sort of effect. The remaining major feature not already mentioned is the presence of a small peak (in the 1.56m case) or a small dip (in the 1.1m case) at the centre of the synthesised plane wave. By the same sort of arguments as applied to the ripple components, it can be seen that a delta function at the centre of the synthesised plane wave will appear not as a spurious far-field source at a particular angle but a substantially constant "background level" at all angles. In the area of the main beam, with normalisation having been carried out, this effect will not be noticeable but in the sidelobes it may well become of significance. One remaining point which could have a bearing on this discrepancy is that the probe has not been fully characterised, as yet, and therefore the approximation of a half-wave dipole field pattern has been used for the probe compensation. It may be that this approximation is not sufficiently accurate. Clearly any error in this respect will be more serious at the wider angles of the probe which in turn means that it will appear more serious in the 1.1m near-field data.

In conclusion of this chapter it may be said that the far-field predictions are encouraging but display certain errors for which a large number of possible sources have been suggested. Some of the future work in the development of

plane wave synthesis will be directed towards investigation of which of the error sources are important and how they can be reduced.

7. CONCLUSION

7.1 Summary of the Work to Date

A technique has been elaborated which it is believed will be capable ultimately of providing predictions of far-field antenna radiation patterns from near-field measurements with an accuracy at least comparable with existing transformation schemes. Furthermore, most of the onerous part of the processing is in fact performed in advance so that this need only be carried out once for a particular antenna size at a particular frequency and the precalculated coefficients held in the form of a library of weighting functions each of which might have an approximate 10% bandwidth as shown in Chapter 5. The actual prediction process contains only complex number multiplications and additions which makes it relatively simple to implement.

In Chapter 2, the processes of the formation of a synthesised plane wave from a weighting function were examined and the various effects leading to imperfections were discussed. Particularly enlightening were the displays, in grey scale, of the field distributions over an area, where it could be seen that some of the worst problems in formation of a high quality plane wave were due to interference between the main plane wave and the grating lobes produced because of the spacing between weighting function samples. Also in Chapter 2, the sampling criterion was carefully examined and a curve describing the necessary reduction in sampling interval with reduction in measurement range was presented.

Chapter 3 considered the problems of the three-dimensional sampling geometry, in particular the elevation-over-azimuth system, and the necessary formulae for production of a primary weighting function and its conversion into a set of composite weighting functions were given. In addition, because the sampling geometry meant that interpolation was required in the transformation from a primary weighting function to its composite equivalents, a number of fairly simple interpolation schemes (all four-point) were considered and it was concluded that the four-point Everett interpolation scheme came out as favoured by a small margin over the four-point Lagrange scheme, with Fourier interpolation rejected because of its time consuming function calculations and failure to reduce to the zero-error condition for small sample intervals.

The equivalent formulae for the polarisation-over-azimuth sampling geometry were presented in Chapter 4 and in addition, because of the advantages to be gained in terms of computer time, the necessary formulae for producing polarisation-over-azimuth composite weighting functions from elevation-over-azimuth primary weighting functions were included.

An analysis of some of the types of practical measurement errors which might occur, together with the possible effects of such errors was included in Chapter 5. In addition to the consideration of practical measurement errors, some thought was given to certain types of systematic errors. The problem of probe compensation was studied and it was demonstrated that certain types of errors

were introduced by incorrect compensation, notably changing of sidelobe levels and null positions. It was demonstrated that compensation for even quite narrow beam probes could produce distinct improvements in the prediction. The technique of Fourier analysis of the synthesised plane wave and non-ideal residual was introduced as a means of quantifying the imperfections in a synthesised plane wave and it was thereby shown that many of the worst effects are due to the edge discontinuity of the weighting function. It was demonstrated that the iteration procedure reduces the edge effects quite effectively. Lastly the frequency tolerance of a typical weighting function was studied and it was shown that about a 10% bandwidth should produce results at least as good as measurements at $2D^2/\lambda$. Furthermore, by scaling of linear dimensions in proportion to the wavelength, this bandwidth could be significantly extended.

Chapter 6 detailed a practical measurement including preliminary predictions and a discussion of the apparent errors present and their sources. It was demonstrated that the full three-dimensional prediction is feasible and can produce useful results and with improved experimental procedures and more stable equipment, substantial accuracy improvements should prove possible.

7.2 Application to Other Measurement Systems

As indicated in Chapter 1, one of the aims of the project was a technique applicable to spherical measurements but also, ideally, adaptable to planar and cylindrical measurements. It is felt that the plane wave synthesis

technique is indeed adaptable to these geometries, however, it would need some modification. While in the spherical geometry, the direction of propagation of the synthesised plane wave is determined simply by the positioning of the weighting function on the data sphere, in the cylindrical geometry, this control can only be exercised in this way for one of the scan coordinates and in the planar geometry, not at all. It is thus necessary to develop a method of producing weighting functions which synthesise plane waves travelling at oblique angles away from them. An investigation has been performed (although still using a spherical surface) of synthesising a plane wave travelling at an oblique angle (although only a relatively small angle) and was shown to be successful. The inherent separable variable nature of these two other geometries may provide considerable simplification in the generation of the weighting functions.

An offshoot of the plane wave synthesis technique (which has developed into a separate project) uses a plane wave synthesised by a single circular scan of a slotted waveguide array. The illumination function of the array provides one dimension of the weighting function and the other is applied computationally, again utilising the separable variable nature of the effective cylindrical scan. Here, however, the test antenna is still scanned in a spherical way producing a set of effective cylindrical scans, the predictions being produced by computational weighting of sets of one dimensional cuts of data. This has already been shown[39] to produce useful results and although theoretically not as flexible as the full plane

wave synthesis technique, could prove quite powerful in certain circumstances.

7.3 Type of Probe

To date, a scalar feed has been used as the probe because of its smoothly varying pattern with very low side and back lobes, thus easy to characterise and not severely prone to reflection from the support structure. This is attached to a circular waveguide, the resulting system being circularly symmetric. This circular symmetry is an important property since the technique, as formulated in this thesis, depends on the property for the ability to obtain the desired probe polarisation by resolution of two measured components. It would introduce further (although not insurmountable) complications, if circular symmetry were not able to be utilised since separate primary weighting functions would need to be created with a knowledge of the actual probe polarisations in each case.

Assuming the circular symmetry, it is clearly desirable to have a probe with an easily definable pattern but beyond this, any probe (assuming it does not have a zero within the solid angle subtended by the test antenna) is applicable as long as it is compensated correctly.

7.4 Processing Efficiency

To date, the software for producing the weighting functions has been developed to perform its processing efficiently (using the present approach) but the actual prediction software has not been completely optimised. It is feasible that the processing could be modified so as to use the FFT to achieve the convolution of data with composite

weighting function in one of the dimensions and, if this were implemented, calculations indicate that the prediction of the full far-field of the 45cm reflector antenna might be achieved in under 30 seconds of CPU time on the V-72 minicomputer presently being used for the processing. The most time consuming part of the processing would then be the initial generation of the weighting function and certain ideas for improving the efficiency of this process are currently being considered. Some of the more promising ideas will now be mentioned briefly.

7.5 Efficient Weighting Function Generation

7.5.1 Small Antennas

The geometry which has been considered throughout this thesis, for production of a weighting function by the iterative procedure, has been with the weighting function on a spherical surface and the plane wave on a planar surface passing through or near the origin of the coordinate system. This seems to provide the potential, within the present computational limits, of providing a weighting function to synthesise a plane wave 60λ - 80λ wide. To be able to handle antennas larger than this, it would be useful to be able to employ a modified geometry which would make use of circular symmetry or some other form of coefficient duplication to ease the processing burden as regards the generation of the weighting function.

Since the weighting function is defined on a spherical surface in an elevation-over-azimuth arrangement of points, a logical way to define the synthesised plane wave, so as to be able to exploit coefficient duplication,

would seem to be on a smaller concentric spherical surface just outside the desired plane wave region, in a similar elevation-over-azimuth geometry. This would mean that the geometrical and probe pattern coefficients would need only to be calculated for one elevation angle and would apply equally for any other. This geometry will be investigated as the plane wave synthesis technique is further developed. Preliminary calculations suggest that this may extend the maximum allowable antenna size to one of the order of 200λ.

7.5.2 Large Antennas

Ideas have been put forward that even larger antennas might be manageable if optical-type approximations can be made to suggest that a weighting function can be achieved with little or no iteration by merely projecting the plane wave back onto the spherical surface in phase (and resolving into the appropriate field components), without any complicated diffraction integral procedures. While such an idea is at a very early stage of development, it may ultimately prove of considerable value.

7.6 The "Standard" weighting Function

It was demonstrated in Chapter 5 that the frequency range of a given weighting function could be extended by scaling all the linear dimensions of the system in proportion to the wavelength. In fact, theoretically, the bandwidth of the weighting function could be made effectively infinite. This leads to the proposition that a single weighting function might be designed to produce a large, high-quality plane wave and that by using the scaling technique, this

could be utilised to evaluate any test antenna (up to the maximum allowable size) at any frequency.

This would unfortunately lead to overheads in terms of an unnecesssarily large measurement range and unnecessarily small sample interval for small antennas. It would, however, be feasible to hold a small library of standard weighting functions categorised according to electrical size of antenna. The library might, for instance, consist of five weighting functions covering the range up to 160λ as follows,

weighting function 1	under 10λ
weighting function 2	10λ - 20λ
weighting function 3	20λ - 40λ
weighting function 4	40λ - 80λ
weighting function 5	80λ - 160λ

If such intervals were considered too wide them more functions could be held in the library as considered appropriate.

7.7 Conclusions

While much developmental work remains to be done to convert the plane wave synthesis technique into a really practical and reliable technique for performing an antenna near-field/far-field transformation, it is believed that it may eventually take its place as a valuable addition to the range of near-field test techniques available. With improvements along the lines of those suggested in sections 7.4 and 7.5, and with the continuing advances being made in computer technology, particularly in the field of array processors, the technique may have the capability of evaluating antennas which at the present time can only be managed by the use of severe paraxial approximations.

Appendix 1: IMPULSE RESPONSE OF THE WEIGHTING FUNCTION

In section 2.2.2, it was shown in an analysis of the basic processes taking place in the synthesis of a plane wave that the actual synthesised plane wave (neglecting the effect of the iterative procedure) is in the form of the ideal plane wave convolved with an impulse response approximating to a sinc (sin y/y) function. The exact shape of the impulse response depends on, of course, its position and also the weighting function geometry. In this appendix, we study the impulse response at the centre and at the edge of the plane wave region for various sizes of weighting function.

All the diagrams shown here are for a weighting function at a 1.0m measurement range and element spacing of 2.0^{o}. In each case the response is illustrated on three planes, z = 0 (the plane on which the impulse was specified as input data), z = -10cm and z = +10cm. The usual one-dimensional weighting function approximation is used here.

Fig. A1.1 shows the impulse response of a weighting function covering the full semicircle ($\pm 90^{o}$) and, as expected, the response on the plane z = 0 is quite narrow but breaks down badly for z = ±10cm. The analysis of section 2.2.2 suggests that as the weighting function is reduced in size, the impulse response will widen on the plane z = 0 and will retain its properties better in depth. As the sequence of figures shows, this conclusion is borne out. The sequence is:

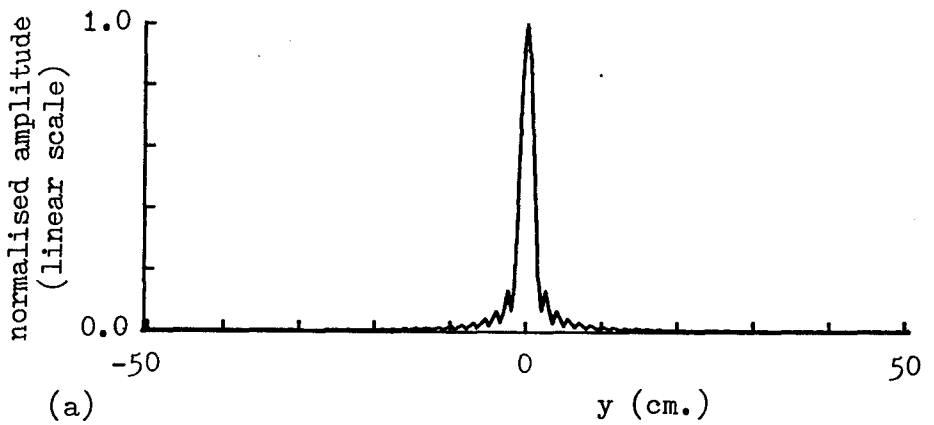

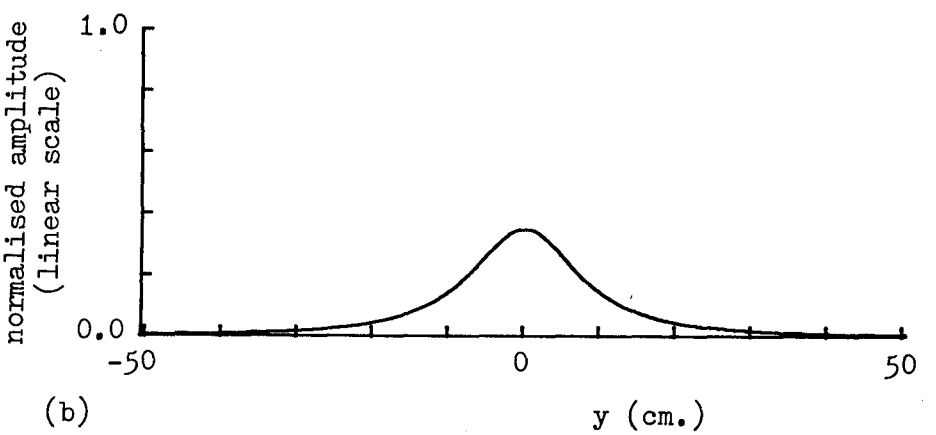

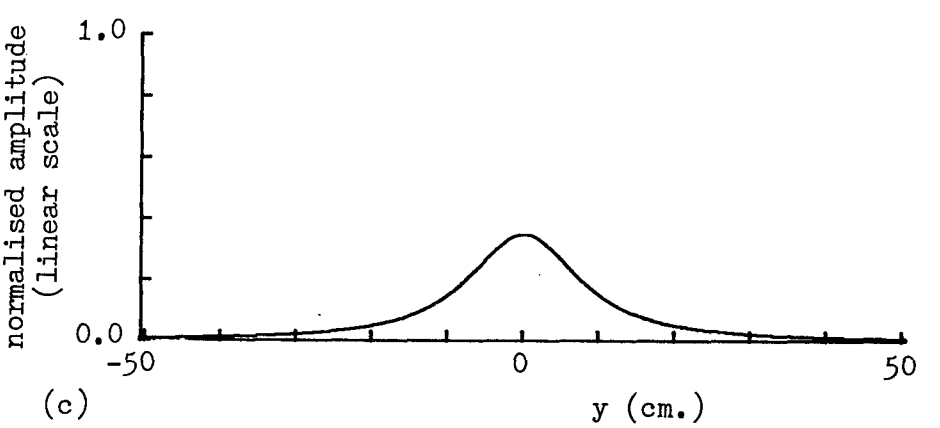

Fig. A1.1. Central impulse response of a weighting function extending over ±90°, R = 1.0m., (a) z = 0, (b) z = -10cm., (c) z = 10cm.

Fig. A1.2 - $\pm 60^{\circ}$ weighting function.

Fig. A1.3 - $\pm 30^{\circ}$ weighting function.

Fig. A1.4 - $\pm 24^{\circ}$ weighting function (by this time the impulse response is maintaining itself much better in depth).

Fig. A1.5 - $\pm 20^{\circ}$ weighting function.

Fig. A1.6 - $\pm 16^{\circ}$ weighting function.

Fig. A1.7 - $\pm 12^{\circ}$ weighting function (by which time the impulse response is showing very little change over the 20cm depth displayed).

In addition, a sequence of graphs is presented for the same set of parameters as above but with the input impulse offset 15cm from the origin. This sequence is as follows:

Fig. A1.8 - $\pm 90^{\circ}$ weighting function.

Fig. A1.9 - $\pm 60^{\circ}$ weighting function.

Fig.A1.10 - $\pm 30^{\circ}$ weighting function.

Fig.A1.11 - $\pm 24^{\circ}$ weighting function.

Fig.A1.12 - $\pm 20^{\circ}$ weighting function.

Fig.A1.13 - $\pm 16^{\circ}$ weighting function.

Fig.A1.14 - $\pm 12^{\circ}$ weighting function.

Again, it will be seen from these graphs that for the wide weighting functions, the impulse response is narrow but does not maintain itself well over any appreciable depth while as the weighting function narrows, the impulse response broadens but retains its properties over a greater depth. It was also concluded in section 2.2.2 that the impulse response would undergo a scale change with changing depth such that it would broaden

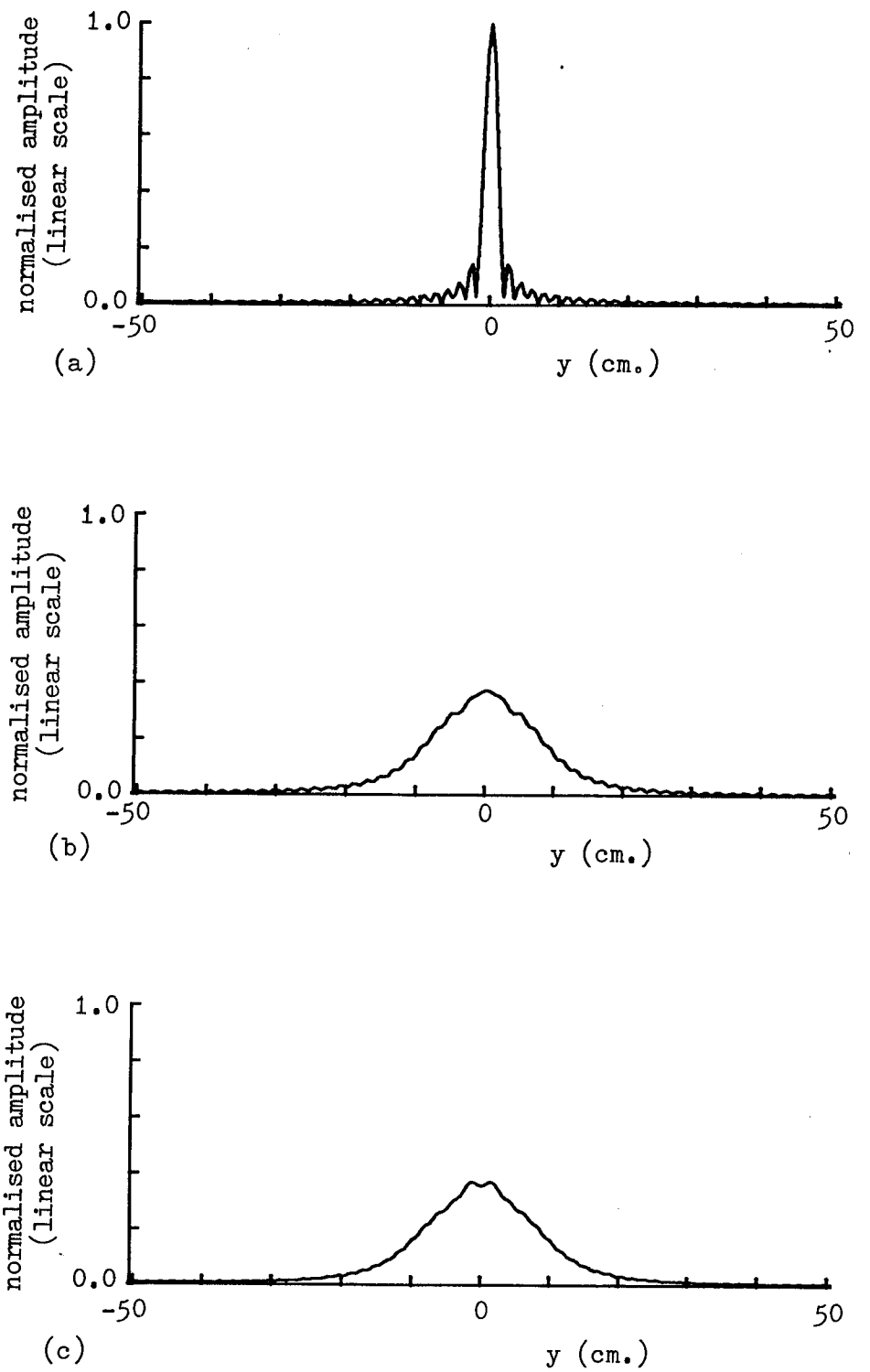

Fig. A1.2. Central impulse response of a weighting function extending over ±60°, R = 1.0m., (a) z = 0, (b) z = -10cm., (c) z = 10cm.

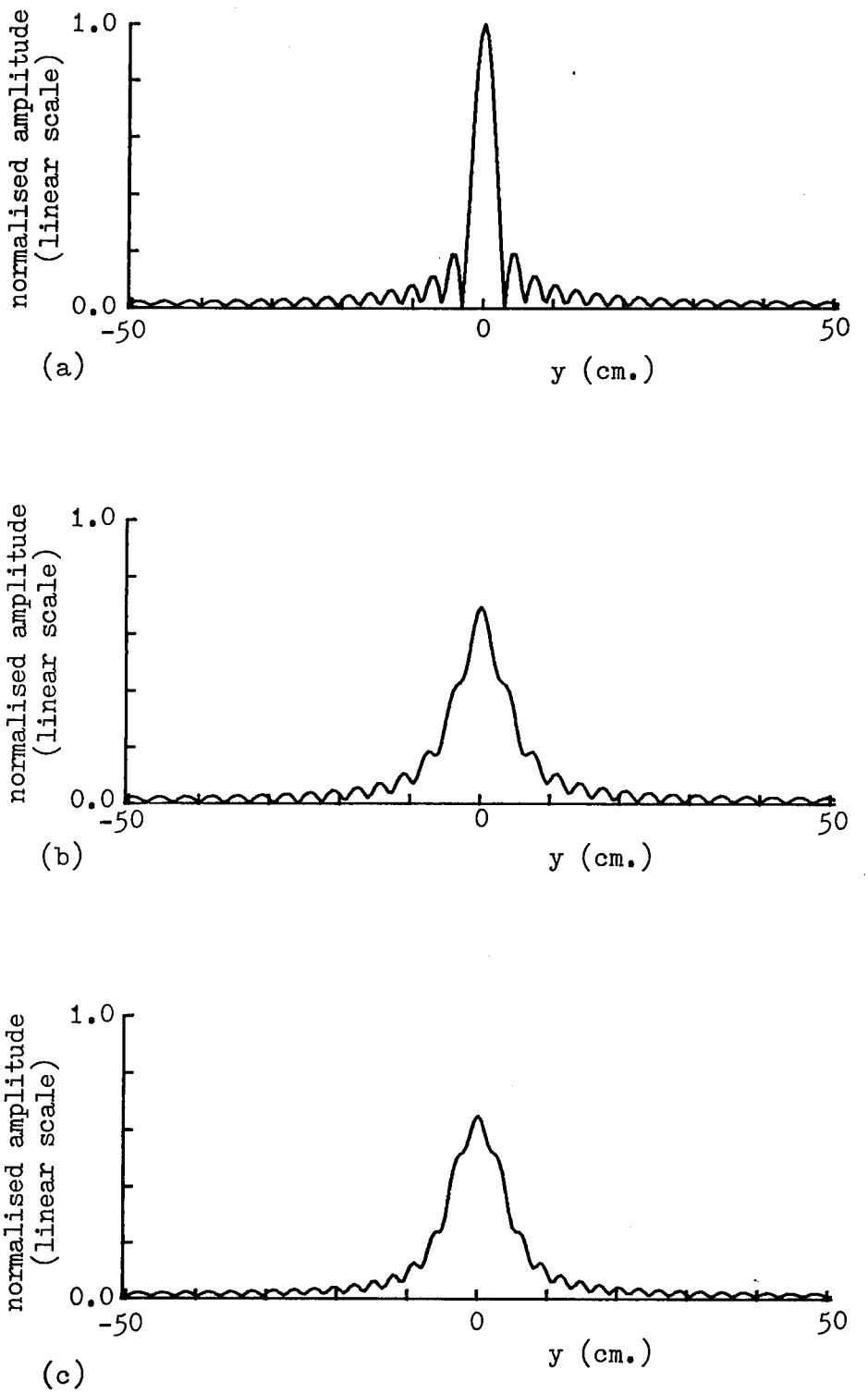

Fig. A1.3. Central impulse response of a weighting function extending over ±30°, R = 1.0m., (a) z = 0, (b) z = -10cm., (c) z = 10cm.

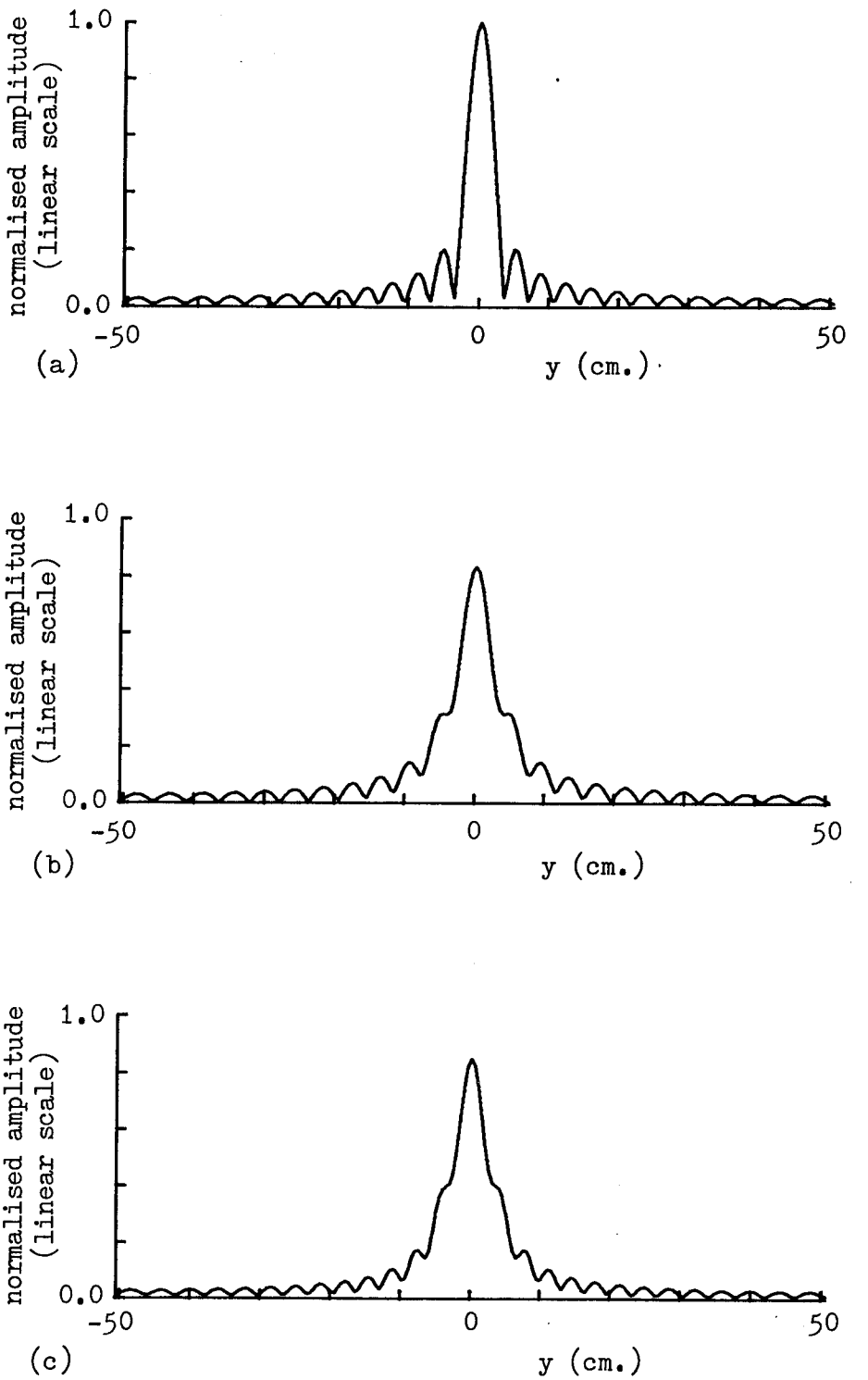

Fig. A1.4. Central impulse response of a weighting function extending over ±24°, R = 1.0m., (a) z = 0, (b) z = -10cm., (c) z = 10cm.

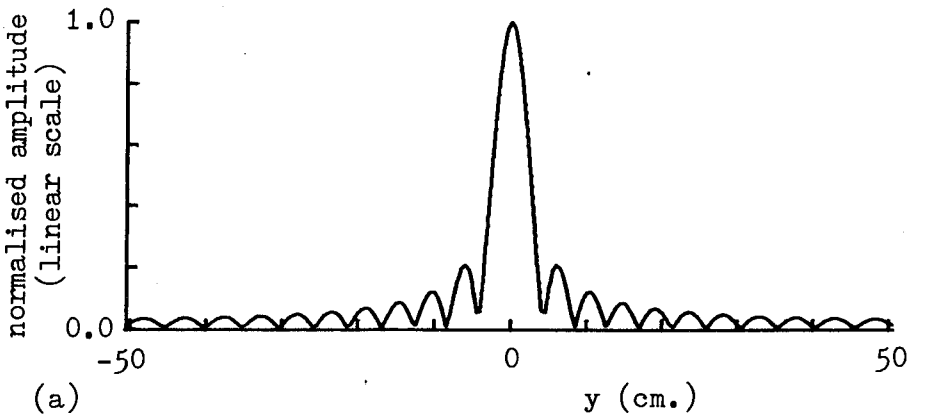

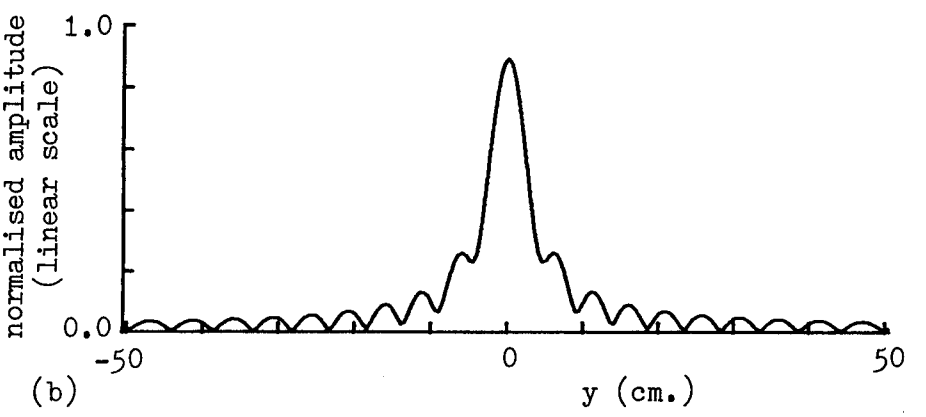

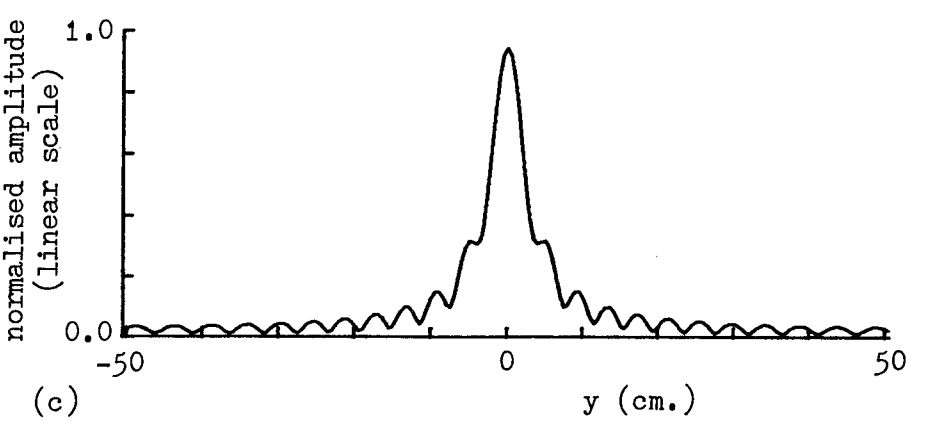

Fig. A1.5. Central impulse response of a weighting function extending over ±20°, R = 1.0m., (a) z = 0, (b) z = -10cm., (c) z = 10cm.

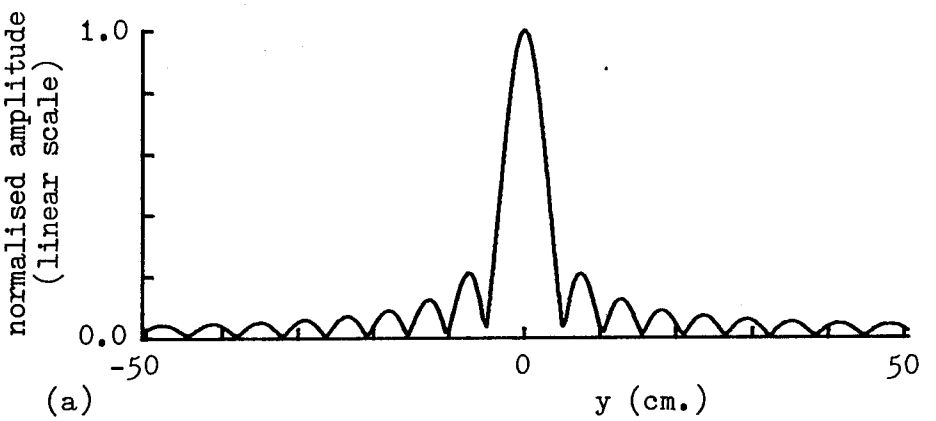

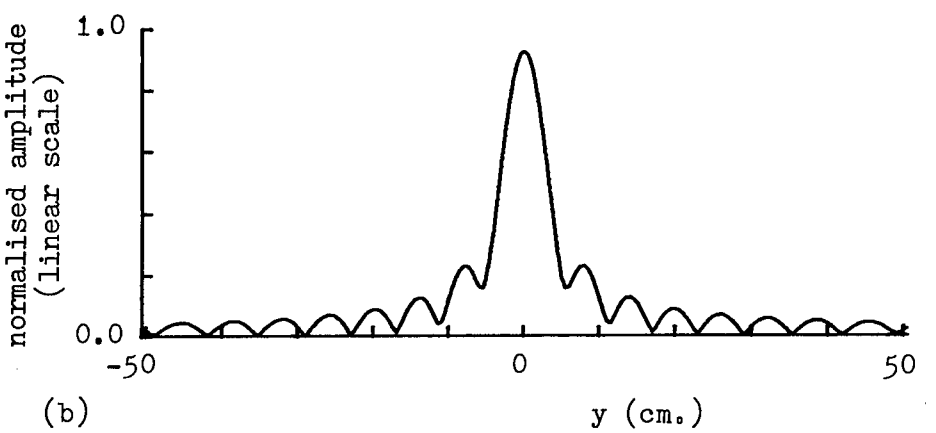

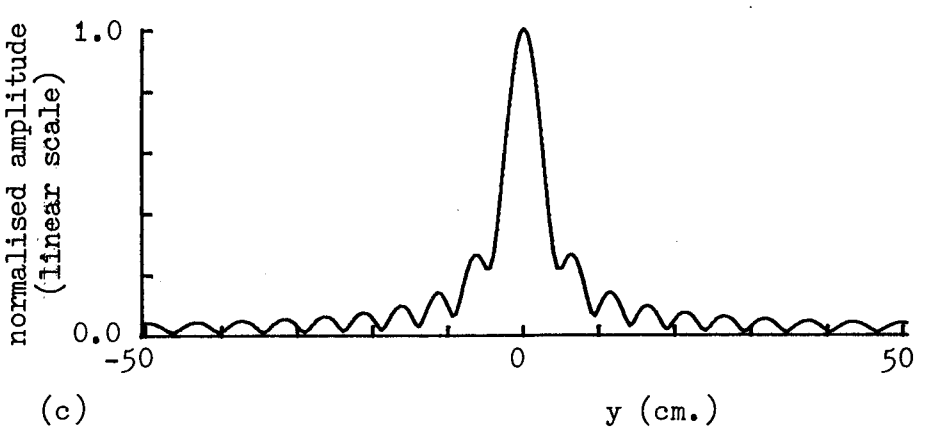

Fig. A1.6. Central impulse response of a weighting function extending over ±16°, R = 1.0m., (a) z = 0, (b) z = -10cm., (c) z = 10cm.

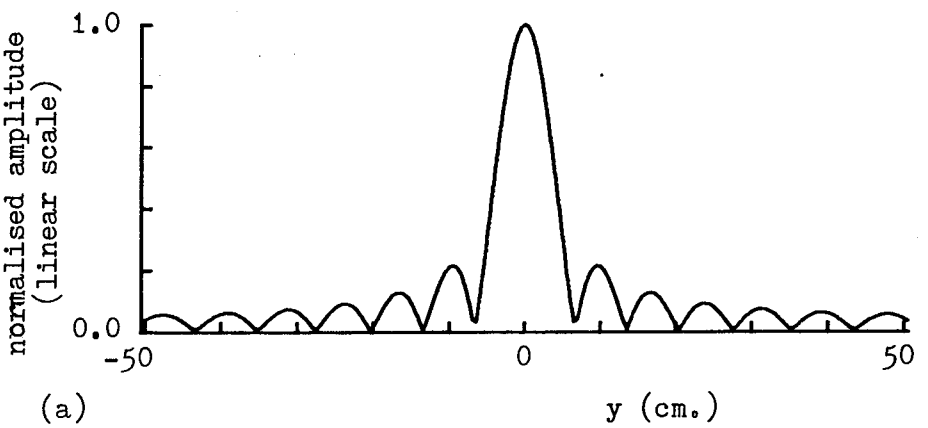

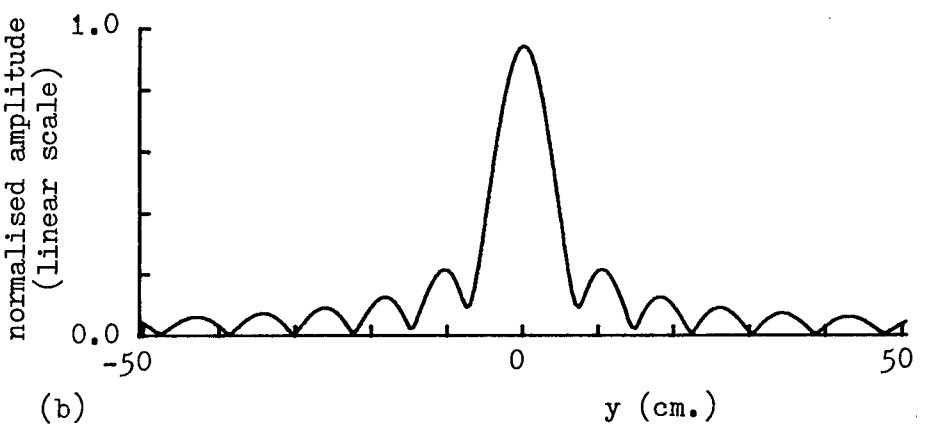

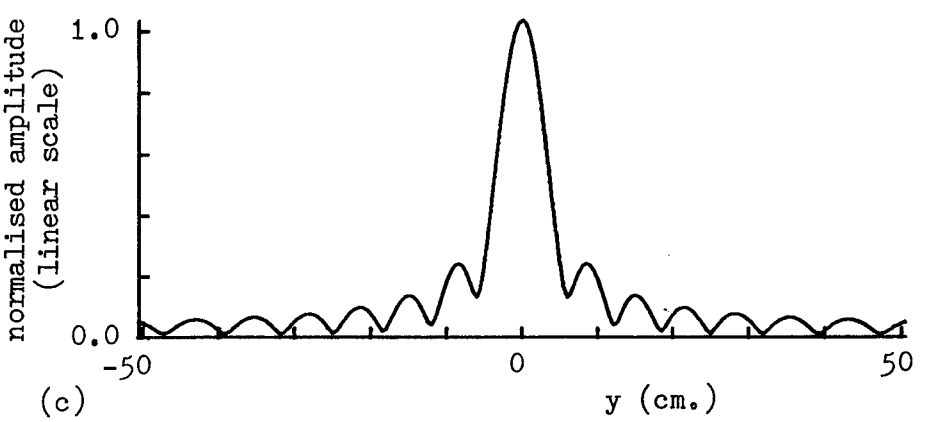

Fig. A1.7. Central impulse response of a weighting function extending over ±12°, R = 1.0m., (a) z = 0, (b) z = -10cm., (c) z = 10cm.

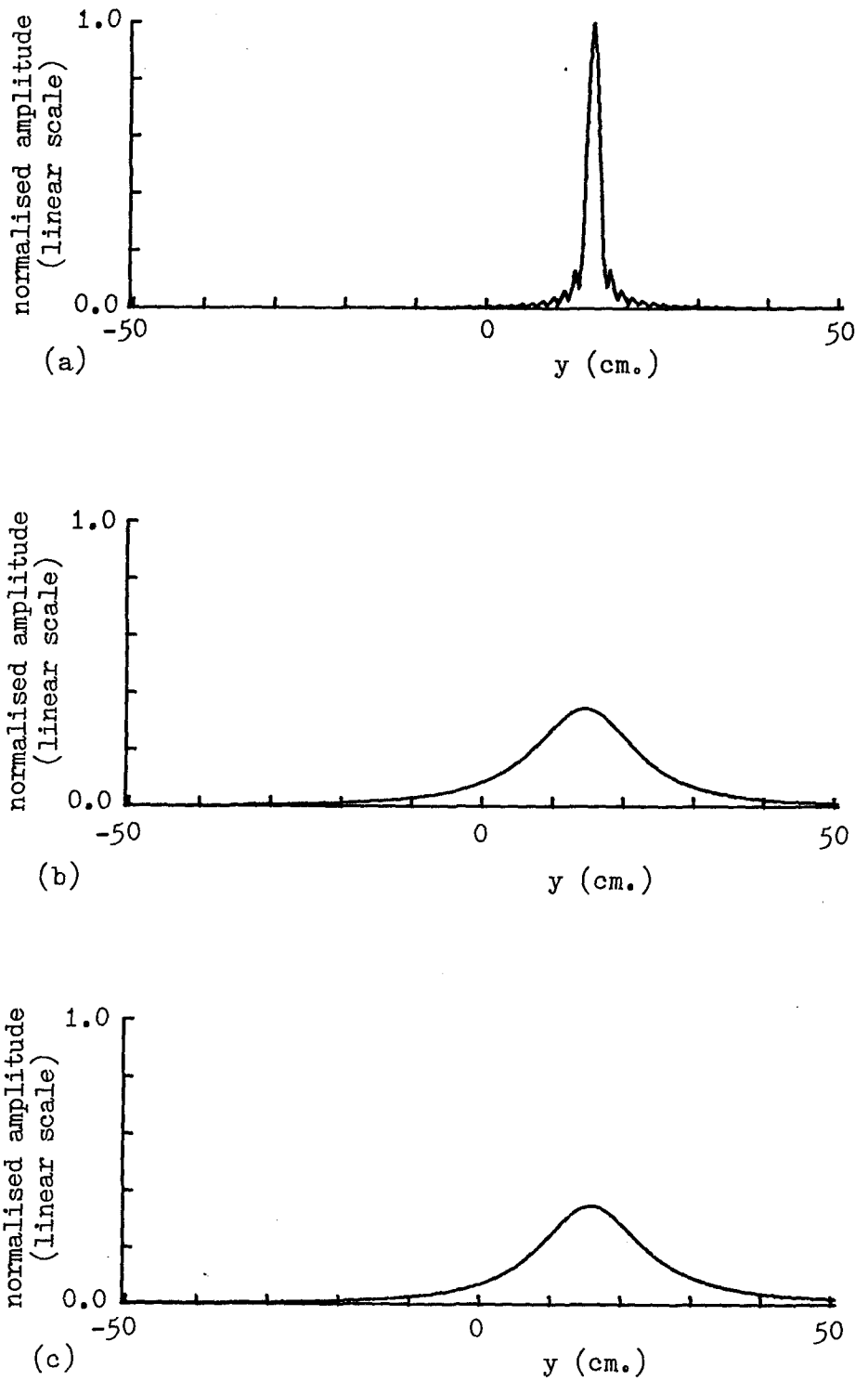

Fig. A1.8. Offset impulse response of a weighting function extending over ±90°, R = 1.0m., (a) z = 0, (b) z = -10cm., (c) z = 10cm.

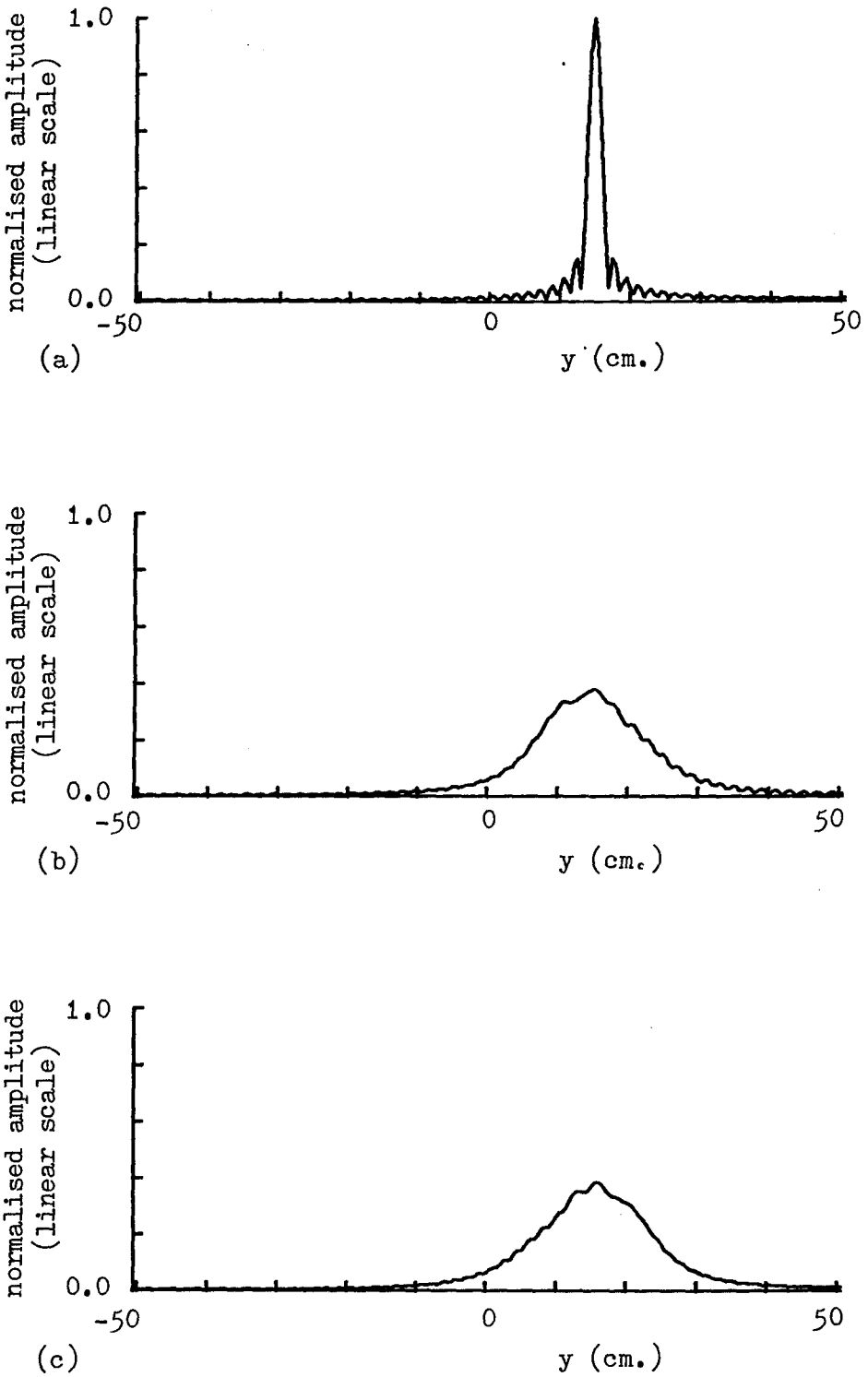

Fig. A1.9. Offset impulse response of a weighting function extending over ±60°, R = 1.0m., (a) z = 0, (b) z = -10cm., (c) z = 10cm.

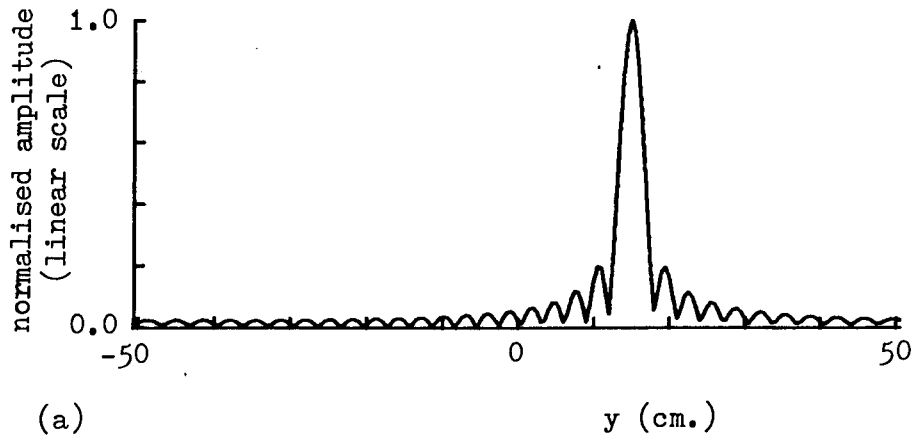

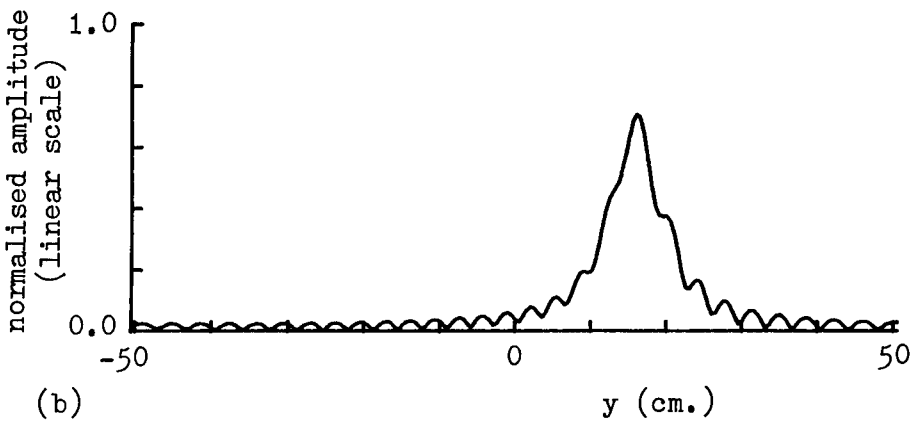

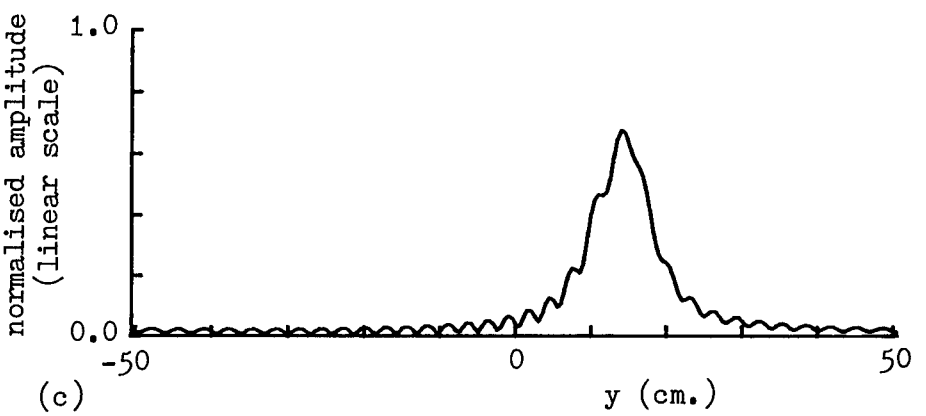

Fig. A1.10. Offset impulse response of a weighting function extending over ±30°, R = 1.0m., (a) z = 0, (b) z = -10cm., (c) z = 10cm.

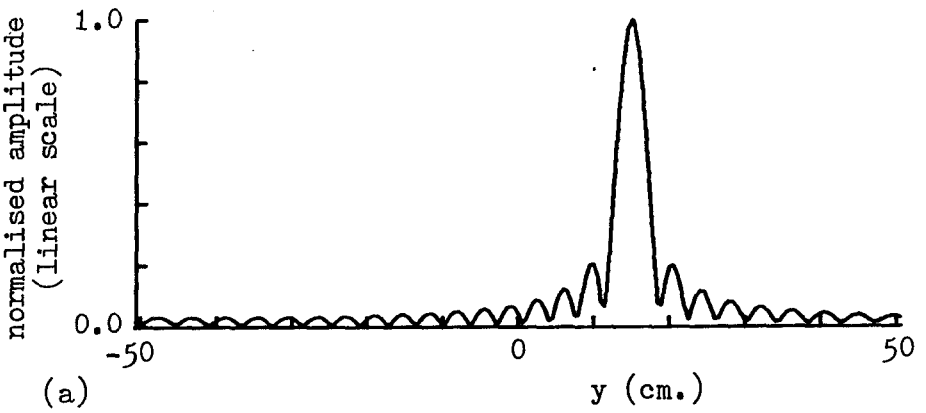

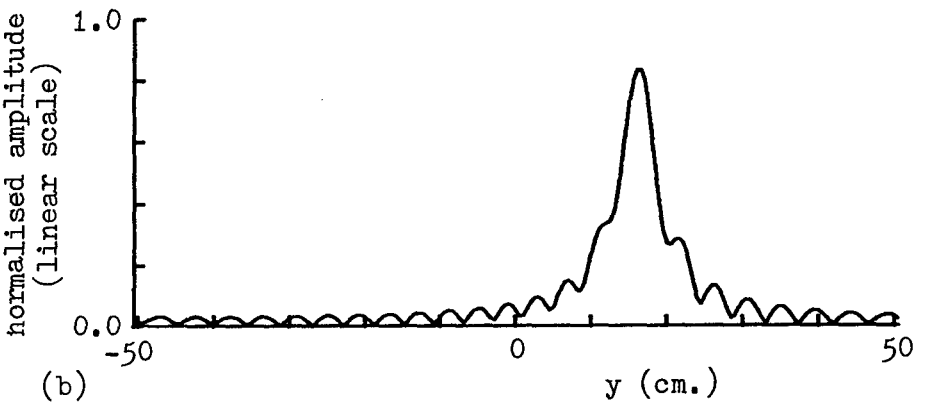

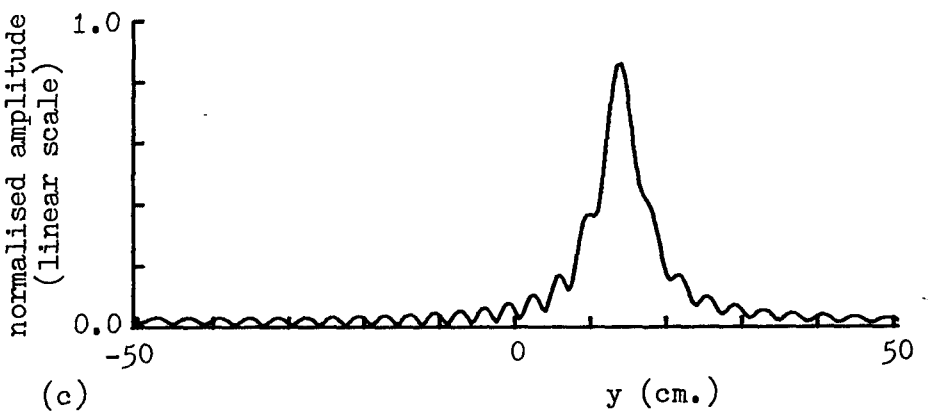

Fig. A1.11. Offset impulse response of a weighting function extending over ±24°, R = 1.0m., (a) z = 0, (b) z = -10cm., (c) z = 10cm.

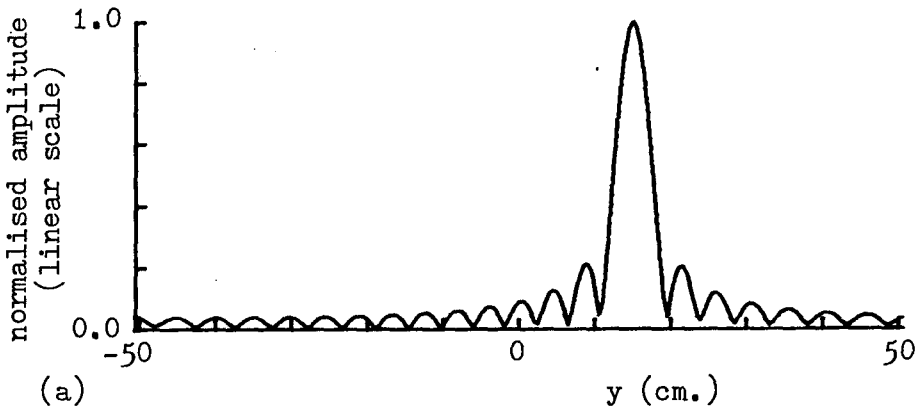

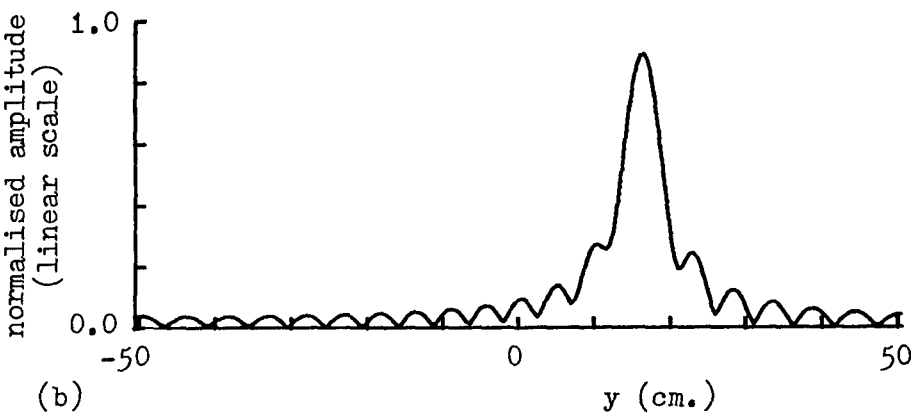

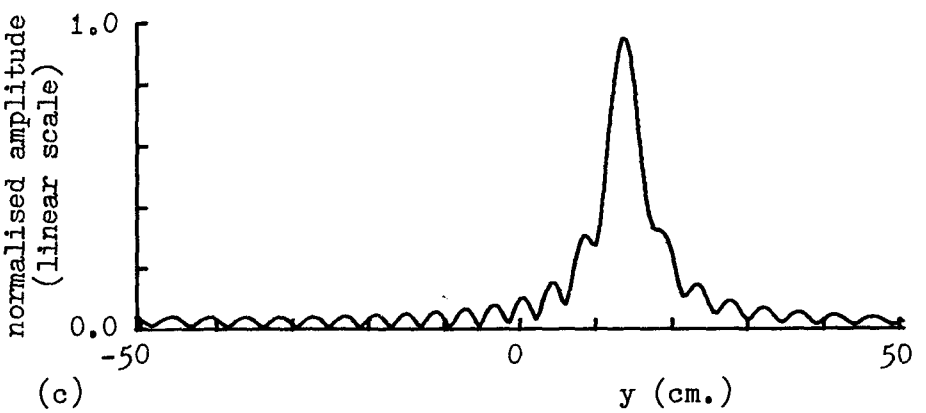

Fig. A1.12. Offset impulse response of a weighting function extending over ±20°, R = 1.0m., (a) z = 0, (b) z = -10cm., (c) z = 10cm.

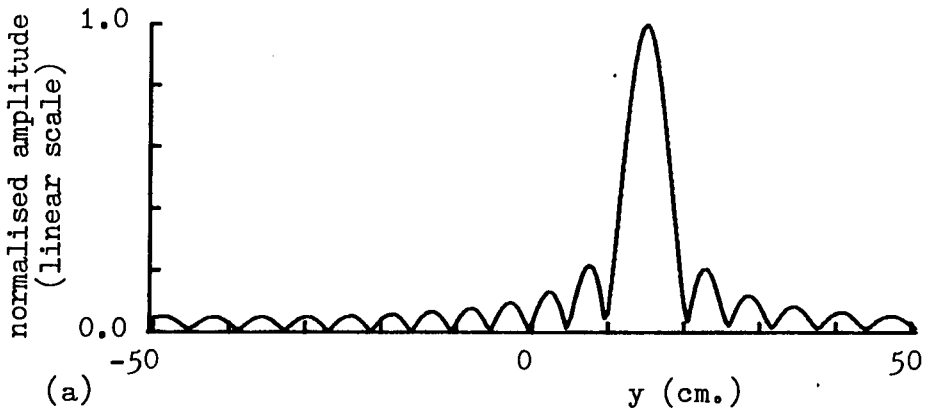

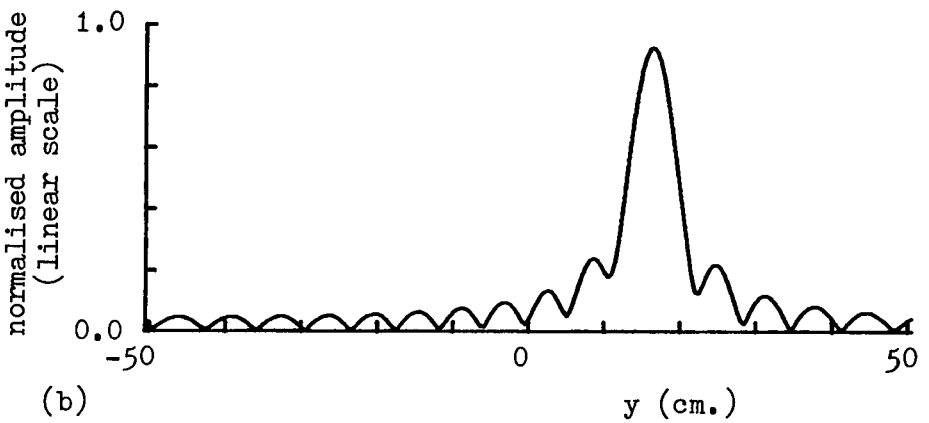

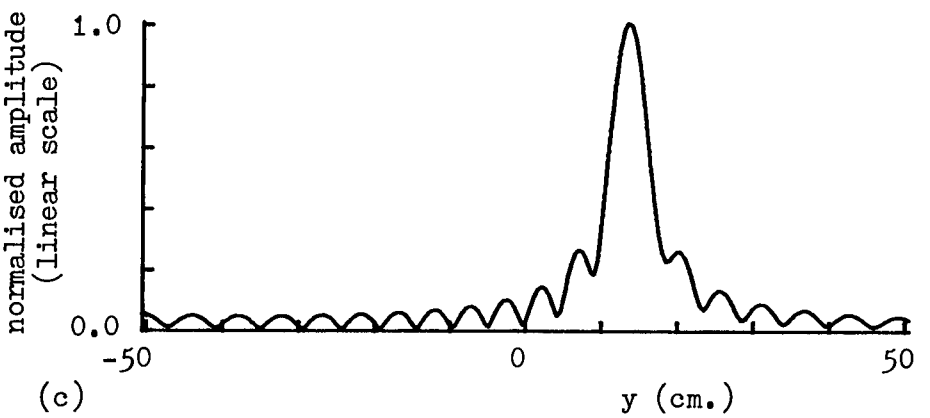

Fig. A1.13. Offset impulse response of a weighting function extending over ±16°, R = 1.0m., (a) z = 0, (b) z = -10cm., (c) z = 10cm.

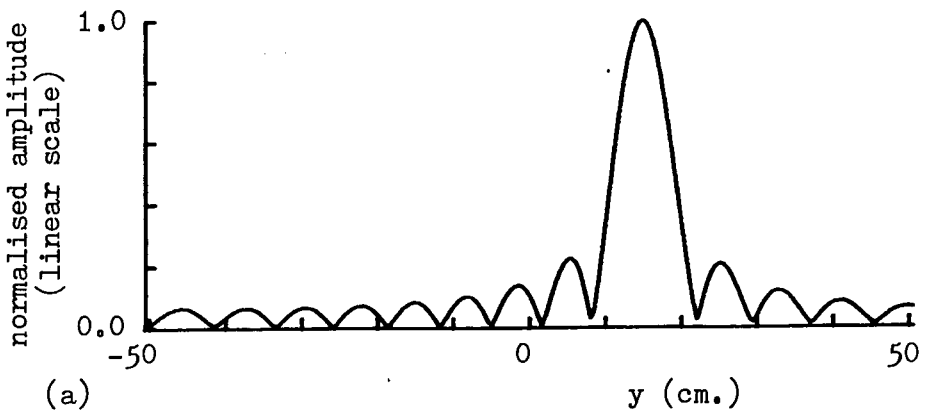

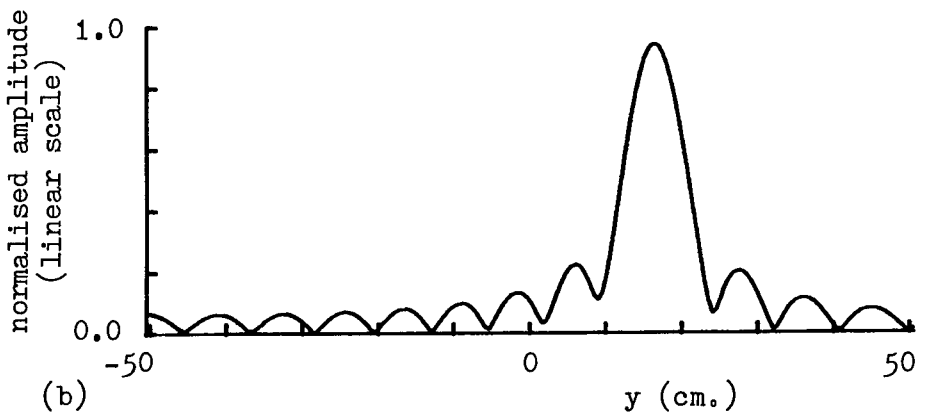

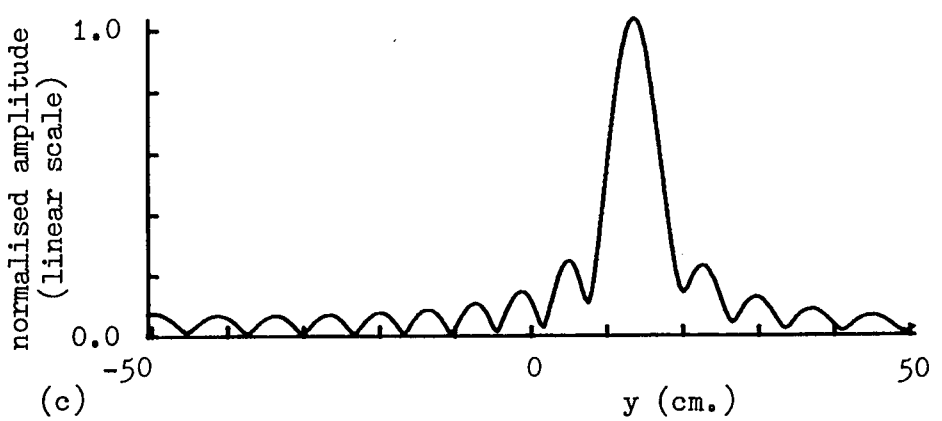

Fig. A1.14. Offset impulse response of a weighting function extending over ±12°, R = 1.0m., (a) z = 0, (b) z = -10cm., (c) z = 10cm.

for negative z and narrow for positive z. This effect too is observed but is only visible in those cases where the response maintains itself well enough for a comparison to be made. In addition, in the case of the offset impulse, it can be seen that the response moves slightly further from the origin for z = -10cm and moves a little towards the origin for z = +10cm. Again this is the effect of the scale change with varying z.

Appendix 2: SAMPLING EFFECTS

In this appendix a study is presented of the effects of variation of the sampling interval in a weighting function on the plane wave which can be synthesised. Near-field and far-field effects are examined. The standard parameters used throughout are that the frequency is 10GHz, all weighting functions extend over $\pm 25^{\circ}$ angular range being designed to yield a 30cm plane wave on the plane z = 0 and 100 iterations were performed in each case.

A2.1 Far-Field Weighting Functions

For the consideration of sampling effects on a weighting function positioned in the far field region, a measurement range of 100m is used as standard. The first example, Fig. A2.1, shows a 101-point weighting function with an angular spacing of 0.5°. The amplitude of the weighting function may be observed to possess the classical $\sin \theta/\theta$ form while the phase shows the corresponding 0° - 180° alternation. Fig. A2.2 shows the resulting synthesised plane wave for z = 0. Because of the fine sampling, no outer periods of the plane wave (grating lobes) are visible within the displayed region while the quality of the plane wave is very acceptable in both amplitude and phase.

The sampling interval is increased to 2.5° (21 points) for the weighting function of Fig. A2.3 and now the synthesised plane wave, shown in Fig. A2.4, shows the encroachment of the neighbouring periods (weighted with a linear phase) upon the displayed area. Continuing with this series, Fig. A2.5 illustrates the weighting function

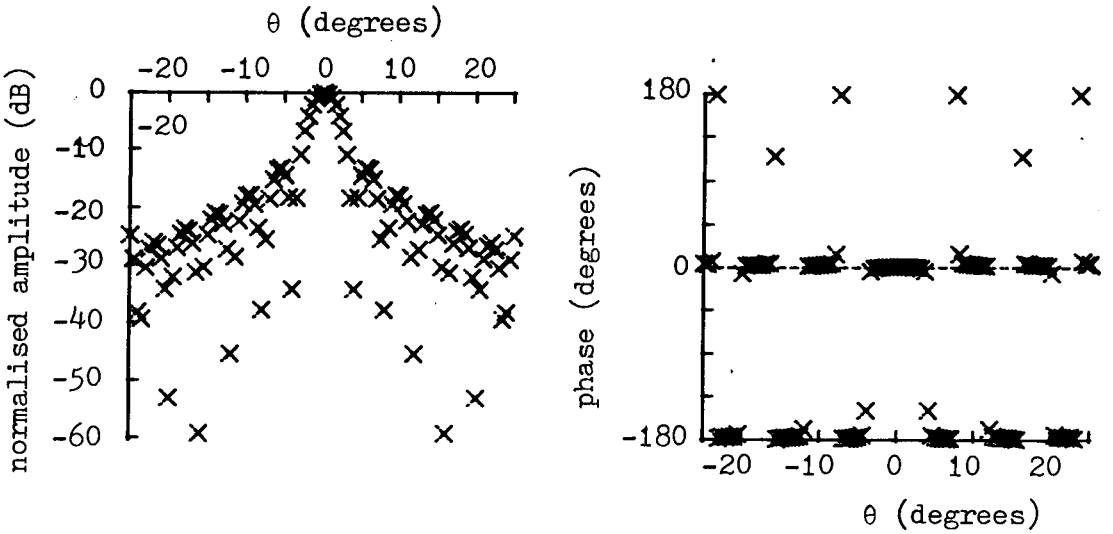

Fig. A2.1. 101-point weighting function for R = 100m.

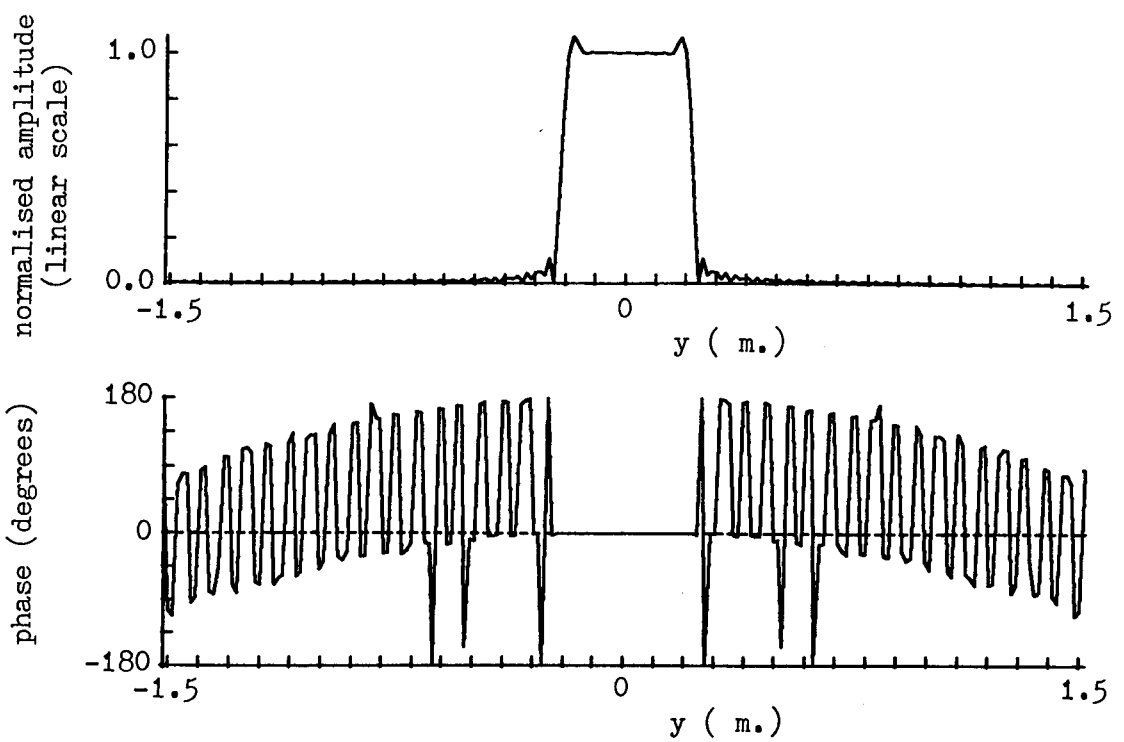

Fig. A2.2. Synthesised plane wave due to weighting function of Fig. A2.1.

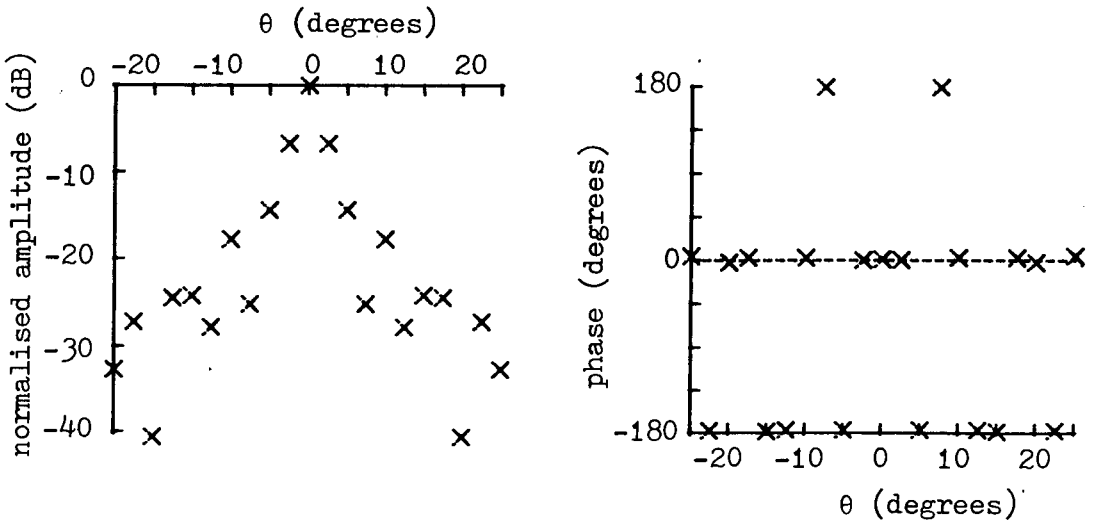

Fig. A2.3. 21-point weighting function for R = 100m.

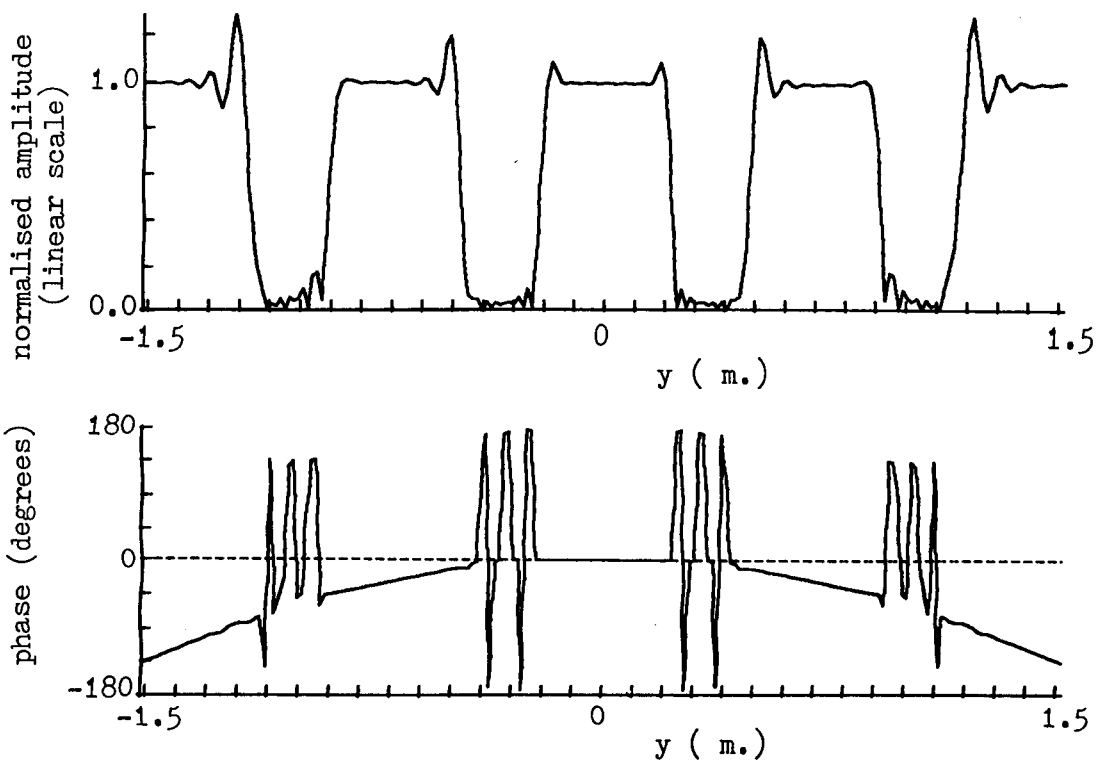

Fig. A2.4. Synthesised plane wave due to weighting function of Fig. A2.3.

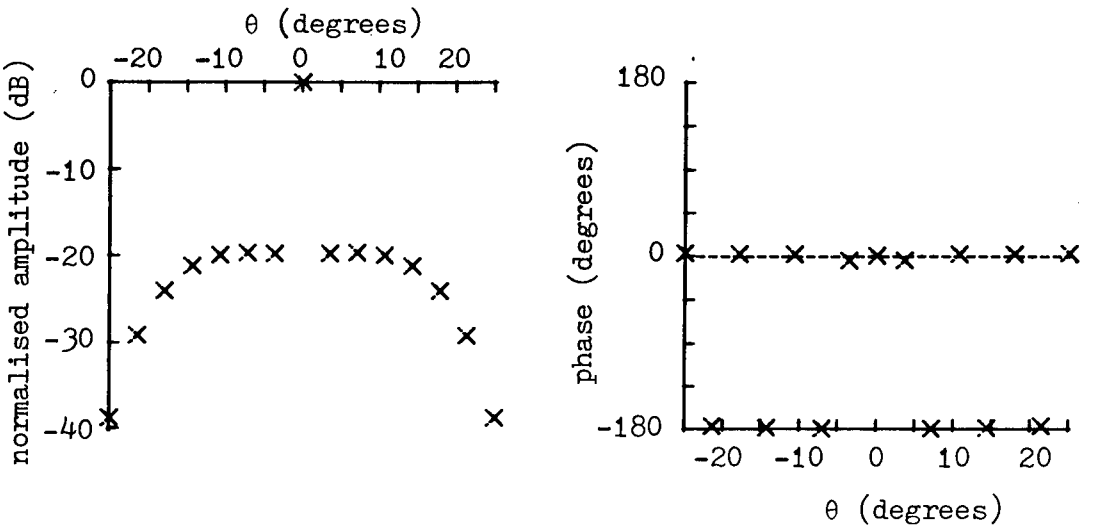

Fig. A2.5. 15-point weighting function for R = 100m.

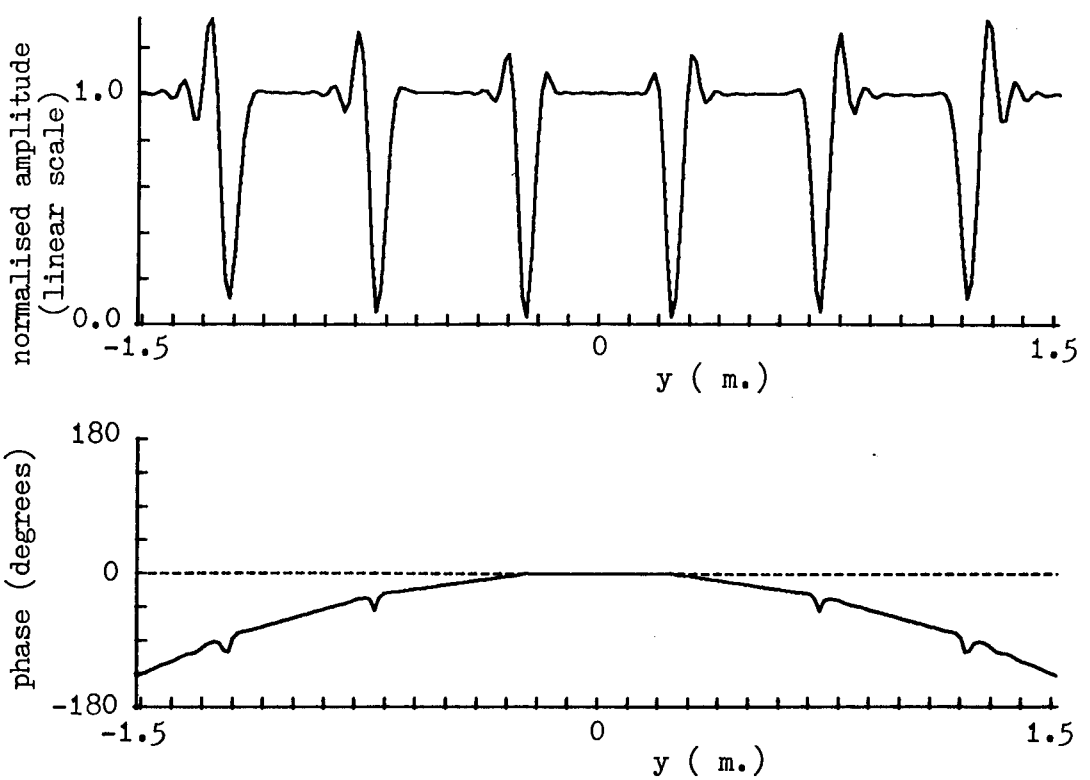

Fig. A2.6. Synthesised plane wave due to weighting function of Fig. A2.5.

with 15 points, spacing 3.57^{o} and it is apparent that points other than that at the centre are beginning to be suppressed in amplitude and the neighbouring plane wave periods (Fig. A2.6) are coming close to overlapping. The trend continues with Fig. A2.7 (13 points at 4.16^{o}) and Fig. A2.8 (the synthesised plane wave) and by Fig. A2.9 (11 points at 5.0^{o}) the points, other than the centre value, of the weighting function have been suppressed to below -40dB and the plane wave neighbouring periods in Fig. A2.10 have almost completely merged (apart from a hint of the residual linear phase areas still discernible). In this latter example, the sampling has almost reached the standard Nyquist rate of λ/D spacing (5.7^{o}). The final example of the far-field is for a 9-point weighting function (Fig. A2.11) spacing 6.25^{o} in which the outer points have been supressed to about -50dB or below. The synthesised plane wave, shown in Fig. A2.12, has now reduced almost completely to a point-source distribution.

A2.2 Near-Field Weighting Functions

Having examined closely the case of a weighting function placed in the far-field region, we now turn our attention to the case of a near-field weighting function. In this case the measurement range of 1.0m has been used. This is equivalent to $0.33D^{2}/\lambda$.

The first example is, as for the far-field case, of a 101-point weighting function with spacing 0.5^{o}, shown as Fig. A2.13. It may be observed that the form is now of a very defocussed, bifurcated function with a strong phase

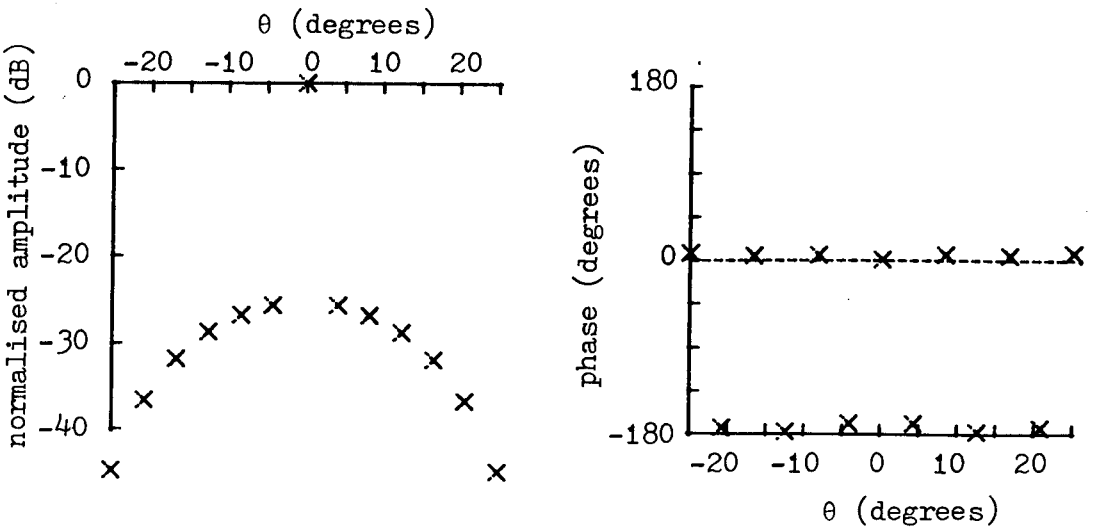

Fig. A2.7. 13-point weighting function for R = 100m.

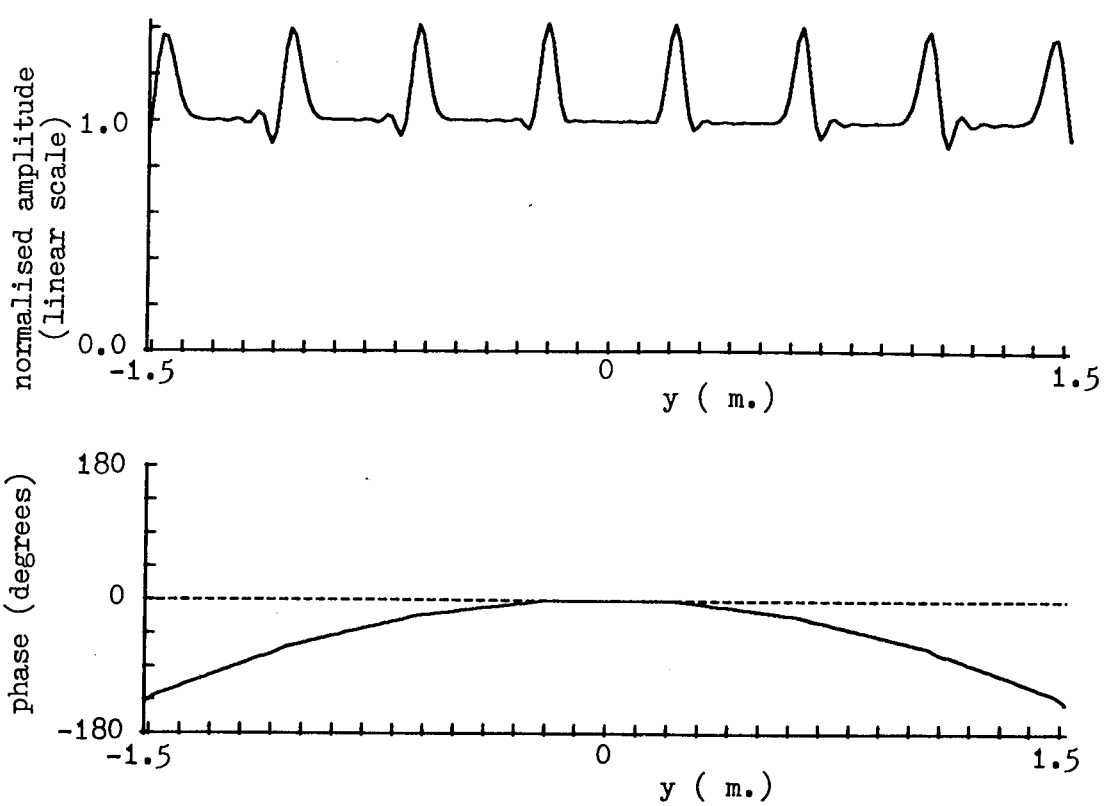

Fig. A2.8. Synthesised plane wave due to weighting function of Fig. A2.7.

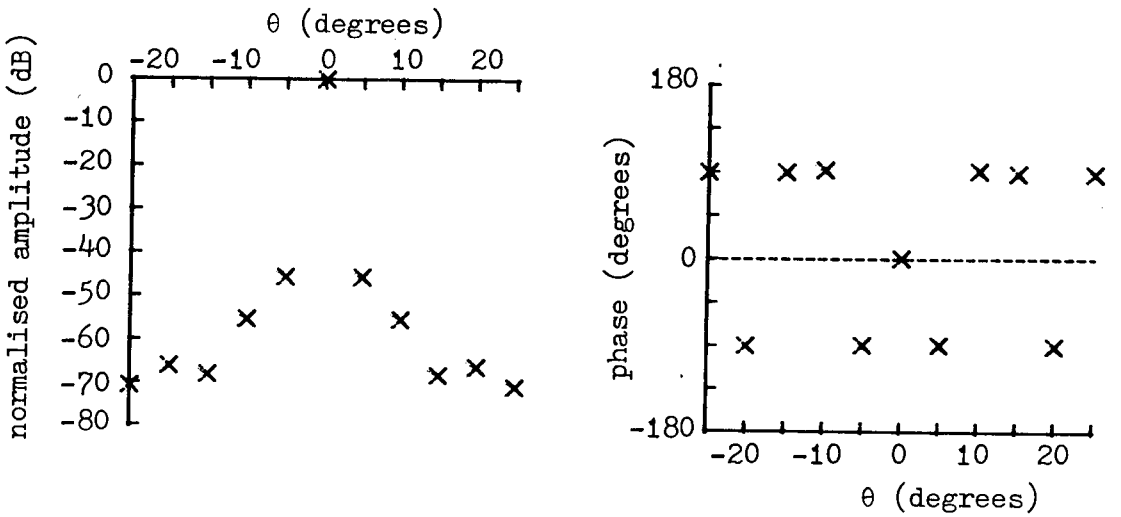

Fig. A2.9. 11-point weighting function for R = 100m.

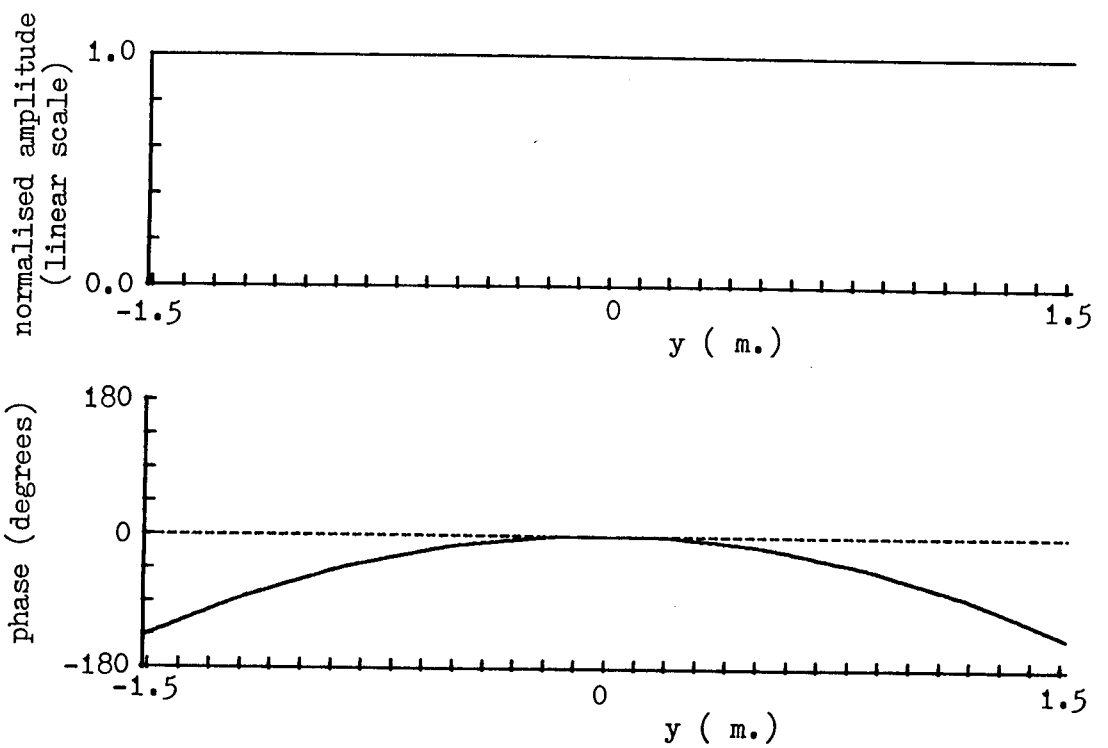

Fig. A2.10. Synthesised plane wave due to weighting function of Fig. A2.9.

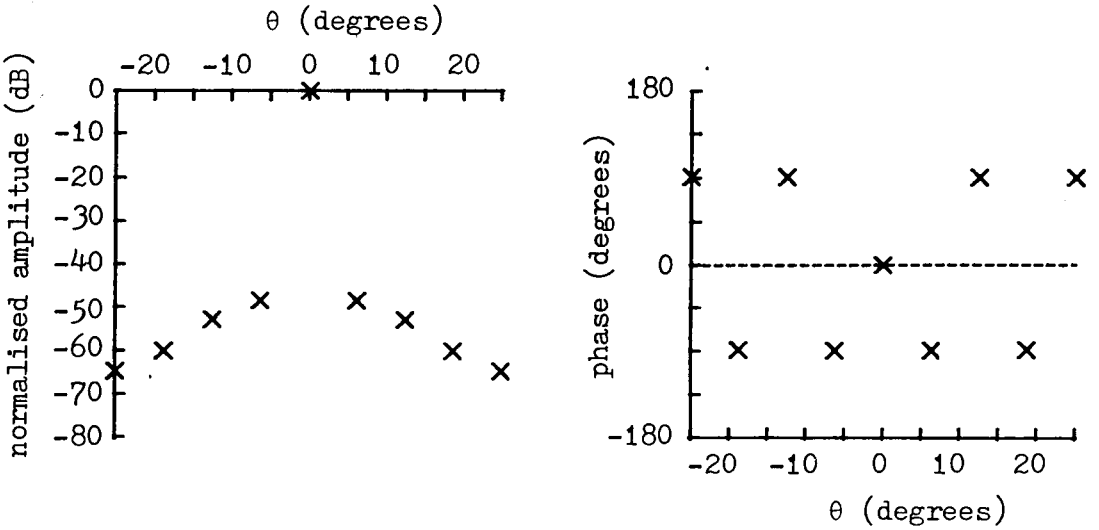

Fig. A2.11. 9-point weighting function for R = 100m.

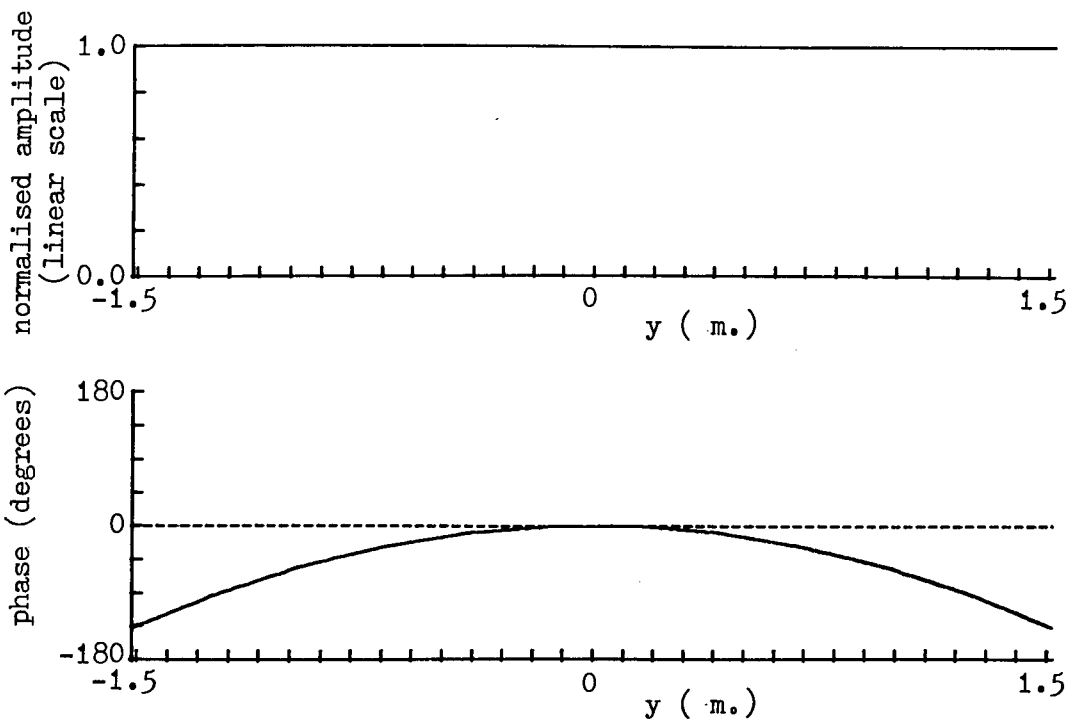

Fig. A2.12. Synthesised plane wave due to weighting function of Fig. A2.11.

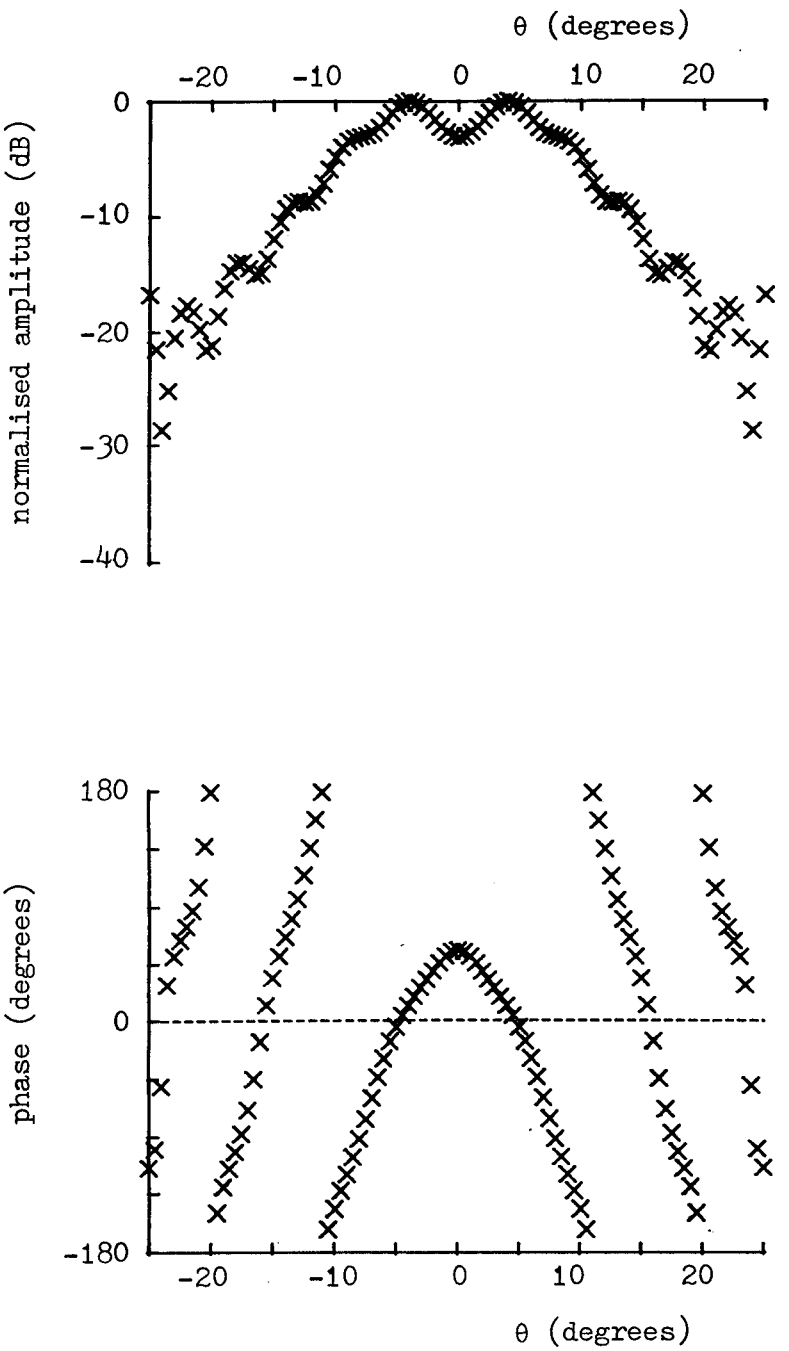

Fig. A2.13. 101-point weighting function for R = 1.0m.

taper. The synthesised plane wave is shown in great detail as Fig. A2.14 (on the plane z = 0) and in expanded form as Fig. A2.15; Fig. A2.16 (z = -15cm) and expanded as Fig. A2.17; and Fig. A2.18 (z = +15cm) and expanded as Fig. A2.19. The high quality of the plane wave is immediately apparent with the expected slight (but unimportant) ringing at the edge of the distribution for z = +15cm.

Fig. A2.20 shows a 21-point (2.5^{o} spacing) weighting function and the synthesised plane wave is shown (for the same paramters as above) in Figs. A2.21 to A2.26. The grating lobes are now appearing at either side of the displayed area on Figs. A2.21, A2.23 and A2.25 and these display particularly clearly the effects of the scale change predicted in Chapter 2. The quality of the plane wave is still quite acceptable.

The next set of graphs illustrate the situation for a 15-point weighting function, spacing 3.57^{o}. The weighting function is illustrated in Fig. A2.27 and the synthesised plane wave in Figs. A2.28 to A2.33. By now the weighting function is taking on a slightly different character with the edge points being suppressed to -30dB and the synthesised plane wave, particularly for z = +15cm, is displaying more severe ringing at the edges as the neighbouring periods of the plane wave approach.

The trend continues in the next case where the weighting function (Fig. A2.34) now has 13 points spaced by 4.16^{o}. The synthesised plane wave is shown in Figs. A2.35 to A2.40. Very minor degradation in the plane wave quality is now becoming apparent particularly in the cases

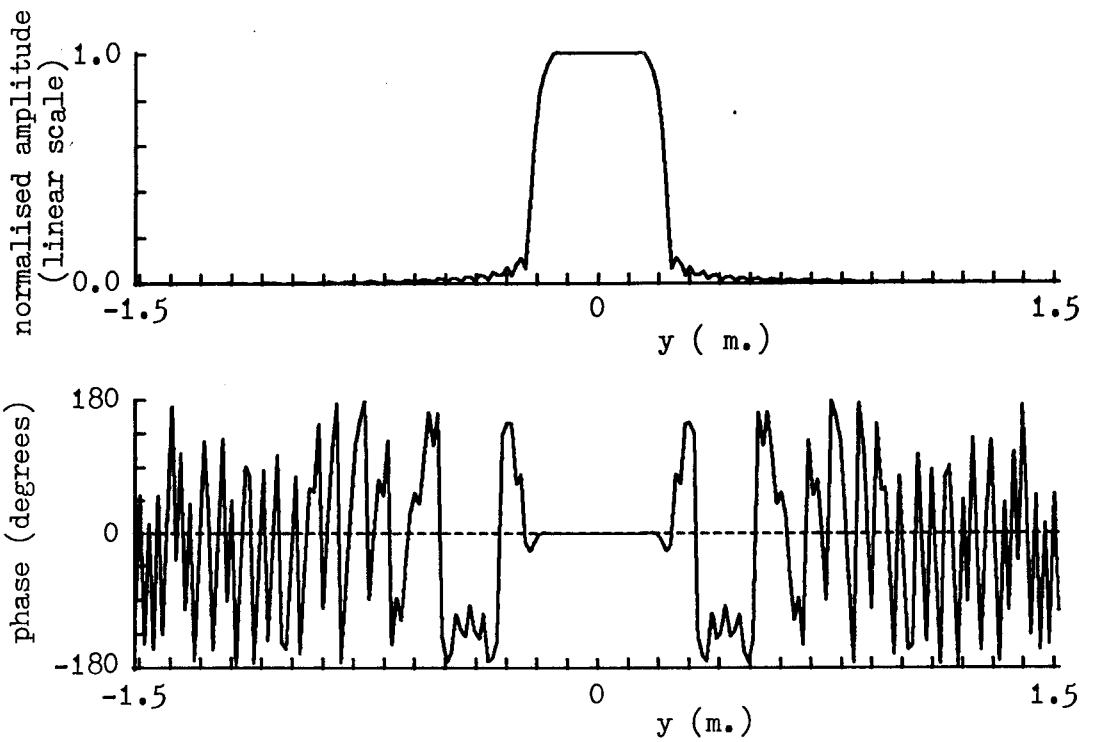

Fig. A2.14. Synthesised plane wave due to weighting function of Fig. A2.13. z = 0.

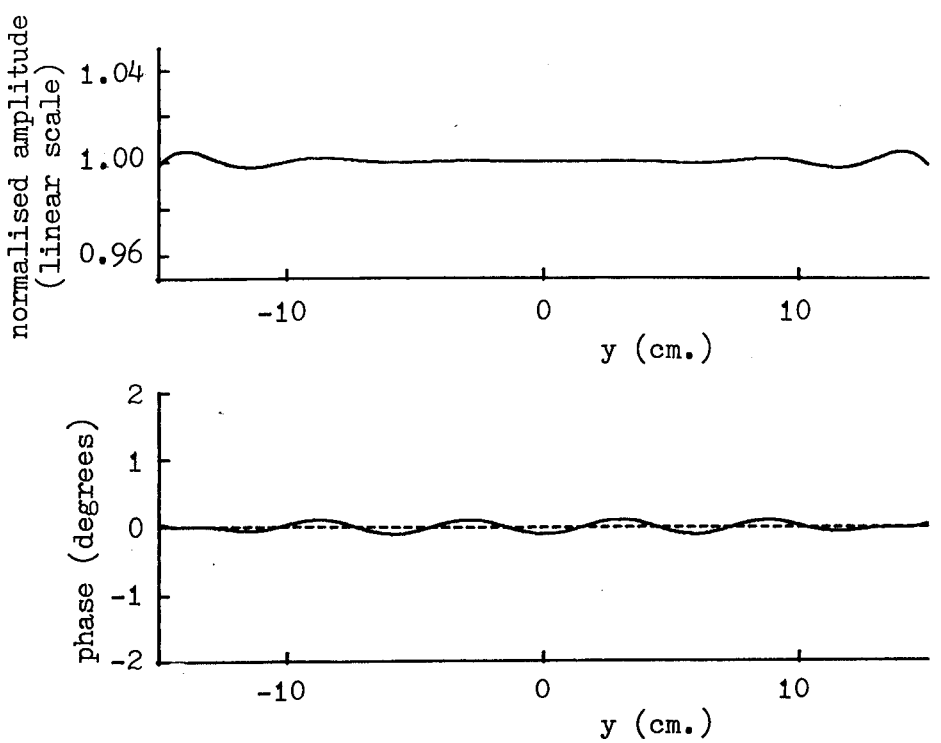

Fig. A2.15 Expanded-scale version of plane wave of Fig. A2.14.

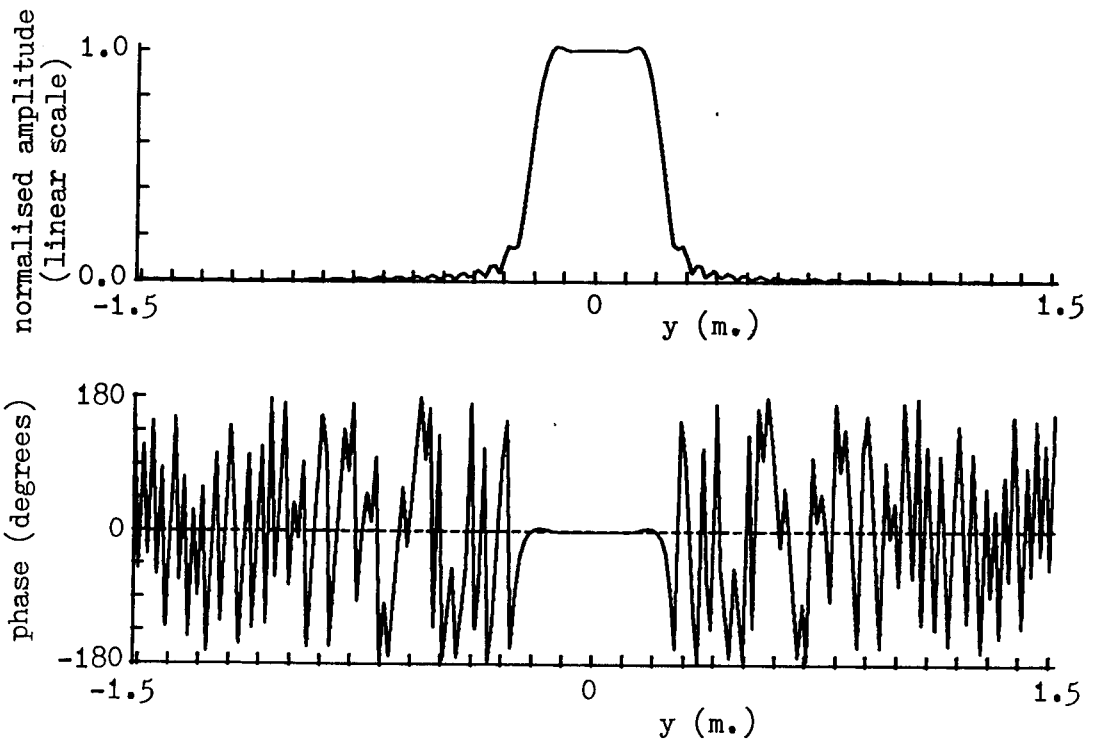

Fig. A2.16. Synthesised plane wave due to weighting function of Fig. A2.13. z = -15cm.

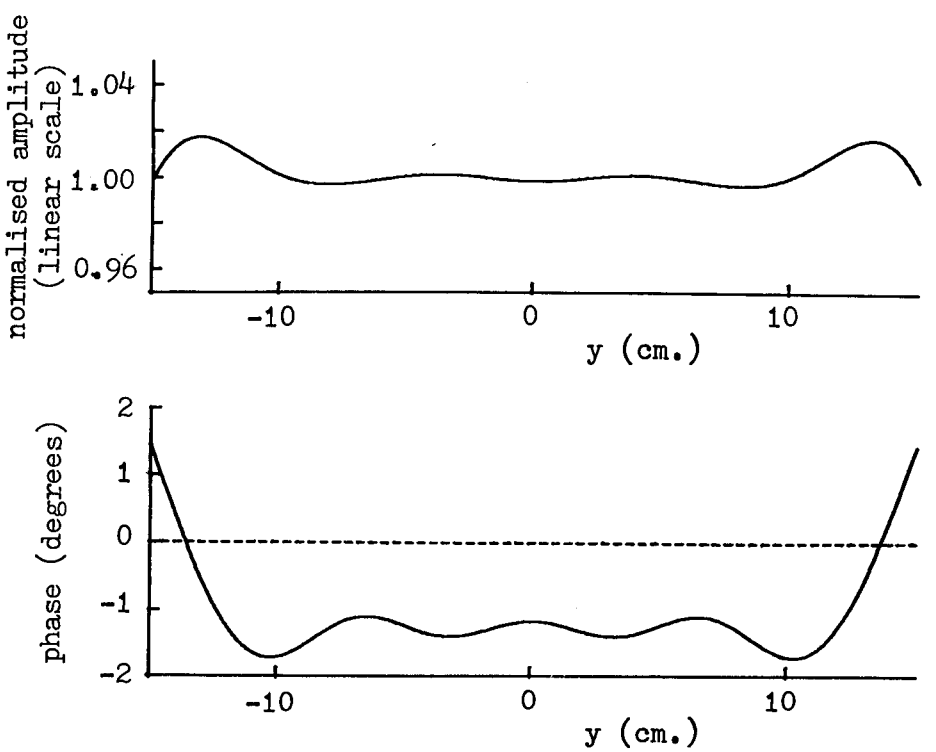

Fig. A2.17. Expanded-scale version of plane wave of Fig. A2.16.

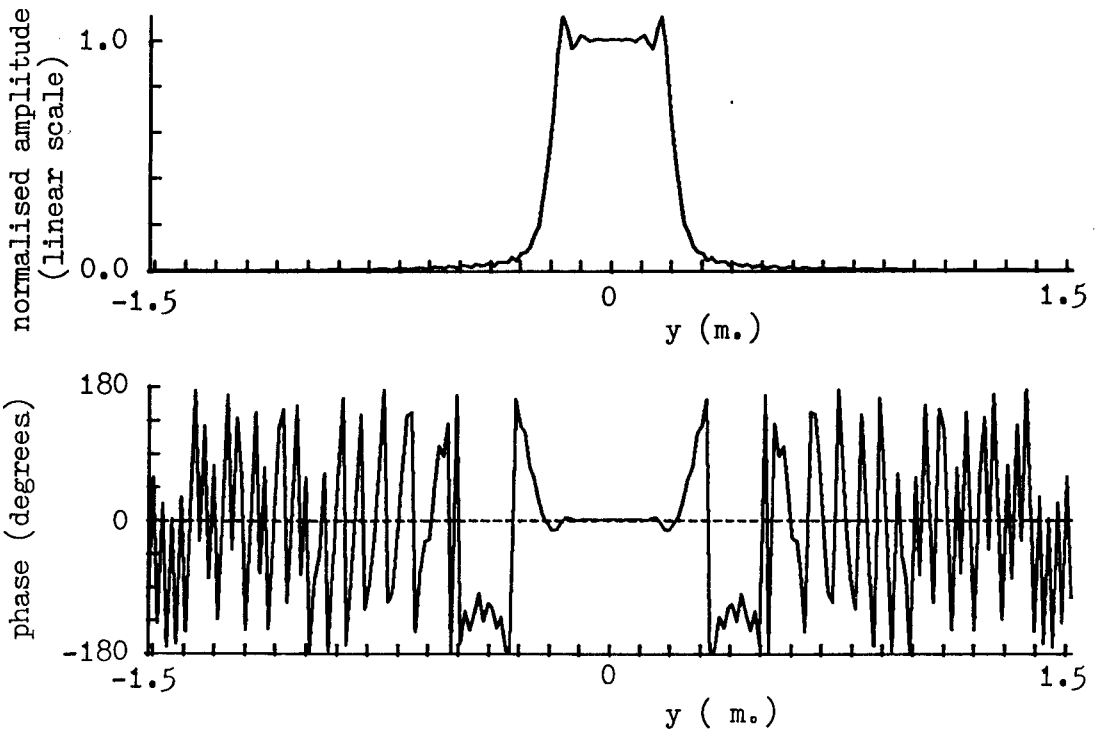

Fig. A2.18. Synthesised plane wave due to weighting function of Fig. A2.13. z = +15cm.

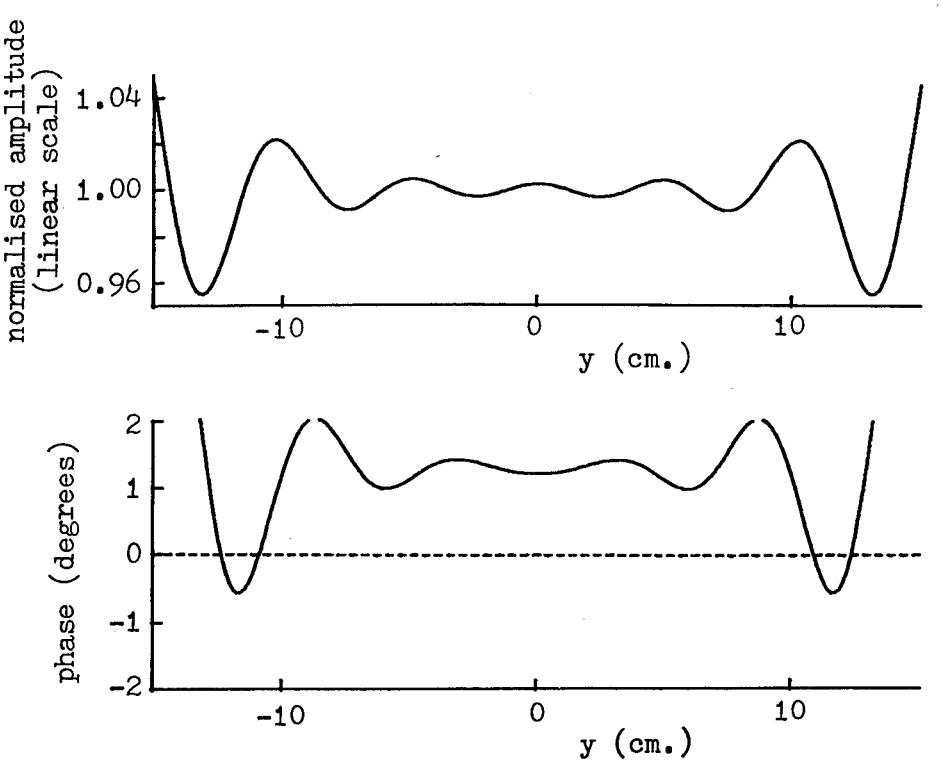

Fig. A2.19. Expanded-scale version of plane wave of Fig. A2.18.

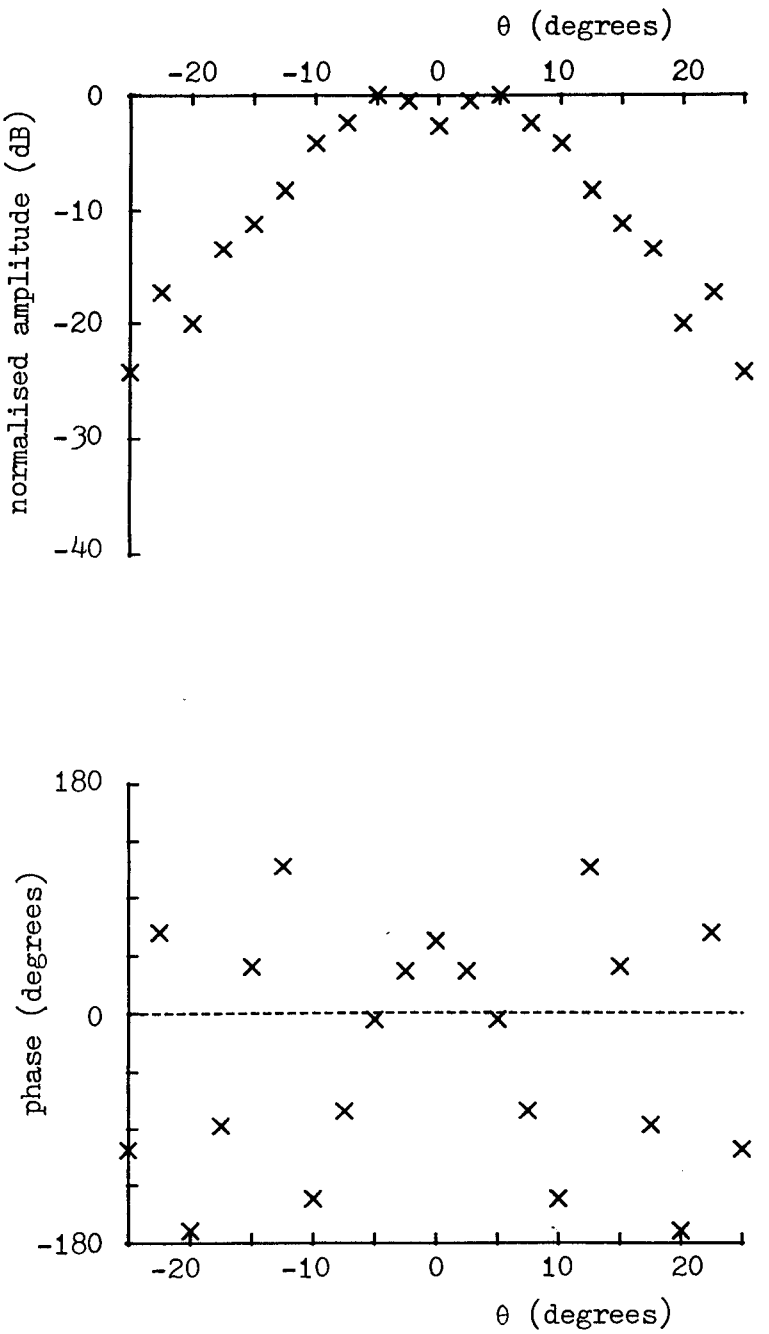

Fig. A2.20. 21-point weighting function for R = 1.0m.

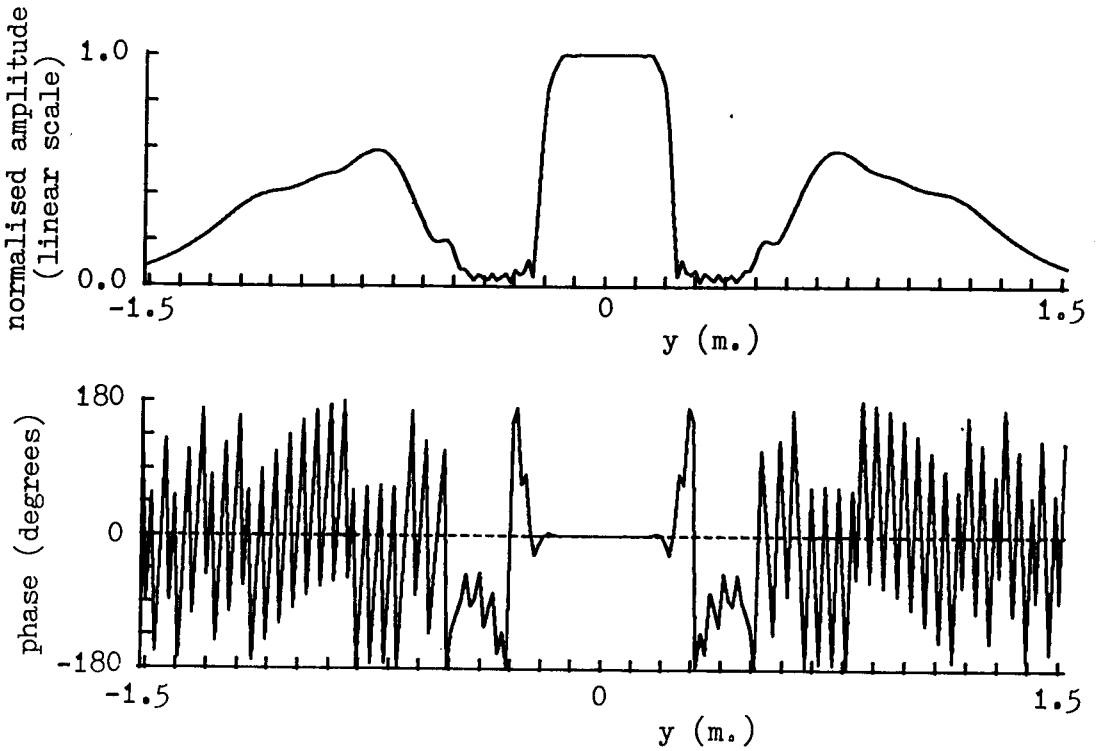

Fig. A2.21. Synthesised plane wave due to weighting function of Fig. A2.20. z = 0.

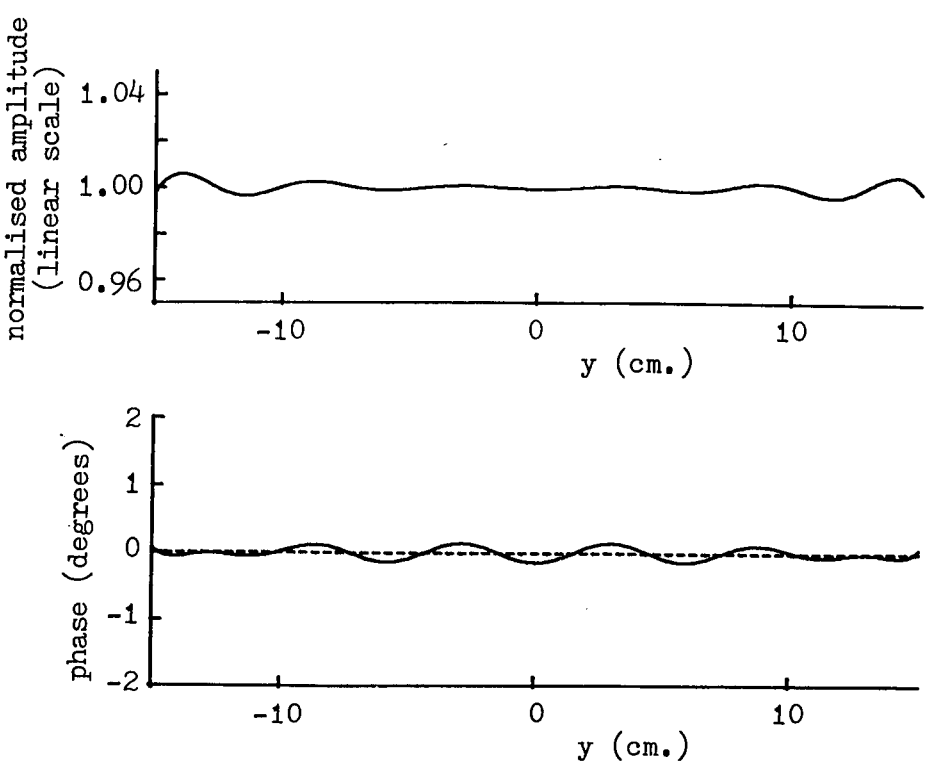

Fig. A2.22. Expanded-scale version of plane wave of Fig. A2.21.

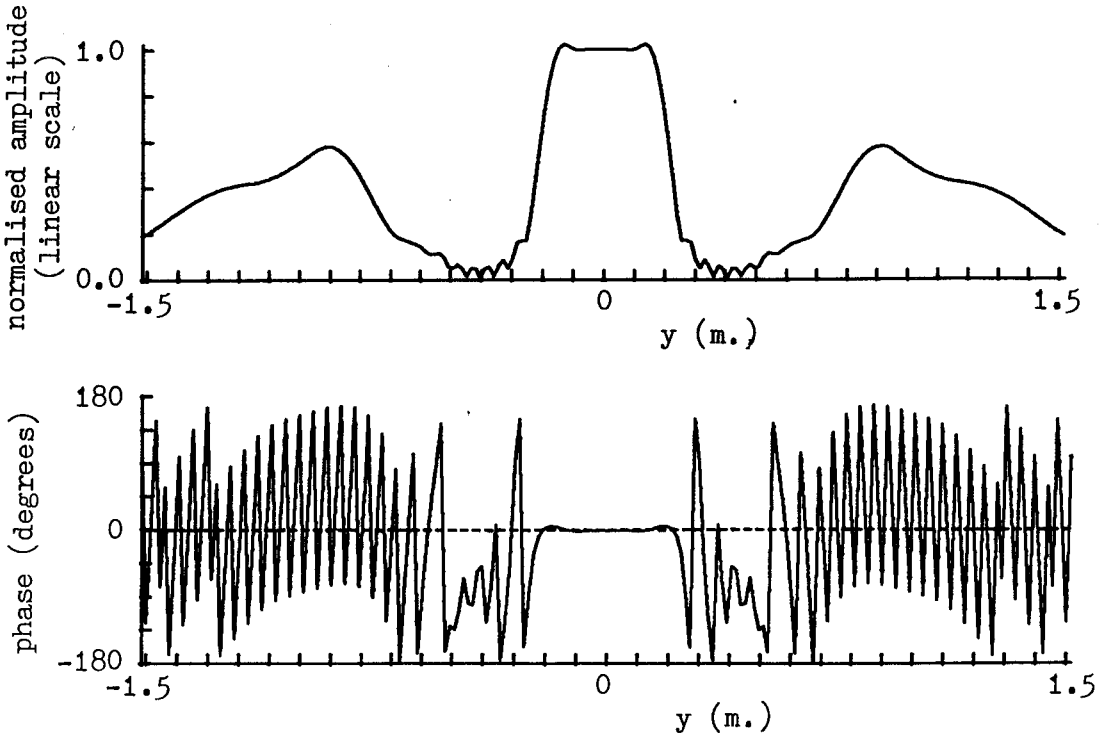

Fig. A2.23. Synthesised plane wave due to weighting function of Fig. A2.20. z = -15cm.

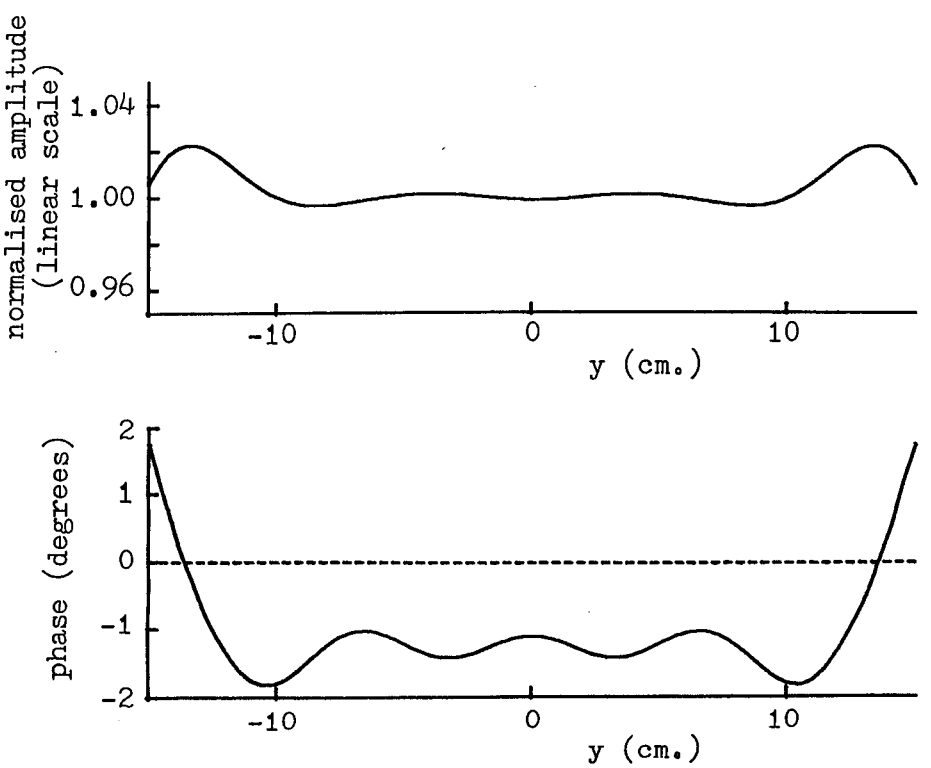

Fig. A2.24. Expanded-scale version of plane wave of Fig. A2.23.

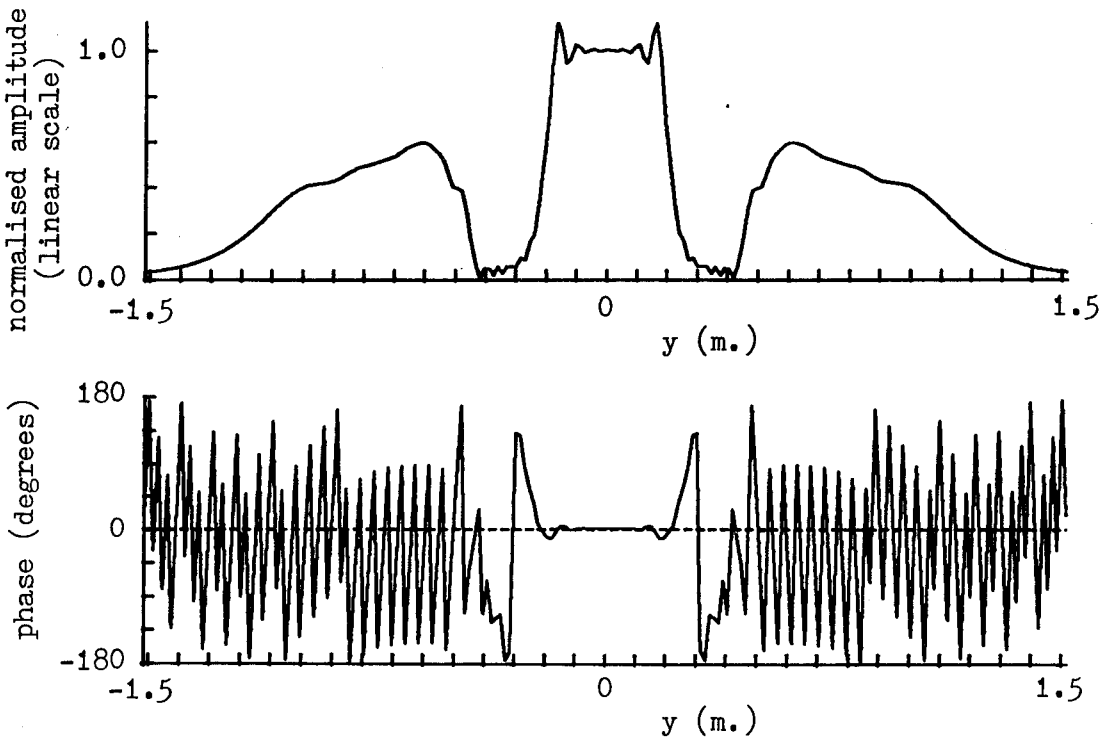

Fig. A2.25. Synthesised plane wave due to weighting function of Fig. A2.20. z = +15cm.

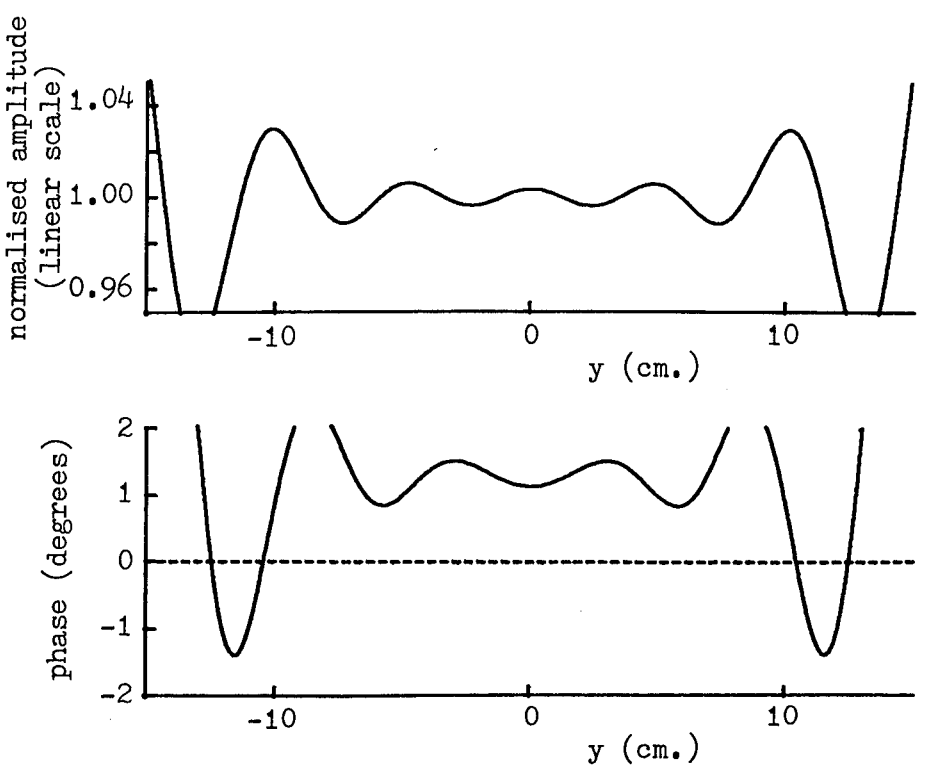

Fig. A2.26. Expanded-scale version of plane wave of Fig. A2.25.

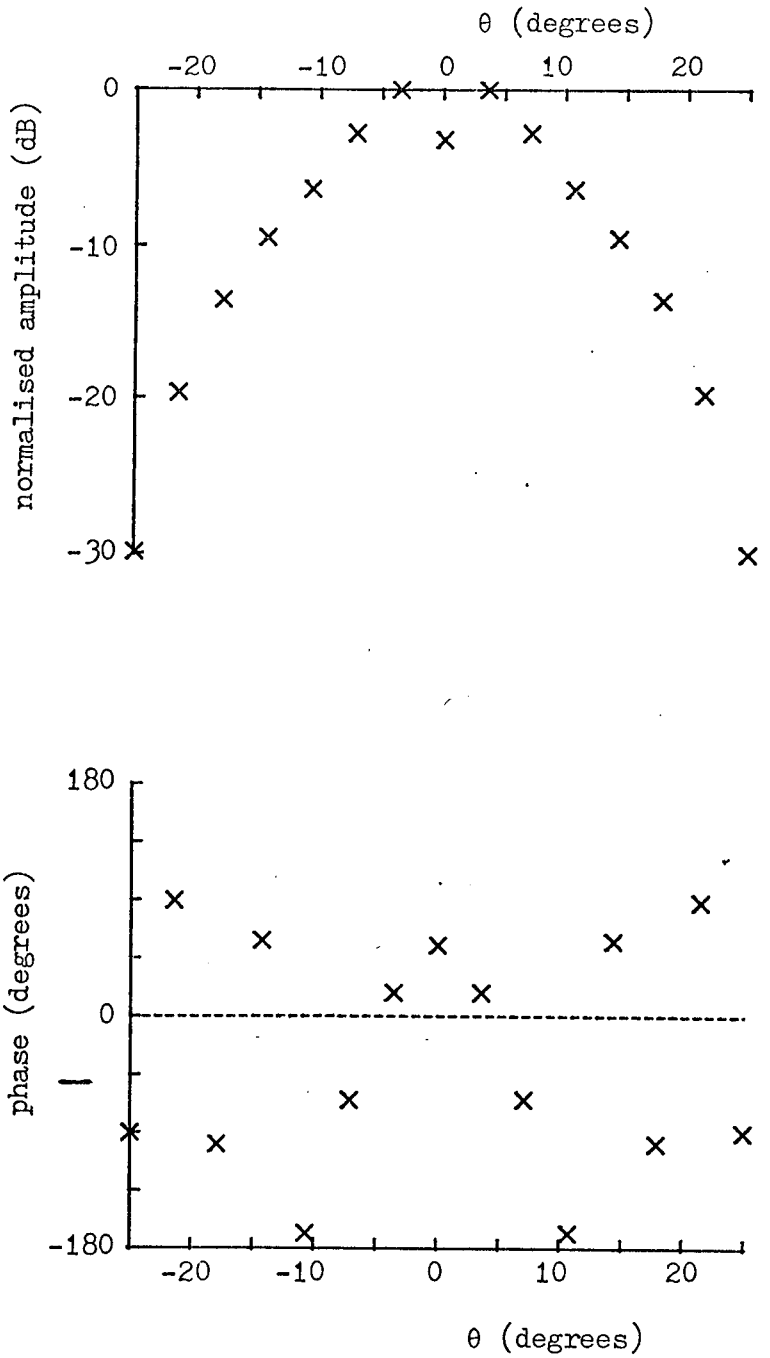

Fig. A2.27. 15-point weighting function for R = 1.0m.

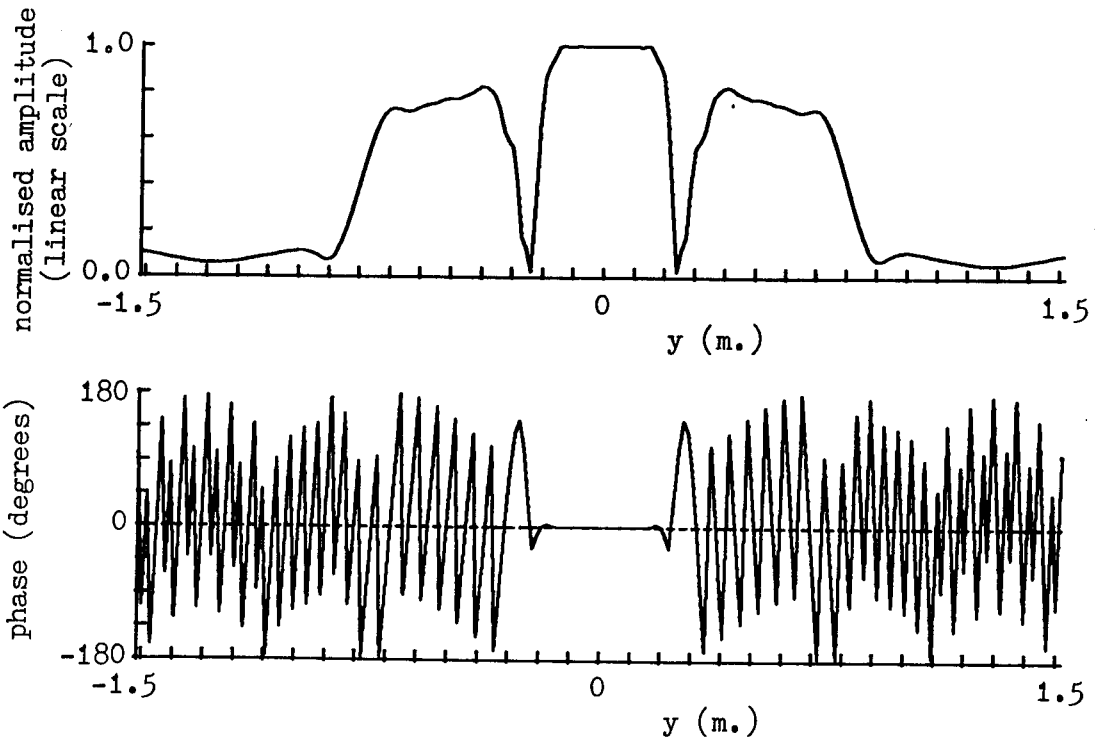

Fig. A2.28. Synthesised plane wave due to weighting function of Fig. A2.27. z = 0

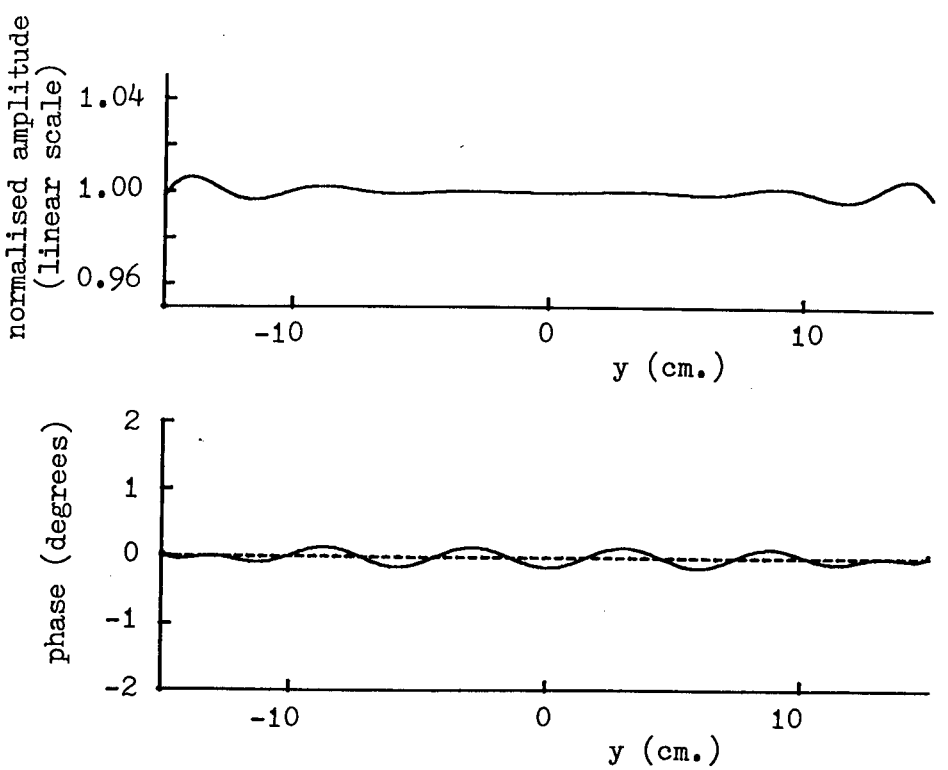

Fig. A2.29. Expanded-scale version of plane wave of Fig. A2.28.

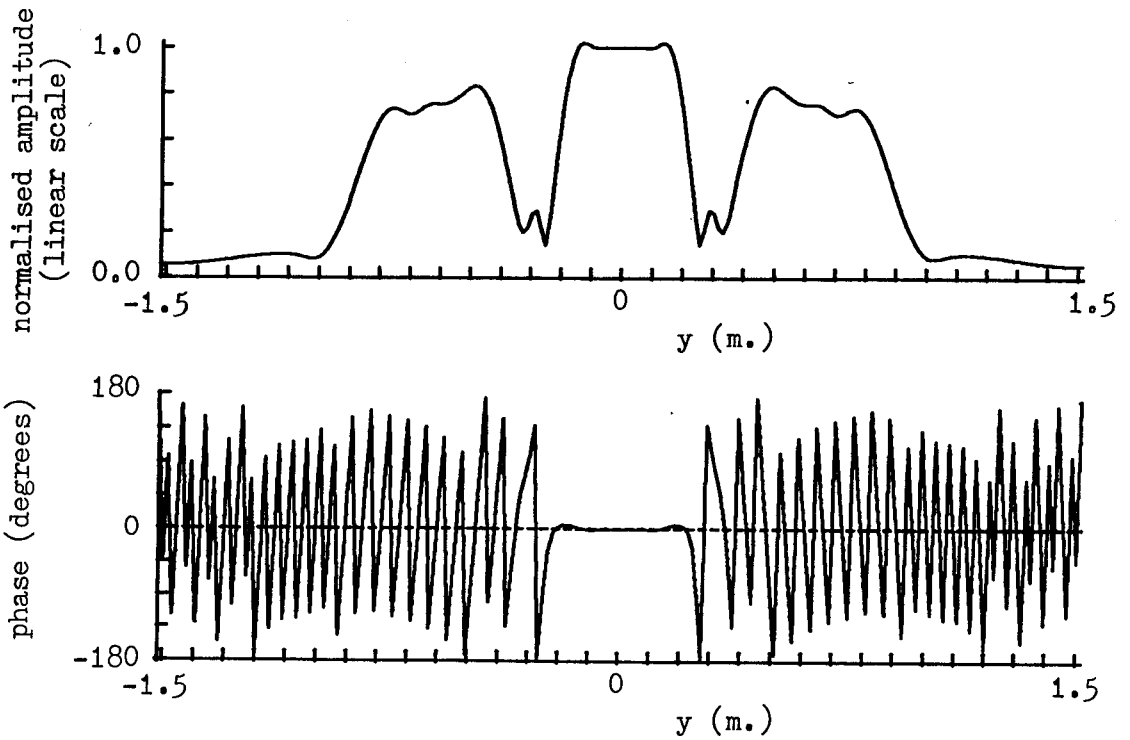

Fig. A2.30. Synthesised plane wave due to weighting function of Fig. A2.27. z = -15cm.

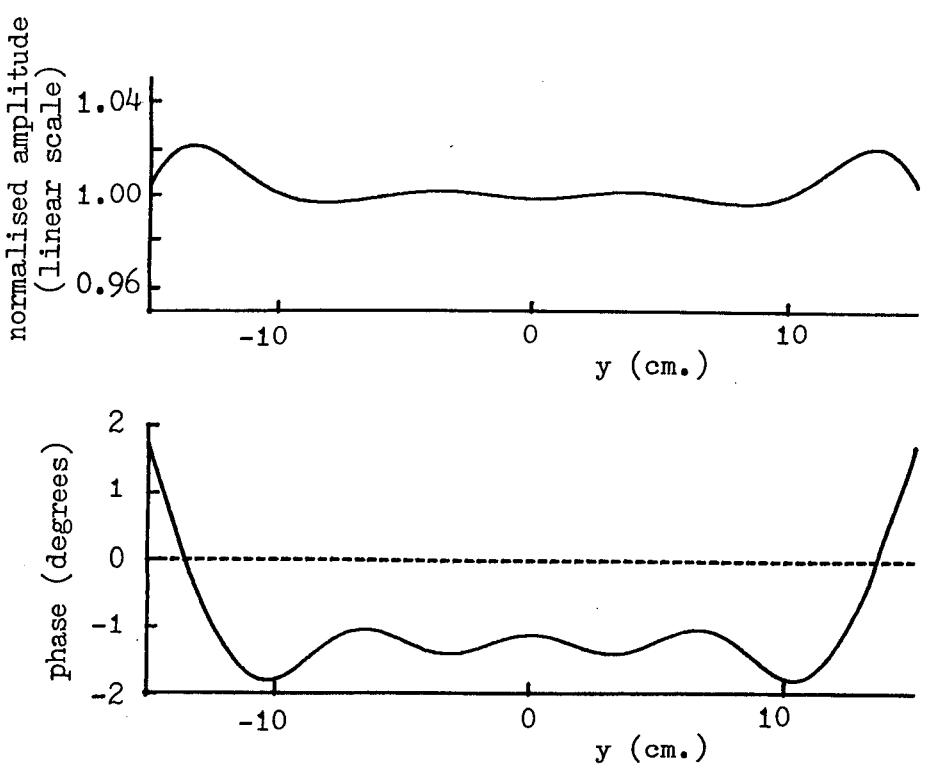

Fig. A2.31. Expanded-scale version of plane wave of Fig. A2.30.

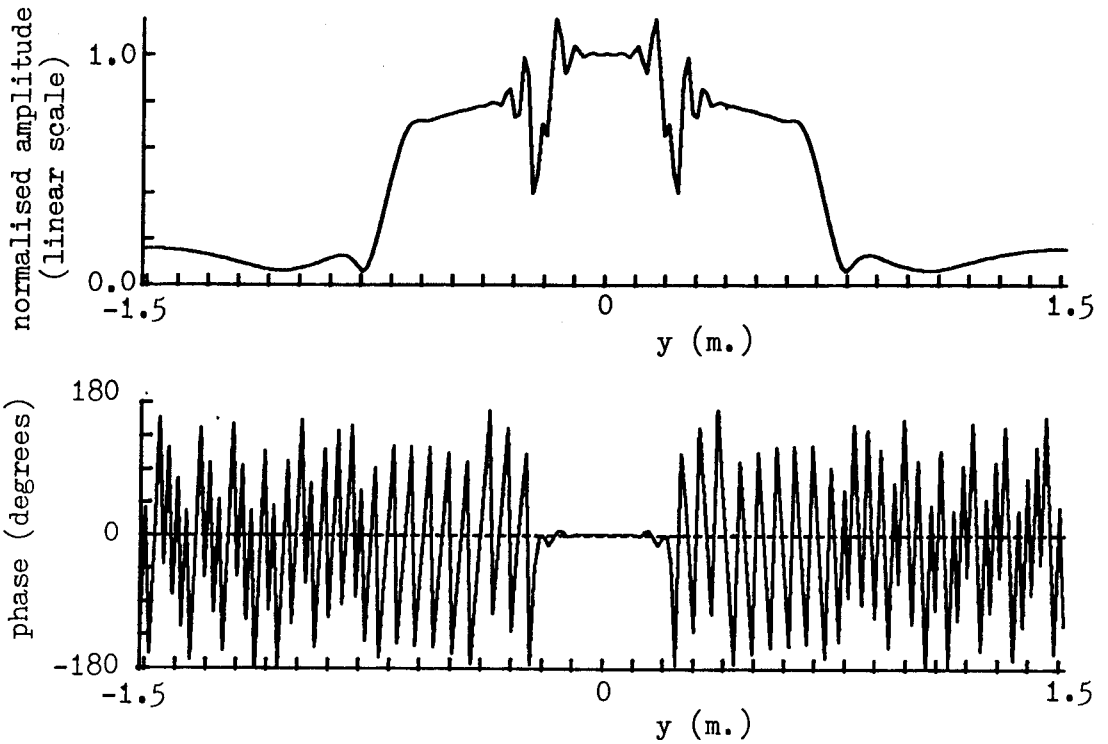

Fig. A2.32. Synthesised plane wave due to weighting function of Fig. A2.27. z = +15cm.

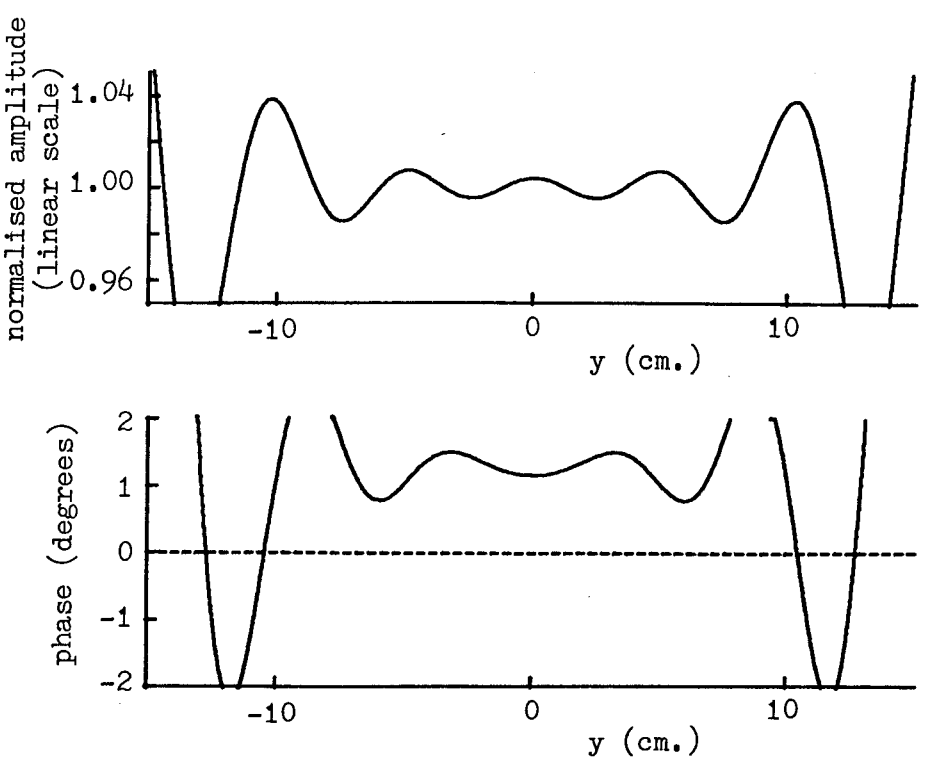

Fig. A2.33. Expanded-scale version of plane wave of Fig. A2.32.

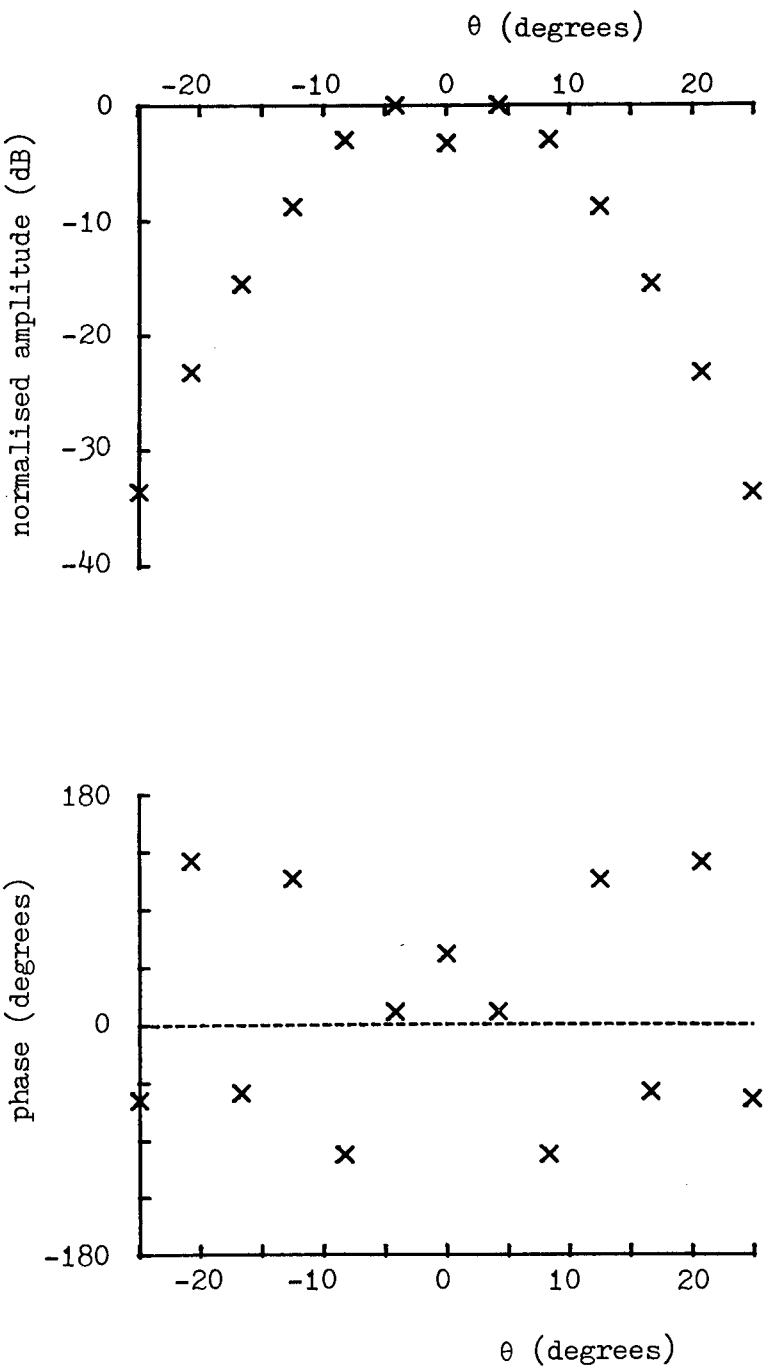

Fig. A2.34. 13-point weighting function for R = 1.0m.

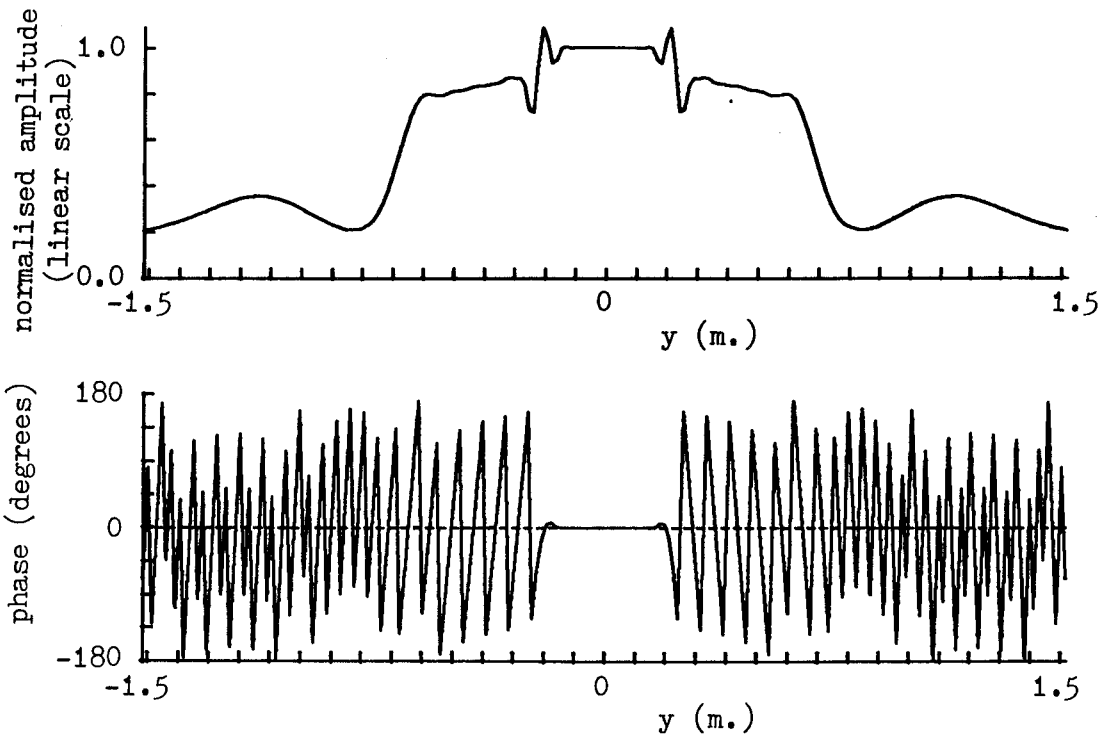

Fig. A2.35. Synthesised plane wave due to weighting function of Fig. A2.34. z = 0.

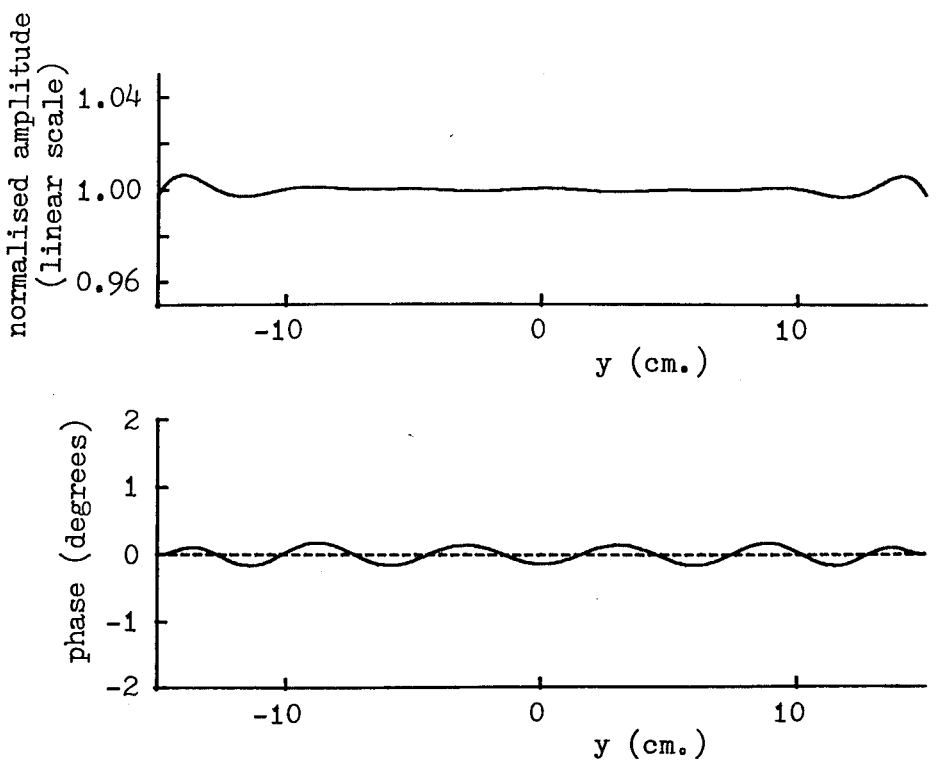

Fig. A2.36. Expanded-scale version of plane wave of Fig. A2.35.

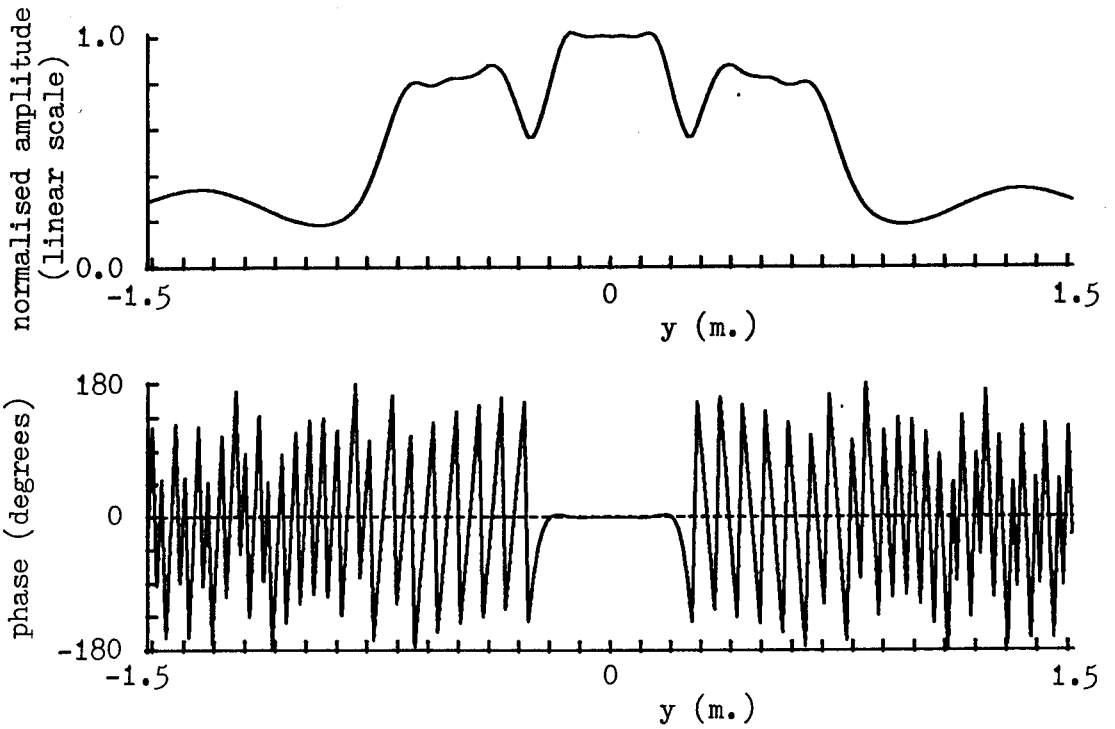

Fig. A2.37. Synthesised plane wave due to weighting function of Fig. A2.34. z = -15cm.

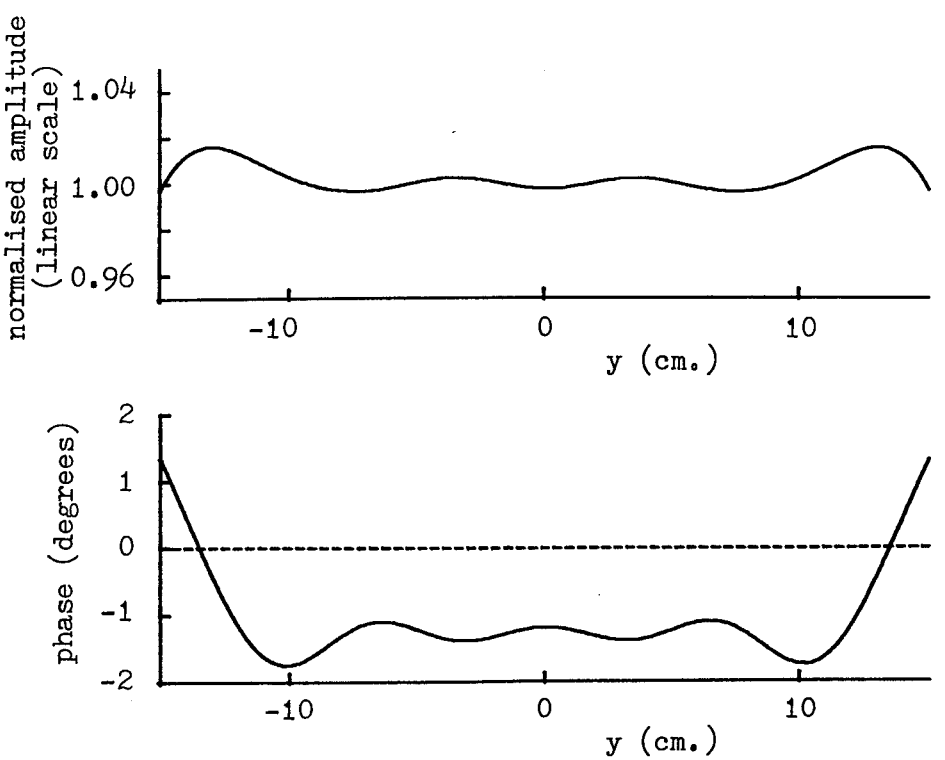

Fig. A2.38. Expanded-scale version of plane wave of Fig. A2.37.

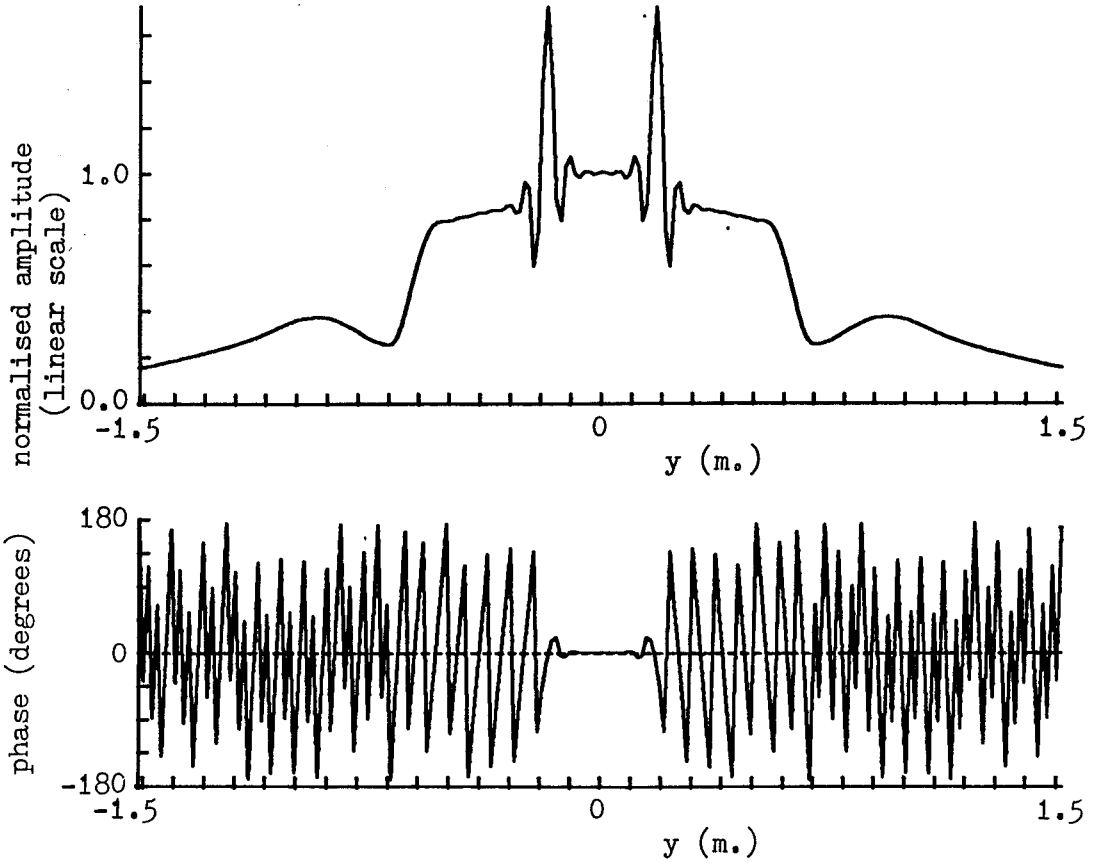

Fig. A2.39. Synthesised plane wave due to weighting function of Fig. A2.35. z = +15cm.

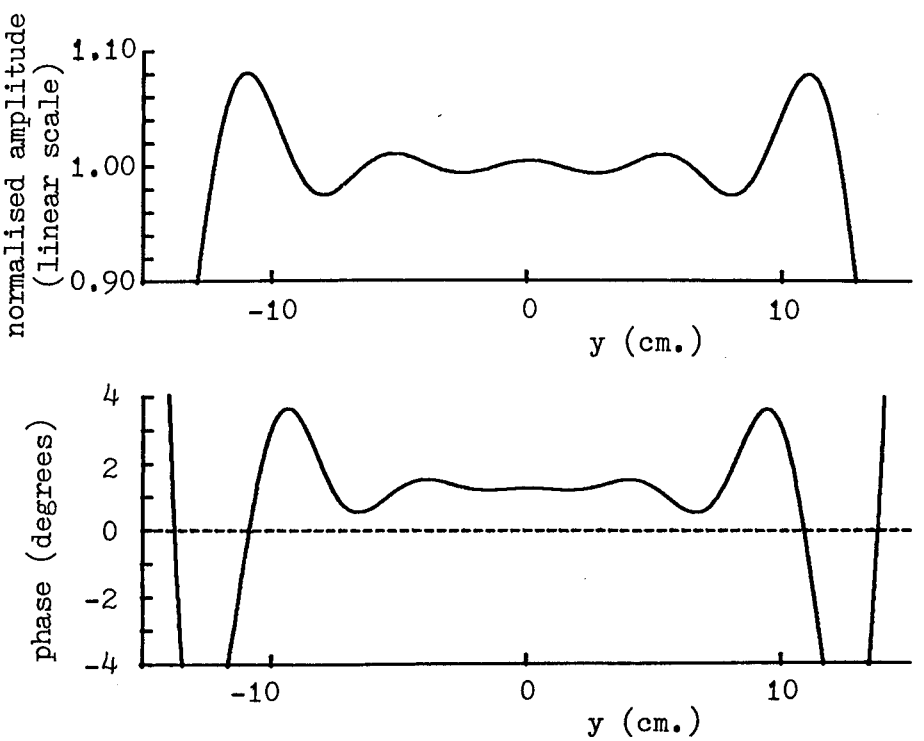

Fig. A2.40. Expanded-scale version of plane wave of Fig. A2.39.

of $z \neq 0$. The ringing at the edge of the synthesised plane wave for z = +15cm (Figs. A2.39 and A2.40) is becoming much more serious although probably still not extending far enough into the plane wave to cause difficulties.

The set of graphs for a weighting function of 11 points (spacing 5.0^{o}) form Figs. A2.41 to A2.47. The edge of the weighting function is now tapered to -35dB. These graphs correspond closely to the sampling criterion (as modified for the near-field measurement range according to the analysis of Chapter 2) and it is clear that the synthesised plane wave is beginning to suffer from the effects of the overlap.

The final example is of a weighting function of 9 points with a 6.25^{o} spacing (Fig. A2.48) and the synthesised plane wave (Figs. A2.49 to A2.54). In this situation where the sampling criterion is violated, it has become impossible to synthesise a good plane wave with severe ripple in evidence for all values of z.

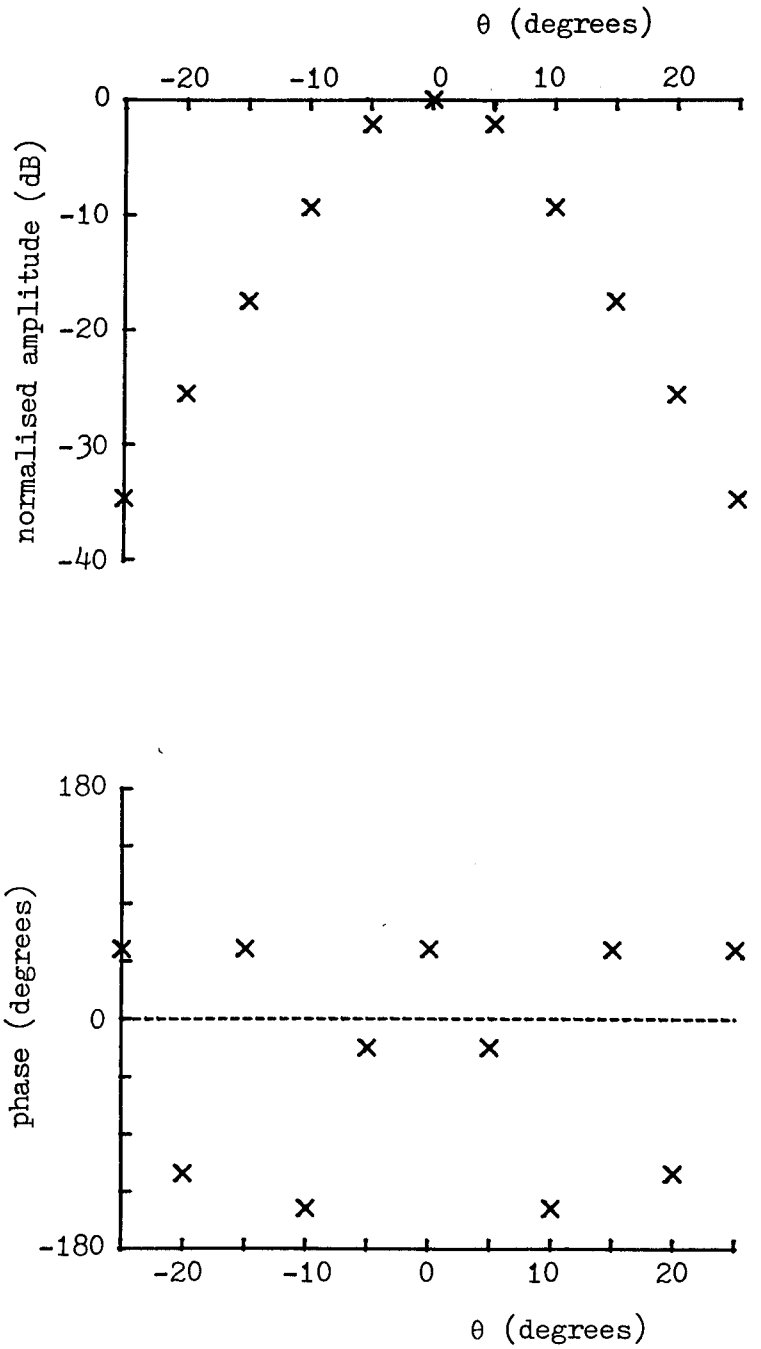

Fig. A2.41. 11-point weighting function for R = 1.0m.

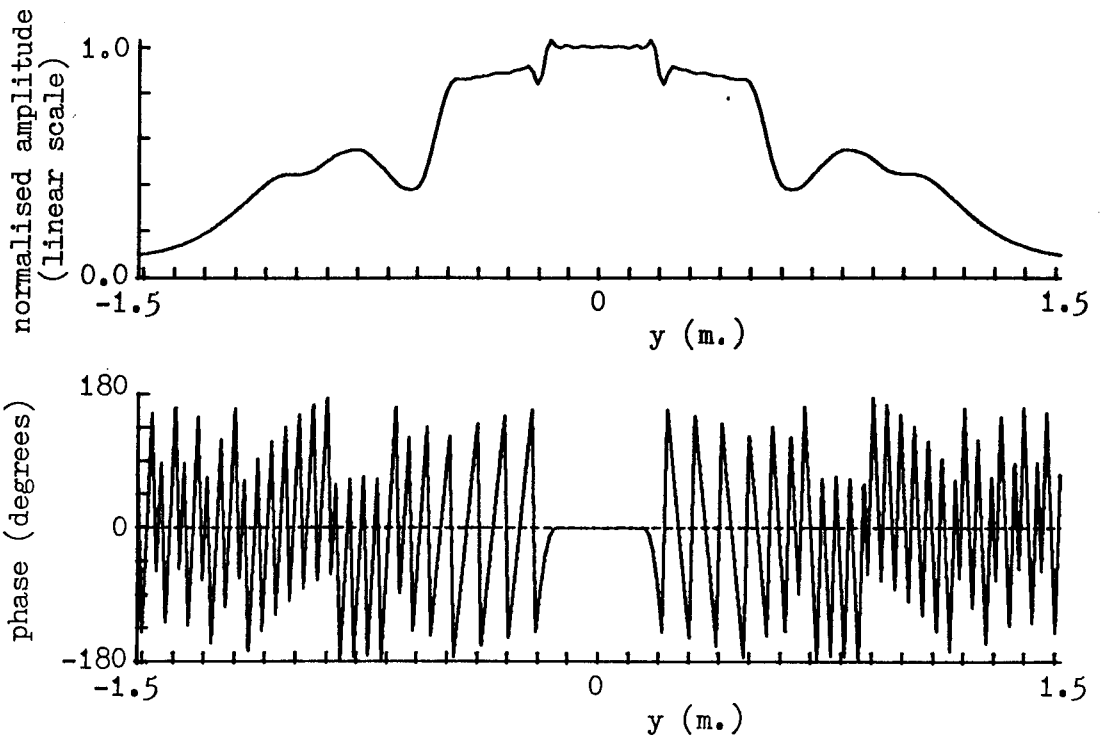

Fig. A2.42. Synthesised plane wave due to weighting function of Fig. A2.41. z = 0.

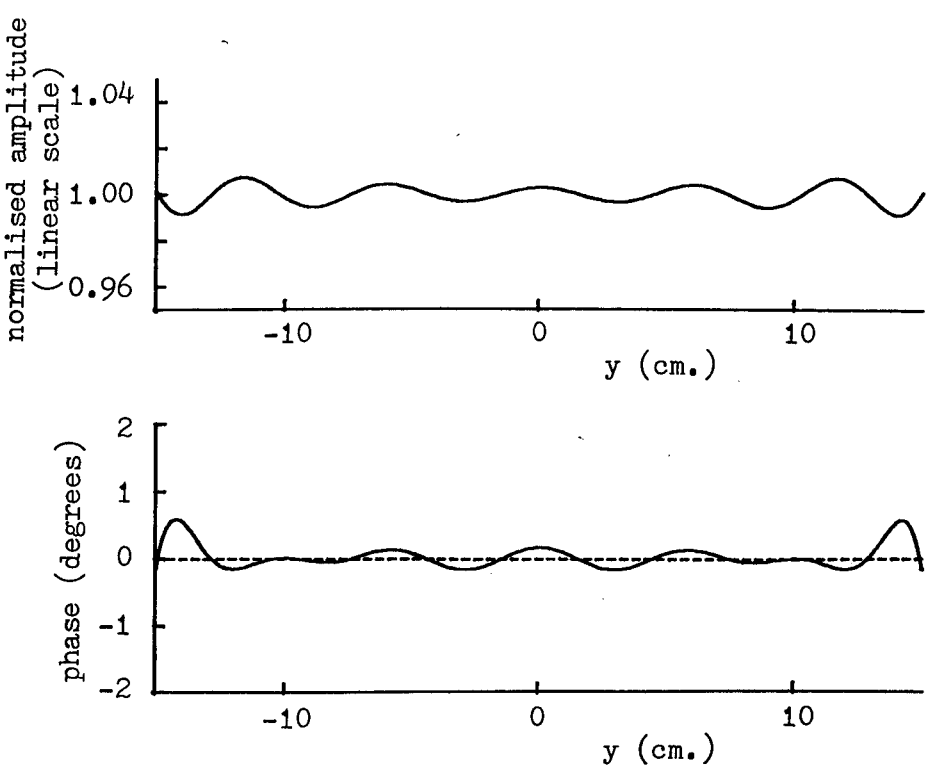

Fig. A2.43. Expanded-scale version of plane wave of Fig. A2.42

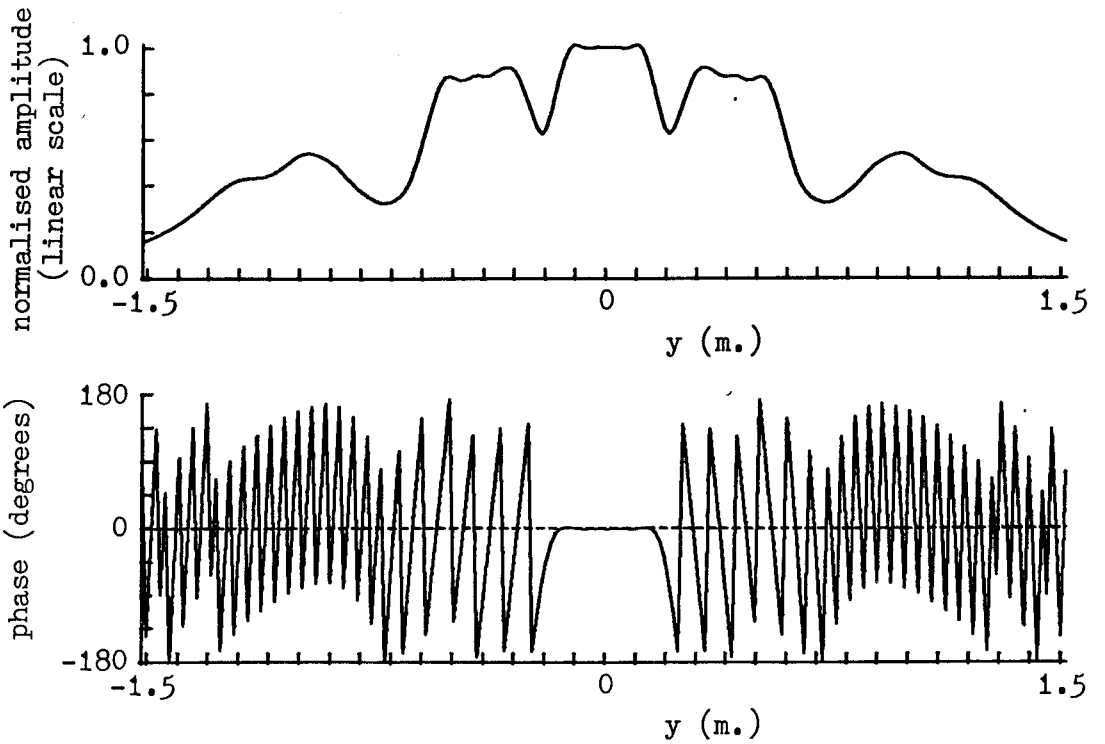

Fig. A2.44. Synthesised plane wave due to weighting function of Fig. A2.41. z = -15cm.

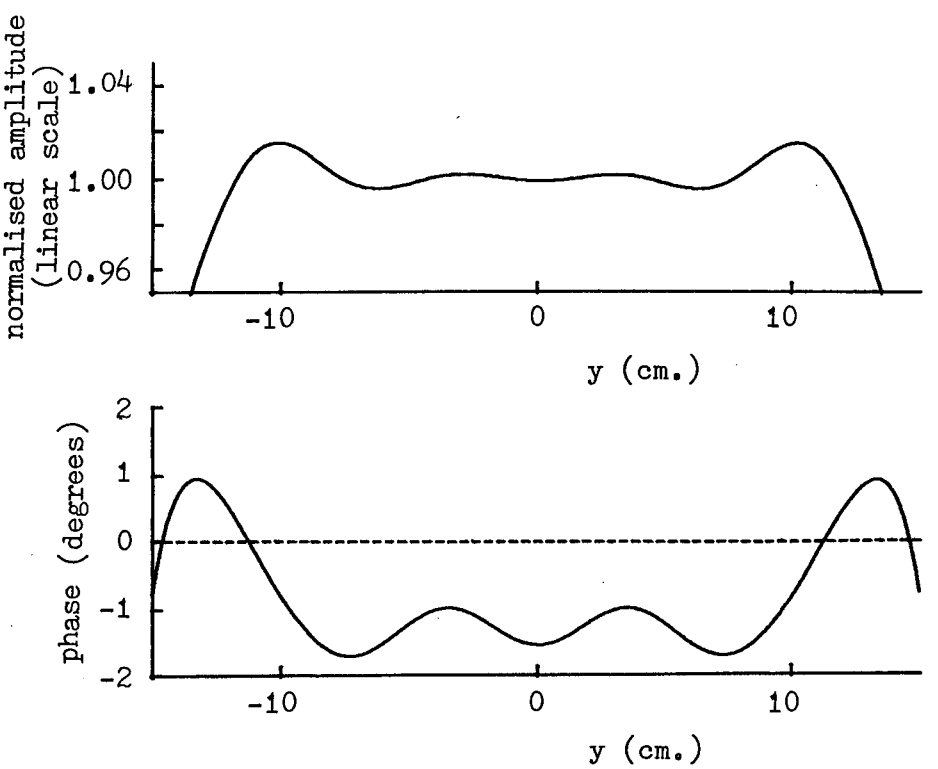

Fig. A2.45. Expanded-scale version of plane wave of Fig. A2.44

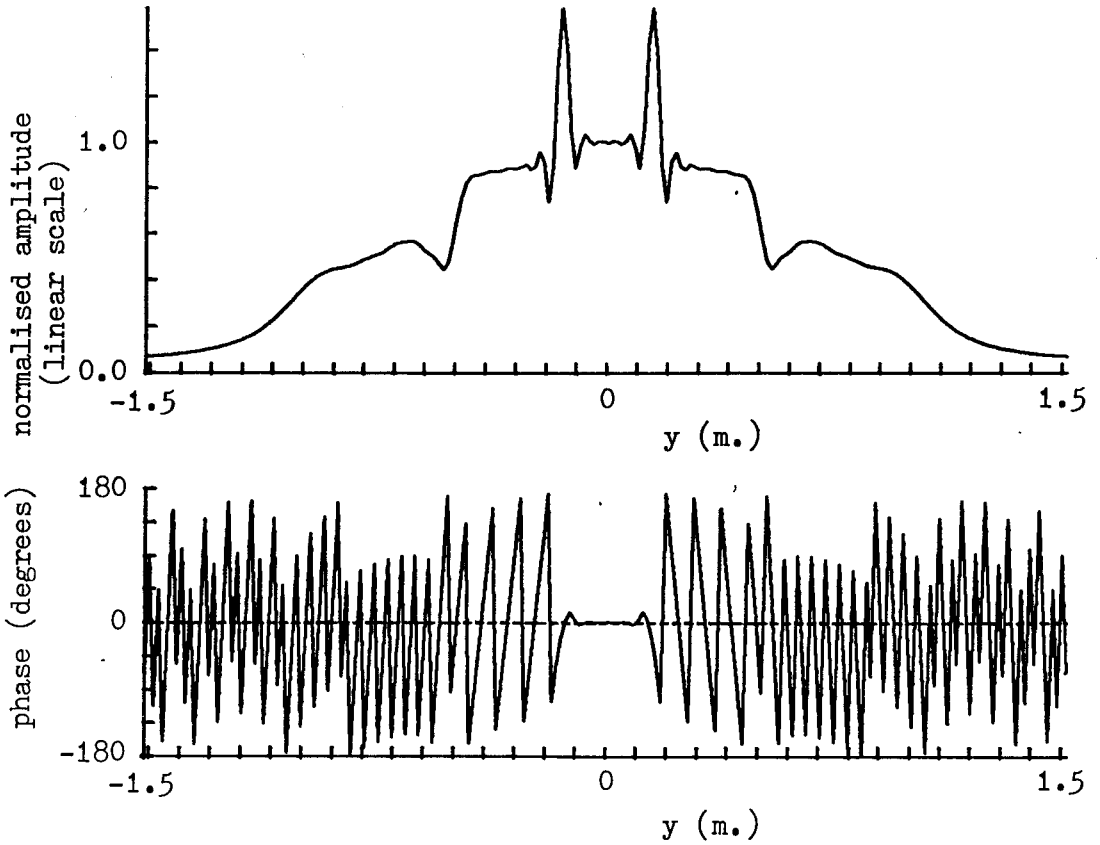

Fig. A2.46. Synthesised plane wave due to weighting function of Fig. A2.41. z = +15cm.

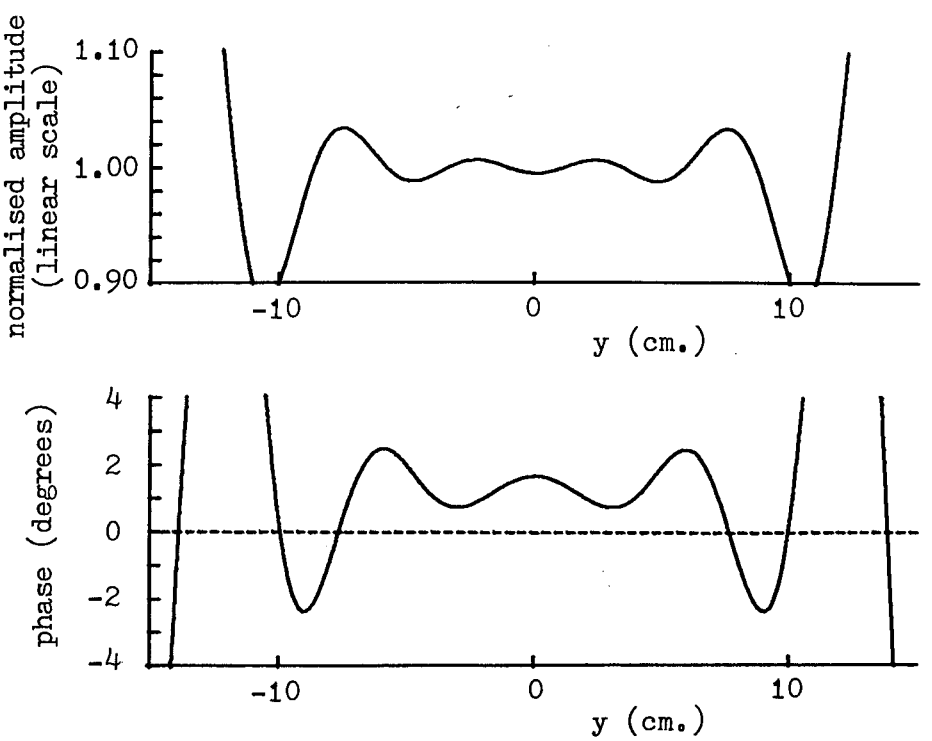

Fig. A2.47. Expanded-scale version of plane wave of Fig. A2.46.

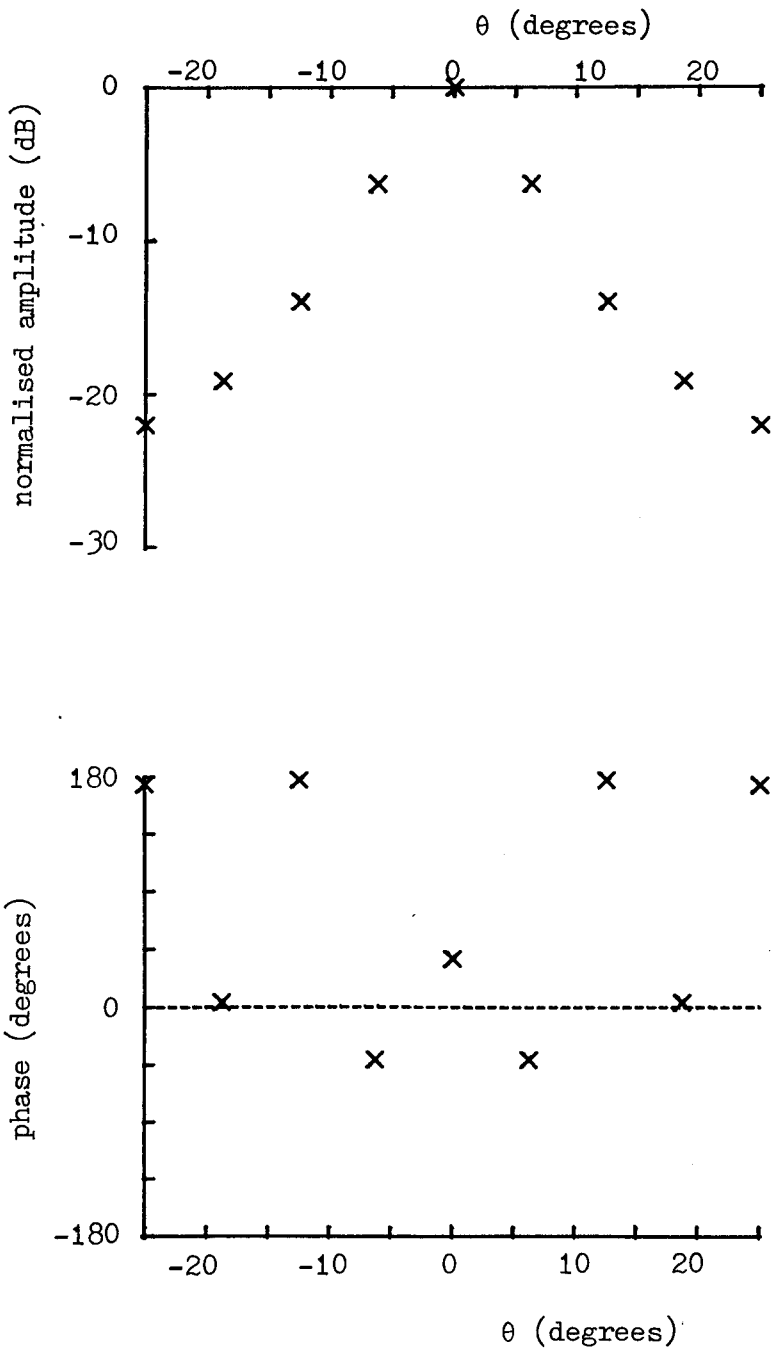

Fig. A2.48. 9-point weighting function for R = 1.0m.

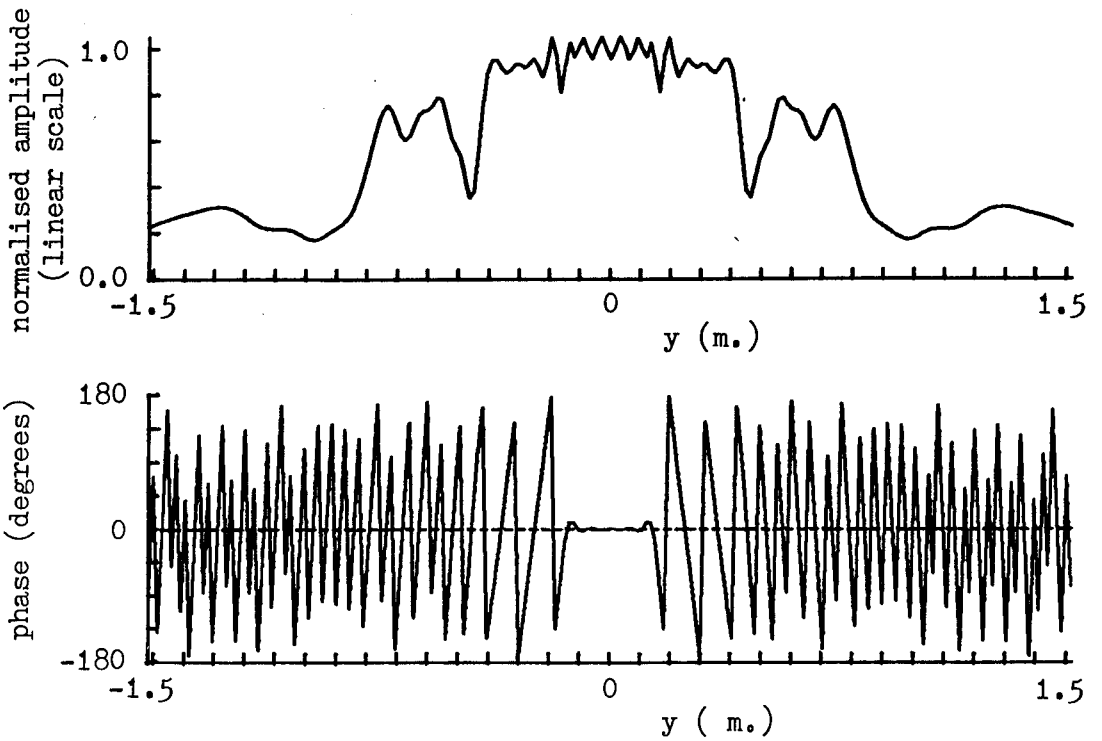

Fig. A2.49. Synthesised plane wave due to weighting function of Fig. A2.48. z = 0.

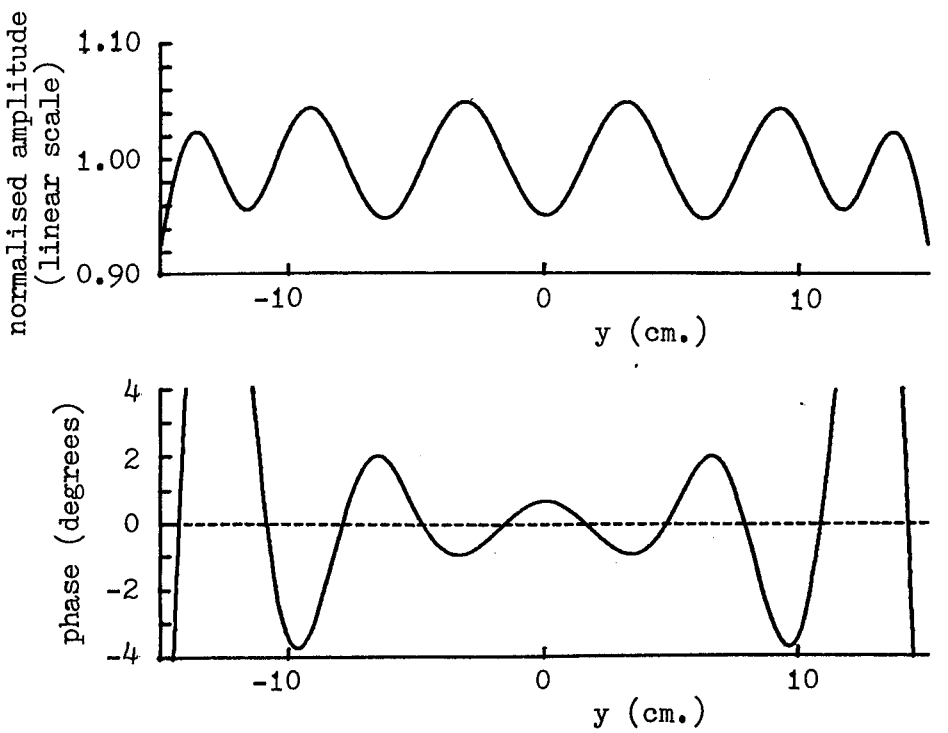

Fig. A2.50. Expanded-scale version of plane wave of Fig. A2.49.

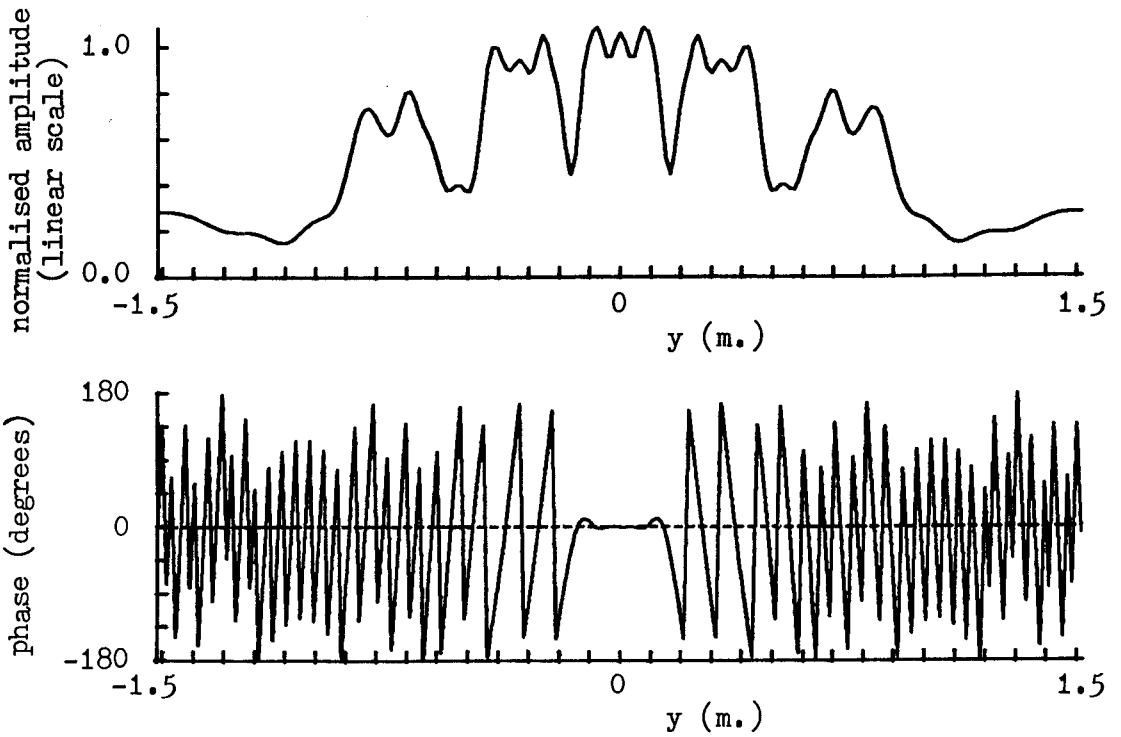

Fig. A2.51. Synthesised plane wave due to weighting function of Fig. A2.48. z = -15cm.

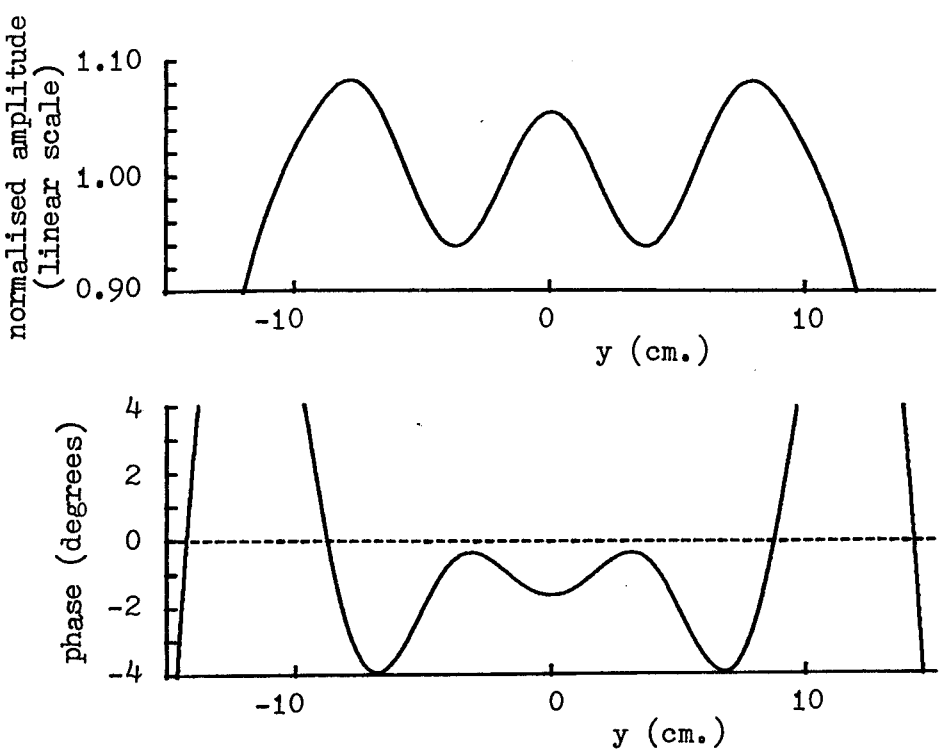

Fig. A2.52. Expanded-scale version of plane wave of Fig. A2.51.

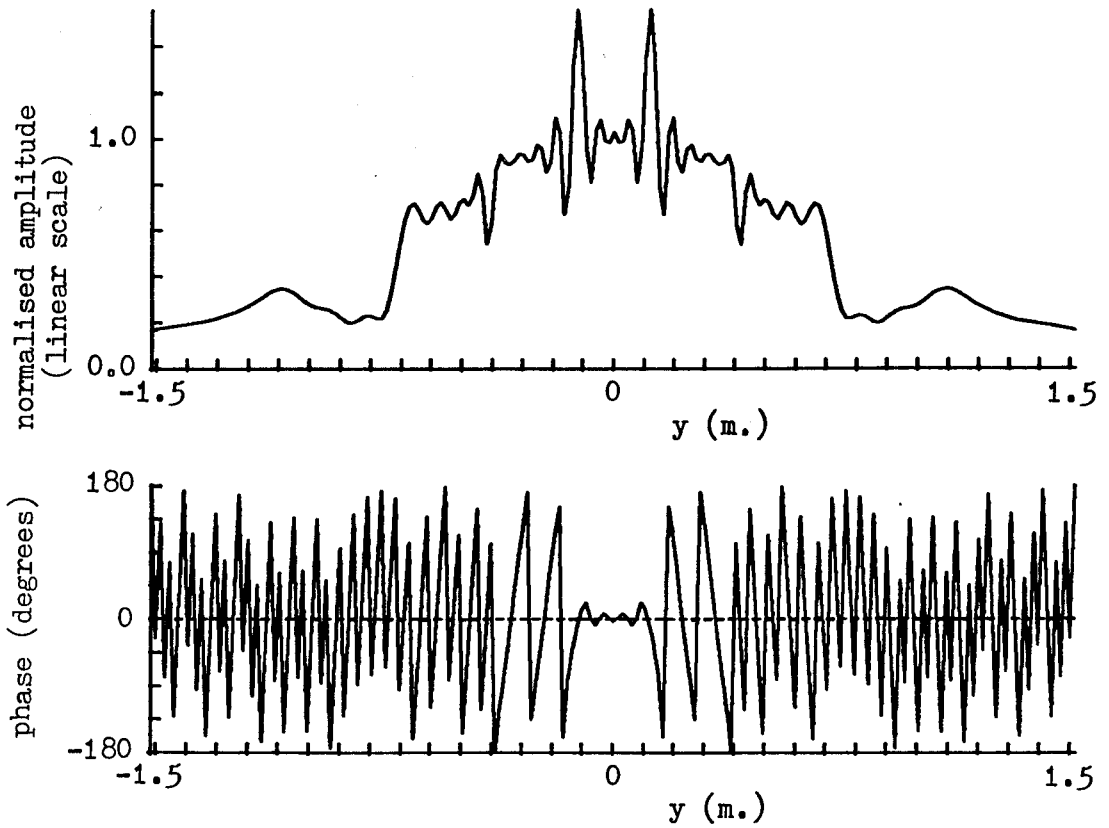

Fig. A2.53. Synthesised plane wave due to weighting function of Fig. A2.48. z = +15cm.

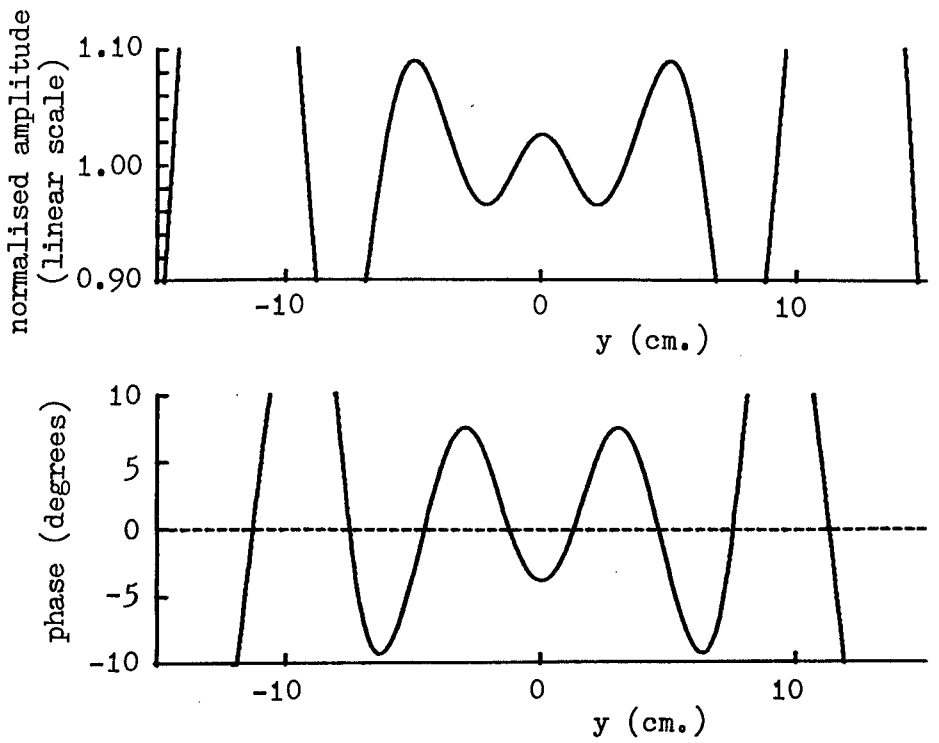

Fig. A2.54. Expanded-scale version of plane wave of Fig. A2.53.

Appendix 3: ANGULAR EXTENT OF THE WEIGHTING FUNCTION

Illustrated in this appendix are a few examples of the effects upon the synthesised plane wave of varying the angular extent of the weighting function (but keeping the point spacing constant). This is related to the study of convolving functions of appendix 1 but, in this case, the results are after 100 cycles of the iterative optimisation procedure. The weighting functions are designed to synthesise a 30cm plane wave from a measurement range of 1.0m. The sample spacing used is 2^{o} in all cases and the frequency used is 10.0GHz.

The first example, Fig. A3.1, shows the synthesised plane wave when the weighting function extends over $\pm 90^{o}$. The quality of the synthesised plane wave is very good on the plane z = 0 but deteriorates for the cases of z = ±10cm so that this configuration would prove unacceptable. Little, if any, improvement, is visible for the case of a weighting function occupying the range $\pm 60^{o}$ (Fig. A3.2).

A sudden improvement appears in the quality of the synthesised plane wave for $z \neq 0$ when the range of the weighting function is halved to $\pm 30^{o}$ (Fig. A3.3) and this configuration would certainly be acceptable. A further improvement is seen in Fig. A3.4 when the range of the weighting function is once again reduced, this time to $\pm 24^{o}$.

A slight deterioration in the quality of the synthesised plane wave becomes apparent when the range of the weighting function is $\pm 20^{o}$, as shown in Fig. A3.5. The reduction in quality continues with Fig. A3.6($\pm 16^{o}$

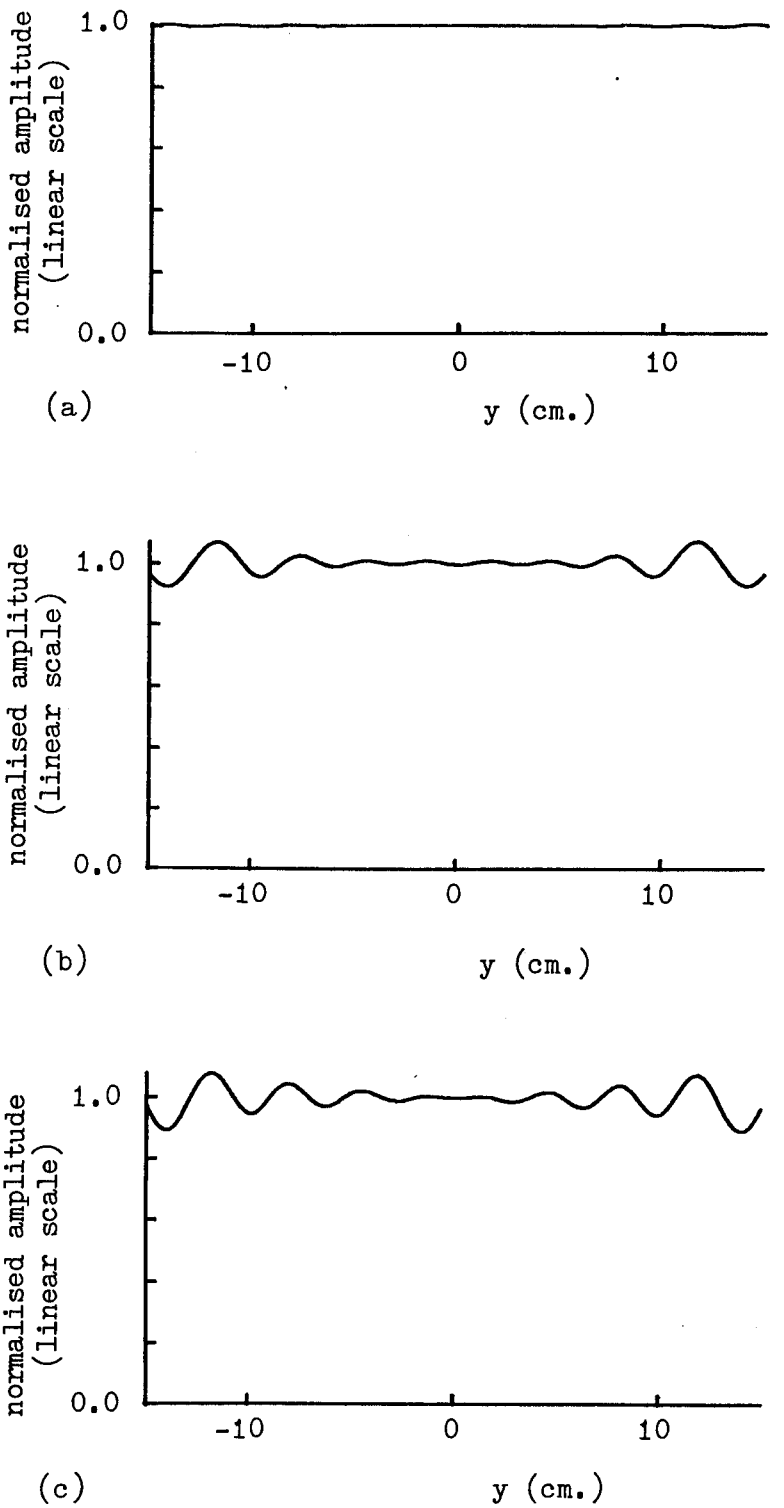

Fig. A3.1. 30cm. synthesised plane wave due to a weighting function extending over ±90° at 1.0m. measurement radius. (a) z = 0, (b) z = -10cm., (c) z = 10cm.

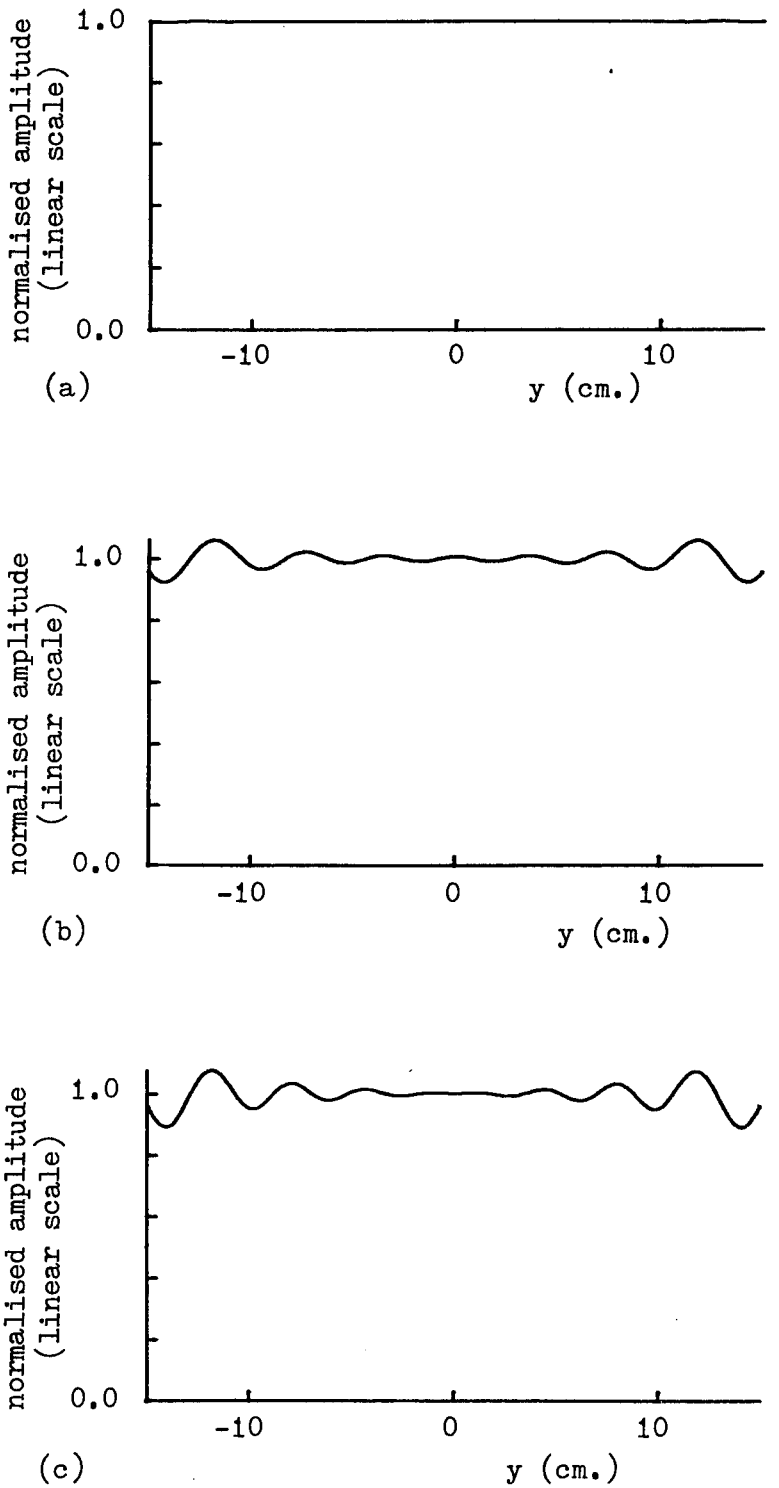

Fig. A3.2. 30cm synthesised plane wave due to a weighting function extending over ±60° at 1.0m. measurement radius. (a) z = 0, (b) z = -10cm., (c) z = 10cm.

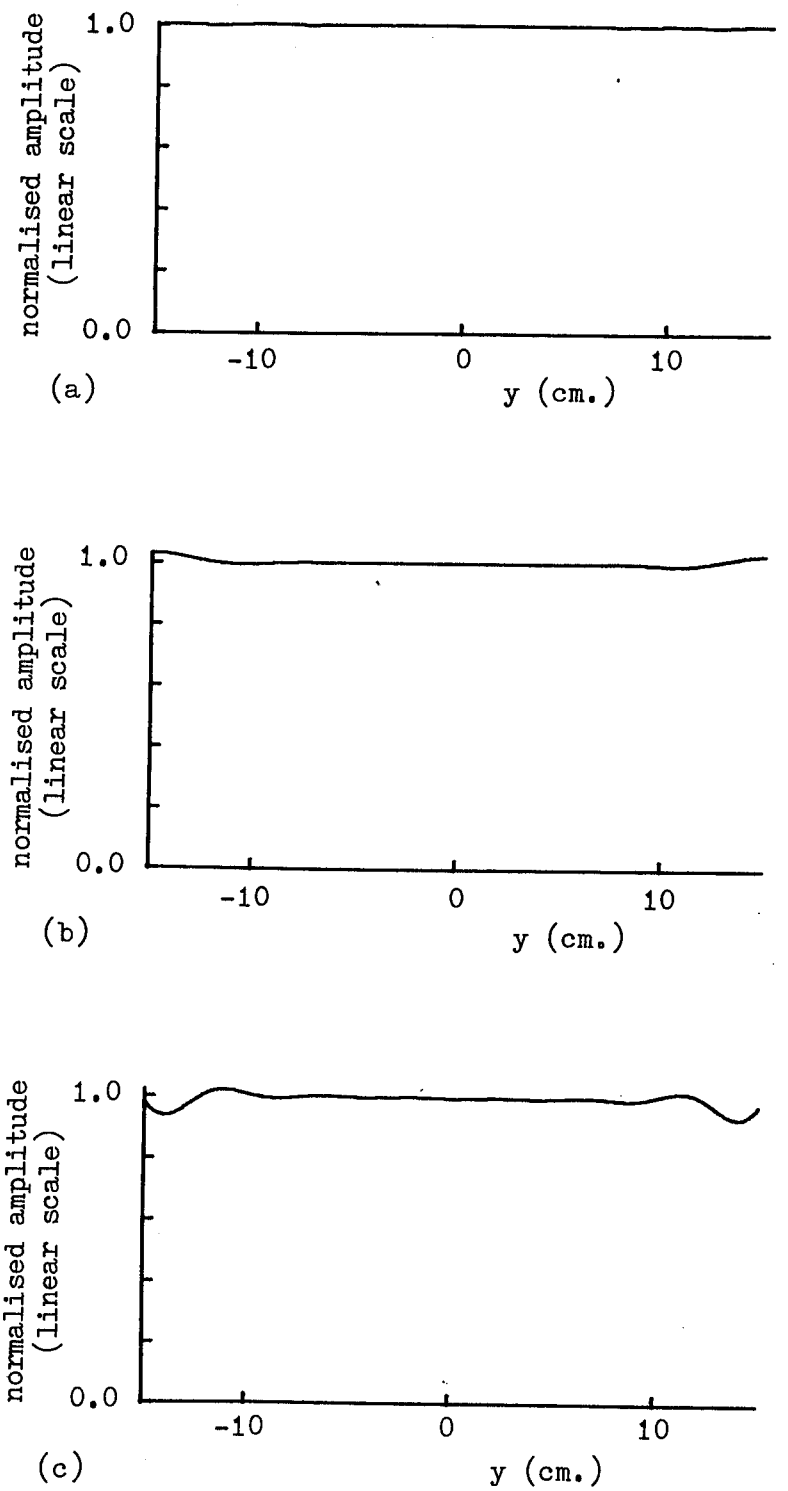

Fig. A3.3. 30cm. synthesised plane wave due to a weighting function extending over ±30° at 1.0m. measurement radius. (a) z = 0, (b) z = -10cm., (c) z = 10cm.

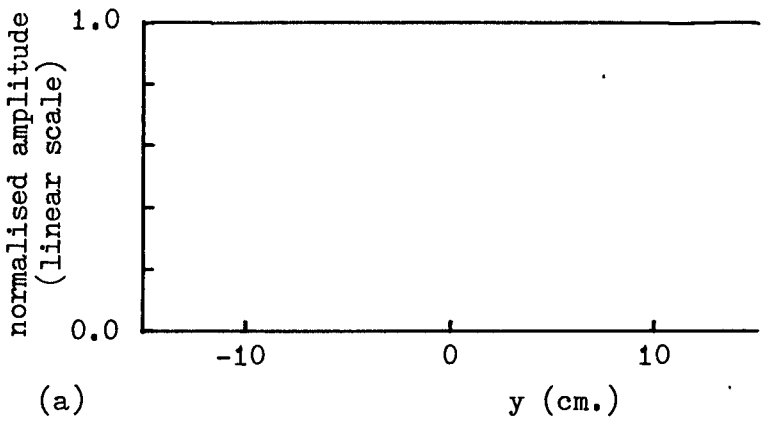

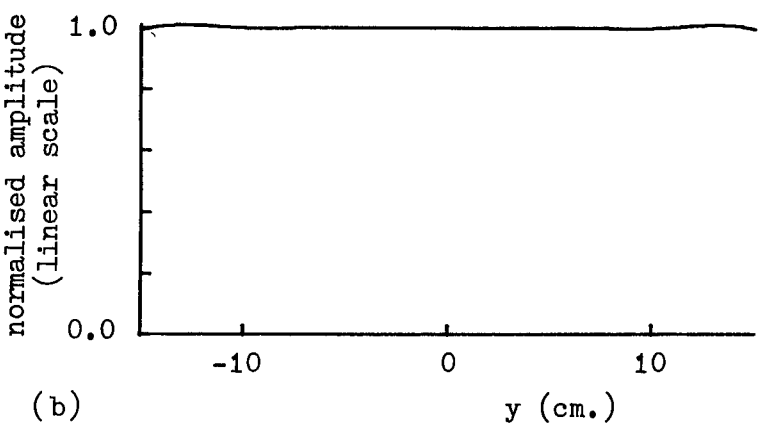

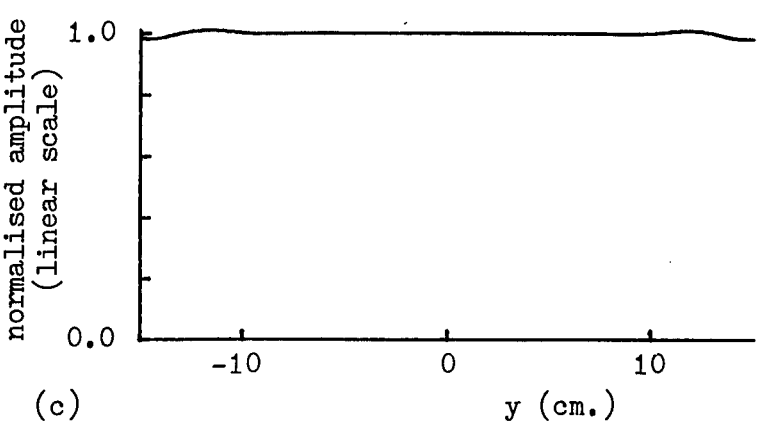

Fig. A3.4. 30cm. synthesised plane wave due to a weighting function extending over ±24° at 1.0m. measurement radius. (a) z = 0, (b) z = -10cm., (c) z = 10cm.

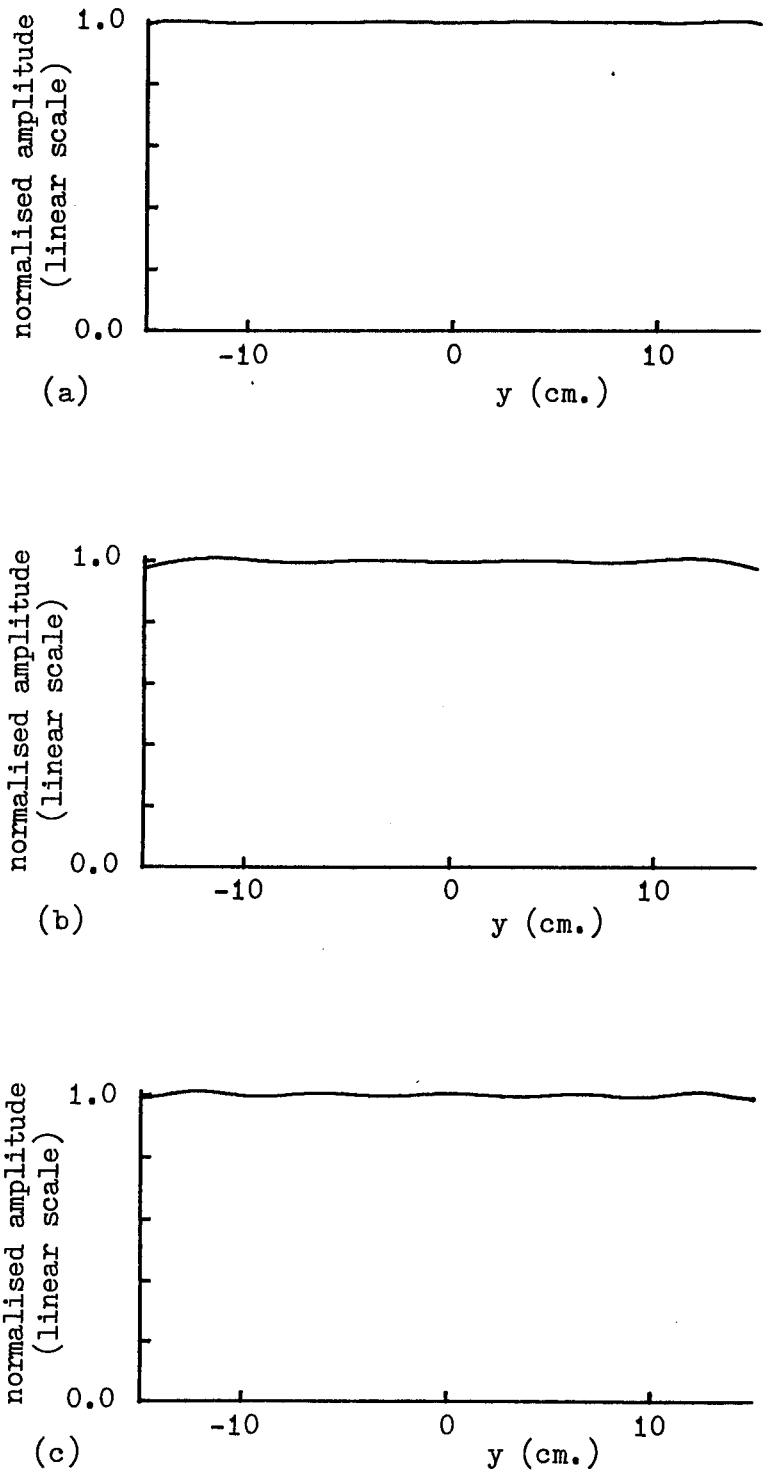

Fig. A3.5. 30cm. synthesised plane wave due to a weighting function extending over ±20° at 1.0m. measurement radius. (a) z = 0, (b) z = -10cm., (c) z = 10cm.

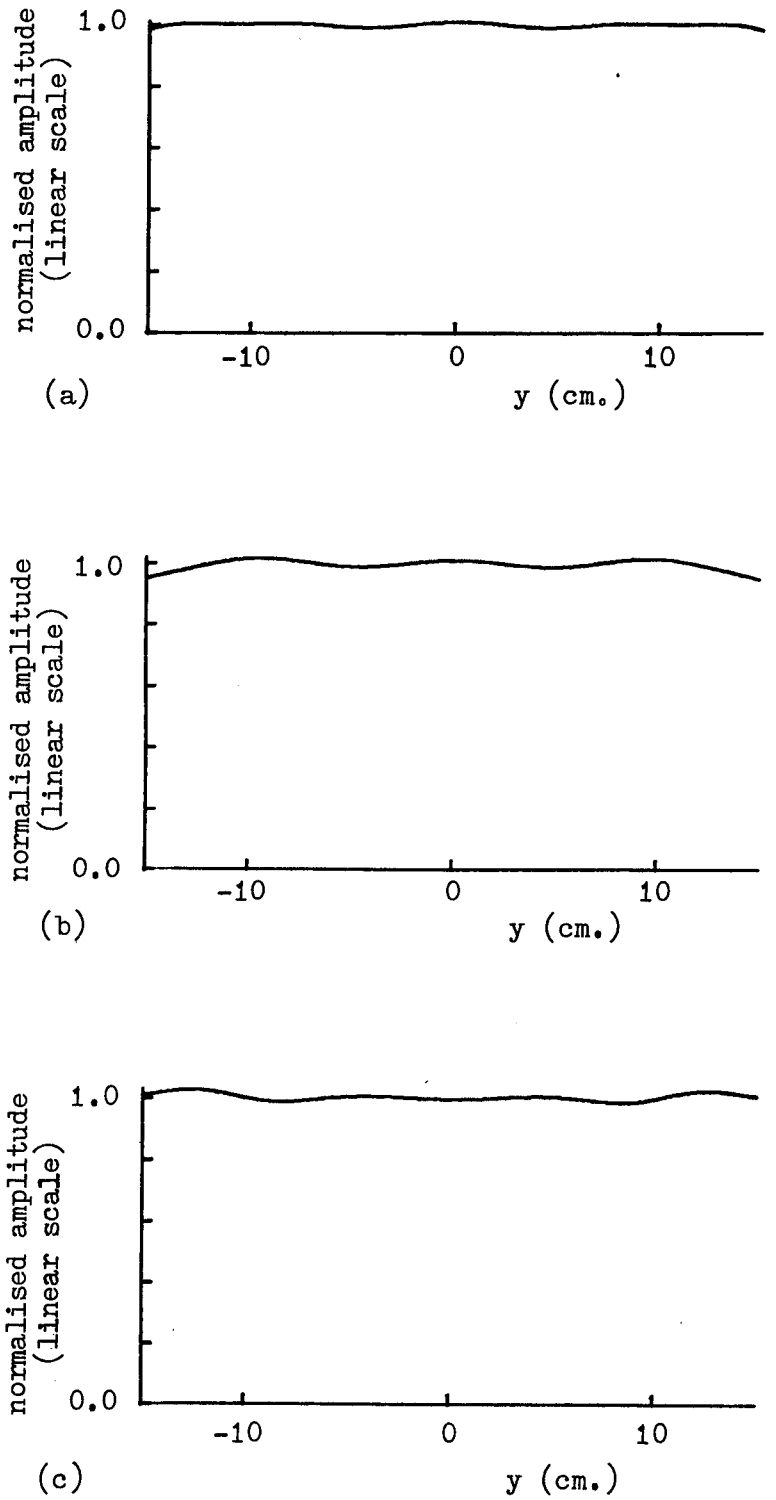

Fig. A3.6. 30cm. synthesised plane wave due to a weighting function extending over ±16° at 1.0m. measurement radius. (a) z = 0, (b) z = -10cm., (c) z = 10cm.

weighting function) and Fig. A3.7 ($\pm 12^{o}$ weighting function.

The effects observed here agree with those predicted from Chapter 2 where it was shown that an improvement of plane wave quality would be expected for wider weighting functions on the plane $z = 0$ but for $z \neq 0$, defocussing terms would become serious as the size of the weighting function became large. Clearly the best range in this case is $\pm 24^{o}$ and this value is in fact typically close to the optimum extent of a weighting function although for very short range measurements, it sometimes becomes necessary to increase the angular range a little.

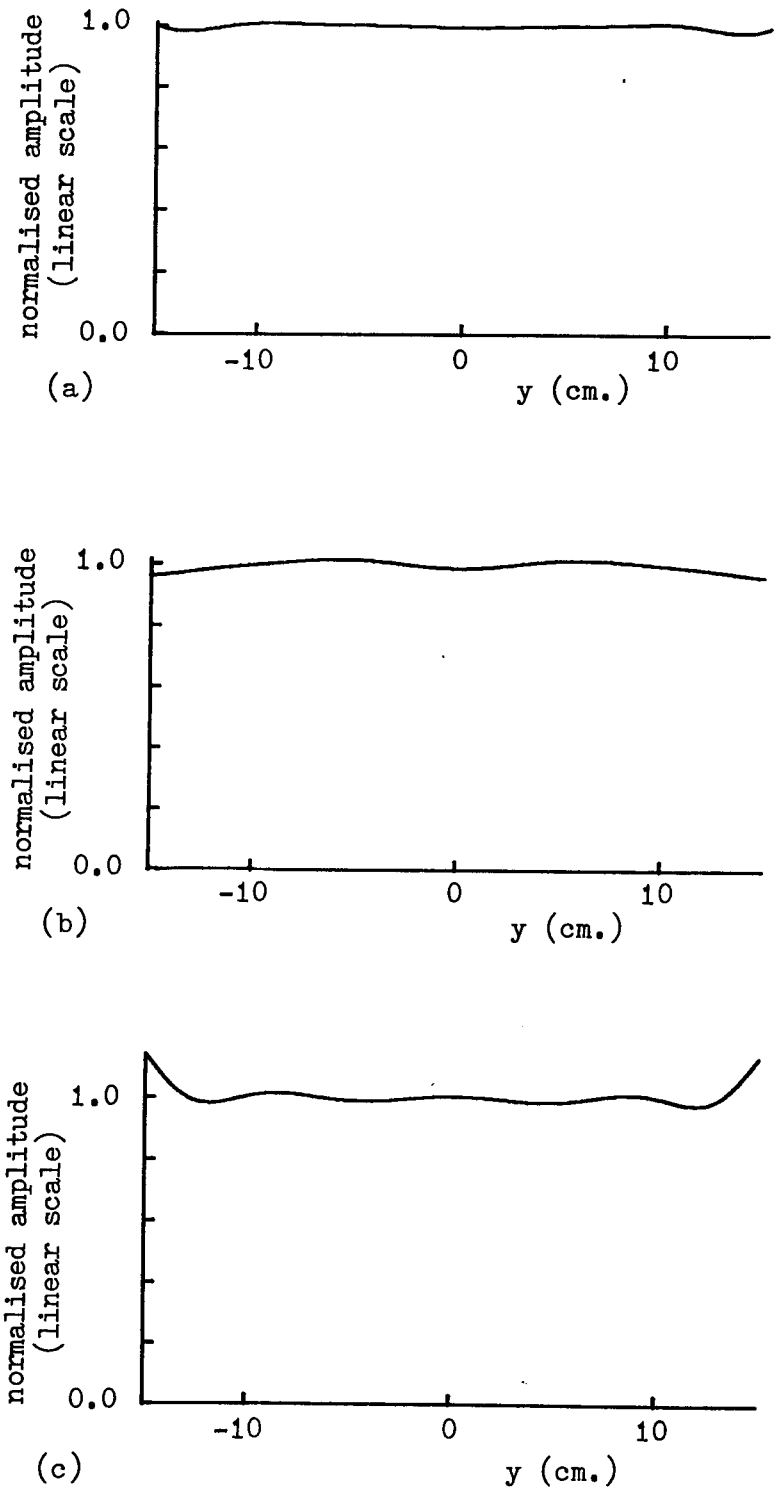

Fig. A3.7. 30cm. synthesised plane wave due to a weighting function extending over ±12° at 1.0m. measurement radius. (a) z = 0, (b) z = -10cm., (c) z = 10cm.

Appendix 4: THE V-72 IMAGE PROCESSING COMPUTER

Much of the work (particularly the two-dimensional simulations) described in this thesis was carried out using the Varian (now Sperry Univac) V-72 image-processing minicomputer of the University of Sheffield, Department of Electronic and Electrical Engineering. The system is described briefly below.

- V-72 CPU, 128k (16-bit) memory. Only 32k is available to a single program at the moment.
- Writeable control store (WCS) - not presently supported by operating system.
- Hardware floating-point processor (FPP).
- Hazletine VDU.
- Pertec dual magnetic disc drive (4.68 M byte).
- Pertec 9-track magnetic tape deck (800 bpi).
- Racal P-72 digital cassette deck.
- Varian (Sperry) 8-track paper tape reader (150 cps).
- Facit 8-track paper tape punch (75 cps).
- Mannesmann matrix printer (200 cps).
- Oscilloscope display (locally made) for simple curves.
- C.I.L incremental plotter (0.1mm step, 250 steps per sec).
- Modified Muirhead electrostatic facsimile display (monochrome hard copy intensity display).
- Mk 6 colour T.V display system (locally built).
- Capabilities for use of modem, direct input of weather satellite pictures and standard x-y (analogue) plotter output.

Two of the non-standard peripherals particularly relevant to the work presented in this thesis will now be described in a little more detail.

A4.1 C.I.L. Incremental Plotter

The great majority of the graphs presented within this volume have been plotted on the C.I.L. incremental plotter. This device is a drum-type plotter with a usable paper width of about 32cm, step size of 0.1mm and plotting speed in the region of 250 steps per second. This device is driven primarily by the "GHOUL" software, written by the present author, providing quite flexible plotting facilities for shapes and figures, output of data arrays, axes, graticules, etc., and callable from FORTRAN programs. In addition, routines have been written to enable graphical data produced in the "GHOST" system, operated on the main University ICL 1906S computer, to be plotted locally (transfer of data by paper tape).

A4.2 Mk 6 T.V. Display

Probably the most generally important device attached to the V-72 computer is the locally constructed Mk 6 colour television display. This is described in more detail by Thomsit[40] and this outline is therefore very brief.

A displayed picture comprises 256 lines each of 256 display points. The picture is stored in a special memory within the device. Each point is defined to be at one of 16 grey-scale levels (0-black to 15-peak white) and the resulting monochrome picture is displayed on a black and white monitor set. In addition, the Mk 6 hardware and specially written software allow a colour table to be defined in which each of the 16 levels is assigned one of an available 4096 colours (16 levels of red, green and blue in any combination) and this "false colour" picture

is displayed on a 3-colour monitor set.

When used with the software written by Dr. A.J.T. Whitaker, the system provides comprehensive facilities for displaying and storing pictures using various predefined or specially designed colour tables, level highlighting, etc. Combined with the capability of the V-72 computer for data manipulation, this provides a very powerful tool in the visualisation of microwave images, field distributions, etc.

Appendix 5: SOFTWARE WRITTEN FOR PLANE WAVE SYNTHESIS

Listed here together with brief descriptions of their functions are some of the more important items of software written in the implementation of, or with direct relevance to, the plane wave synthesis technique and the work described in this thesis.

PCMP1D — The program written for the V-72 minicomputer (see Appendix 4) for creation of one-dimensional weighting functions with probe compensation. Incorporates a large number of features for investigation of various effects associated with the plane wave synthesis technique. Described in more detail in Chapter 1.

SAMPCR — Used on the V-72 computer for the investigation of the sampling criterion described in Chapter 2, for a single polar (angular) coordinate. Uses an interval-dividing technique to find the minimum allowable sampling interval for points within the significant volume and for various measurement distances.

FLDPIC)
FLDISP) — For displaying, on the Mk 6 T.V. display system, pictures of the synthesised field distribution due to a particular weighting function. Run on the V-72 minicomputer.

POLAR1)
POLAR2)
POLAR3) — For creating the coefficients relating a plane wave and weighting function for a polarisation-over-azimuth scan system, iterating to produce the primary weighting function and producing a printout of the synthesised plane wave. Run on the University of

Manchester Regional Computing Centre, CDC 7600 machine.

NPLR1)
NPLR2)
NPLR3) For creating the coefficients relating the plane wave and weighting function for an elevation-over-azimuth scan system, iterating to produce the primary weighting function and producing a printout of the synthesised plane wave. Run on the CDC 7600

CPWTFN Inputs to the V-72, a primary weighting function (created by the above programs) on paper tape and, given details of the measurement geometry, creates a composite weighting function, stored efficiently on magnetic tape, corresponding to polarisation-over-azimuth scan system. At present, only one prediction polarisation is available but the other polarisation (as formulated in Chapter 4) will be incorporated in the next version.

DTRANS A utility program for creating an appropriately formatted disc file of a data main scan from an original file held on magnetic tape (V-72).

CTRANS A utility program for transferring calibration scans from magnetic tape to specified disc files (V-72).

DATAN1 When the main scan and calibration scans have been transferred into their respective V-72 files, it is useful to have a facility for initially sorting through the main set and printing out a summary of the data (in terms of maximum, minimum and mean amplitude and phase values) scan by scan,

thus facilitating rapid detection of possible problem areas. In addition to performing this function, the program enables a detailed comparison of selected main scan and calibration scan data by means of graphical output and printout.

DATAN2 For greater thoroughness or where problems of data are suspected, this second data analysis program can be called into action to output plots of all or selected data scans (V-72).

DCORR To read a data main scan from its V-72 disc file and apply a selected correction for slow drift of amplitude and/or phase before storing it in another file. Corrections of four types can be applied in the present version; (a) constant, (b) Gaussian, (c) cosine, (d) $1/\phi$ type, in any combination.

PRDICT The prediction program on the V-72. The composite weighting function is read from magnetic tape, the corrected data from disc file and any selected radial cut (from boresight) of the far-field pattern is computed and stored on another disc file.

GETPRD)
GETCAL)
GETCUT) Programs on V-72 for assembling cuts across the pattern of a far-field prediction, calibration scan or main scan data for output to a file for use of the display program.

COMPAR To display comparisons between cuts across the data. Used for comparisons of measured near-field calibration and main scans or predicted and measured far-field.

REFERENCES

1. Cheng, D.K., 'On the simulation of Fraunhofer radiation patterns in the Fresnel region', IRE Trans., AP-5, 1957, pp.399-402.

2. Chu, T.S., 'A note on simulating Fraunhofer radiation patterns in the Fresnel region', IEEE Trans., AP-19, 1971, pp.691-692.

3. Scientific Atlanta Inc., 'The compact range', Microwave Journal, 17, October 1974, pp.30-32.

4. Johnson, R.C., Ecker, H.A. and Moore, R.A., 'Compact range techniques and measurements', IEEE Trans., AP-17, 1969, pp.568-576.

5. Olver, A.D., 'The practical performance of compact antenna ranges', Proc.Workshop on Antenna Testing Techniques, ESTEC, Netherlands, 1977, pp.129-133.

6. Wickenden, B.V.A., 'The use of a lens for compact range measurements', Proc.Seminar on Compact Antenna Ranges, RSRE, Malvern, 1980, item 6.

7. Silver, S., 'Microwave Antenna Theory and Design', McGraw Hill, 1949, pp.129-199.

8. Bennett, J.C., Anderson, A.P., McInnes, P.A. and Whitaker, A.J.T., 'Microwave holographic metrology of large reflector antennas', IEEE Trans., AP-24, 1976, pp.295-303.

9. Strickland, R.N., 'The prediction of antenna far-field patterns from measurements made in the near-field region', University of Sheffield, Department of Electronic and Electrical Engineering, undergraduate thesis, 1975.

10. Anderson, A.P., Bennett, J.C., Whitaker, A.J.T. and Godwin, M.P., 'Measurement and optimisation of a large reflector antenna by microwave holography', Proc. International Conference on Antennas and Propagation, London, 1978, pp.128-131.

11. Booker, H.G. and Clemmow, P.C., 'The concept of an angular spectrum of plane waves and its relationship to that of polar diagram and aperture distribution', Proc.IEE, 97(3), 1950, pp.11-17.

12. Paris, D.T., Leach, W.M. and Joy, E.B., 'Basic theory of probe-compensated near-field measurements', IEEE Trans., AP-26, 1978, pp.373-379.

13. Joy, E.B., Leach, W.M., Rodrigue, G.P. and Paris, D.T., 'Applications of probe-compensated near-field measurements', IEEE Trans., AP-26, 1978, pp.379-389.

14. Joy, E.B. and Paris, D.T., 'Spatial sampling and filtering in near-field measurements', IEEE Trans., AP-20, 1972, pp.253-261.

15. Kerns, D.M., 'Plane wave scattering matrix theory of antennas and antenna-antenna interactions', Nat.Bureau of Standards, report NBSIR 78-890, 1978.

16. Brown, J. and Jull, E.V., 'The prediction of aerial radiation patterns from near-field measurements', Proc.IEE, 108B, 1961, pp.635-644.

17. Leach, W.M. and Paris, D.T., 'Probe-compensated near-field measurements on a cylinder', IEEE Trans., AP-21, 1973, pp.435-445.

18. Borgiotti, G.V., 'Integral equation formulation for probe-corrected far-field reconstruction from measurements on a cylinder', IEEE Trans., AP-26, 1978, pp. 572-578.

19. British Aerospace Dynamics, 'Presentation of CNFT Antenna Measurement Facility', Stevenage, 1979.

20. Stratton, J.A., 'Electromagnetic Theory', McGraw Hill, 1941, pp.392-423.

21. Wood, P.J., 'Reflector Antenna Analysis and Design', Peter Peregrinus, 1980, pp.36-85.

22. Ludwig, A.C., 'Near-field/far-field transformations using spherical wave expansions', IEEE Trans., AP-19, 1971, pp.214-220.

23. Larsen, F.H., 'SNIFTC. Spherical near-field transformation program with probe compensation', Experimental spherical near-field test facility, final report, VII, Technical University of Denmark, Electromagnetics Institute, report R201, 1978.

24. Martsafey, V.V., 'Measurement of Electrodynamic antenna parameters by the method of synthesised apertures', Radio Eng. and Electron.Phys., 13, 1968, pp.1869-1873.

25. Ludwig, A.C., 'The definition of cross-polarisation', IEEE Trans., AP-21, 1973, pp.116-119.

26. Bracewell, R., 'The Fourier Transform and its Applications', McGraw Hill, 1965.

27. Ludwig, A.C., 'Numerical check on the accuracy of spherical-wave expansions', Electron.Lett., 8, 1972, pp.202-203.

28. Marvin, A., 'Inadequacy of the Rayleigh range criterion for superdirective arrays', Electron.Lett., 12, 1976, pp.415-416.

29. Arsac, J., 'Fourier Transforms and the Theory of Distributions', Prentice Hall, 1966.

30. Hamming, R.W., 'Numerical Methods for Scientists and Engineers', McGraw Hill, 1962.

31. Abramowitz, M. and Stegun, I.A., (ed) 'Handbook of Mathematical Functions', Dover, 1965.

32. Joy, E.B., 'Maximum near-field measurement error specification', Digest, IEEE AP-S, International Symposium, Stanford, 1977, pp.390-393.

33. Bach, H., Lintz Christensen, E., Hansen, J.E., Jensen, F. and Larsen, F.H., 'Facility design and test runs', Experimental spherical near-field test facility, final report, I, Technical University of Denmark, Electromagnetic Institute, report R208, 1979, pp.25-29.

34. Bennett, J.C., University of Sheffield, private internal communication.

35. Jensen, F., 'Computer simulation studies', Experimental spherical near-field test facility, final report, VI, TICRA ApS, report S-86-03, 1979.

36. Hess, D.W., Willwerth, F.G. and Johnson, R.C. 'Compact range improvements and performance at 30GHz', Digest, IEEE AP-S, International Symposium, Stanford, 1977, pp.264-267.

37. Evans, D., 'Microwaves', Radio Communication, 52, 1976, p.757.

38. Silver, S., 'Microwave Antenna Theory and Design', McGraw Hill, 1949, p.348.

39. Muntanga, E., University of Sheffield, private internal communication.

40. Thomsit, D.I., 'Colour display of microwave fields', Electronics and Power, 25, 1979, pp.408-412.